

# **Terrestrial and Space-based Applications of Microchannel Plate X-ray Optics**

Thesis submitted for the degree of  
Doctor of Philosophy  
at the University of Leicester

by

*James Peter Nussey*

Space Projects and Instrumentation Group  
Department of Physics and Astronomy  
University of Leicester

11<sup>th</sup> July 2005

## ***Declaration***

I hereby declare that no part of this thesis has been previously submitted to this or any other university as part of the requirement for a higher degree. The work described herein was conducted solely by the undersigned except for those colleagues and other workers acknowledged in the text.

---

**James Peter Nussey**

**11<sup>th</sup> July 2005**



***For Dad***

# Terrestrial and Space-based Applications of Microchannel Plate X-ray Optics

James Peter Nussey

## *Abstract*

This thesis describes the continued development of square pore microchannel plate (MCP) X-ray optics with a view to their application on terrestrial and space-based instrumentation.

The development of a lab-based Imaging X-ray Fluorescence Spectrometer (IXRFS) is described, incorporating an MCP optic to relay fluorescent flux, excited from uniformly illuminated target samples onto a Charge Coupled Device (CCD). Applications in mineralogy and scientific instrument calibration are investigated, with elemental maps spatially correlated to observed sample features in each case.

The soft X-ray focusing properties of one planar and two slumped MCP optics are evaluated with a view to their application on the future Lobster-ISS all-sky monitor. Best FWHM foci of 9.4' x 7.5' (planar) and 9.1' x 9.1' (slumped) are reported. Observed temporal variation in the angular resolution of a slumped MCP optic is attributed to the mechanical deformation of the optic during focusing. Multifibre misalignment is determined to be the major source of error in the focusing properties of the planar MCP.

The metallisation of the reflecting surfaces of MCP optics improves their high energy and wide angle response; metal films of iridium, ruthenium and nickel, deposited onto MCP optics using the Atomic Layer Deposition (ALD) and Electroless Nickel (EN) methods are characterised using the techniques of Auger Electron Spectroscopy (AES) and X-ray Reflectivity (XRR). Ruthenium and nickel-coated MCPs exhibit a shortfall in low-grazing angle reflectivity, not observed in the case of iridium, which is modelled with an RMS surface roughness of 26 Å.

The Lobster-ISS all-sky monitor is modelled to a range of specifications using a Monte-Carlo raytrace code to optimise performance. Iridium-coated MCP optics are found to provide the best modelled sensitivity for a variety of astrophysical objects. In this configuration, Lobster-ISS is modelled to have a 1 day limiting sensitivity of 0.32 mCrab.

## *Acknowledgements*

First and foremost, thanks go to my supervisor, Professor George Fraser, whose support and guidance over the last four years have been invaluable. Special thanks also go to John Lees, Jim Pearson, Nigel Bannister, Richard Ambrosi, Adam Brunton and Gareth Price for their seemingly limitless patience and encouragement during my time in the Space Research Centre.

Thanks also go to all the bad influences, namely James Carpenter, Adrian Martindale, Dave Smith, Steve Smith, Dean Talboys and Dan Thompson, who are responsible for many an enjoyable night out. To this effect, I would like to give a further mention to Richard Ambrosi, whose desperate attempts to keep us all on the straight and narrow were, unfortunately, always doomed to failure.

Thanks in particular to those survivors of the class of 2001, Jonathan Nichols, Scott England, Grant Allen and Fraser Hamilton, who have been there from the beginning; our experience as sub-wardens was one of the most harrowing of my life.

Special thanks go to Jonathan Parkinson, my sixth form teacher who persuaded me to understand physics instead of just learning it. Now look what's happened!

The completion of this thesis would not have been possible without the extraordinary support of my family. This is dedicated to all of you (even though you'll never understand it). In particular, Mum and Claire; you will never know how much I appreciate your support.

Finally, I would like to gratefully acknowledge the financial support received from the Engineering and Physical Sciences Research Council during my research studentship.

## *List of Publications*

Some of the results presented in this thesis have been incorporated into the following papers. The chapters to which these papers refer are given in brackets.

1. G.J. Price, G.W. Fraser, J.F. Pearson, I.B. Hutchinson, A.D. Holland, J.P. Nussey, D. Vernon, D. Pullan and K. Turner  
*"Imaging X-ray fluorescence spectroscopy using microchannel plate X-ray optics"*  
Spectroscopy Europe, 15, 8-13 (2003) [Chapter 2]
2. G.J. Price, G.W. Fraser, J.F. Pearson, J.P. Nussey, I.B. Hutchinson, A.D. Holland, K. Turner and D. Pullan  
*"Prototype imaging X-ray fluorescence spectrometer based on microchannel plate optics"*  
Review of Scientific Instruments, 75, 2314-2319 (2004) [Chapter 2]
3. J.P. Nussey, G.W. Fraser, N.P. Bannister and R. Fairbend  
*"Soft X-ray focusing using microchannel plate optics"*  
In preparation [Chapter 3]
4. J.P. Nussey, J.F. Pearson, G.W. Fraser, A.N. Brunton, N.P. Bannister, J.D. Carpenter, A. Martindale, F.J. Hamilton, R. Fairbend, S. Nenonen, T. Aaltonen, M. Ritala, M. Leskelä and D.D. Hall  
*"Characterisation of bare glass and metallised MCP X-ray optics"*  
In preparation [Chapters 4 and 5]
5. J.P. Nussey, N.P. Bannister and G.W. Fraser  
*"The Lobster-ISS X-ray all-sky monitor"*  
In preparation [Chapter 6]

# *Table of Contents*

<i>List of Abbreviations .....</i>	<i>v</i>
------------------------------------	----------

<b>Chapter 1</b>	<b>Ground and Space-based Applications of Microchannel Plate Optic Technology.....</b>	<b>1</b>
------------------	--	----------

1.1	Introduction.....	1
1.2	The Microchannel Plate .....	1
1.2.1	Microchannel Plate Detectors.....	2
1.2.2	MCPs as X-ray Optics .....	4
1.3	X-ray Focusing with MCP Optics.....	6
1.4	MCP Fabrication.....	11
1.4.1	MCP Slumping .....	14
1.4.2	MCP Coating .....	14
1.5	Terrestrial Applications of MCP Optics .....	15
1.5.1	Imaging X-ray Fluorescence Spectroscopy.....	15
1.5.2	High Intensity X-ray Sources .....	16
1.6	Space-based Applications of MCP Optics .....	16
1.6.1	Lobster-ISS.....	16
1.6.2	Bepi-Colombo .....	18
1.6.3	Auroral Imager .....	19
1.7	Overview.....	20

<b>Chapter 2</b>	<b>The Imaging X-ray Fluorescence Spectrometer .....</b>	<b>21</b>
------------------	--	-----------

2.1	Introduction.....	21
2.1.1	Imaging X-ray Fluorescence at Leicester .....	22
2.2	Experimental Configuration.....	26
2.3	Mineralogical Samples.....	30
2.4	Beagle 2 Calibration Target .....	35
2.5	IXRFS Source Development.....	44
2.6	Future Applications.....	47
2.6.1	Synchrotron Collaborations.....	47



2.6.2	Botany and Marine Biology .....	47
2.7	Conclusions.....	48
<b>Chapter 3</b>	<b>MCP Optics for Lobster-ISS .....</b>	<b>50</b>
3.1	Introduction.....	50
3.1.1	Lobster-ISS as an X-ray All Sky Monitor .....	50
3.1.2	Development of the Lobster-ISS X-ray All Sky Monitor.....	54
3.1.3	The Lobster Micropore Optics .....	56
3.2	Experimental Instrumentation.....	57
3.2.1	The Vacuum Test Facility .....	57
3.2.1.1	<i>The Microfocus X-ray Source</i> .....	59
3.2.2	The Tunnel Test Facility.....	61
3.2.3	MCP Detector .....	63
3.2.4	MCP Holding Jigs .....	63
3.3	Soft X-ray Focusing by Lobster Optics .....	65
3.3.1	Slumped MCP Optics .....	65
3.3.1.1	<i>HC001-A1</i> .....	65
3.3.1.2	<i>HC001-A2</i> .....	70
3.3.2	Planar MCP optics.....	71
3.4	Conclusions.....	78
<b>Chapter 4</b>	<b>Auger Electron Spectroscopy of MCP Optics.....</b>	<b>79</b>
4.1	The Coating Processes .....	79
4.1.1	Electroless Nickel .....	79
4.1.2	Atomic Layer Deposition .....	82
4.2	Depth Profiling of MCP Optics .....	86
4.2.1	Auger Electron Spectroscopy .....	86
4.2.2	Experimental Arrangements .....	88
4.2.3	Bare Glass MCP Optics.....	88
4.2.4	Metallised MCP Optics .....	91
4.2.4.1	<i>Ruthenium-coated MCP RU-1</i> .....	91
4.2.4.2	<i>Nickel-coated MCPs</i> .....	98
4.3	Conclusions.....	102

4.3.1	Bare Glass MCP [HC001-A4].....	102
4.3.2	Ruthenium-coated MCP [RU-1].....	103
4.3.3	Nickel-coated MCPs [NI-1, NI-3].....	103
<b>Chapter 5</b>	<b>The Soft X-ray Reflectivity of MCP Optics.....</b>	<b>104</b>
5.1	Introduction.....	104
5.2	X-ray Reflectivity Theory.....	105
5.3	Reflectivity Measurements at Daresbury SRS.....	107
5.3.1	Experimental Configuration .....	107
5.3.2	X-ray Reflectivity Modelling .....	110
5.3.3	Bare Glass MCPs.....	111
5.3.4	Nickel-coated MCPs.....	114
5.3.5	Ruthenium and Iridium-coated MCPs.....	124
5.4	Conclusions.....	129
5.4.1	Bare Glass MCPs [A4 and A8/1] .....	129
5.4.2	Nickel-coated MCPs.....	129
5.4.3	Ruthenium and Iridium-coated MCPs [RU-1 and IRID-1] .....	130
<b>Chapter 6</b>	<b>The Projected Capabilities of Lobster-ISS.....</b>	<b>131</b>
6.1	MCPTRACE: A Microchannel Plate X-ray Optic Raytrace Model .....	131
6.1.1	Reflection .....	132
6.1.2	Transmission.....	134
6.2	Effective Area of Lobster-ISS.....	135
6.3	Scientific return from Lobster-ISS.....	142
6.3.1	GRBs and AGN.....	142
6.3.2	Stellar Coronae .....	143
6.3.3	Cold Absorbers.....	144
6.4	Modelling the Sensitivity of Lobster-ISS .....	144
6.5	Discussion.....	149
6.6	Conclusions.....	157

**Chapter 7      Conclusions and Future Work..... 158**

7.1    The Imaging X-ray Fluorescence Spectrometer ..... 158

7.2    X-ray Focusing with MCP Optics..... 158

7.3    Characterisation of Bare Glass and Metallised MCP Optic Reflecting Surfaces ..... 159

7.4    The Lobster-ISS All-Sky Monitor ..... 161

*List of Addresses..... 162*

*Bibliography      ..... 164*



## *List of Abbreviations*

<b>ADC</b>	Analogue to Digital Converter
<b>AES</b>	Auger Electron Spectroscopy
<b>AFM</b>	Atomic Force Microscope
<b>AGN</b>	Active Galactic Nuclei
<b>ALD</b>	Atomic Layer Deposition
<b>ASM</b>	All-Sky Monitor
<b>BCC</b>	Body-Centred Cubic
<b>BESSY</b>	Berliner Elektronenspeicherring-Gesellschaft für Synchrotron Strahlung
<b>CAD</b>	Computer Aided Design
<b>CAM</b>	Centrifuge Accommodation Module (on ISS)
<b>CCD</b>	Charge Coupled Device
<b>CEM</b>	Channel Electron Multiplier
<b>CVD</b>	Chemical Vapour Deposition
<b>DIU</b>	Detector Interface Unit (on Lobster-ISS)
<b>EDX</b>	Energy Dispersive X-ray spectroscopy
<b>EN</b>	Electroless Nickel
<b>EPF</b>	Exposed Payload Facility (on ISS)
<b>EPSRC</b>	Engineering and Physical Sciences Research Council
<b>ESA</b>	European Space Agency
<b>ESCA</b>	Electron Spectroscopy for Chemical Analysis
<b>EXOSAT</b>	European X-ray Observatory SATellite
<b>FCC</b>	Face-Centred Cubic
<b>FOV</b>	Field Of View
<b>FWHM</b>	Full Width at Half Maximum
<b>FWZM</b>	Full Width at Zero Maximum
<b>GRB</b>	Gamma Ray Burst
<b>GRBM</b>	Gamma Ray Burst Monitor (on Lobster-ISS)
<b>GSC</b>	Gas Slit Camera (on MAXI)
<b>GSPARC</b>	Geological SPecimen ARChive
<b>HC</b>	Hardware Control (IXRFS data acquisition software)
<b>HRC</b>	High Resolution Camera (on Chandra)
<b>HRI</b>	High Resolution Imager (on Einstein)

<b>HV</b>	High Voltage
<b>IC</b>	Ion Chamber
<b>IDD</b>	Instrument Definition Document
<b>ISS</b>	International Space Station
<b>IXRFS</b>	Imaging X-Ray Fluorescence Spectrometer
<b>JEM</b>	Japanese Experiment Module (on ISS)
<b>LEO</b>	Low Earth Orbit
<b>MAXI</b>	Monitor of All-Sky X-ray Image
<b>MBS</b>	MossBauer Spectrometer (on Beagle 2)
<b>MCP</b>	MicroChannel Plate
<b>MEDA</b>	Medium Energy Detector Array (on EXOSAT)
<b>MIC</b>	MICroscope (on Beagle 2)
<b>MIXS</b>	Mercury Imaging X-ray Spectrometer (on Bepi-Colombo)
<b>MOXE</b>	MOnitoring X-ray Experiment (on Spectrum X-Gamma)
<b>NASA</b>	National Aeronautics and Space Administration
<b>NASDA</b>	NAtional Space Development Agency of Japan
<b>PALI</b>	Planetary Analogue Library
<b>PCTFE</b>	Poly-Chloro-Tetra-Fluoro-Ethylene
<b>PIPSS</b>	PPARC Industrial Programme Support Scheme
<b>PIXE</b>	Proton Induced X-ray Emission
<b>PPARC</b>	Particle Physics and Astronomy Research Council
<b>PSF</b>	Point Spread Function
<b>PSPC</b>	Position Sensitive Proportional Counter(s) (on ROSAT)
<b>RAL</b>	Rutherford Appleton Laboratory
<b>ROSAT</b>	RÖntgen SATellite
<b>RMS</b>	Root Mean Square
<b>RSPP</b>	Radio and Space Plasma Physics
<b>RXTE</b>	Rossi X-ray Timing Explorer
<b>SAA</b>	South Atlantic Anomaly
<b>SCS</b>	Stereo Camera System (on Beagle 2)
<b>SEM</b>	Scanning Electron Microscope
<b>SIMS</b>	Secondary Ion Mass Spectrometry
<b>SMBH</b>	SuperMassive Black Hole
<b>SMEX</b>	Small Mission EXplorer

<b>SPI</b>	Space Projects and Instrumentation
<b>SRS</b>	Synchrotron Radiation Source
<b>SSC</b>	Solid-state Slit Camera (on MAXI)
<b>STP</b>	Solar Terrestrial Physics
<b>SuperDARN</b>	Super Dual Auroral Radio Network
<b>TEC</b>	ThermoElectric Cooler
<b>TMP</b>	TurboMolecular Pump
<b>TRP</b>	Technology Research Programme
<b>TTF</b>	Tunnel Test Facility
<b>UHV</b>	Ultra-High Vacuum
<b>UV</b>	Ultra Violet
<b>VTF</b>	Vacuum Test Facility
<b>VUV</b>	Vacuum Ultra Violet
<b>WABS</b>	Wisconsin ABSorption
<b>XEUS</b>	X-ray mission for Evolving Universe Spectroscopy
<b>XRF</b>	X-Ray Fluorescence
<b>XRR</b>	X-Ray Reflectivity
<b>XRS</b>	X-Ray Spectrometer (on Beagle 2)



# Chapter 1      Ground      and      Space-based      Applications      of Microchannel Plate Optic Technology

## 1.1      Introduction

Microchannel plate (MCP) optics are a novel form of X-ray optic, part of a larger family of capillary optics. Capillaries, or channels as they are commonly referred, are stacked together to form a *capillary array*; light is transported along their length through the process of reflection from the intrachannel surfaces. The refractive index of a dielectric in the X-ray waveband is slightly less than unity, thus it is the phenomenon of total external reflection rather than refraction that most lends itself to the focusing of X-rays (Underwood, 1979; Willingale, 1984). While *refractive* X-ray optics are currently in development (Lengeler, 2001; Artemiev, 2005), the technology remains in its infancy. The continued development of MCP optics over the past 15 years has meant that they are now reaching a level of technical maturity where they may begin to have both terrestrial and space-based applications, and the exploitation of MCP optics forms the basis of this thesis.

This chapter begins with a chronological history of the MCP describing its original, intended application as a charge multiplier and its subsequent use in X-ray detection (*Section 1.2*). An insight into the evolution of MCP optics in the broader context of X-ray optics is followed by an introduction to the focusing properties of MCP optics (*Section 1.3*). The process of MCP optic manufacture is covered in *Section 1.4*, with an introduction to a variety of both ground and space-based applications of MCP optic technology given in *Sections 1.5* and *1.6* respectively. Finally, a general overview of this body of work is given in *Section 1.7*.

## 1.2      The Microchannel Plate

The origin of the MCP may be traced back to continuous dynode Channel Electron Multipliers (CEMs), which were independently developed at the Metallurgical Institute of the Academy of Sciences in the former Soviet Union, (Oschepkov et al. 1960), the US-based Bendix Research Laboratories (Goodrich and Wiley, 1962) and the Mullard Research Laboratories in the UK (Adams and Manley, 1965). CEMs are tubes, manufactured from either ceramic or glass, with a thin semiconducting layer along the length of the inner surface. It was realised that if these tubes could be miniaturised and stacked into arrays, they could be used as position sensitive photon

counting detectors, subsequently named *microchannel plates*; to this end, they were developed secretly by the military as image intensifiers during the cold war, but were ultimately declassified in the late 1960s (Ruggieri, 1972). Since then, MCPs have been widely used in the scientific community for the detection of UV, visible and X-ray radiation and for the detection of charged particles. Although not the focus of this thesis, a discussion of MCP detectors follows, to provide a historical background to the MCP, and because many of the images in *Chapter 3* of this thesis were generated using MCP detector technology.

### 1.2.1 Microchannel Plate Detectors

When a photon or charged particle with sufficient energy enters an MCP channel and strikes the intrachannel wall, it interacts via the photoelectric effect; upon its emergence into the channel, the ‘primary’ photoelectron may be accompanied by one or more secondary electrons. (Fraser, 1989). A potential difference applied across the length of the channel then accelerates the liberated electrons down the channel, where further interactions with the intrachannel surfaces cause an exponential growth in current along the channel length (*Figure 1.1*). In this way, a single incident photon or electron may cause a sizeable charge to be developed at the channel exit (gains are typically  $< 10^4$  for a single MCP; Fraser, 1989). Channels must be sufficiently evacuated that the mean free path of the secondary electrons is of the order of the distance between subsequent collisions with the intrachannel surfaces.

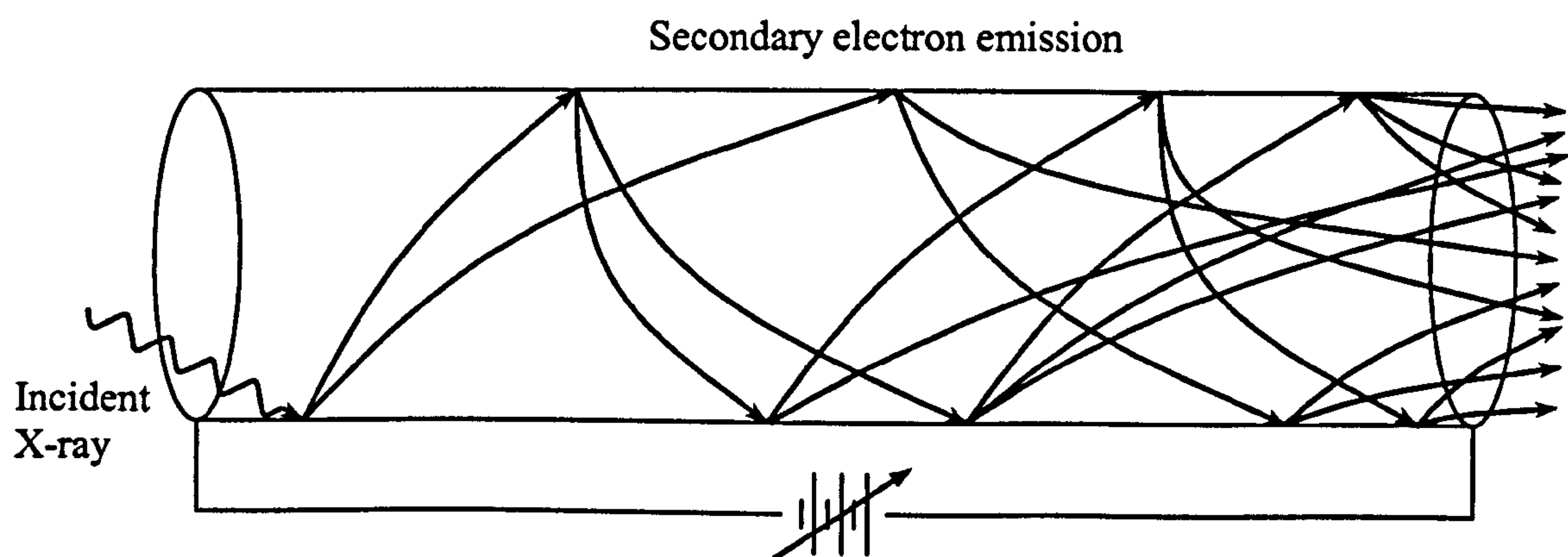


**Figure 1.1.** *The principle of operation of a microchannel plate detector. A charged particle or photon (in this case an X-ray) excites a number of secondary electrons from the intrachannel surface. The electrons are accelerated according to an applied bias, where subsequent collisions with the channel walls create an electron avalanche at the channel exit. Gains of  $10^4$  are possible from a single photon or charged particle incident at the channel entrance.*



In practice, a succession of MCPs may be applied to further increase signal gains (for the work described in this thesis, a detector comprising two MCPs is used). For this application, the channels are not orientated perpendicular to the surface of the MCP but are *tilted* by an angle known as the *bias angle*, typically between  $6^\circ$  and  $13^\circ$ . The two MCPs are then stacked in the *chevron* configuration shown in *Figure 1.2*.

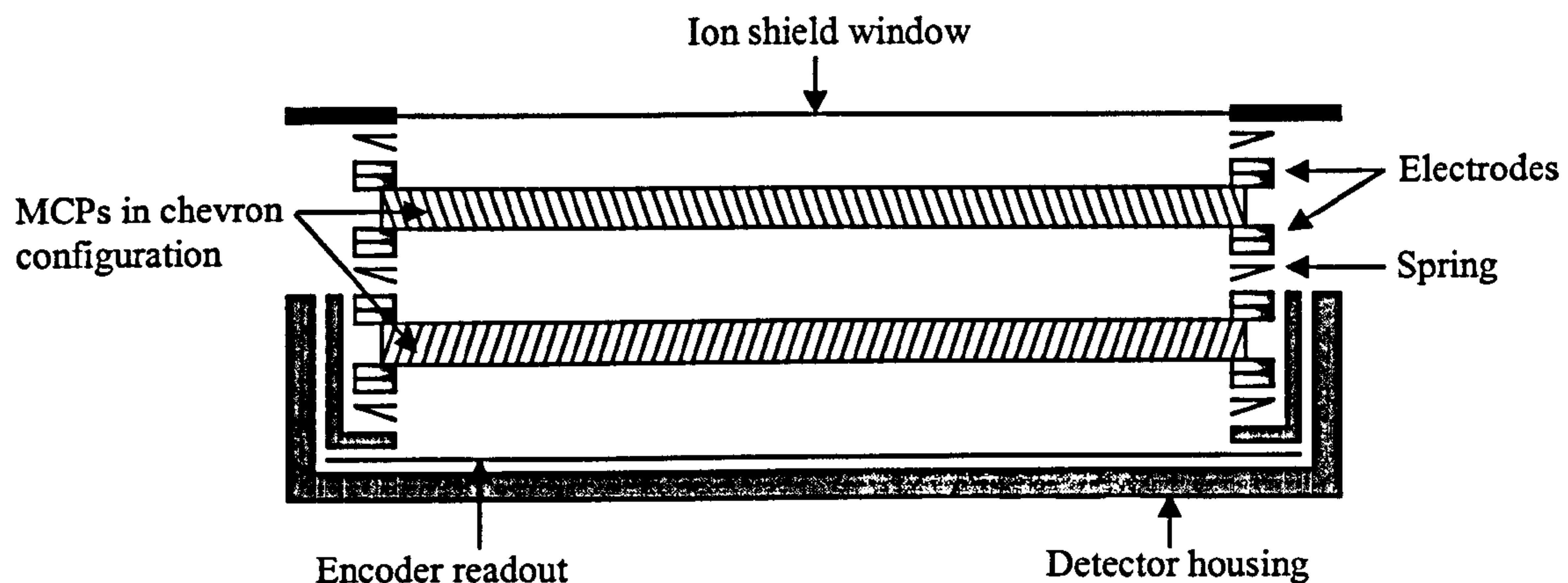


**Figure 1.2.** A two stage microchannel plate detector in the chevron configuration. The MCPs are orientated such that the channel tilts are set opposite one another in order to prevent ion feedback. Each electrode is electrically insulated from the supporting metal springs.

During charge multiplication, electrons collide with residual gas molecules; the resulting ions are then accelerated in the opposite direction to the electron flow and also have the opportunity to collide with the intrachannel walls, liberating additional secondary electrons. Ion generation occurs more commonly in the rear MCP due to the presence of increased numbers of electrons. Ion fluxes in the front MCP must be minimised since the resultant secondary electrons will be amplified into a significant measurable signal at the exit of the rear MCP; these electrons can introduce considerable noise levels into the system. The chevron configuration minimises the passage of ions from the bottom to the top MCP and thus reduces noise in the image.

Microchannel plate detectors have been at the forefront of X-ray astronomy since their use in the High Resolution Imager (HRI) aboard the first dedicated X-ray telescope, Einstein, in 1978 (Schreier, 1980). MCP detectors currently form the basis of the High Resolution Camera (HRC) aboard NASA's Chandra observatory, launched in 1999 (Winkler et al. 1993, Zombeck et al. 1995). In this particular case, large format  $100 \times 100 \text{ mm}^2$  square MCPs of circular channel

cross-section and diameter  $12.5\ \mu\text{m}$  (on a  $15\ \mu\text{m}$  pitch) are employed, with an MCP channel aspect ratio (the ratio of channel length  $L$  : channel width  $D$ ) of 120:1. It is this ratio, rather than  $L$  alone, that determines the gain of an MCP as a charge multiplier; gains are also varied by altering the potential difference across the MCP. A photocathode (for example CsI) may also be used to further increase the detection efficiency. More detailed discussions of MCP-based detectors may be found in Wiza, 1979 and Fraser, 1989.

### 1.2.2 MCPs as X-ray Optics

Ehrenberg first proposed the idea of X-ray focusing using the reflective properties of polished substrates (Ehrenberg, 1947). In the following year, Kirkpatrick and Baez proposed a configuration where reflective ellipsoid surfaces are positioned orthogonally to one another, as shown in *Figure 1.3* (Kirkpatrick and Baez, 1948). When a point source is reflected from an ellipsoid, the result is a line focus; the Kirkpatrick-Baez configuration uses the two successive mirrors to bring X-rays back to a point focus.

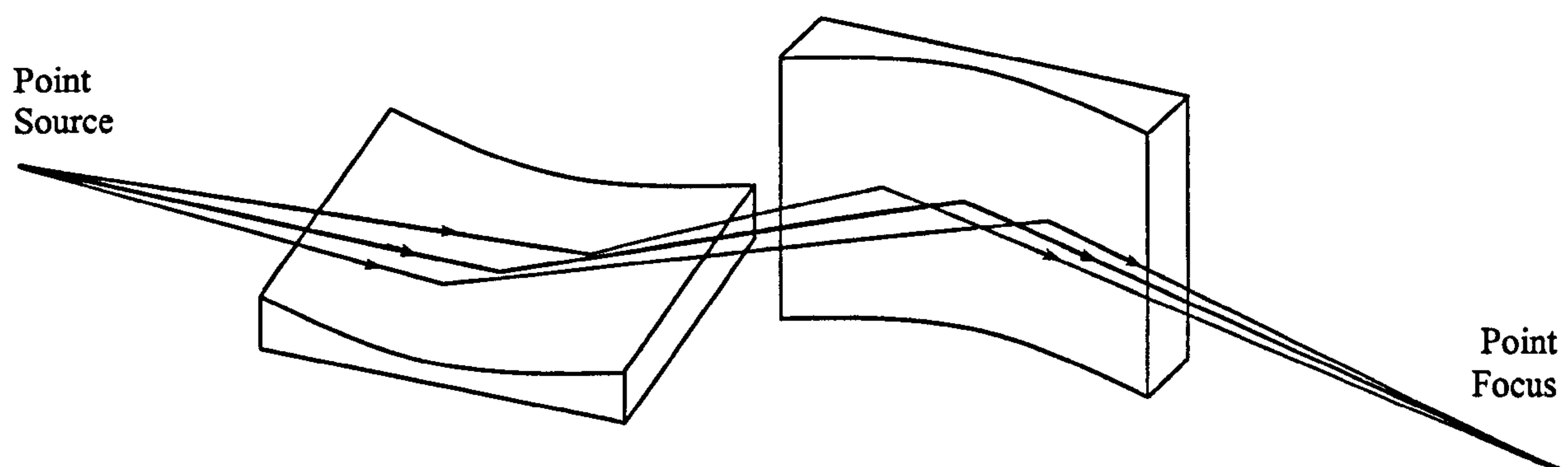


**Figure 1.3.** *The Kirkpatrick-Baez mirror configuration. A point source focused from a mirror of ellipsoid profile is brought to a line focus. The subsequent, orthogonal mirror (again of ellipsoid surface profile) reflects the rays back to a point focus. Such mirrors may be positioned in grid-like arrays; Square pore microchannel plate optics approximate a grid-like array of these optical elements.*

The basis for capillary X-ray optics appeared in 1975, when Schmidt (1975) proposed a configuration where two sets of reflecting planes are positioned perpendicular to the surface of a cylinder (and to one another). An optic with a potentially unlimited Field Of View (FOV) in 1 dimension could be created, focusing X-rays down onto a cylinder at half the radius of curvature



of the optic (*Figure 1.4*). Angel (1979) extended the idea, by proposing that square arrays of mirrors could be “slumped” or elastically bent onto the surface of a sphere, thus providing a 2-D imaging device. However, Angel could not take the credit for the concept; he read a paper published by Land (1978) which identified this as the mechanism by which lobsters and other crustaceans ‘see’. Optics operating under this principle are thus named *lobster-eye optics*.

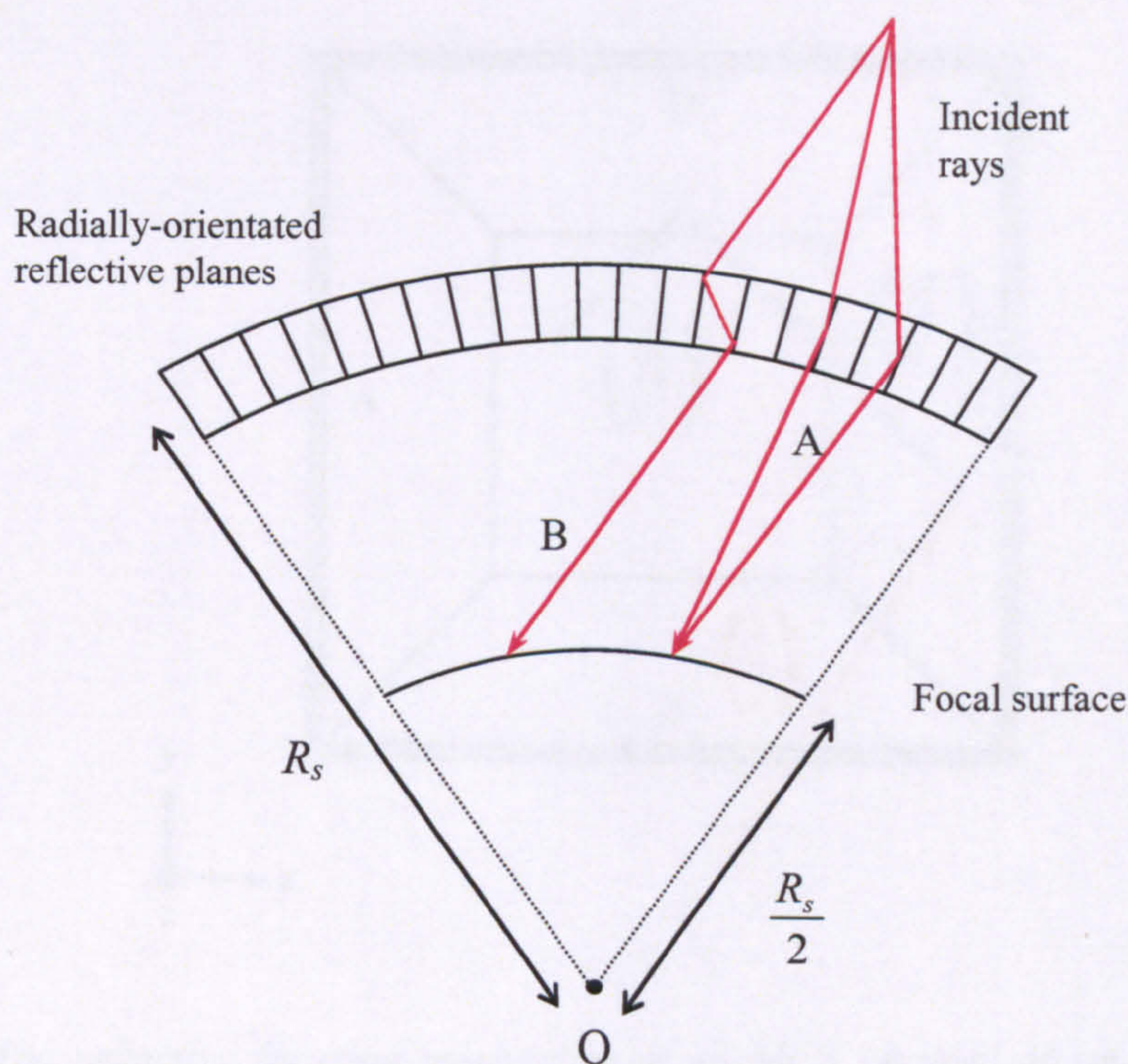


**Figure 1.4.** Schematic cross-section of Schmidt’s one dimensional ‘focusing collimator’. Incident rays undergoing an odd number of reflections (A) from the radially orientated walls, arranged on the surface of a cylinder (with radius of curvature  $R_s$ ) are focused into a line on the surface of a cylinder with radius  $\frac{R_s}{2}$  (with both cylinders sharing a common centre O). Rays not reflected or reflected an even number of times (B) are not focused.

The ellipsoid profiles of the two mirror surfaces in the Kirkpatrick-Baez configuration have a large radius of curvature, which may be approximated by planes (Joy and Weisskopf, 1992). A paper published by Wilkins et al. (1989) recognised that if channels of square cross-section could be manufactured, an MCP could provide an approximation to the Kirkpatrick-Baez configuration and thus a means of realising the lobster-eye geometry.



Another form of capillary X-ray optic is the *Kumakhov lens* (Kumakhov and Komorov, 1990). In this case, glass fibres are bundled together and act as waveguides; light is transported from one end to the other through a series of total external reflections from the intrafibre wall, where grazing angles are minimised to reduce absorption. However, each fibre must be set by hand and so Kumakhov lenses are currently very expensive to produce and have no true imaging capability.

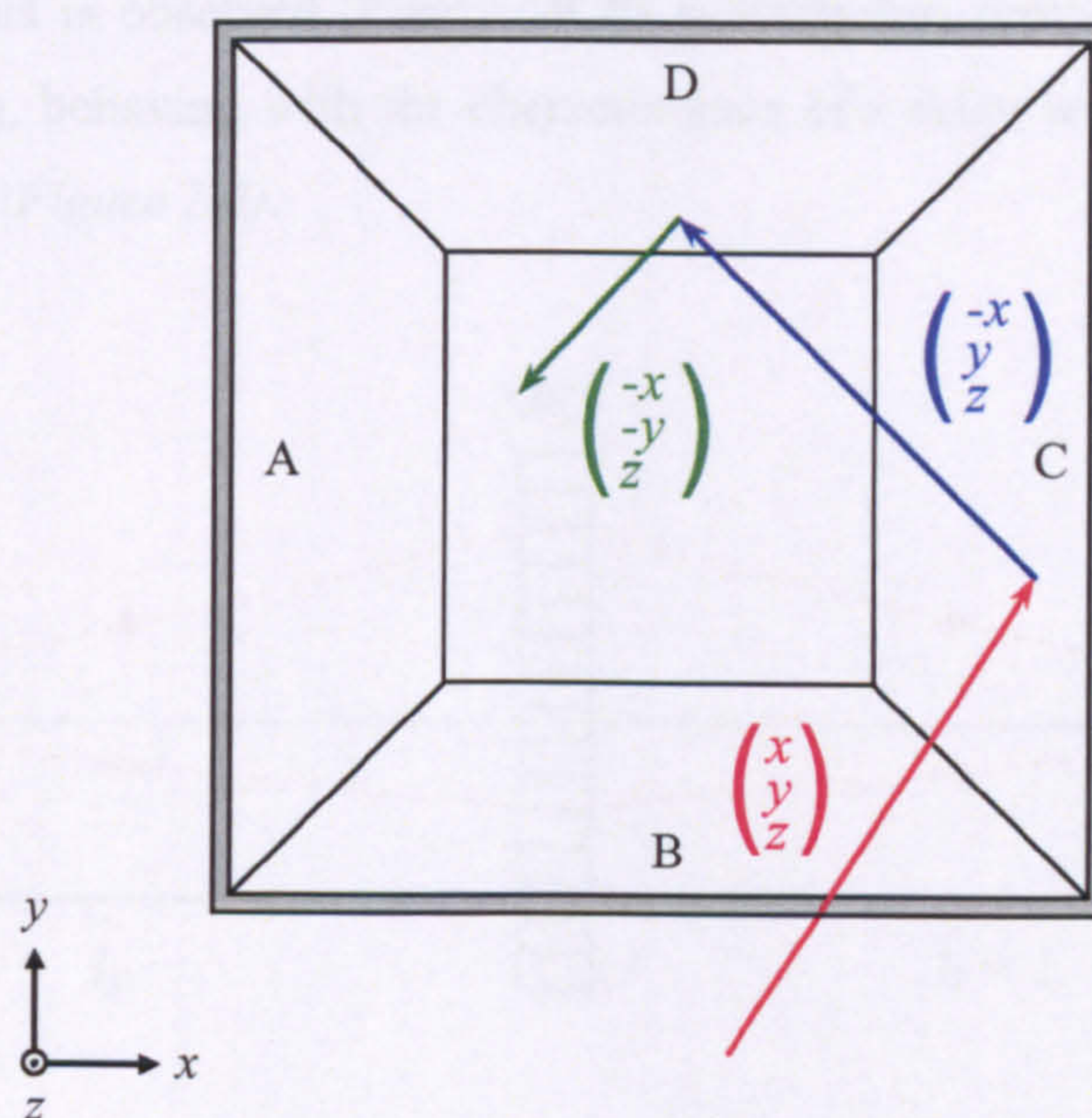


**Figure 1.5.** The reflective focusing mechanism of an MCP channel of square cross-section. Rays reflected an odd number of times by each of the orthogonal channel walls become part of the central or ‘true’ focus. An incident ray (red) is reflected from the channel wall described by the  $yz$  plane (wall C). This reflected ray (blue) is further reflected from the orthogonally positioned wall D (defined by the  $xz$  plane) and emerges from the channel on the other side (green). Through the channel, the  $x$  and  $y$  velocity components of the ray have been reversed; thus, providing source distance  $l_s = \text{image distance } l_i$ , a ray originating at a point  $(x,y)$  on the source plane is focused to the same 2 dimensional coordinate  $(x,y)$  on the image plane.

### 1.3 X-ray Focusing with MCP Optics

The focusing mechanism of MCP optics is based on the specular reflection of X-rays from the MCP intrachannel surfaces (Figure 1.5). Upon entering a channel, an X-ray may reflect from a surface, thus reversing the velocity component in the direction perpendicular to the plane defined



by the channel wall. In the case of planar MCPs, if a ray originating from the source plane at a point  $(x,y)$  enters the MCP and is reflected once from two orthogonal channel walls before exiting the MCP (e.g. walls  $C$  and  $D$  in *Figure 1.5*), it will be focused onto the image plane at the same coordinates  $(x,y)$  providing source and image distances are equal ( $l_s = l_i$ ). Strictly, this is only true if the reflections (in each plane) take place at the midpoint of the channel; as previously mentioned, the MCP geometry is only an approximation to the Kirkpatrick-Baez configuration; as, in practice, reflections occur either side of this midpoint,  $l_s$  and  $l_i$  are no longer equidistant and a smearing of the focus is observed. Planar MCPs nevertheless provide a means of achieving point to point focusing, behaving with the characteristics of a relay lens of unity magnification (Chapman et al. 1991) (*Figure 1.6*).

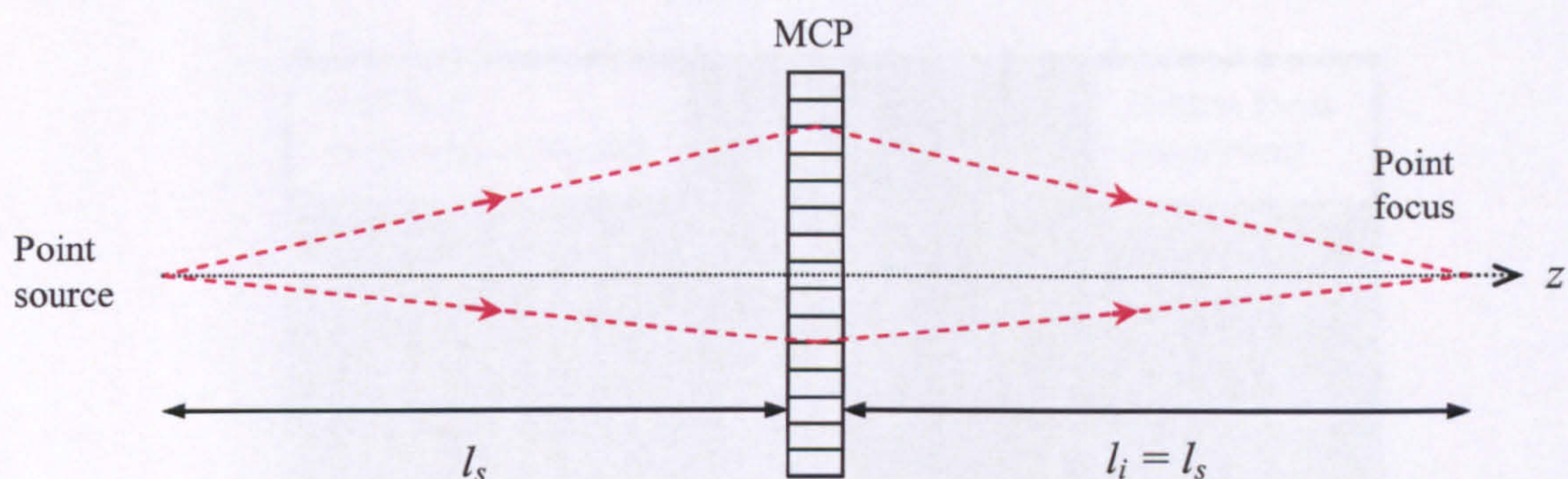


**Figure 1.6.** Point to point focusing using planar MCP optics.

The Point Spread Function (PSF) of a square pore MCP optic comprises three separate components; a ray contributing to a particular focal component will have followed a particular path through the MCP, characterised by the number of reflections it has undergone from each of the two channel wall orientations. For example, if a ray is reflected an odd number of times from one channel orientation, (e.g. from either walls  $A$  or  $C$  on *Figure 1.5*) and an even number of times in the other channel orientation (e.g. walls  $B$  or  $D$ ) it is referred to as an *odd-even* or an *even-odd* ray. The three focal components, intrinsic to square pore MCP focusing may be described as follows:

- **odd-odd** rays contribute to the central or true focus; the ray in *Figure 1.5* is reflected once from each channel orientation.



- *even-odd and odd-even rays contribute to two line foci, perpendicular to one another and coinciding at the true focus, providing a cruxiform focal component. The 'cross-arms' are orientated perpendicular to the channel surface from which they were reflected.*
- *even-even rays (including rays that are unreflected or 'straight-through' rays) form a diffuse 'halo' over the square area defined by the extents of the two cross-arms.*

An experimental image of a point source with a planar, square pore, square-packed MCP optic comprising all three focal components is shown in *Figure 1.7*.

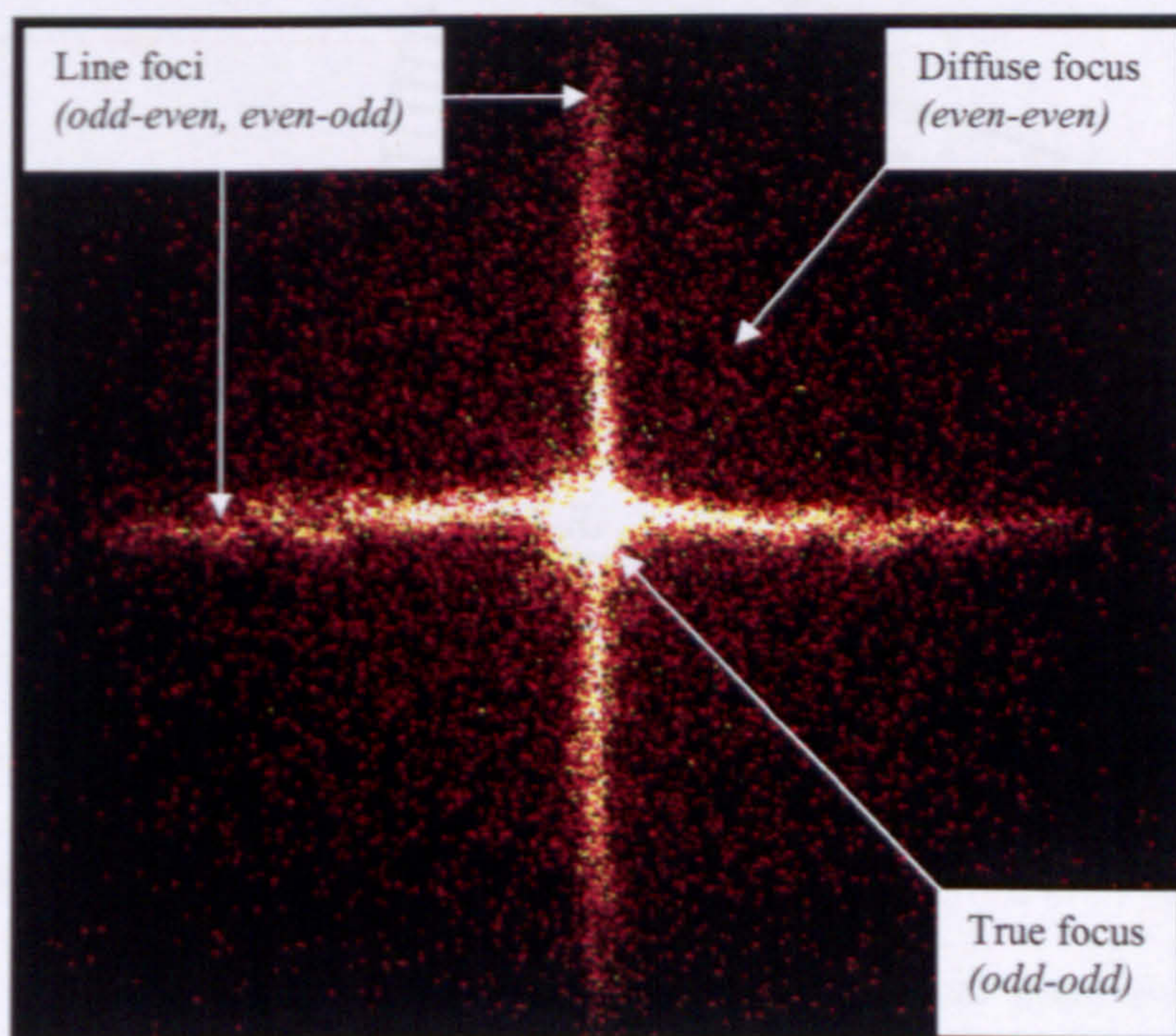


**Figure 1.7.** *A point source imaged with a planar, square pore, square-packed MCP optic showing the contributions from the individual true, line and diffuse foci. Image taken using Cu-L (930 eV) X-rays in the Tunnel Test Facility, a 20 m beamline at the University of Leicester.*

For astronomical applications, a different optical geometry is required due to large source distances. Angel's lobster-eye geometry, illustrated in *Figure 1.8*, is realised by spherically 'slumping' planar MCP optics, such that all channels point towards a common centre. The radius of curvature of the optic is termed the *slump radius*, hereafter denoted  $R_s$ . With this geometry, a quasi-parallel beam of X-rays may be focused onto the surface of a second sphere of half the



radius of curvature of the optics, both sharing a common origin. This optical configuration obeys the lens equation

$$\frac{1}{l_i} - \frac{1}{l_s} = \frac{2}{R_s} \quad (1.1)$$

where  $R_s > 0$  when the source is positioned to the convex side of the optic (Chapman et al. 1991). The first true slumped MCP-based lobster-eye focusing images were reported by Brunton (1995).

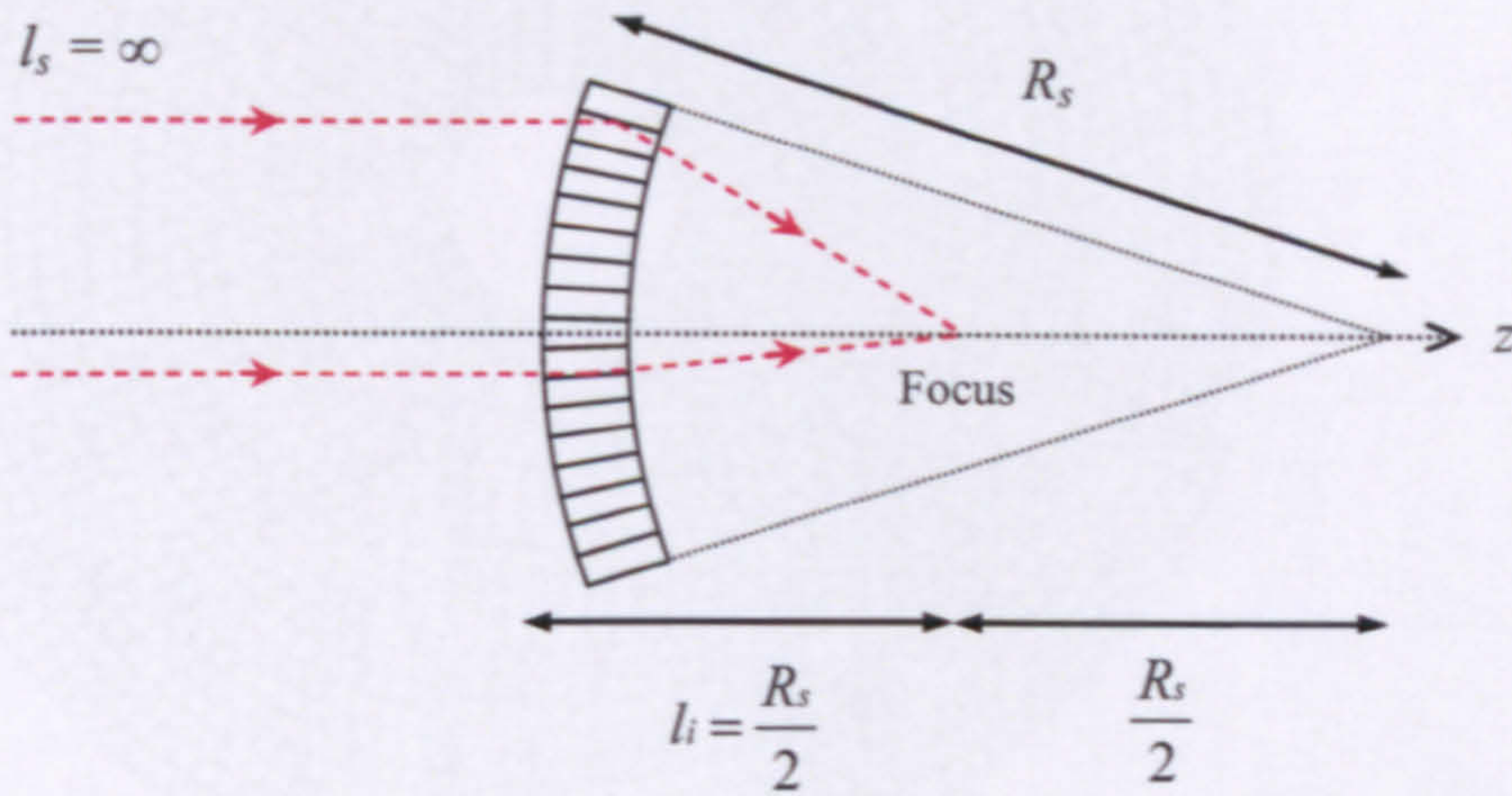


**Figure 1.8.** A slumped MCP optic will focus quasi-parallel X-rays from infinity ( $l_s = \infty$ ) to a point on the optical ( $z$ ) axis where  $l_i = \frac{R_s}{2}$ . Conversely, this optical geometry may be used to expand a point source to a quasi-parallel beam (by positioning the point source ‘behind’ the optic, at the ‘focus’). This MCP optic – point source coupling is the principle behind high intensity X-ray sources (Section 1.5.2).

An alternative packing geometry for channels of square cross section was proposed by Willingale et al. (1998). In this *radial-packing* geometry, multifibres are stacked in concentric rings around a circular, solid core (Figure 1.9). The resulting focus has a PSF with circular symmetry, advantageous over the cruxiform image structure provided by the square-packing geometry. By combining two slumped, radially-packed MCP optics, a conical approximation to the Wolter type I geometry may be achieved (Wolter, 1952). Unfortunately, due its circular symmetry, the radially-packed geometry is not easily tiled, resulting in a limited FOV compared to that of the



square-packing geometry. The radial-packing / Wolter I MCP optic geometries are not studied in this thesis; Price (2001) and Price et al. (2002) cover the subject in detail.

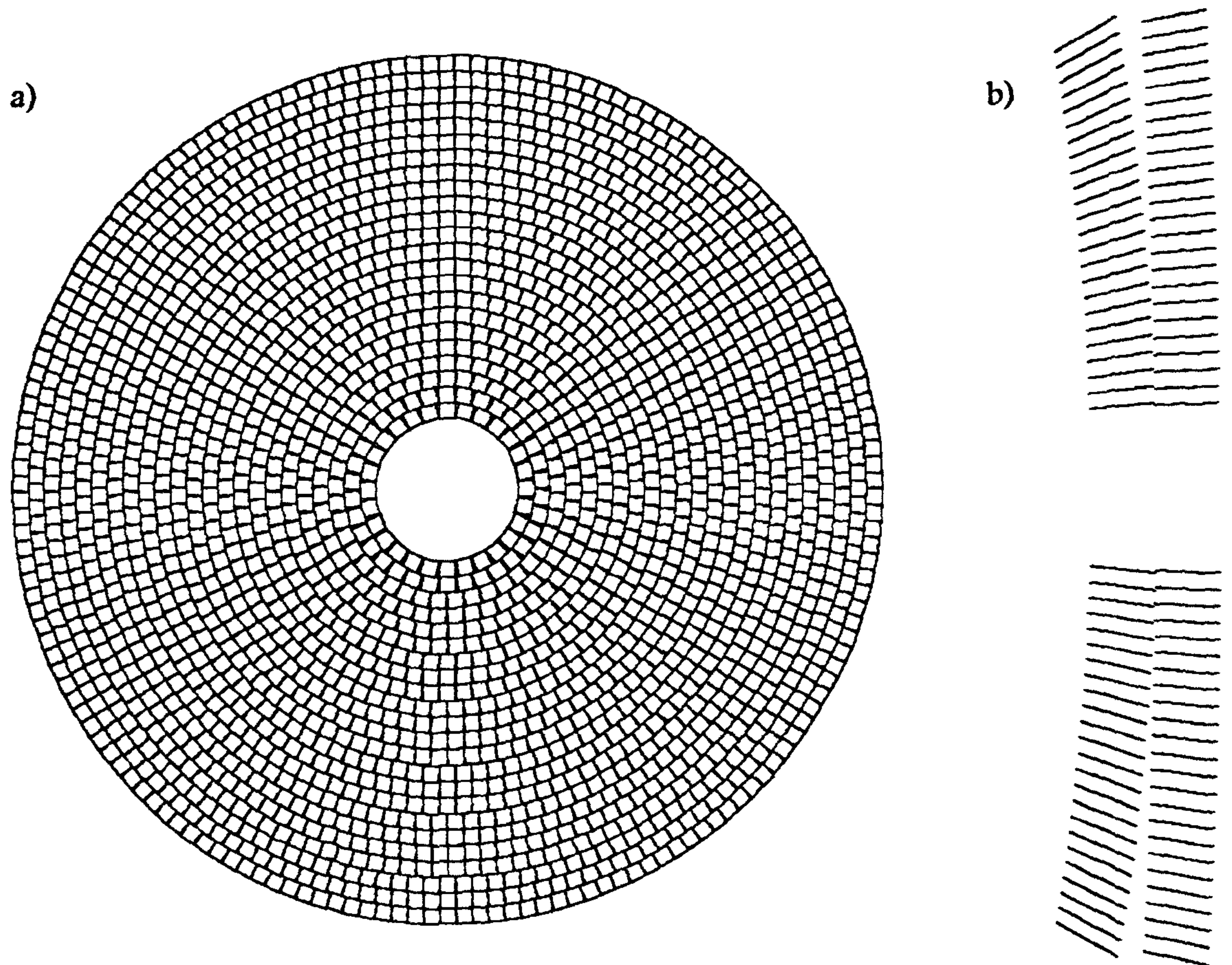


**Figure 1.9.** *The radial packing geometry of a single square pore MCP optic (a), showing the arrangement of the square multifibres in concentric rings around a solid circular core. The Wolter I geometry may be approximated by combining two successive radially-packed MCPs, with (b) illustrating how they are slumped relative to one another (Rays enter the channels from the right). From Price (2001).*

In the X-ray waveband, diffraction effects from MCP channel apertures are negligible; X-ray energies of 100 eV and above correspond to wavelengths shorter than 125 Å, whereas MCP optics with channel widths of 20 µm have been used throughout this work. The majority of work was performed with MCP optics manufactured to the same specification, shown in *Table 1.1*. All MCPs were manufactured by Photonis SAS. A photograph of a variety of MCP optics is shown in *Figure 1.10*.



---

<i>Side length (mm)</i>	<i>40 x 40</i>
<i>Channel width <math>D</math> (<math>\mu\text{m}</math>)</i>	<i>20</i>
<i>Channel length <math>L</math> (mm)</i>	<i>1.0</i>
<i>Channel pitch <math>P</math> (<math>\mu\text{m}</math>)</i>	<i>24</i>
<i>Channel aspect ratio (<math>L:D</math>)</i>	<i>50:1</i>
<i>Open area fraction (%)</i>	<i>69</i>
<i>Glass material</i>	<i>Philips type 297</i>
<i>Radius of curvature <math>R_s</math> (mm)</i>	<i>750</i>

---

**Table 1.1.** *Nominal manufacturing specifications of MCP optics used in this thesis (unless otherwise stated). The radius of curvature, or slump radius  $R_s$ , applies to slumped MCPs only. All MCP optics manufactured by Photonis SAS.*

## 1.4 MCP Fabrication

Irrespective of their intended application, microchannel plates are manufactured using essentially the same process (*Figure 1.11*). An acid soluble core glass of the required channel cross-section (i.e. square) is inserted into a hollow cladding glass tube to form what is known as a *couple*. The core glass provides support during manufacture. The couple is hung at the top of a heated drawing tower and drawn until it is of the order of 1 mm wide. It is then cut to lengths of approximately 500 mm, which are named the *first draw fibres*. These are manually stacked into *multifibre bundles*, with the stacking configuration dependent on the cross-sectional shape of the fibres. The multifibre bundles are drawn again and cut down to suitable lengths of around 100 mm. This process is repeated until the required channel widths are obtained (up to four draws have been used at Photonis SAS; Martin, 2000).

If the intended MCP channel geometry is square, then the multifibres are then stacked into a *block*, which has the final cross-sectional dimensions of the desired microchannel plate. The block is encased within a steel box and fused in a high-temperature furnace, where it is also subject to large mechanical pressures; this process is named *ram fusion*. For MCPs with channels of circular cross-section, multifibres are instead stacked in a hexagonal configuration and encased within a glass envelope, named a *boule*. In this case, the high pressures applied mechanically in the ram fusion process are replaced by raising the air pressure within the furnace; this process is named *bomb fusion*.



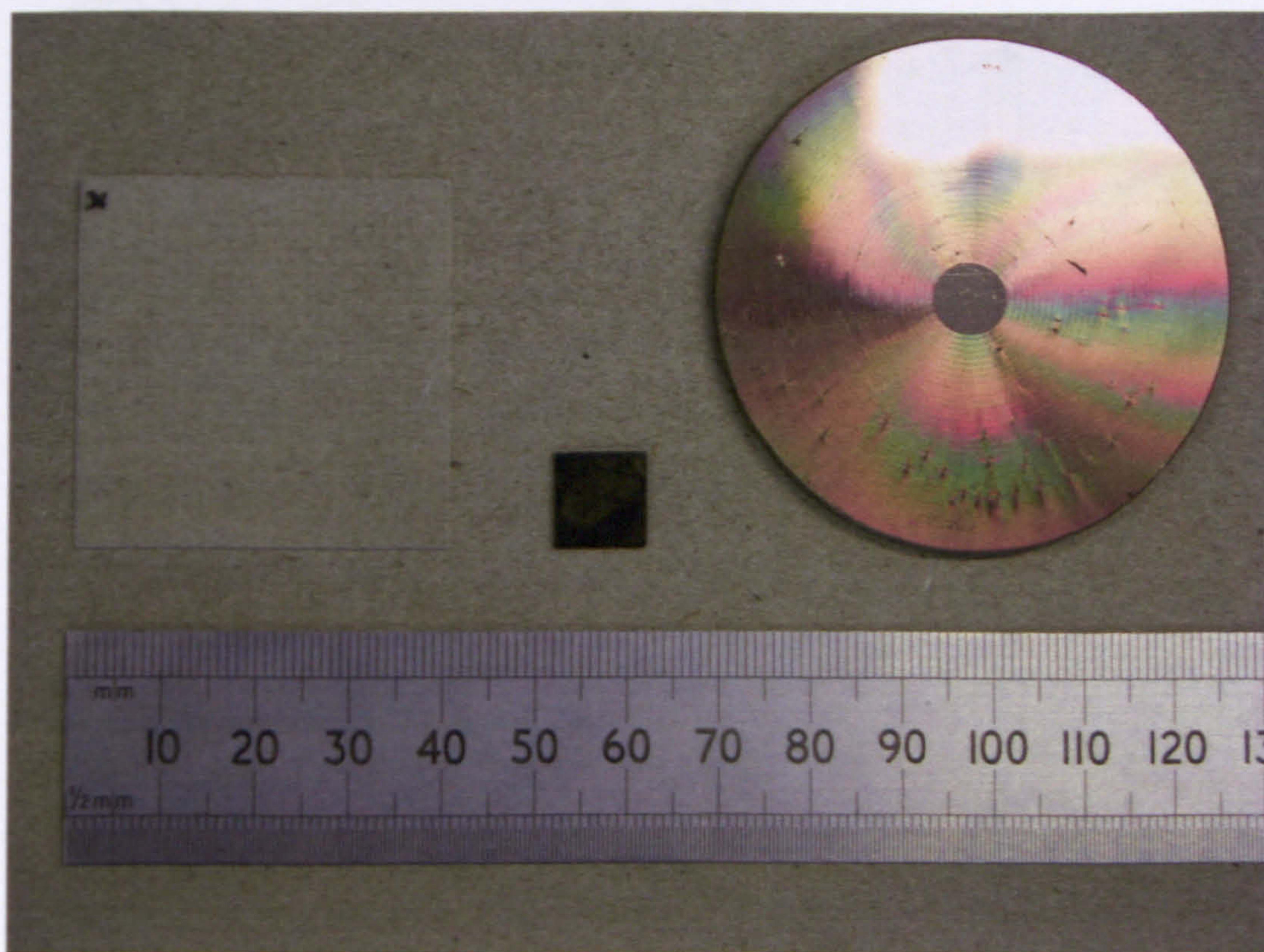


**Figure 1.10.** A selection of microchannel plate optics. On the left is a planar, bare glass, square pore, square-packed MCP optic manufactured to the specifications in Table 1.1. In the centre is a nickel-coated MCP optic, with a radially-packed, square pore optic to the right.

A diamond saw is used to cut slices from the block, which are subsequently ground and polished. For MCPs intended to be used in detector applications, bias angles are controlled by the angle at which the saw meets the block; bias angles may be manufactured to an accuracy of  $0.1^\circ$  (Price, 2001). The MCP ‘blanks’ are then etched in a constantly flowing solution of hydrochloric acid for several hours, removing the softer core glass from the outer cladding glass. What emerges from the acid bath is a planar MCP.

MCPs intended for use as charge multipliers (detector plates) require further processing. They are heated in a hydrogen atmosphere, a *hydrogen reduction* process causing a semiconducting layer to be formed on the channel surfaces, raising the secondary electron yield. A conductive electrode coating is deposited on both MCP faces and depending on their environment and application, a suitable photocathode may be applied to one side of the MCP. The manufacturing process is discussed further in Brunton (1994) and Martin (2000).



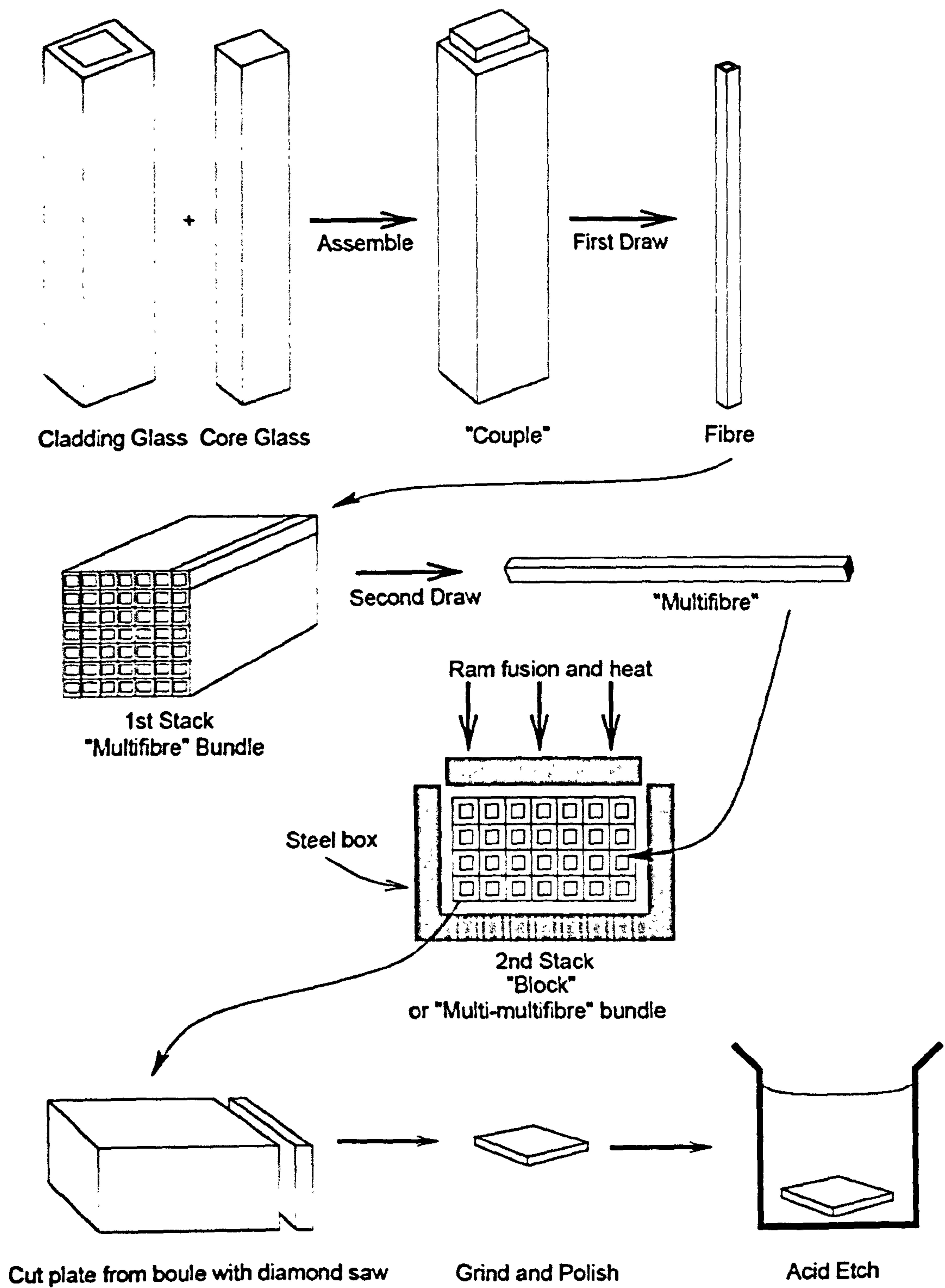


**Figure 1.11.** Diagrammatic overview of the manufacturing process of square pore MCP optics.  
 From Martin (2000).



### 1.4.1 MCP Slumping

The lobster-eye geometry may be realised by slumping planar MCP optics (*Figure 1.12*). The planar MCP is sandwiched between two heavy, positive and negative stainless steel formers which have been machined to the required radius of curvature. In order to maintain this profile, a thermal cycle is required; to this end, the MCP is then annealed at around 440 °C (for Philips type 297 lead glass) and slowly cooled to remove mechanical stresses.

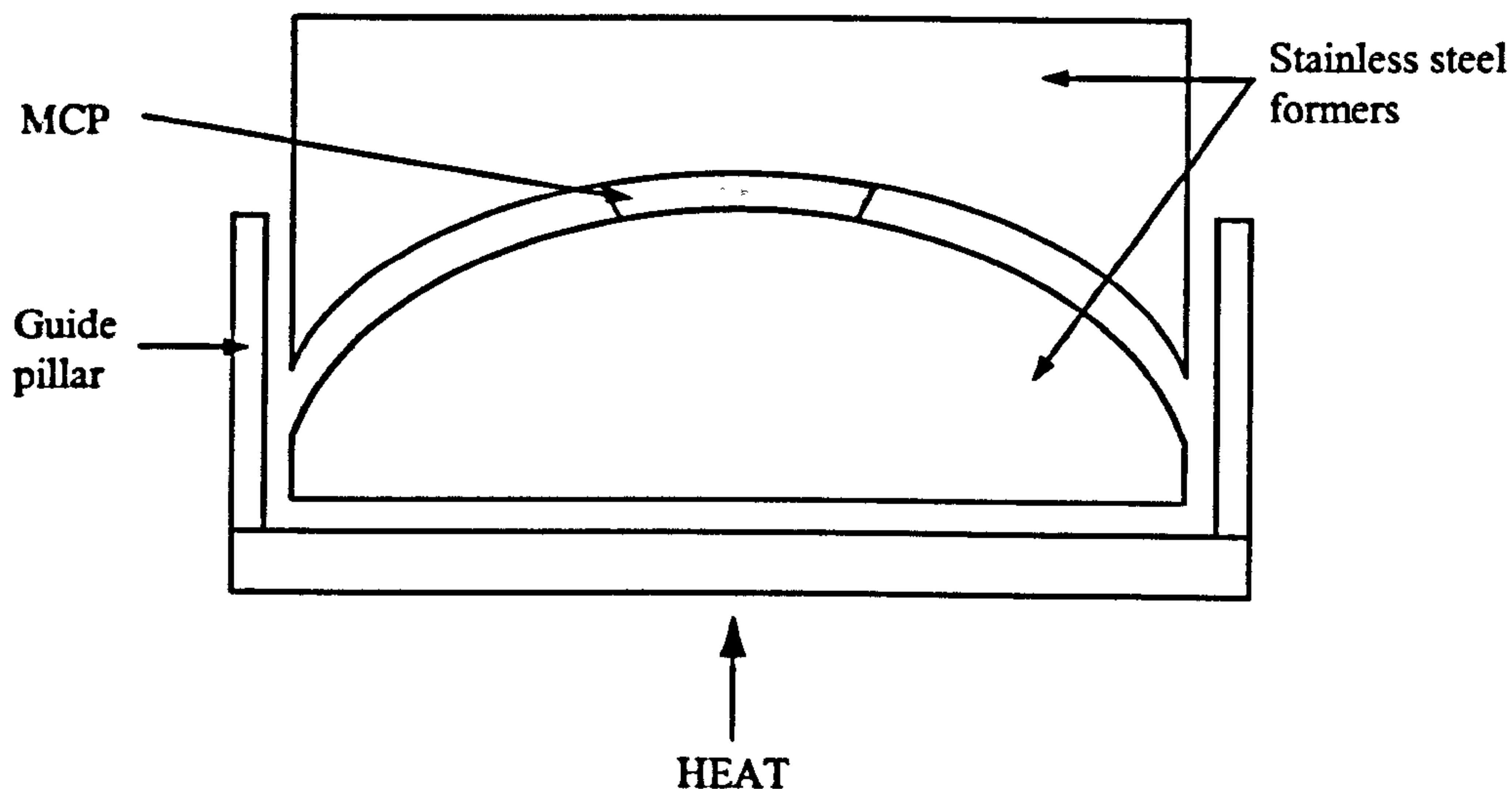


*Figure 1.12. The MCP slumping process currently used at Photonis SAS (Fairbend, 2005).*

### 1.4.2 MCP Coating

The reflection efficiency of an X-ray mirror may be enhanced by coating the substrate with a thin metal layer. Reflectivity is boosted at higher photon energies and at higher grazing angles. The application of such a coating to the reflecting surfaces of the optical element in an X-ray telescope, for example, will enhance the high energy and wide angle response. MCP optic metallisation is studied in detail in this thesis, with particular emphasis on the characterisation of the coatings and their scientific potential when applied to the Lobster-ISS X-ray all-sky monitor (*Section 1.6.1*).

The application of a uniform metal coating along the length of thin capillaries of high channel aspect ratio is a non-trivial task; existing coating processes must be refined and in some cases new coating processes developed to perform this task alone. In this thesis, coatings from the Atomic Layer Deposition (ALD) and Electroless Nickel (EN) methods are compared, with MCP

optics metallised with ruthenium, iridium (ALD) and nickel (EN). Each coating technique is discussed in further depth in *Section 4.1*.

## **1.5 Terrestrial Applications of MCP Optics**

Although MCP optics were conceived with space applications in mind, a number of terrestrial applications have arisen over recent years. *Sections 1.5.1* and *1.5.2* detail the exploitation of MCP optics in imaging X-ray fluorescence spectroscopy and in the development of high intensity X-ray sources.

### **1.5.1 Imaging X-ray Fluorescence Spectroscopy**

X-ray fluorescence spectroscopy is a common tool for determining the elemental composition of unknown samples. However, most laboratory-based equipment is non-imaging; fluorescent X-rays from a sample area are obtained, with X-ray spectra being integrated over the extent of this “footprint”. Spatially resolved elemental maps are usually generated by mechanically rastering a small spot X-ray beam over a target sample. This is either performed in the laboratory, using capillary optics to generate the small spot size X-ray source required, or at synchrotrons; in each case costs may be prohibitive and due to the slow nature of the rastering process, there is little scope for monitoring the time evolution of a sample.

A prototype terrestrial fluorescence spectrometer was developed at the University of Leicester in 1999 (Martin et al. 1999). The development of the Imaging X-Ray Fluorescence Spectrometer (IXRFS) is an extension of this work, made possible by a substantial EPSRC grant awarded in 1999. A planar MCP optic is employed in the point to point focusing configuration, relaying fluorescent X-rays from a uniformly illuminated target sample onto a photon counting, open electrode Charge Coupled Device (CCD) detector. IXRFS thus produces 2D elemental maps of a target specimen to sub-millimetre spatial resolution (observed to scale on the CCD), with the MCP acting as a relay lens with unity magnification. With a CCD active pixel area of 24 x 24 mm<sup>2</sup>, larger target specimens may be imaged by mosaicing individual intensity maps taken from different regions of the sample.

The non-destructive nature of this technique makes IXRFS particularly suitable for quality control applications in industry; for example, an envisaged key application of IXRFS is in the semiconductor industry, where imaging spectroscopy can be used to detect low Z element



contamination on silicon wafers (Fraser et al. 1999). A novel X-ray source, based on an annular anode is currently in development to achieve this goal. In conjunction with a commercial X-ray source, applications of IXRFS in mineralogy and as a scientific calibration tool are presented in *Chapter 2*.

### **1.5.2 High Intensity X-ray Sources**

Capillary optics, in particular Kumakhov lenses have been used in conjunction with X-ray sources to produce a concentrated beam (Wollman et al. 1997; Cappuccio and Dabagov, 2000). However, at a cost of several thousand pounds each, Kumakhov lenses are prohibitively expensive for many applications, and it has been suggested that MCPs could provide an alternative to the Kumakhov lens, with manufacturing costs around an order of magnitude cheaper (Brunton et al. 2000). Shimadzu Research Laboratory (Europe) Ltd. and JMAR Research Inc. expressed a written interest in the technology and indeed to collaborate with Leicester on the work, but a proposal to EPSRC in 2000 was not funded, despite encouraging feedback.

## **1.6 Space-based Applications of MCP Optics**

As MCP optic technology is now reaching a level of technical maturity, its importance in space instrumentation is being recognised with several missions making use of MCP optics as low mass X-ray mirrors. What follows is a synopsis of three future missions, with MCP optics central to the design concept in each case.

### **1.6.1 Lobster-ISS**

The lobster-eye geometry has a theoretically unlimited ( $4\pi$  steradian) FOV making it ideally suited for wide-field instruments; indeed, with necessity being the mother of ‘invention’, Angel’s motivation behind his landmark publication in 1979 was that the geometry be applied to an X-ray All-Sky Monitor (ASM) telescope (Angel, 1979). After Wilkins’ assertion that microchannel plates could be used as the optical element a full ten years later (Wilkins et al. 1989), an in-depth feasibility study of such an ASM was performed by Priedhorsky et al. (1996). After an unsuccessful proposal of the LOBSTER concept to the NASA Small Explorer Missions Proposal (SMEX) in 1997 (Priedhorsky et al. 1997), the proposal was updated in 2000 (following MCP optic development via an ESA Technology Research Programme (TRP), Fraser et al. 2000) and resubmitted in response to the ESA Call for Mission Proposals for the Flexi-Missions F2 and F3.



The mission, now called Lobster-ISS, an ASM for the International Space Station (ISS), was approved for an ESA Phase A study in 2002 and successfully completed this study in 2005. At the time of writing, Lobster-ISS is due to be launched in late 2010.

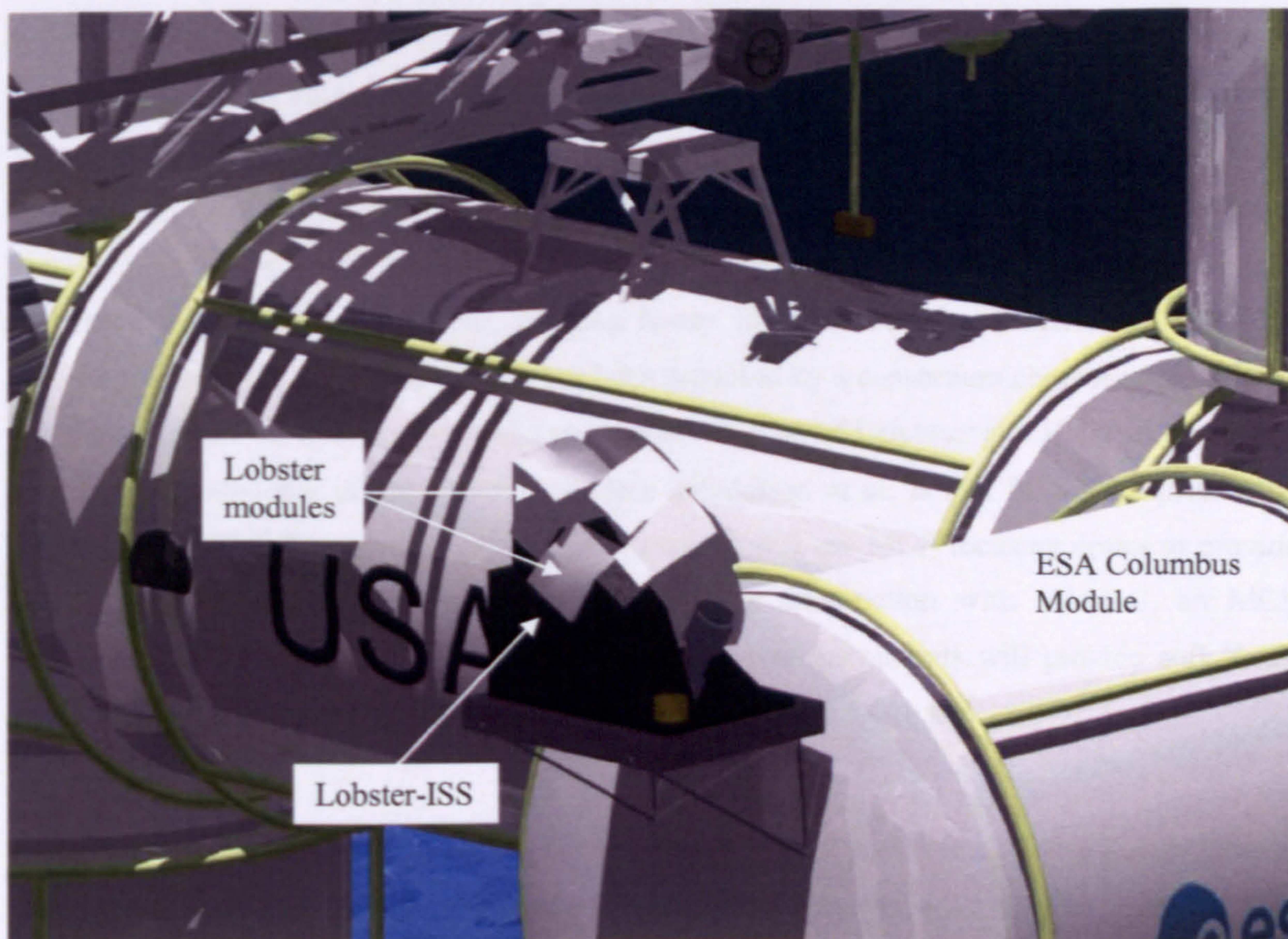


**Figure 1.13.** *Lobster-ISS as currently envisaged on the International Space Station. The six Lobster-ISS telescope modules are orientated to provide an instantaneous field of view of  $162^\circ \times 22.5^\circ$ . (Image courtesy of D.J. Watson, University of Leicester).*

In the current design, slumped MCP optics (with a baseline specification defined in *Table 1.1*) are tessellated in an  $8 \times 6$  matrix. A proportional counter-based microwell detector approximates the surface of a sphere of slump radius  $\frac{R_s}{2}$ , matching the focal surface of the optics. Both the optic array and detector are housed within a *module*, of which Lobster-ISS has six, arranged to provide an instantaneous FOV of  $162^\circ \times 22.5^\circ$ . It is currently envisioned that Lobster-ISS will be mounted externally on the zenith platform Exposed Payload Facility (EPF) located on ESA's Columbus Module (*Figure 1.13*). Lobster-ISS will use the orbit of the ISS to map almost the



entire X-ray sky every 90 minute orbit (Pearson et al. 2003). The Lobster-ISS mission provides the motivation behind much of the work in this thesis, with the mission design, history and scientific potential being discussed in greater depth in *Chapters 3 - 7*.

### 1.6.2 Bepi-Colombo

Bepi-Colombo is an ESA cornerstone mission to revisit Mercury for the first time since Mariner 10 conducted its three orbits of the planet in 1975 (Wakeling, 1975). With a baseline launch date of 2012, the mission aims to provide complete mapping of the planetary surface in addition to detailed information on the structure of the Mercurian magnetic field over a two year period of operations (Grard et al. 2000). An imaging X-ray fluorescence spectrometer, named MIXS (Mercury Imaging X-ray Spectrometer) has been proposed by a consortium composed of CCLRC Rutherford Appleton Laboratory (RAL) and the universities of Leicester and Helsinki to provide 2D elemental mapping of the planetary surface (Maddison et al. 2004). MIXS comprises two components; MIXS-T (an MCP optic-based telescope) will use MCP focusing optics to provide true imaging of the Mercurian surface, operating in conjunction with MIXS-C, an MCP collimator with a wide FOV. The coupling of these two instruments will provide soft X-ray remote-sensing of Mercury's surface over a spectral range of 0.5 - 10 keV.

In the case of MIXS-T, two 210 mm diameter, Ir-coated MCP optics in a Wolter I configuration will image fluorescent X-rays onto a Ga-As pixel array detector with a focal length of 1 m (*Figure 1.14*). MIXS-C uses an slumped MCP of  $R_s = 1$  m to throughput flux onto an identical Ga-As pixel-array detector, placed 50 cm from the optic (Carpenter, 2005). The angular resolution of MIXS-T is of order 2' FWHM (Price et al. 2002), such that when mounted aboard the Mercury Planetary Orbiter module (which has an altitude of 400 km at perihelion), a surface resolution of 200 m will be achieved. The mineralogical classification of the surface of Mercury will yield historic information on the planet's tectonic and volcanic activity, contributing towards a better understanding of the least well-known of the terrestrial planets and the evolution of the solar system.



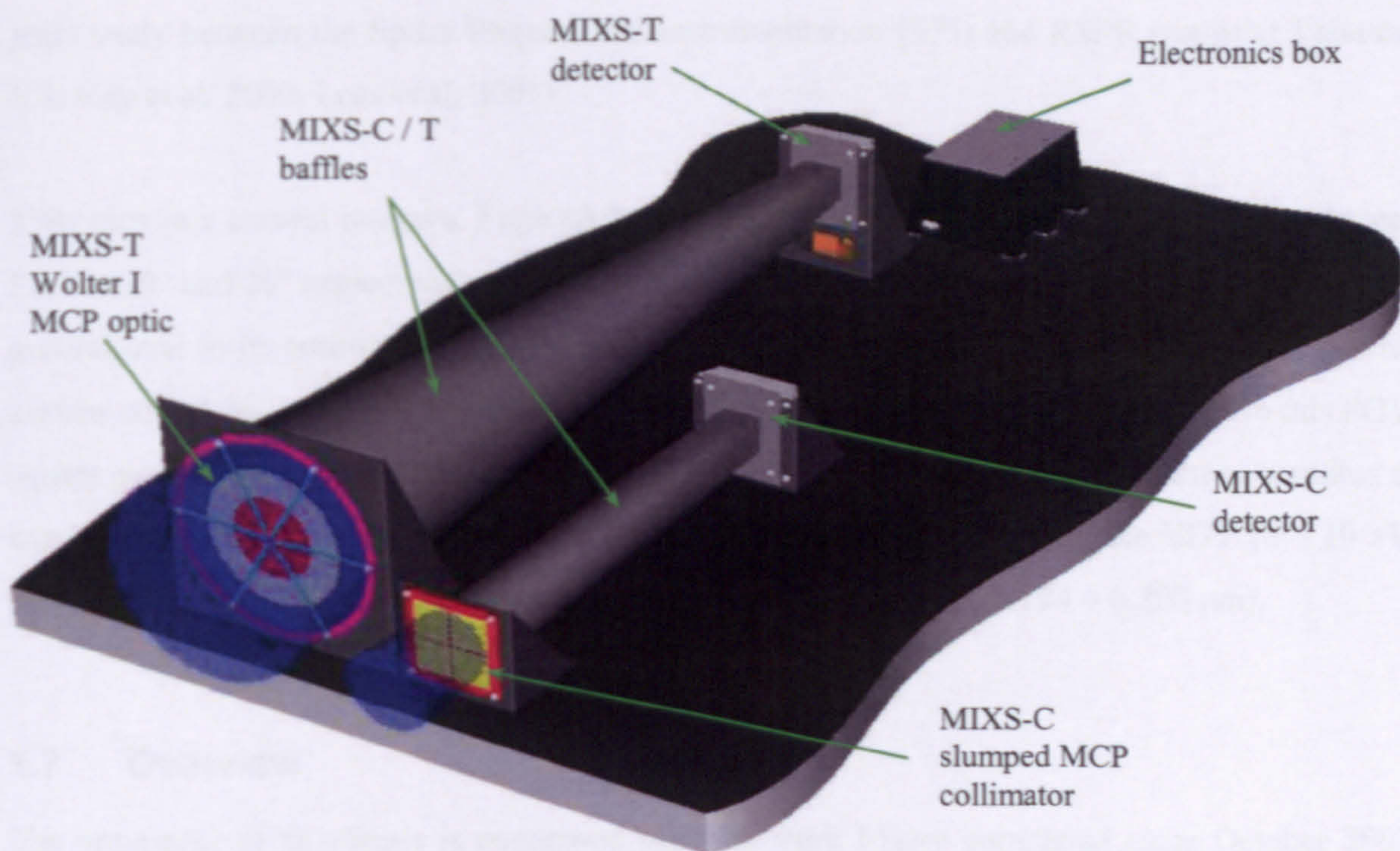


*Figure 1.14. The MIXS instrument design currently baselined for the Bepi-Colombo mission to Mercury.*

### 1.6.3 Auroral Imager

The dynamics of plasma populations in the terrestrial magnetosphere are broadly governed by the interactions between the solar wind and the planetary magnetic field; unfortunately, very little radiation is emitted in this region of space making in-situ imaging unfeasible (Yeoman, 2005). Instead, the spatial and temporal evolution of the magnetic field at the polar regions of the Earth may be used to infer three dimensional models of the magnetosphere (McWilliams et al. 2001). Plasma flowing along the magnetic field lines (to which it is intrinsically coupled) is incident on the ionosphere in the Earth's polar regions. Here, the particle density is sufficiently high that significant radiation is emitted due to collisional de-excitation; it is this radiation that forms the aurora. Coupling images of the aurora to ground-based measurements can be used to reconstruct plasma dynamics in the magnetosphere.

The Radio and Space Plasma Physics (RSPP) group at Leicester are (in part) concerned with the field of Solar - Terrestrial Physics (STP). As partners in the Super Dual Auroral Radio Network (SuperDARN), they have access to ground-based data regarding plasma flow in the polar regions of the ionosphere (Greenwald et al. 1995). The concept of the Auroral Imager was born out of a need to complement this ground-based data with images of the aurora and was the product of a



joint study between the Space Projects and Instrumentation (SPI) and RSPP groups at Leicester (Cowley et al. 2000, Lees et al. 2001).

Two previous auroral imagers, Freja (Adema, 1993) and POLAR (Frank et al. 1995) had small FOVs ( $25^\circ$  and  $20^\circ$  respectively), and thus required orbits of  $h \geq 3000$  km in order to image the auroral oval in its entirety. With a proposed FOV of  $90^\circ \times 90^\circ$ , the Auroral Imager will provide similar coverage, yet from a Low Earth Orbit (LEO) of  $h \approx 800$  km. In order to achieve this FOV, square pore, lobster-eye MCP optics of channel width  $85 \mu\text{m}$  are slumped down to a radius of curvature  $R$ , of 70 mm. It is envisioned that observations will be made in the VUV (6 – 10 eV) band, with optic diffraction effects negligible at these wavelengths ( $0.124 - 0.200 \mu\text{m}$ ).

## 1.7 Overview

The remainder of this thesis is concerned with the work I have completed since October 2001, during my PhD at the University of Leicester.

*Chapter 2* describes the development of the Imaging X-ray Fluorescence Spectrometer (IXRFS), the terrestrial application of MCP optics considered in this thesis. A summary of previous work is followed by a description of the IXRFS system in its current configuration. IXRFS is used to image a mineralogical specimen of Garnetiferous Anorthosite and a diagnostic calibration target used in the Beagle 2 mission to Mars. Finally, further applications of the IXRFS system are identified and discussed.

*Chapters 3 - 6* concern the Lobster-ISS all-sky monitor, the space-based application of MCP optics considered in this thesis. *Chapter 3* examines the soft X-ray focusing properties of the latest planar and slumped MCP optics, with angular resolutions determined and compared with those baselined for Lobster-ISS. *Chapters 4* and *5* examine the properties of the reflecting surfaces of bare glass and metallised MCP optics using the Auger Electron Spectroscopy (AES) and X-Ray Reflectivity (XRR) techniques respectively. The performance of Lobster-ISS is modelled in *Chapter 6*, for different MCP coatings, detector windows and input source spectra in order to optimise the baseline design.

Finally, *Chapter 7* summarises the conclusions drawn in this thesis and examines the future of MCP optics.

## Chapter 2 The Imaging X-ray Fluorescence Spectrometer

### 2.1 Introduction

When primary radiation is incident upon an absorbing medium, electron de-excitation results in the emission of secondary radiation, whose wavelength is characteristic of the elemental composition of the absorbing medium. This process is named *fluorescence*; *X-ray fluorescence* is a special case when both primary and secondary radiation are in the X-ray band.

Imaging X-ray fluorescence spectroscopy is a tool used to generate 2D elemental maps of target specimens; a fluorescence spectrum is obtained from an illuminated area, or ‘footprint’, of a uniformly irradiated sample. The technique by its very nature is non-destructive, and therefore of particular use for the analysis of precious or rare samples.

To date, imaging X-ray fluorescence spectroscopy techniques have largely involved the systematic 2D scanning of a mounted target sample using a highly-collimated X-ray beam, usually  $< 10 \mu\text{m}$  in diameter (Morton and Witherspoon, 1992). For the short integration times desired for this ‘rastering’ method, an intense, focused, primary X-ray beam is required as the fluorescence yield  $\omega$  (the probability of a core hole in a shell being filled by a radiative rather than a non-radiative process) is low in the soft X-ray waveband of interest ( $\omega = 0.05$  at Si-K $_{\alpha}$ ; Krause, 1979), which practically necessitates the use of a synchrotron. This chapter describes the development of, and scientific output from, the laboratory-based Imaging X-ray Fluorescence Spectrometer (IXRFS), with a view to its possible future application in a range of scientific and industrial fields.

In order to put the work into perspective, a brief review of the development of IXRFS is detailed in *Section 2.1.1*. This is followed by a description of the experimental arrangement of IXRFS in its current configuration (*Section 2.2*). Then, the imaging capabilities of IXRFS are investigated, using a mineralogical sample (*Section 2.3*) and a flight-spare calibration target designed for use on the Beagle 2 mission to Mars (*Section 2.4*). The future addition of an alternative X-ray source with a novel annular geometry is described in *Section 2.5* with further potential applications of IXRFS discussed in *Section 2.6*.



### 2.1.1 Imaging X-ray Fluorescence at Leicester

The development of IXRFS began at the University of Leicester in 1999 with two proof of principle experiments. The first, detailed in Martin et al. (1999) involved the imaging of a simple binary sample described in *Figure 2.1(a)*. Flux from the picosecond pulsed laser plasma source at the Rutherford Appleton Laboratory Central Laser Facility was incident upon a slowly moving Fe target tape. The ensuing X-rays irradiated the sample, with fluorescent X-rays imaged onto a CCD using an MCP relay optic. A composite spectrum of eight individual ‘sub-spectra’ is shown in *Figure 2.1(b)*. The energy resolved images in *Figure 2.2* illustrate the spatial distribution of fluorescent X-rays from each element in the binary sample. The characteristic cruxiform image structure intrinsic to square pore MCP focusing (*Section 1.3*) is in evidence, with a clear spatial separation between the Al and Ni centroids.

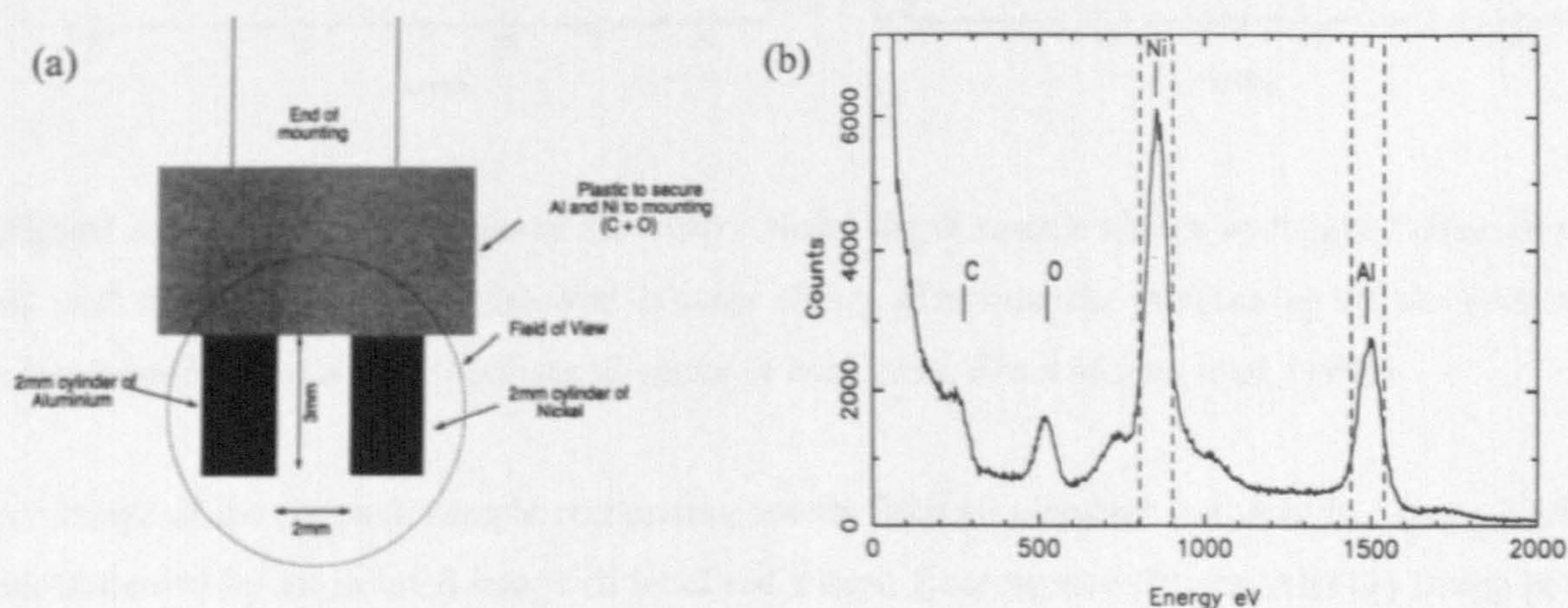


*Figure 2.1. The structure, scale and composition of a simple binary metal target are shown in (a); the composite spectrum obtained is shown in (b). From Martin et al. (1999).*

Following the success of the synchrotron-based experimentation, in-house development of a self-contained, prototype Imaging X-ray Fluorescence Spectrometer with no moving parts began in earnest (Martin et al. 2001) funded by an EPSRC grant (reference number GR/M51550/01). The work at RAL was extended using an MCP of higher quality (with a Full Width at Half Maximum (FWHM) angular resolution of  $\sim 6$  arcmin) and a laboratory-based X-ray source providing greater control over the output spectrum. A vertically mounted electron-bombardment source was positioned directly above a Micro-Analysis Consultants XRF microstandard target ‘six-pack’ sample (*Figure 2.3*). Fluorescent X-rays were imaged using a square pore MCP onto a deep-depleted X-ray CCD. *Figure 2.4* illustrates the experimental configuration.



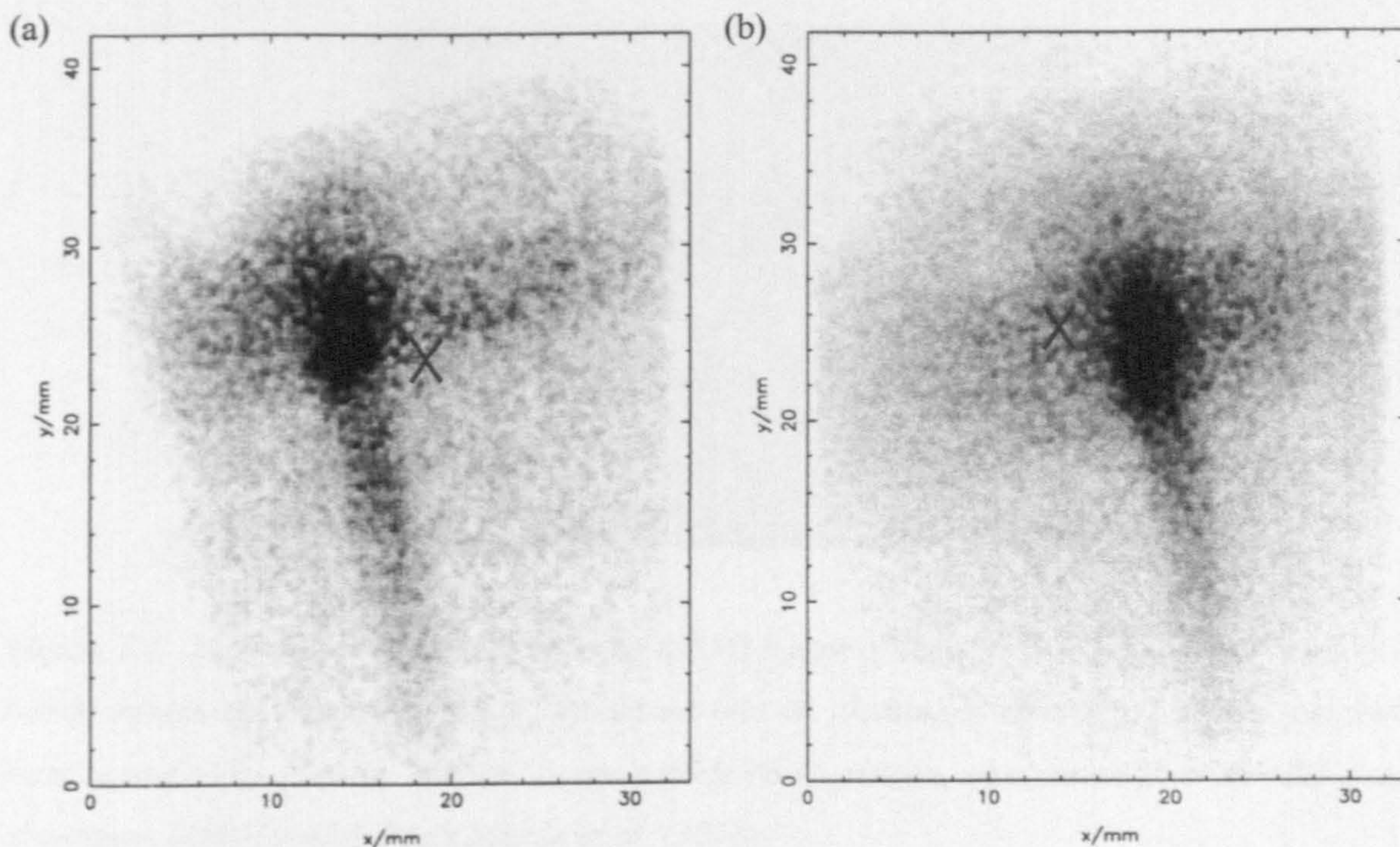


**Figure 2.2.** Fluorescent images of the binary metal target sample shown in Figure 2.1(a), in (a) Al and (b) Ni X-rays. The labelled crosses (blue) illustrate the positioning of the centroid corresponding to the other (unimaged) metal in each case. From Martin et al. (1999).

An image of the six-pack sample comprising counts from all elements is shown in Figure 2.5(b), accompanied by an isolated image of localised silicon fluorescence (a). An Al(111) Bragg peak was observed at 3.72 keV (Figure 2.6) demonstrating a capability for diffraction imaging. In the semiconductor industry, overlayers of metals (e.g. aluminium) are deposited on silicon wafers to create contacts and connectors during silicon chip manufacture. The mismatch in the lattice spacing at the Al/Si interface gives rise to stresses which are capable of introducing breaks in the fine Al interconnects. For a given primary X-ray angle of incidence, changes in the lattice spacing correspond to energies at which the Al and Si Bragg peaks occur. Thus, in principle, it may be possible to realise ‘stress maps’ over the extent of an aluminised silicon wafer using the diffraction imaging capabilities of IXRFS; this was identified as a potential key application of IXRFS in the EPSRC grant application (Fraser et al. 1999) yet has not been investigated to date.

The two proof of principle experiments detailed in this section were carried out prior to the involvement of the author in the IXRFS project. Work carried out by the author is detailed in the remainder of this chapter.



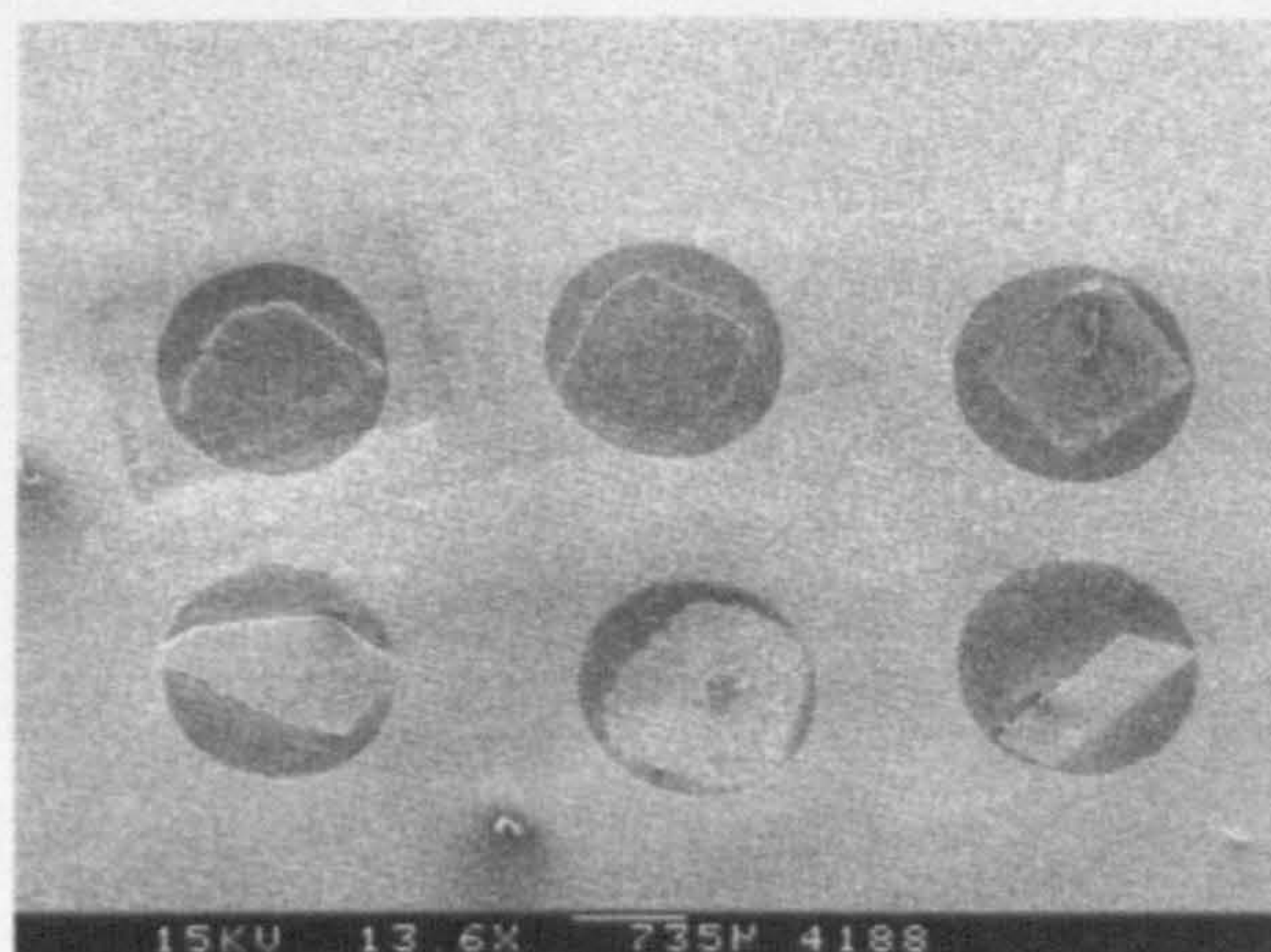


**Figure 2.3.** Scanning Electron Microscope (SEM) image of the six-pack target, consisting of six known substances fixed into ‘wells’, machined into an aluminium disc. The samples, clockwise from top-left are; carbon, carbon, boron-nitride (BN), silicon, aluminium fluoride ( $\text{AlF}_3$ ) and aluminium oxide ( $\text{Al}_2\text{O}_3$ ). From Martin et al. (2001).

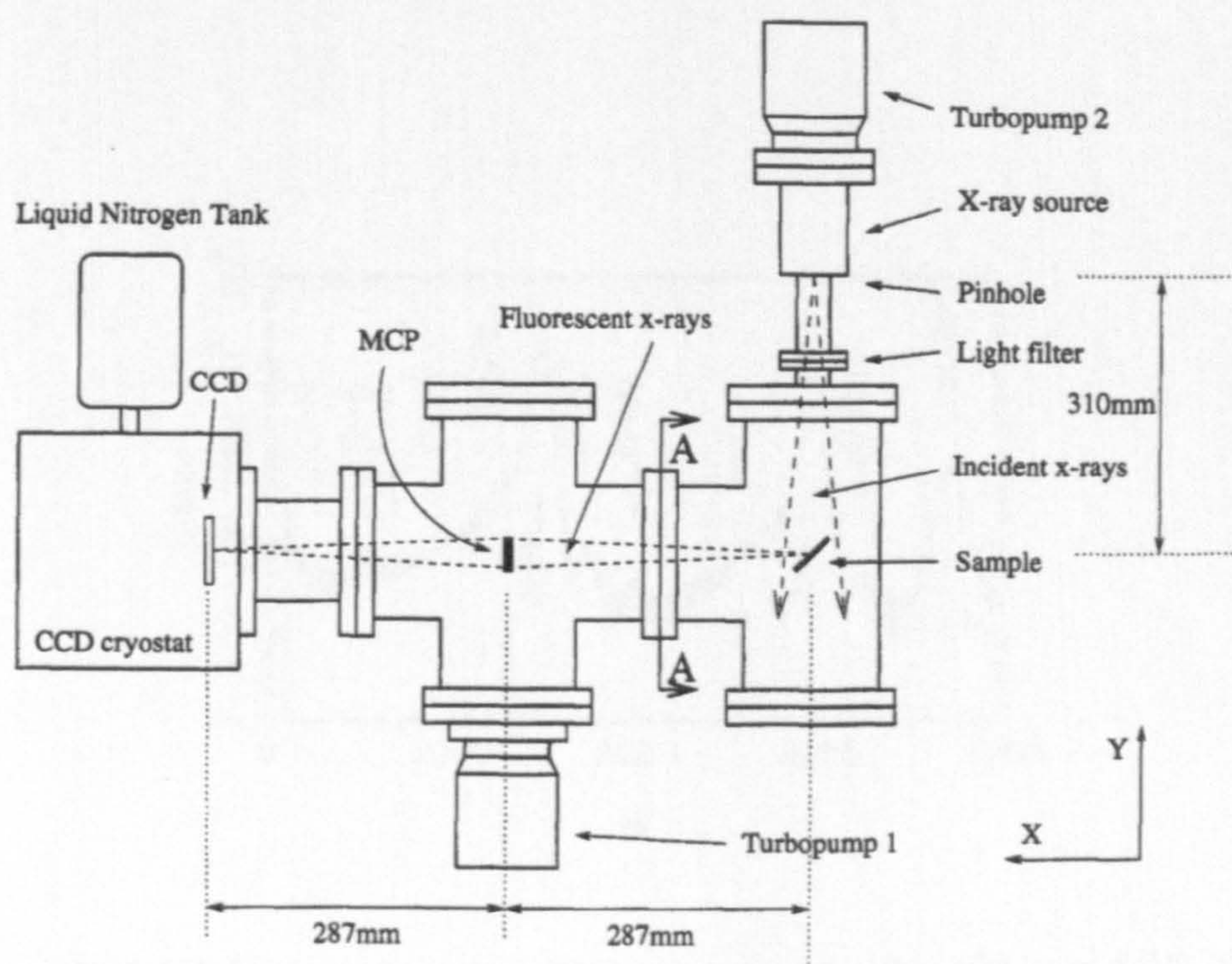


**Figure 2.4.** Schematic view of prototype lab-based IXRFS at Leicester. From Martin et al. (2001).



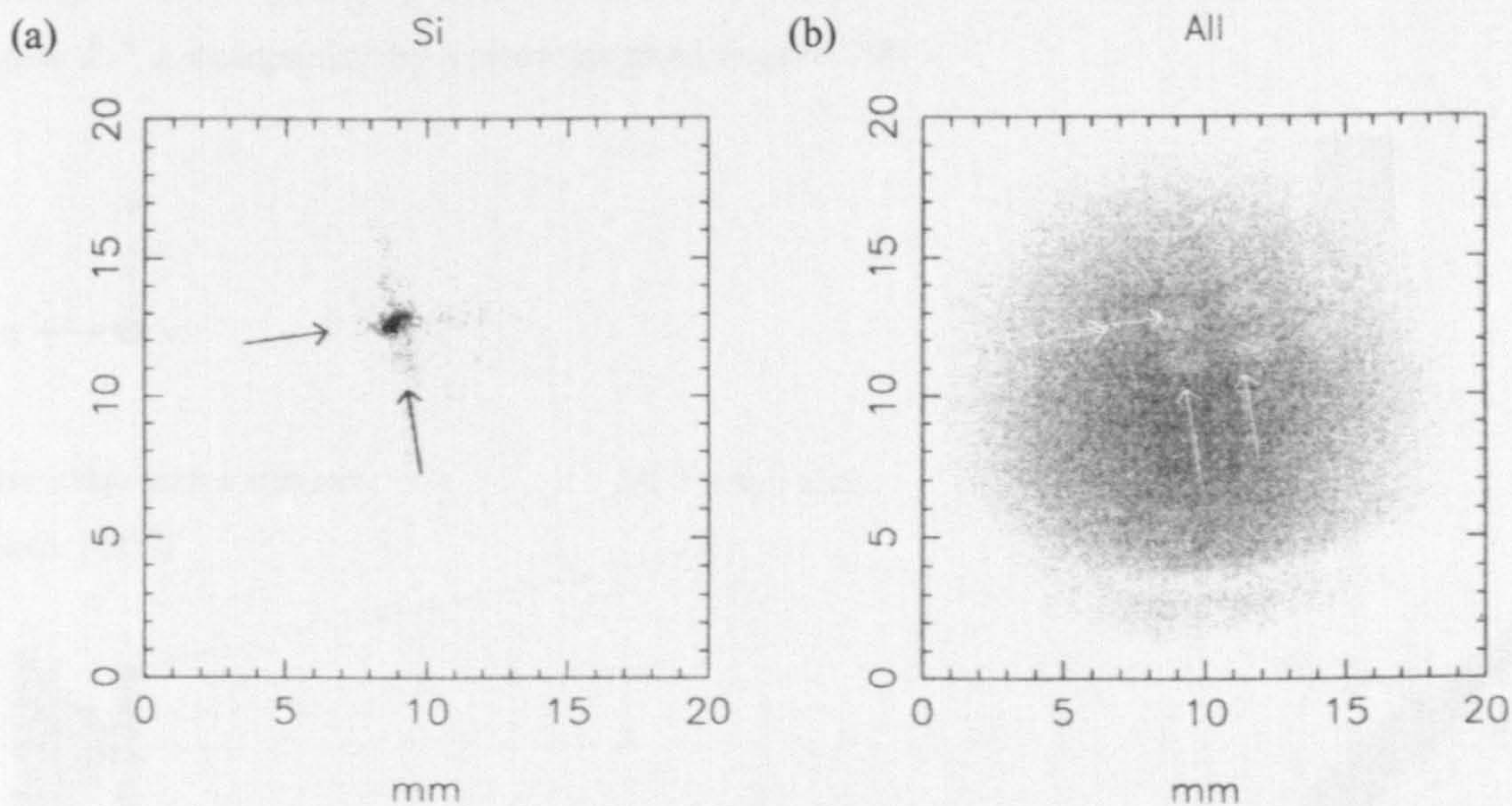


**Figure 2.5.** IXRFS prototype imaging of the six-pack sample in (a) Si- $K_{\alpha}$  and (b) all X-rays. The cruxiform image structure is visible from the silicon in (a), while in (b) the six samples appear as 'holes' in the aluminium disc support. From Martin et al. (2001).

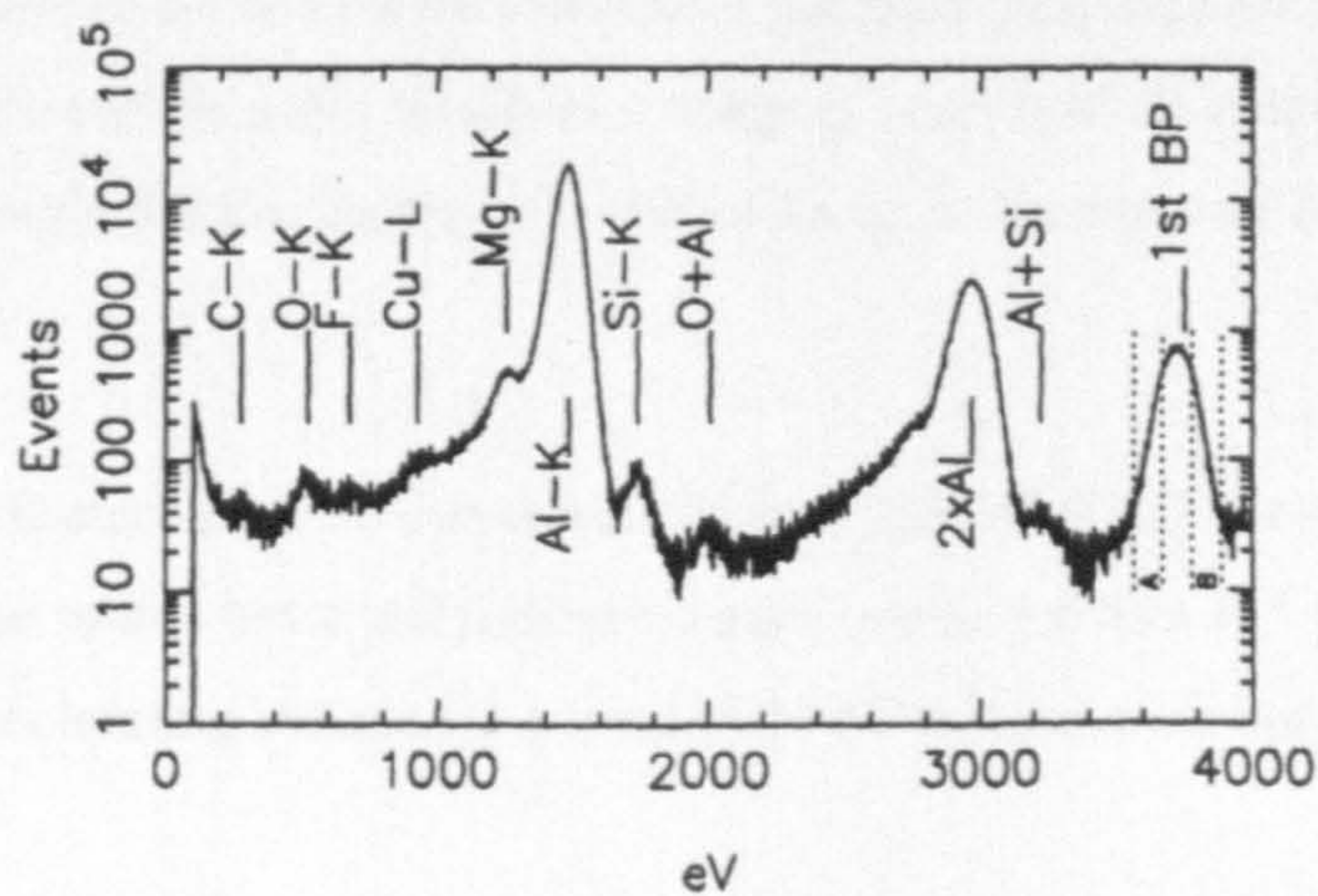


**Figure 2.6.** Fluorescent target spectrum with accelerating anode voltage of 5 kV. The Al(111) Bragg reflection peak is clearly observed at 3.72 keV. From Martin et al. (2001).



## 2.2 Experimental Configuration

The experimental geometry of the IXRFS system in its current configuration is illustrated in Figure 2.7, accompanied by a photograph in Figure 2.8.

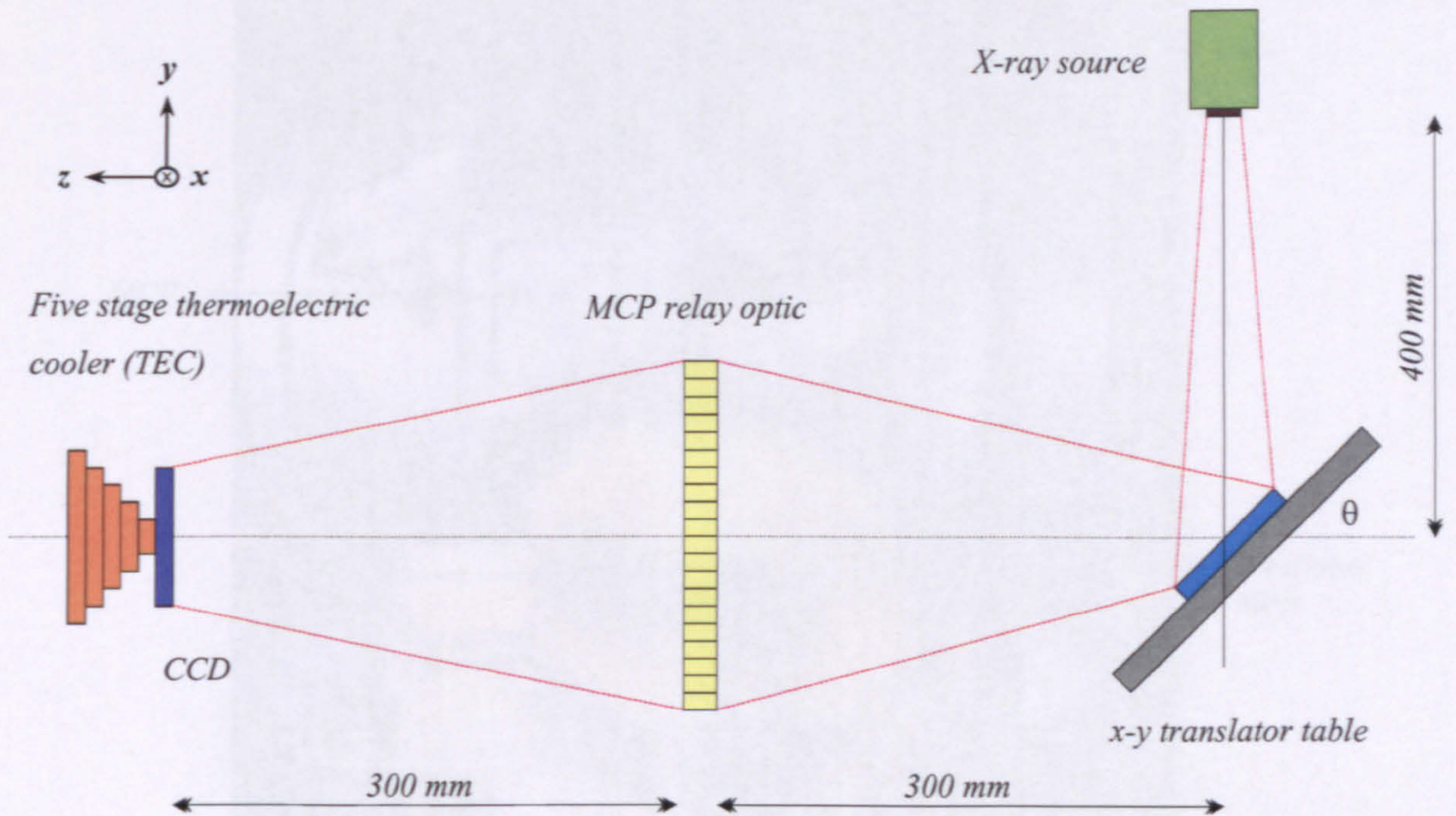


**Figure 2.7.** Experimental geometry of the IXRFS system. The sample (blue) is mounted on the x-y translator table, which is shown orientated a nominal  $\theta = 45^\circ$  to the optical axis. The components are mounted on and encased within a stainless steel support structure (Figure 2.8). The orientation of the sample table results in a range of source-MCP distances; thus in this point to point focusing configuration, images are out of focus at the top and bottom of the CCD (as shown above).

A target sample is illuminated by a commercial Kevex K5039MO-C X-ray tube placed 400 mm vertically above. The source has a molybdenum anode coupled with a 125  $\mu\text{m}$  beryllium window, and can be run at accelerating voltages in excess of 20 kV with an emission current of 1 mA.

Fluorescent X-rays produced from the excitation of the target sample are imaged onto a deep-depleted X-ray CCD (of  $\sim 30 \mu\text{m}$  average depletion depth) with the use of an MCP relay optic. The MCP optic is located at a 300 mm midpoint between the  $45^\circ$  sample table and the CCD, mounted in a stepper motor-driven frame with two rotational degrees of freedom. A third



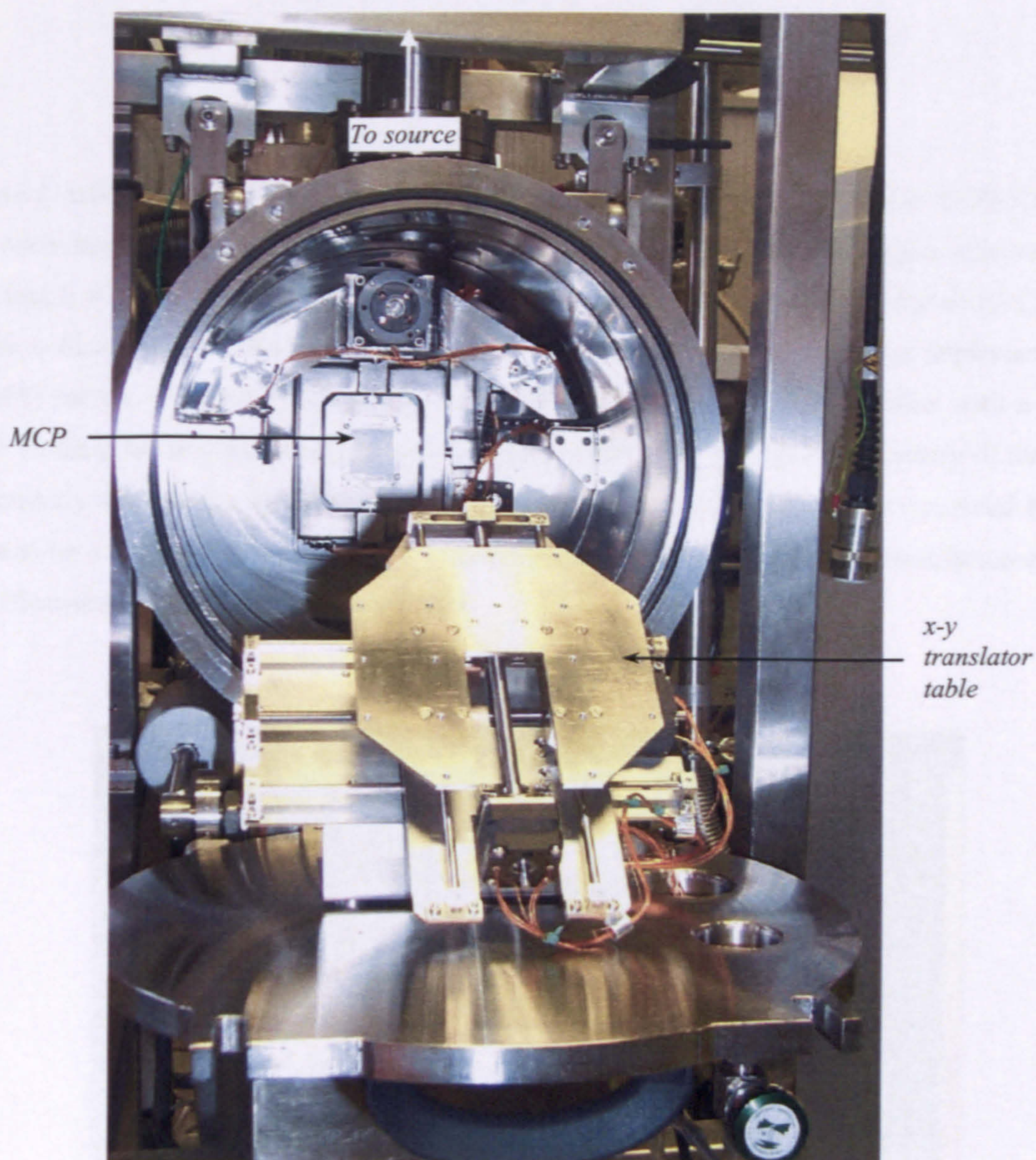


**Figure 2.8.** Primary X-rays from the source above illuminate a target sample, which is mounted on the x-y translator table. The MCP relay optic can be seen in the background, housed within a holding jig attached to a two-axis manipulator. The CCD is positioned behind the MCP. Note that in this figure, the x-y translator table is rotated 90° from its actual working position.

stepper motor is employed to displace the MCP frame along the optical ( $z$ ) axis to optimise X-ray focusing. The selected experimental geometry means the MCP acts as a relay lens of unity magnification; a feature of cross-sectional area  $A$  on the target sample (tilted at 45°) viewed along the optical axis will theoretically be imaged with an equivalent area  $A$  by the CCD. In conjunction with a slumped MCP optic, the system would have a transverse magnification  $M_T$  (Chapman et al. 1991) given by



$$M_T = \frac{l_i}{l_s} \quad (2.1)$$

where  $l_s$  and  $l_i$  are the sample-MCP and MCP-CCD distances respectively. The IXRFS system has been designed to allow  $\pm 100$  mm longitudinal travel of a slumped MCP optic relative to the nominal  $l_s = l_i = 300$  mm, with a view to magnifying X-ray images of the sample at the CCD by up to a factor of two. However, this optical configuration has not yet been implemented in IXRFS; for the purposes of this work, we use the IXRFS system in conjunction with a planar MCP in the point to point configuration shown in *Figure 2.7*. The optical geometry of the MCP is currently the limiting factor in the spatial resolution of system, which was measured by G.J. Price to be  $\sim 0.67$  mm (*Figure 2.9*). The square-packed, square pore MCP is manufactured to the specifications in *Table 1.1* by Photonis SAS.

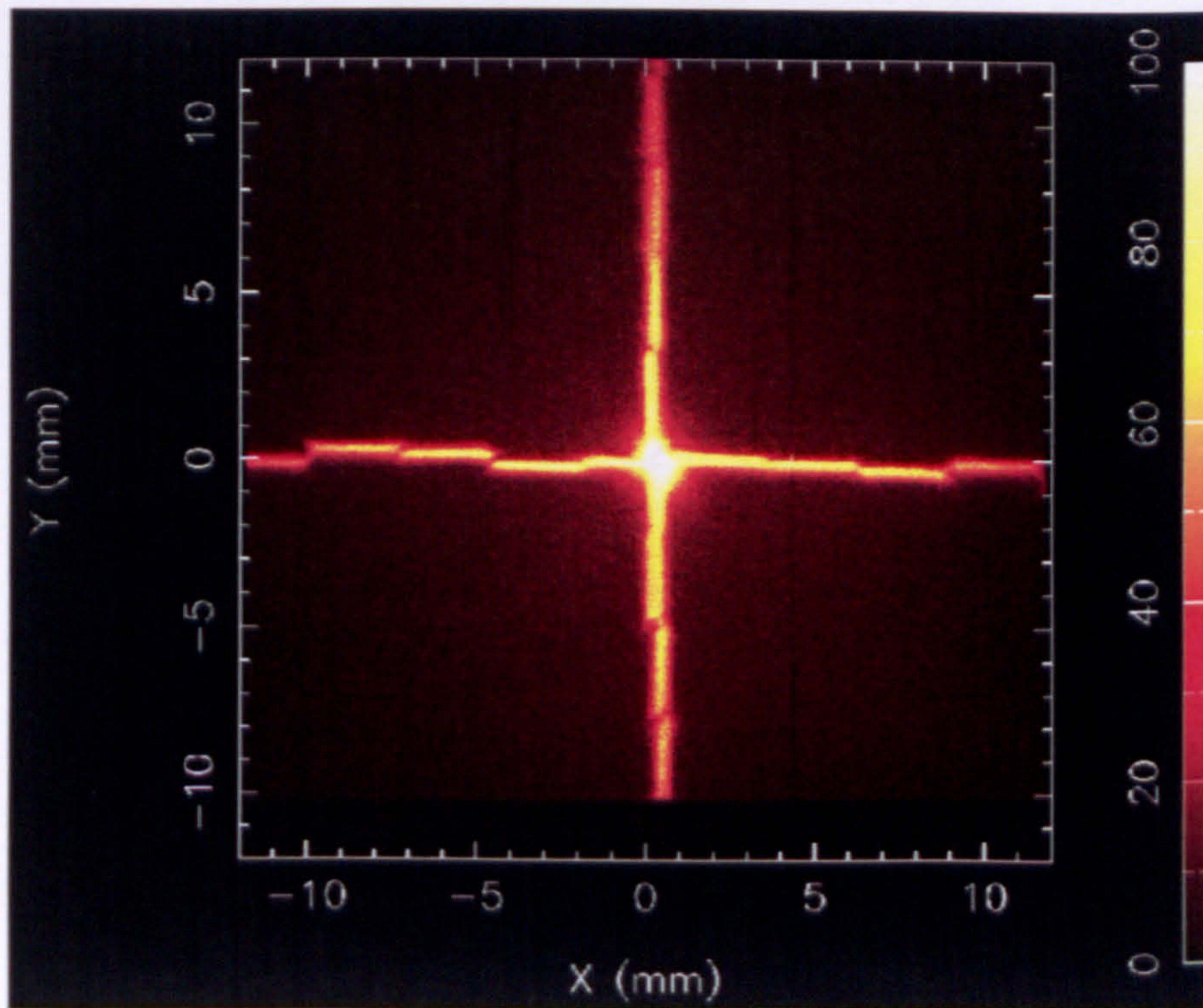


**Figure 2.9.** The FWHM 200  $\mu\text{m}$  spot-size Kevex X-ray source directly imaged onto the CCD using the MCP relay optic (serial number HC001-A5) positioned at the midpoint for point to point focusing (where  $l_s = l_i = 370$  mm in this case due a differing IXRFS configuration required for direct illumination). The FWHM angular resolution was measured to be  $\sim 6.5$  arcmin, corresponding to a system spatial resolution of  $\sim 0.67$  mm.



An E2V front-illuminated Type 22 CCD was selected for IXRFS. This is the same design as that used on the Swift gamma-ray burst experiment (Gehrels et al. 2005) and similar to that used for the European Photon Imaging Camera on XMM-Newton (Turner et al. 2001, Short et al. 2002). The CCD has an open-electrode structure and comprises a 602 x 610 square 40  $\mu\text{m}$  pixel array corresponding to a total active area of  $\sim 24 \times 24 \text{ mm}^2$ . The CCD operates at a characteristic temperature of  $-75^\circ\text{C}$ , cooled by a five stage Thermo-Electric Cooler (TEC) in conjunction with a  $10^\circ\text{C}$  chilled water supply. An associated read-noise of 7-9  $e^-$  RMS at  $-75^\circ\text{C}$  was measured at 5.9 keV (Mn- $K_\alpha$ ), corresponding to a FWHM energy resolution of 150 eV (Price et al. 2003a). The quantum efficiency curve for the CCD at  $-80^\circ\text{C}$  is shown in *Figure 2.10*. The associated energy of each incoming photon is recorded accurately by the CCD *subject to the provision that no more than one photon per pixel per frame is detected*. Otherwise, the energy of each individual photon will be lost with only the total energy recorded; this condition is known as *pile-up*, and limits the maximum count rate  $R_c$  on the CCD; for example, with the CCD used in IXRFS, to restrict event confusion to the 1% level,  $R_c < 0.15$  photons per pixel per frame (Fraser, 1989).

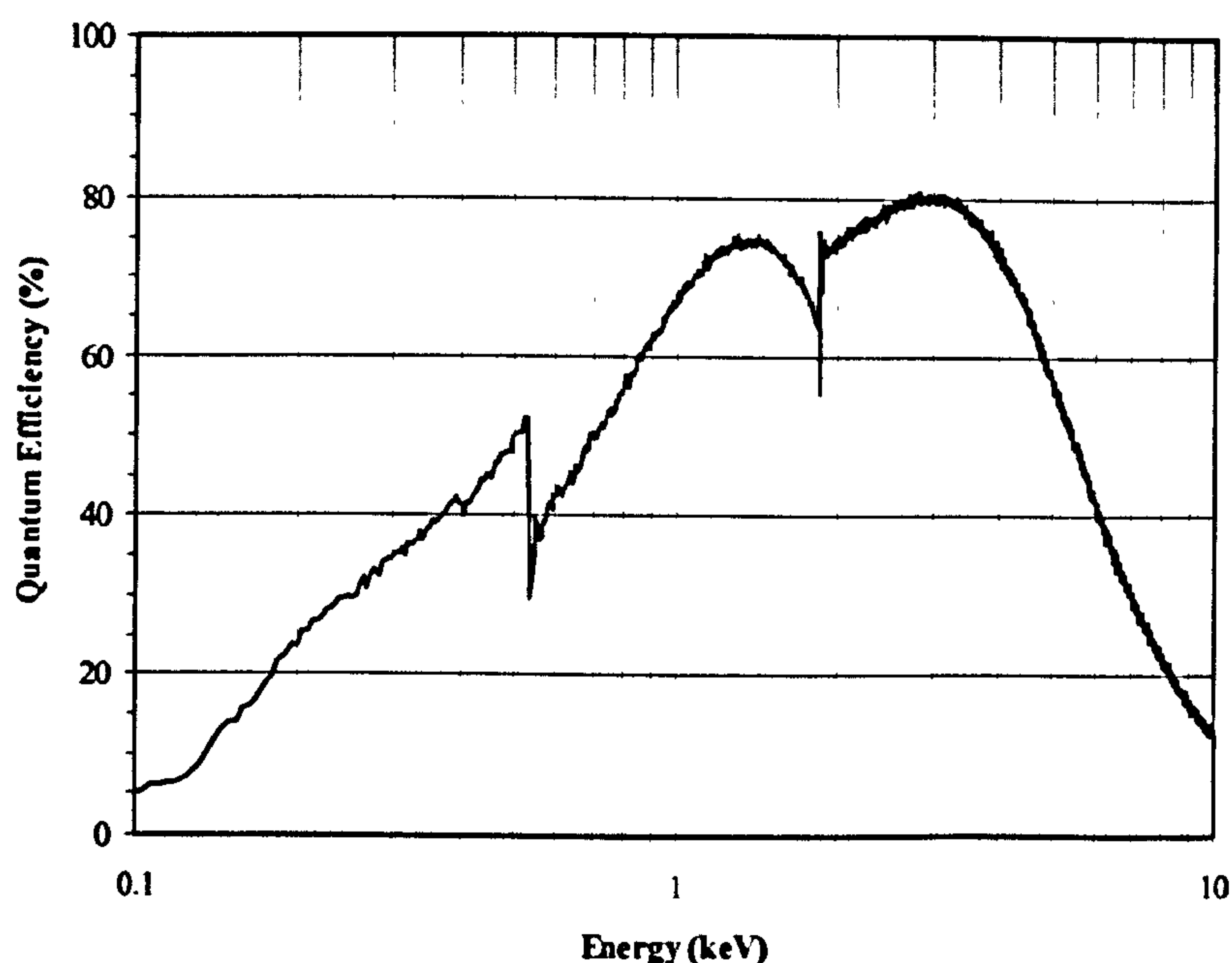


**Figure 2.10.** Quantum efficiency versus energy curve of the E2V Type 22 CCD at  $-80^\circ\text{C}$  used in IXRFS (Keay et al. 1999). O-K (from the silica dielectric layer) and Si-K absorption edges are identified at 543.1 and 1839 eV respectively (Bearden and Burr, 1967; Cardona and Ley, 1978).



The IXRFS system is evacuated to a pressure of  $< 10^{-6}$  mbar by two scroll pump-backed TurboMolecular Pumps (TMPs). The CCD is isolated from the rest of the system by a gate valve which allows the user to change a sample without breaking vacuum in the 'CCD chamber', therefore not exposing the CCD to atmospheric contaminants; one backing / TMP combination independently pumps each of the two volumes, with the gate-valve opened when both volumes are sufficiently evacuated for data collection.

IXRFS Hardware Control (HC) software was developed in-house by K. Turner and I.B. Hutchinson to be used in conjunction with IXRFS. The HC software outputs an event list containing the position and energy of each X-ray imaged on the CCD. The spectral and positional information for each event are coupled, permitting the spatial origins of spectral peaks on the sample to be determined and vice versa. Further, a Fortran-77 based program named CCDREAD (written in-house by G.J. Price) was developed to read in the event list and output it in the form of the HDS file structure, so that the data may be easily manipulated for subsequent image processing using the Q Interactive Programming Language, developed by R. Willingale at the University of Leicester.

## 2.3 Mineralogical Samples

A mineralogical sample of Garnetiferous Anorthosite originating from Bergen, Norway was selected for analysis with the intention of mapping the population of garnets (red pebble-like features in this case) present within the structure. A length of 250  $\mu\text{m}$  diameter copper wire was wrapped around the sample, with the intersecting points used as fiducial markers, whose purpose was to generate a look-up table to enable the mapping of X-ray data onto a photograph of the sample. In this way, visual characteristics could be correlated with those present in the IXRFS X-ray dataset. The fiducial markers should be made up of an element that is not expected to be abundant within the sample; this way, the element is easily identified in the X-ray spectrum. All mapping software was written in-house by Price (2004a). A photograph of the garnetiferous sample, referred to in the GSPARC [Geological Specimen ARChive] - PALI [Planetary Analogue Library] catalogue as 0042-RS-0071 (Pullan; 2005a, 2005b) as seen from the CCD is shown in *Figure 2.11*.

An isolated events spectrum from the imaged region of the sample is shown in *Figure 2.12*. The spectrum contains 22 million events collected over 12 hours in 4900, 1 second frames, each with a readout time of 8.7 seconds. The source was configured to run with an accelerating voltage of



10 kV with a 1 mA emission current. X-ray fluorescence from the stainless steel IXRFS structure often contribute significantly toward the presence of titanium, vanadium, chromium, iron, nickel and zinc seen in *Figure 2.12*.

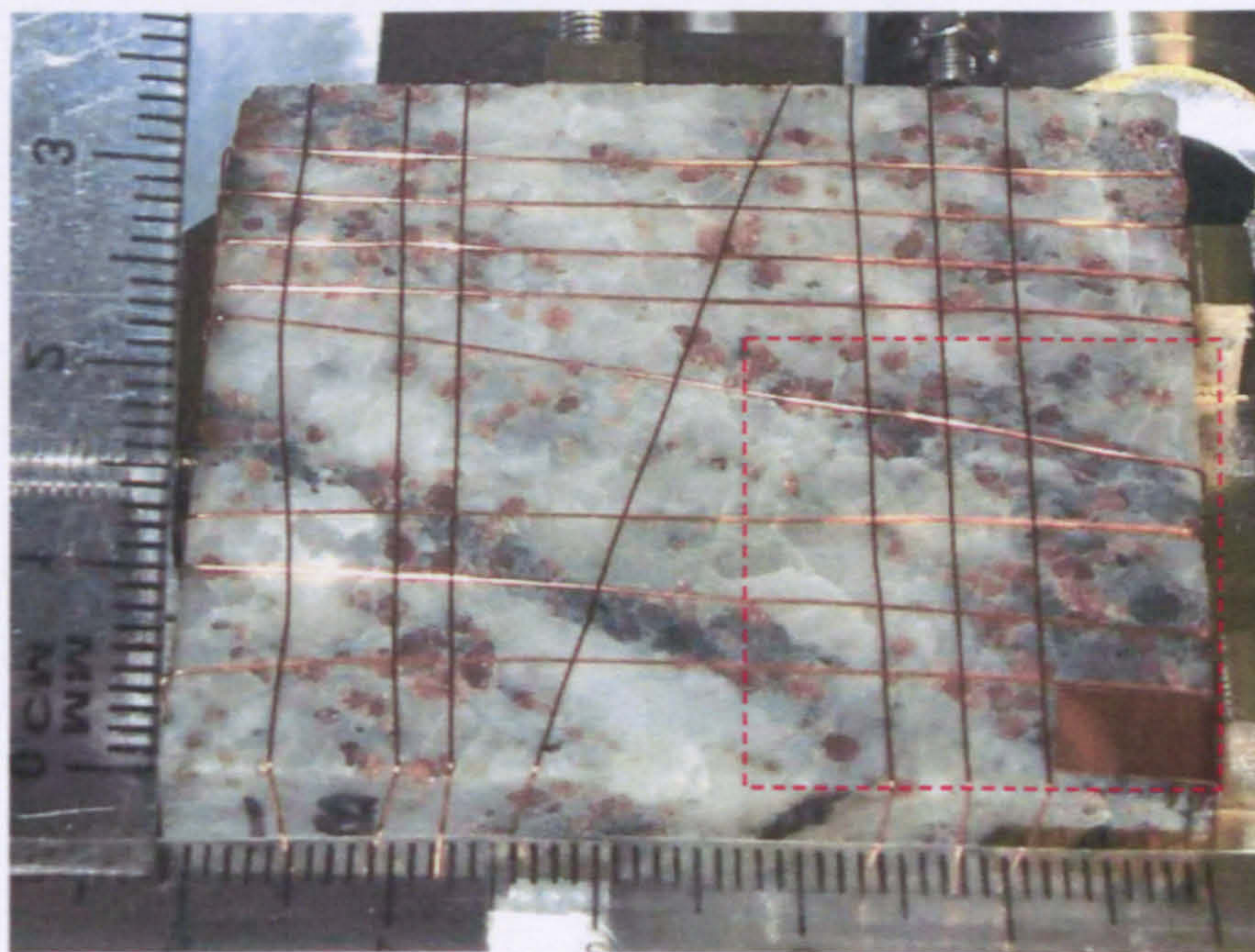


**Figure 2.11.** Garnetiferous Anorthosite sample mounted on the x-y translator table in IXRFS. High purity (99.99%) copper wire was meshed around the sample with nodal points used as fiducial markers for the mapping of X-ray data onto the photograph. As seen by the scale on the left-hand side (cm), the sample is too large to be imaged by the  $24 \times 24 \text{ mm}^2$  CCD using the MCP relay optic at unity magnification. The imaged region is indicated (red-dashed lines).

Two dimensional elemental mapping of individual lines aids in the differentiation between those elements present in the steel and those in the mineralogical sample itself. The identification of spectral features must take account of (a) scattered X-rays from the primary (Mo) source, (b) pile-up in the CCD pixels, (c) escape peaks from the silicon and (d) Bragg diffraction peaks. The Mo-L peak is attributed to (a), with pile-up (b) identified by the addition of two lines in *Figure 2.12*. There appears to be no evidence of escape peaks (c) or Bragg peaks (d).



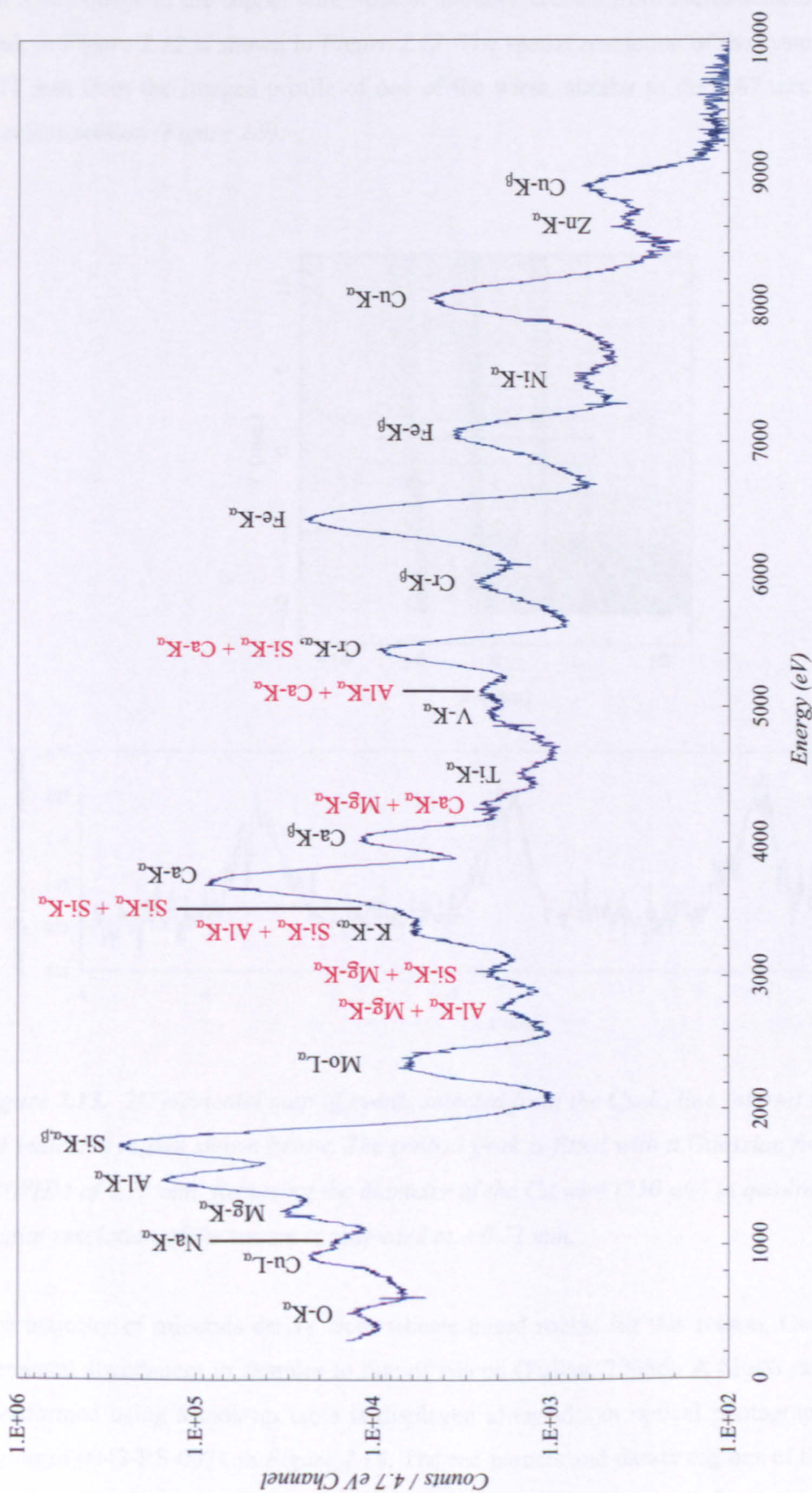


**Figure 2.12.** Isolated events spectrum of the imaged region of the Garnetiferous Anorthosite sample shown in Figure 2.11. X-ray lines are identified, with charge pile-up events denoted by the addition of two such lines (red). Scattered primary X-rays from the molybdenum anode are also in evidence at 2293 eV (Mo-L<sub>α</sub>).



An X-ray image of the copper wire fiducial markers, created from events selected from the Cu- $L_\alpha$  peak in Figure 2.12 is shown in Figure 2.13. The spatial resolution of the system is estimated at 0.71 mm from the imaged profile of one of the wires, similar to the 0.67 mm measured in the previous section (Figure 2.9).

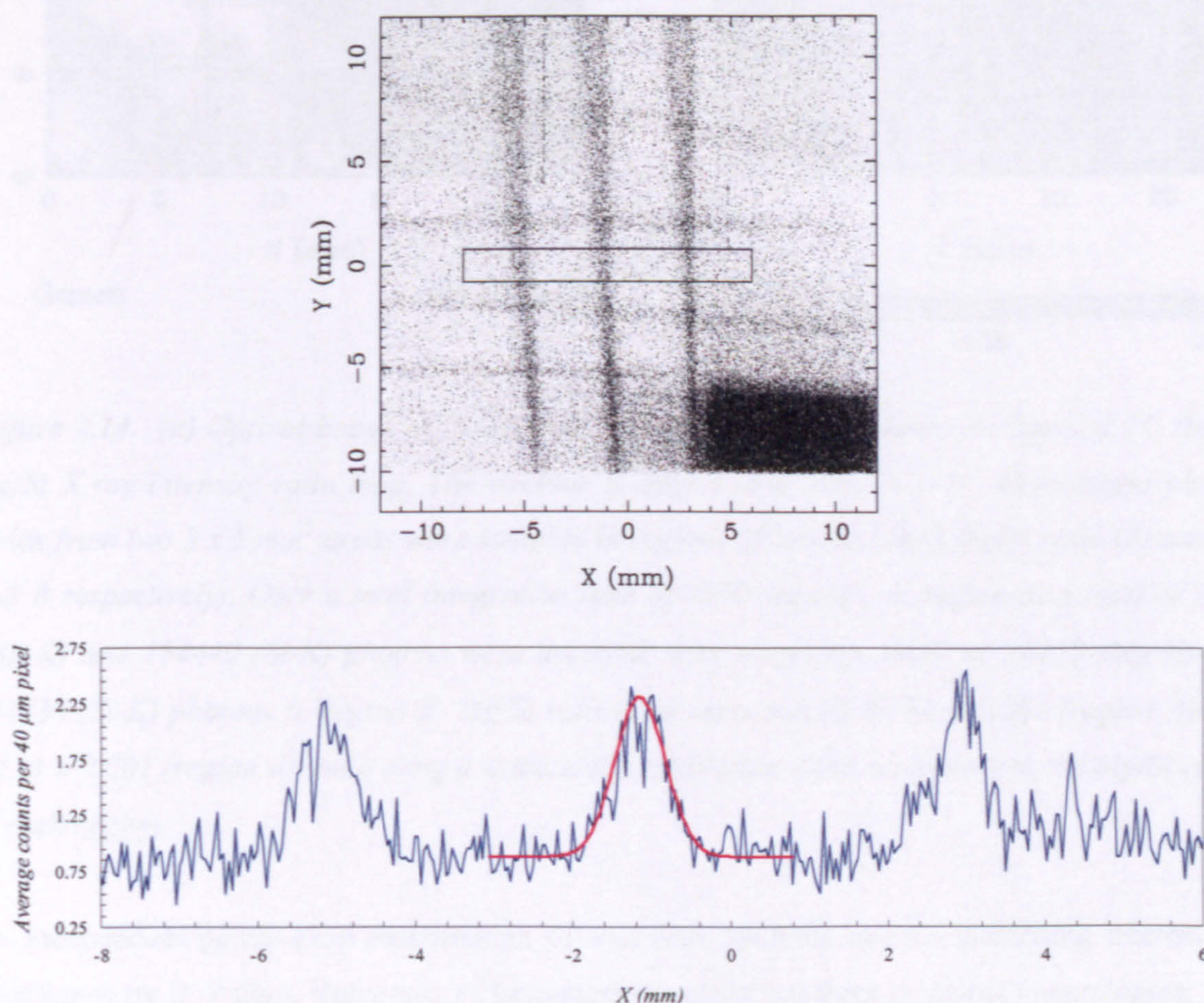


**Figure 2.13.** 2D elemental map of events selected from the Cu- $L_\alpha$  line (above) with a cut across the indicated region shown below. The central peak is fitted with a Gaussian function (red) with a FWHM of 0.75 mm. Removing the diameter of the Cu wire (250  $\mu\text{m}$ ) in quadrature, the FWHM spatial resolution of the system is estimated at  $\sim 0.71$  mm.

The majority of minerals derive from silicate-based rocks; for this reason, Geologists compare elemental abundances in samples to that of silicon (Pullan, 2005c). A Mg/Si ratio intensity map transformed using a look-up table is displayed alongside an optical photograph of the imaged region of 0042-RS-0071 in Figure 2.14. The red garnets and darker regions of the rock appear to be magnesium-rich in comparison with the remaining, paler background mineral matrix.



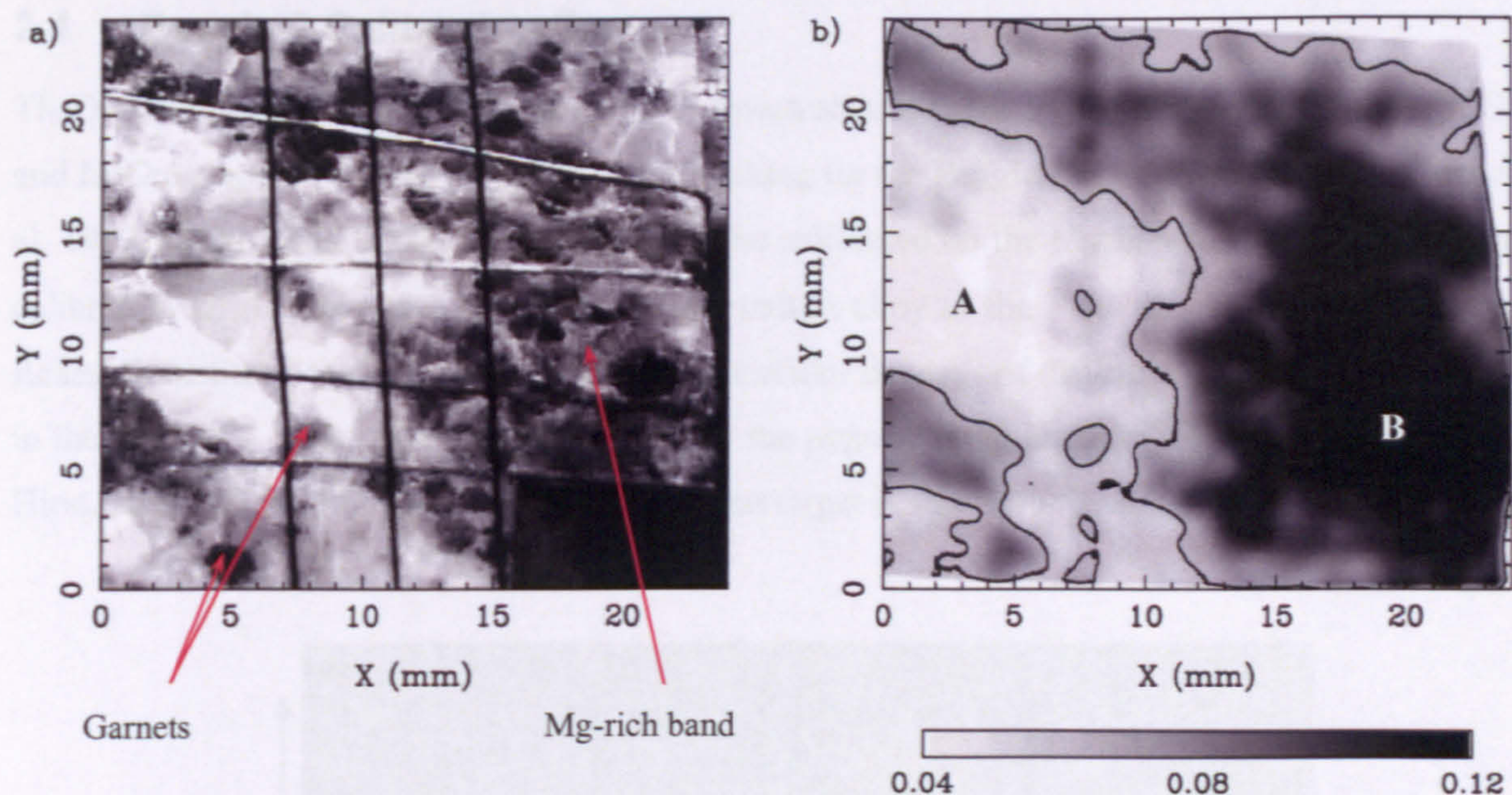


**Figure 2.14.** (a) Optical image of the exposed area of the sample shown in Figure 2.11. (b) An Mg/Si X-ray intensity ratio map. The contour is drawn at a ratio of 0.07. Fluorescent photon yields from two  $5 \times 5 \text{ mm}^2$  areas were sampled in regions of low and high Mg/Si ratio (denoted A and B respectively). Over a total integration time of 4900 seconds, in region A, a total of 7993 (Mg-K) and 154440 (Si-K) photons were detected, with respective totals of 16125 (Mg-K) and 141438 (Si-K) photons in region B. Mg/Si ratios are estimated at  $0.053 \pm 0.001$  (region A) and  $0.114 \pm 0.001$  (region B), indicating a statistically significant difference between the Mg/Si ratios in each region.

An independent petrological examination of thin rock sections using a polarising microscope (performed by D. Pullan, University of Leicester) has identified three principal mineralogies:

- (i) a plagioclase feldspar background rock matrix [as microcline ( $\text{KAlSi}_3\text{O}_8$ ) and albite ( $\text{NaAlSi}_3\text{O}_8$ )]
- (ii) pyroxene bands running through the feldspar (probably augite  $[(\text{Ca},\text{Na})(\text{Mg},\text{Fe},\text{Al},\text{Ti})(\text{Si},\text{Al})_2\text{O}_6]$ )
- (iii) Garnets associated with the pyroxene, probably almandine  $[\text{Fe}_3\text{Al}_2(\text{SiO}_4)_3]$  towards pyrope  $[\text{Mg}_3\text{Al}_2\text{Si}_3\text{O}_{12}]$ .

Despite its complexity, a simple intensity map of the rock performed in IXRFS has successfully identified the magnesium rich pyroxene bands and garnets.



## 2.4 Beagle 2 Calibration Target

The X-ray Spectrometer (XRS), MossBauer Spectrometer (MBS), Stereo Camera System (SCS) and MICroscope (MIC) instruments, in part making up the Beagle 2 instrument package (Sims et al. 1999, Pullan et al. 2004) were designed to be calibrated on the Martian surface; to this end, a calibration target was machined from an aluminium alloy at the Planetary and Space Sciences Research Institute, Open University, featuring circular deposits of different minerals, all arranged in the form of a ‘spot’ painting and applied by the popular artist Damien Hirst (Rosenthal, 1998; Hirst, 2005a; 2005b). A picture of the calibration target is shown in *Figure 2.15*.

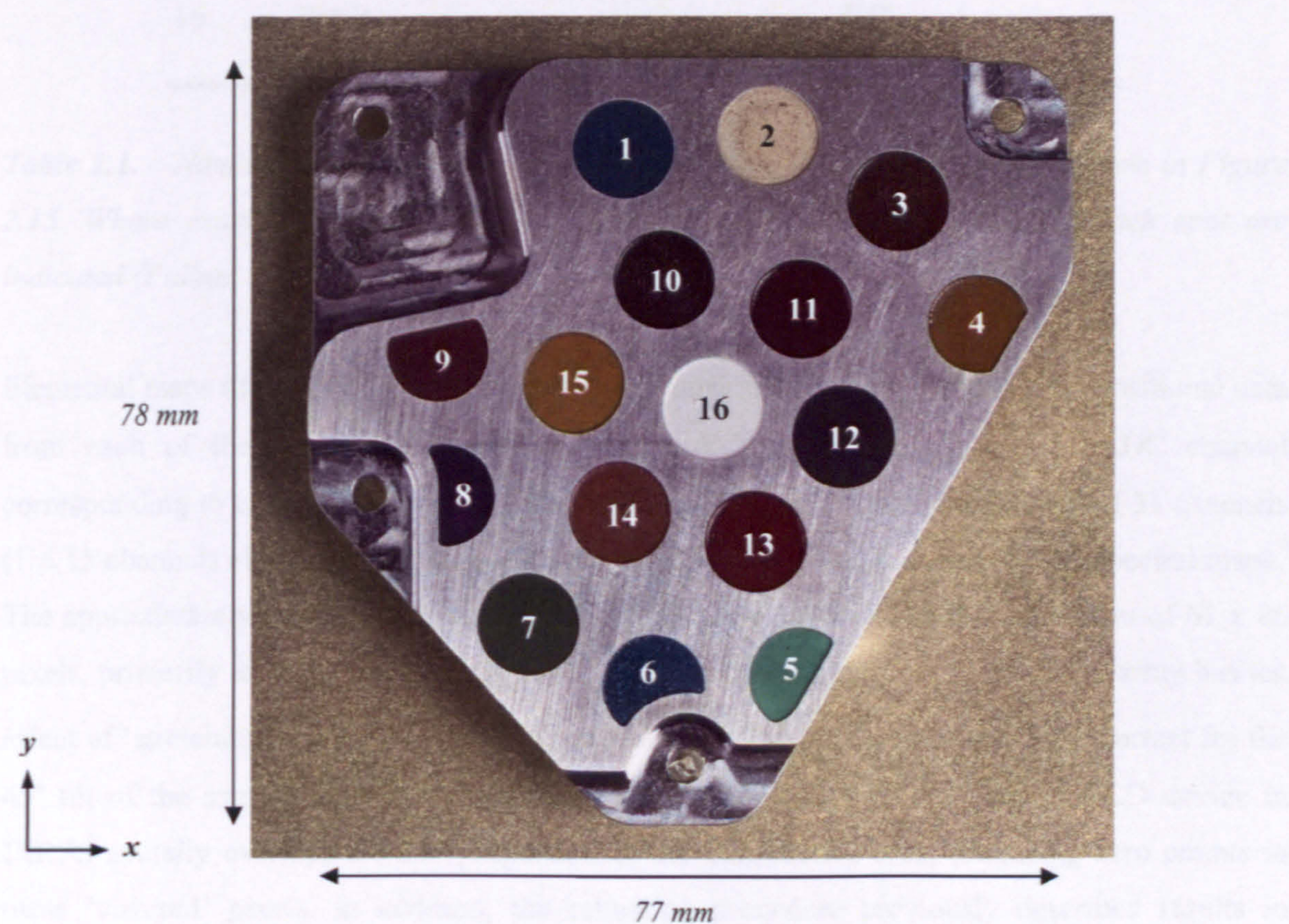


**Figure 2.15.** Annotated photograph of the Beagle 2 calibration target; spots 1-16 have nominal elemental compositions shown in Table 2.1. Image from <http://www.beagle2.com/resources/photo-album.htm>. All Rights Reserved Beagle 2.

The calibration target was securely mounted on the x-y translator table in IXRFS, and was mapped in its entirety by performing ten separate exposures, each on different regions of the target. The sample table was translated in the x and y directions in order to image the different regions of the target.



<i>Spot</i>	<i>Mineral</i>	<i>Composition</i>
1	<i>Azurite</i>	$Cu_3(CO_3)_2(OH)_2$
2	<i>Wulfenite</i>	$PbMoO_4$
3-4	<i>Iron oxides</i>	$Fe, O$
5	<i>Malachite</i>	$Cu_2CO_2(OH)_2$
6	<i>Complex spinel</i>	$Co, Li, Ti, Zn$
7	<i>Terra verte</i>	$Si, Ca, Al, Fe$
8	<i>Manganese ammonium phosphate</i>	$Mn(NH_4)PO_4$
9	<i>Robertson's red</i>	$Fe, O$
10-15	<i>Iron oxides</i>	$Fe, O$
16	<i>Rutile</i>	$TiO_2$

**Table 2.1.** *Nominal compositions of spots in the Beagle 2 calibration target shown in Figure 2.15. Where exact compositions are not known, the principal constituents of each spot are indicated (Pullan, 2005c).*

Elemental maps of each of the ten individual exposures were generated by sorting positional data from each of the required line energies into individual image arrays. The ADC channel corresponding to each of the required lines was identified, and events from a total of 31 channels ( $1 \pm 15$  channels either side of the peak channel), were selected to make up the 2D spectral maps.<sup>i</sup> The approximately square image arrays (610 x 602 pixels) were rebinned into arrays of 61 x 86 pixels, primarily to make the datasets more manageable; changing the shape of the array has the effect of ‘stretching’ images along the y-axis (*Figure 2.7*) by a factor of  $\sim \sqrt{2}$ , to correct for the 45° tilt of the sample table in this orientation. The framestore of the type 22 CCD device in IXRFS actually overlaps a small proportion of the CCD active area, producing zero counts in these ‘covered’ pixels. In addition, the rebinning procedure previously described results in erroneous results in each of the pixels comprising the border of each image. Both effects are removed by transferring the useful pixels into a 59 x 75 image array. The HC software that reads out the raw image data into the 5 byte event file also laterally inverts the image from the CCD. This was corrected for by ‘flipping’ the array (denoted by  $A_{ij}$ ), reflecting it in the y-axis. In this

<sup>i</sup> For event selection purposes, in this case a FWHM CCD energy resolution of 150 eV (*Section 2.2*) is assumed across the energy range. At 4.7 eV per channel, a sampling width of 31 channels approximates a FWHM energy resolution of  $\sim 150$  eV.



case, the transformed, or flipped array  $A'_{i,j}$  containing  $N_i \times N_j$  pixels, with the position of each pixel denoted by indices  $i$  and  $j$  (in the  $x$  and  $y$  axes respectively) is described by

$$A'_{i,j} = A_{N_i+1-i,j} \quad (2.2)$$

For each of the ten exposures (indexed  $k$ ), the X-ray source was operated with an accelerating voltage of 15 kV and an emission current of 0.7 mA, with a different number of frames  $N_k$  recorded in each case; each exposure was therefore normalised to the same number of frames as that of the exposure containing the fewest number of frames  $N_{min}$ , such that the number of counts within each pixel element in each exposure was scaled down by a factor  $f$  given by

$$f = \frac{N_{min}}{N_k} \quad (2.3)$$

This normalisation process was performed in order to provide closer contrasts in the final mosaiced images between the ten individual component exposures, minimising any undesirable 'edges' where the images were joined. Composite images of the calibration target for a variety of elements are shown in *Figure 2.16*.

The body of the calibration target is manufactured from the aluminium alloy A97075, which is comprised largely of pure aluminium, with around 5.1-6.1% zinc, 2.1-2.9% magnesium and 1.2-2.0% copper by weight (Bringas and Wayman, 1995). Each element is imaged in *Figure 2.16*, with the Al, Zn and Mg seen to be distributed throughout the body of the calibration target as expected. The presence of copper in the Azurite and Malachite (Spots 1 and 5 respectively) is clearly identified in *(k)*, with the Cu- $K_\alpha$  flux from the calibration target body limited in comparison.

Molybdenum is observed in the Wulfenite spot *(e)* as expected, yet there also appear to be traces of Mo in the Terra Verte spot; in actual fact, this is sulphur in the latter case. The Mo- $L_\alpha$  (2.293 keV) and S- $K_\alpha$  (2.308 keV) lines are sufficiently close together that the process adopted to select 'Mo' events has selected a quantity of 'S' events (the energy window width for event selection is  $\sim 70$  eV either side of the desired line energy). Furthermore, within the Wulfenite spot, some of the 'Mo' events may be 'Pb' events, due to the proximity of the Pb- $M_{\alpha,1}$  line (2.345 keV).



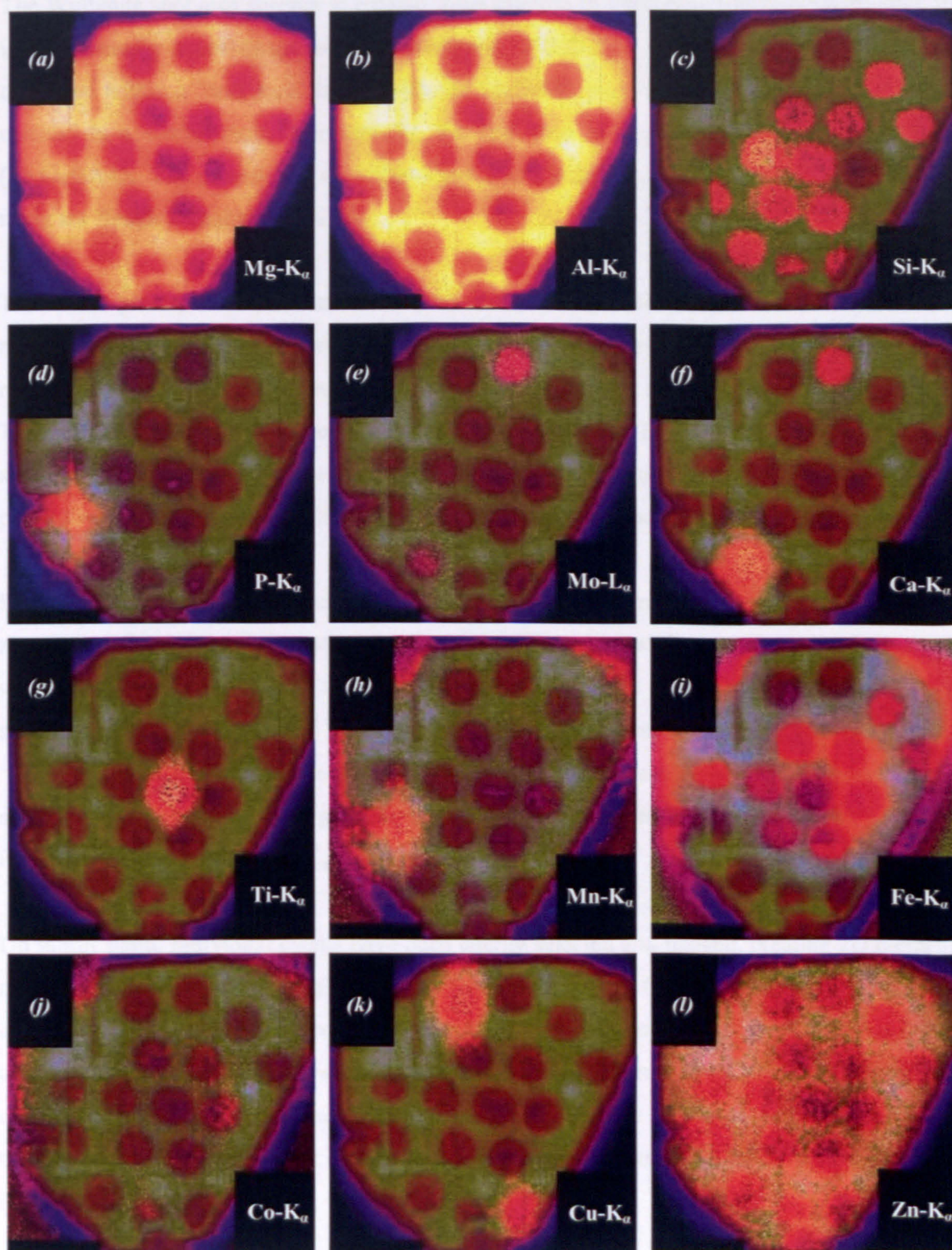


**Figure 2.16.** Composite elemental maps, each comprising 10 IXRFS exposures, of the Beagle 2 calibration target (Figure 2.15), viewed in elements labelled (a-l). Each is superimposed onto a dulled Al- $K_{\alpha}$  image background (excluding the Al- $K_{\alpha}$  image itself) to facilitate spot identification.



The Wulfenite spot also appears to contain some calcium (*f*), distributed throughout the spot; this is not normally a constituent of pure Wulfenite (*Table 2.1*). It is possible that calcium was contained within a ‘host rock’ from which the Wulfenite may have been extracted and thus the calcium is a contaminant. Alternatively, the spot may be comprised of Calcian Wulfenite<sup>ii</sup> (Pb,Ca)MoO<sub>4</sub>. The presence of Ca within Spot 2 was independently verified by Talboys (2003) using the Beagle 2 flight-spare XRS.

Two of the principal constituents of the Terra Verte spot are silicon and iron, seen in (*c*) and (*i*) respectively. Si appears in the majority of spots, those containing minerals derived from silicate rocks. Similarly, Fe is evident in a variety of spots, principally in the iron oxide spots (3–4, 10–15) and in Robertson’s Red (Spot 9) as expected. Additionally, Fe is the major constituent of the stainless steel support structure on which the calibration target was positioned. A ‘haze’ is present surrounding the calibration target, where the support structure itself is fluorescing (*i*).

Perhaps the best demonstration of IXRFS is seen when imaging the phosphorus (*d*) and manganese (*h*) in Spot 8. In each case, the contrast is such that the cruxiform image structure, characteristic of MCP focusing is observed. Titanium is clearly identified in the Rutile spot (*g*), and there appears to be a small quantity of cobalt within the complex spinel spot (*j*). Apparent ‘Co’ events in the iron oxide-based Spot 12 and in the stainless steel support structure surrounding the calibration target can be attributed to the Fe-K<sub>β</sub> line (6.931 keV) which is indistinguishable from the Co-K<sub>α</sub> line (6.930 keV) in IXRFS.

Up to this point, individual events have been energy selected and imaged, creating 2D elemental maps of both the mineralogical specimen (*Section 2.3*) and the Beagle 2 calibration target; conversely, it is possible to select events based on their position and sort them into energy bins, creating spectra. Events were selected from a ~ 3.4 x 6.3 mm<sup>2</sup> area in Spot 8 (nominally containing manganese ammonium phosphate, shown in *Figure 2.17*) and processed to produce the spectrum shown in *Figure 2.18*. The spectrum of the entire imaged area shown in *Figure 2.17* is also shown for comparison.

As expected, the elements contained within Spot 8 (Mn, P, Si) are more prominent in the ‘Spot 8 spectrum’ in comparison to that from the ‘full spectrum’; similarly, the elements contained within the stainless steel x-y translator table (Fe, Cr, Ni) are less prominent.

---

<sup>ii</sup> Details of Calcian Wulfenite may be found at <http://www.mindat.org/min-9713.html>



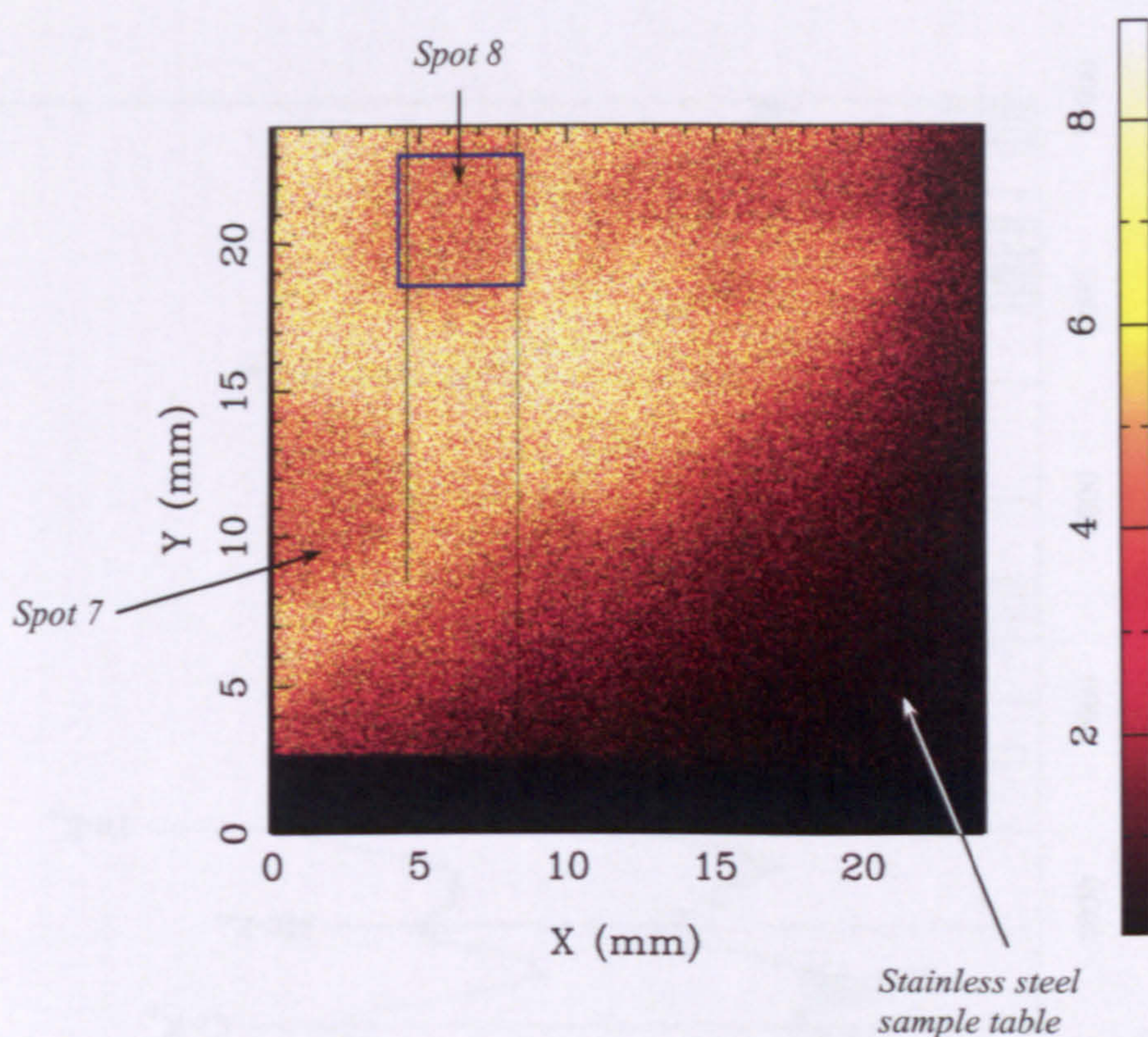


**Figure 2.17.** Raw 610 x 602 CCD exposure containing aluminium selected events. Spots 7 and 8 appear as 'holes' in the image, indicative of a relative absence of aluminium. The spectrum of Spot 8 (Figure 2.18) is comprised of events selected from the area within the indicated rectangle. The rectangular sample area is 85 x 112 pixels, corresponding to a geometrical area of  $\sim 3.4 \times 6.3 \text{ mm}^2$  on the calibration target. Events for the spectrum were selected prior to the binning, stretching and the flipping of each image array; thus this image appears 'squashed' in the vertical axis and laterally inverted when comparing it to Figure 2.15. The framestore, overlapping the CCD active area is also seen towards the bottom of the image.

The origin of 'Peak X' labelled in Figure 2.18 is unclear upon initial inspection; occurring at  $\sim 4.20 \text{ keV}$ , X is believed to be the superposition of two 'component peaks'. The low energy shoulder is attributable (in part) to the Ca- $K_{\beta}$  line as shown in Figure 2.19. A significant fraction of the X-ray flux at this energy however appears to have originated from the stainless steel sample table; indeed, this is confirmed when Peak X is imaged about its maximum in Figure 2.20. There are no elements contained within the stainless steel that may be responsible for fluorescent X-ray lines at this energy; the major component of Peak X is deduced to be a Bragg peak, caused by X-ray diffraction from successive atomic planes of one of the constituent elements of the stainless steel.



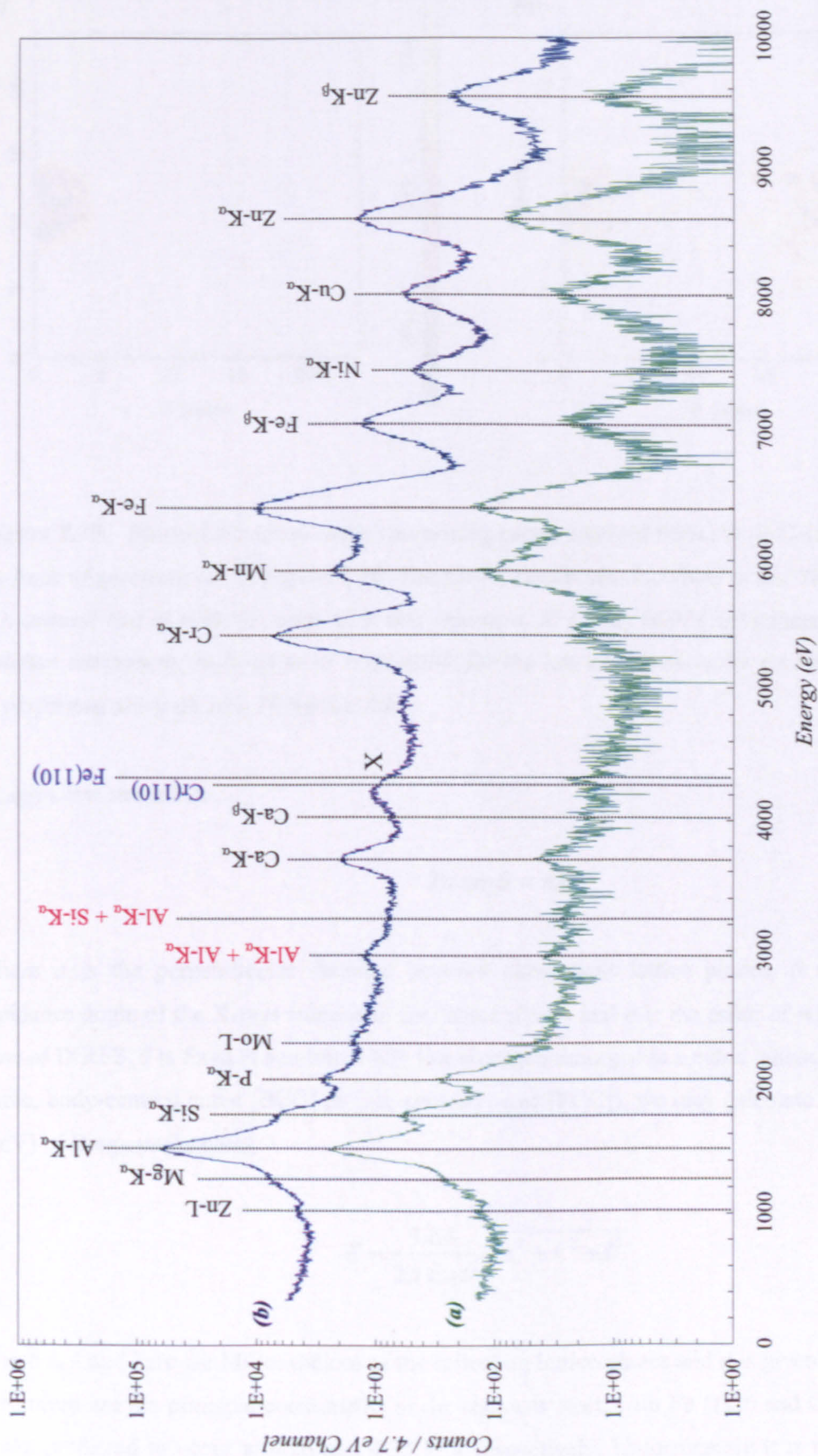


**Figure 2.18.** Two isolated events spectra, compiled from events selected from (a) the indicated region (green) and (b) the entire imaged region (blue) of the Beagle 2 calibration target shown in Figure 2.17. Spectrum (a) contains a total of 179,677 isolated events, selected from spectrum (b), which comprises 5.3 million events collected over 4 hours in 881, 1 second frames, with a readout time of 8.7 seconds.



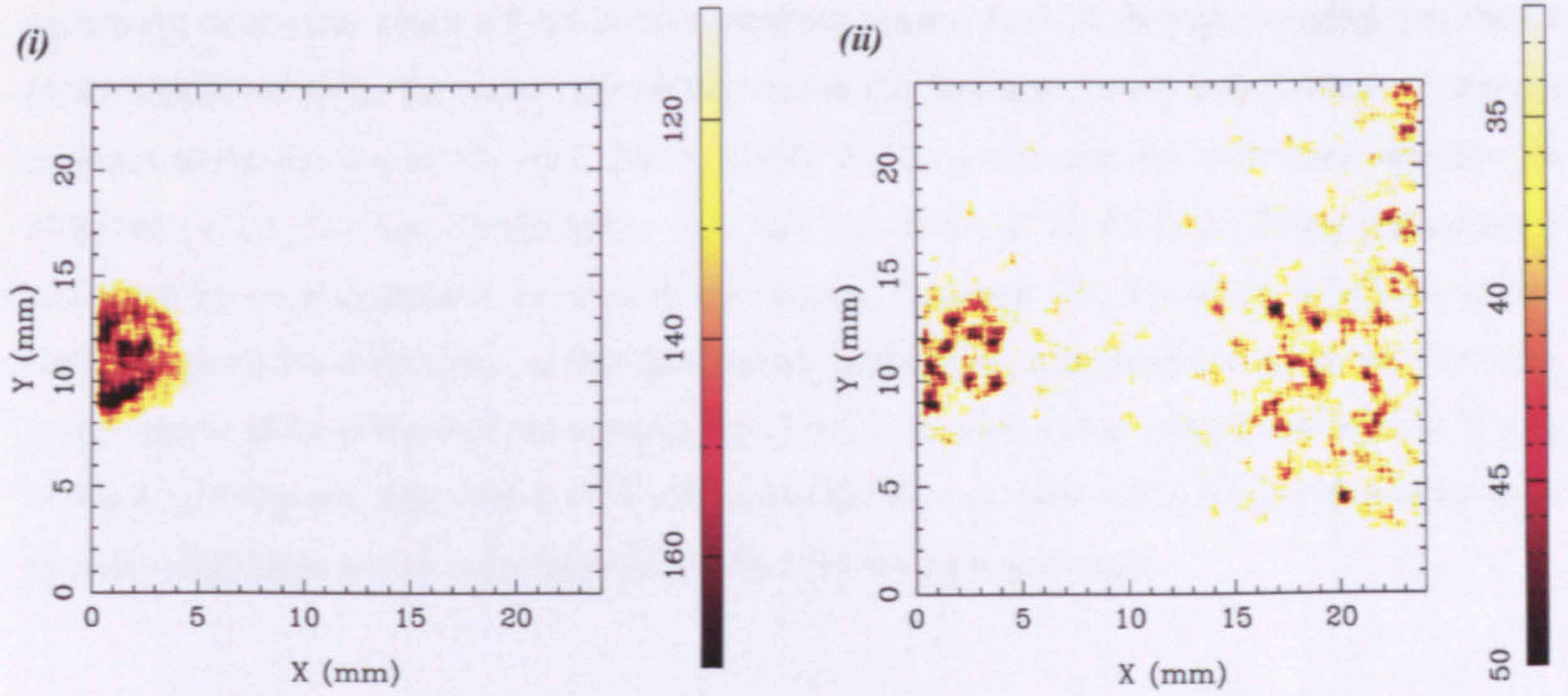


**Figure 2.19.** Blurred elemental maps comprising events selected from the (i)  $\text{Ca-K}_\alpha$  and (ii)  $\text{Ca-K}_\beta$  lines of spectrum (a) in Figure 2.18. The  $\text{Ca-K}_\alpha$  counts are localised in the Terra Verte spot (7), around half of which is imaged in this exposure. At  $\text{Ca-K}_\beta$  (4.013 keV) there is a localised calcium component, believed to be responsible for the low energy shoulder on Peak X. Blurring is performed using an  $18 \times 18$  top hat filter.

Bragg's law states that

$$2d \sin \theta = n\lambda \quad (2.3)$$

where  $d$  is the perpendicular distance between subsequent lattice planes,  $\theta$  is the grazing incidence angle of the X-rays relative to the lattice planes and  $n$  is the order of reflection. In the case of IXRFS,  $\theta$  is fixed at a nominal  $45^\circ$ . For elements arranged in a cubic lattice, (either simple cubic, body-centred cubic [BCC] or face-centred cubic [FCC]), we may calculate the energies  $E$  (keV) of Bragg peaks using

$$E = \frac{12.4}{2a \sin \theta} \sqrt{h^2 + k^2 + l^2} \quad (2.4)$$

where  $h$ ,  $k$  and  $l$  are the Miller indices of the reflecting lattice planes and  $d$  is given in Å. Iron and chromium are the principal constituents of the stainless steel, with Fe (110) and Cr (110) Bragg peaks predicted to occur at 4.26 and 4.33 keV respectively. Unfortunately it is not possible to



accurately determine which (if not both) contribute toward Peak X through imaging, yet the Cr (110) is believed to be the major contributor due to the fact that during manufacture, chromium migrates to the surface of the steel (Binns, 2005). If this is the case, the difference between the observed ( $\sim 4.20$  keV) and predicted ( $\sim 4.26$  keV) positions of the Cr (110) Bragg peak may be explained by an experimental error in  $\theta$ ; rearranging *Equation 2.3*,  $\theta \sim 45.8^\circ$ , which is entirely plausible given the difficulties in machining (and assembling) components such as the mounting to the sample table to the level of accuracy required. A further, minor contributor to Peak X may be the Al (200) peak, expected at 4.34 keV, although it is not possible to resolve this component through imaging as events originating from the stainless steel dominate.

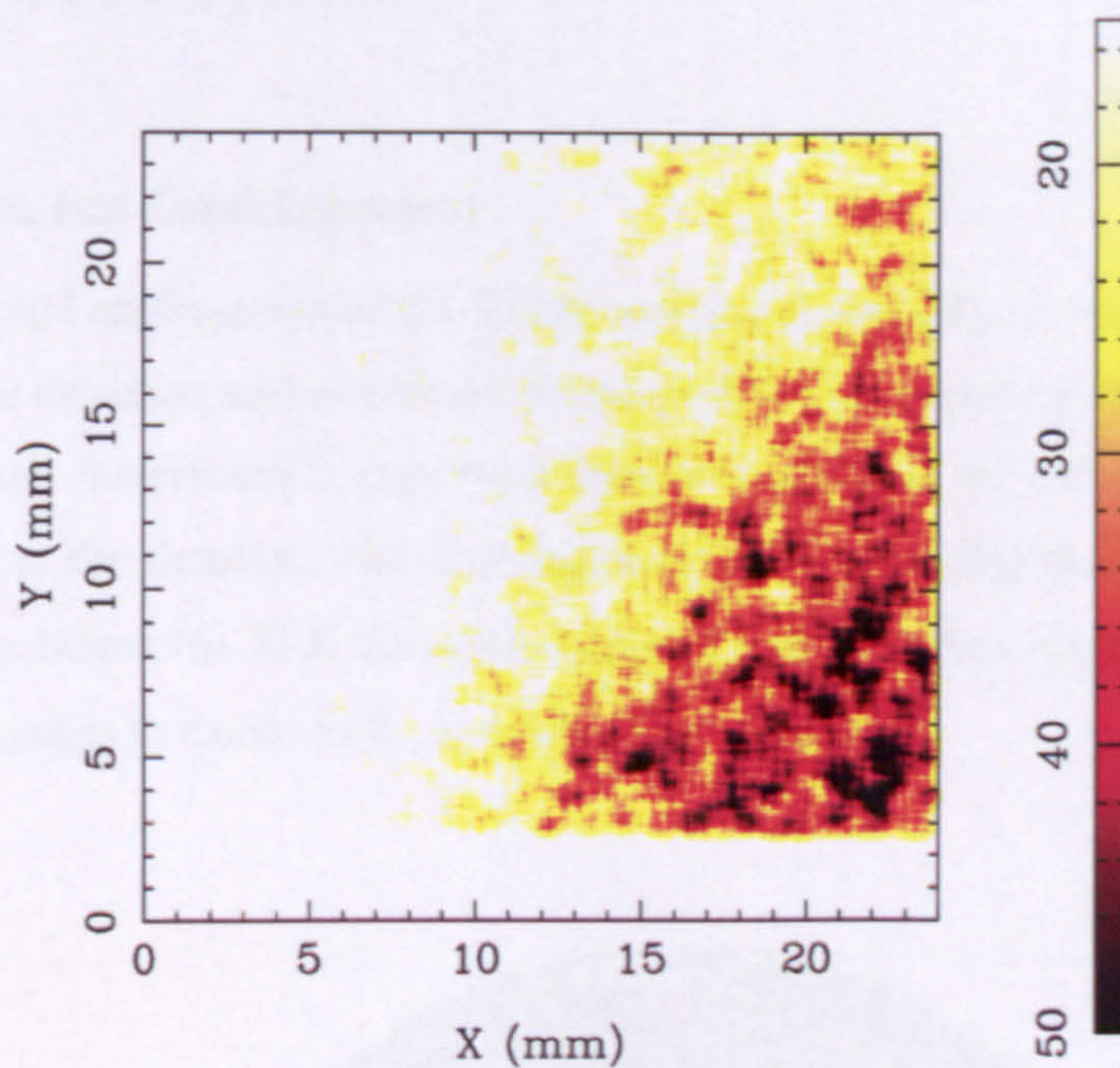


**Figure 2.20.** A blurred elemental map comprising events selected from Peak X. The imaged flux originates from the stainless steel sample table upon which the calibration target is mounted. Blurring is performed using an  $18 \times 18$  top hat filter.

A simple diagnostic to confirm that Peak X is a result of Bragg diffraction would be to repeat the experiment with the sample tilted at a different orientation (i.e.  $\theta = 60^\circ$  rather than  $\theta = 45^\circ$ ); a Bragg peak would then appear at a different energy (for Cr [110],  $E \sim 3.48$  keV for  $\theta = 60^\circ$  as opposed to  $E \sim 4.26$  keV for  $\theta = 45^\circ$ ). Unfortunately, due to high demand for the calibration target elsewhere in the scientific community, there was insufficient time to test this hypothesis. An alternative diagnostic would be to consider the profiles of each of the peaks in *Figure 2.18*. The FWHM energy resolution  $\Delta E$  of any solid state detector is related to the energy  $E$  of the



detected photon (to first order) as  $\Delta E \propto \sqrt{E}$ , intrinsically limited by Fano statistics (Fraser, 1989). In our experimental configuration, a Bragg peak would be slightly broader (and thus not follow the relationship) due to an additional error associated with the range of angles  $\Delta\theta$  sampled during the integration. However, as previously mentioned, *Figure 2.19* shows Peak X to have a contribution from the Ca-K $_{\beta}$  line and so this diagnostic would not be appropriate in this case. Peak X is not believed to be a Mn-K $_{\alpha}$  escape peak (which in principle would be observed at 4.16 keV); in an E2V type 22 CCD, the magnitude of such a peak is expected at around the 1% level of the observed Mn-K $_{\alpha}$  line (Short et al. 1998) rather than the ~50% level observed in *Figure 2.18*. Furthermore, Peak X photons are shown in *Figure 2.20* to originate from the stainless steel sample table and *not* the Mn-based Spot 8.

## 2.5 IXRFS Source Development

One of the commercial applications of the IXRFS system identified prior to its development was its suitability for the detection and elemental mapping of low-Z element contamination on silicon wafers. However, any fluorescent X-rays from such contaminants are currently swamped by the silicon background at the detector. The problem is solved by running the X-ray source with an accelerating voltage below the Si-K absorption edge (1840 eV), thus providing primary X-rays with insufficient energies to excite Si-K $_{\alpha}$  and Si-K $_{\beta}$  line emission.

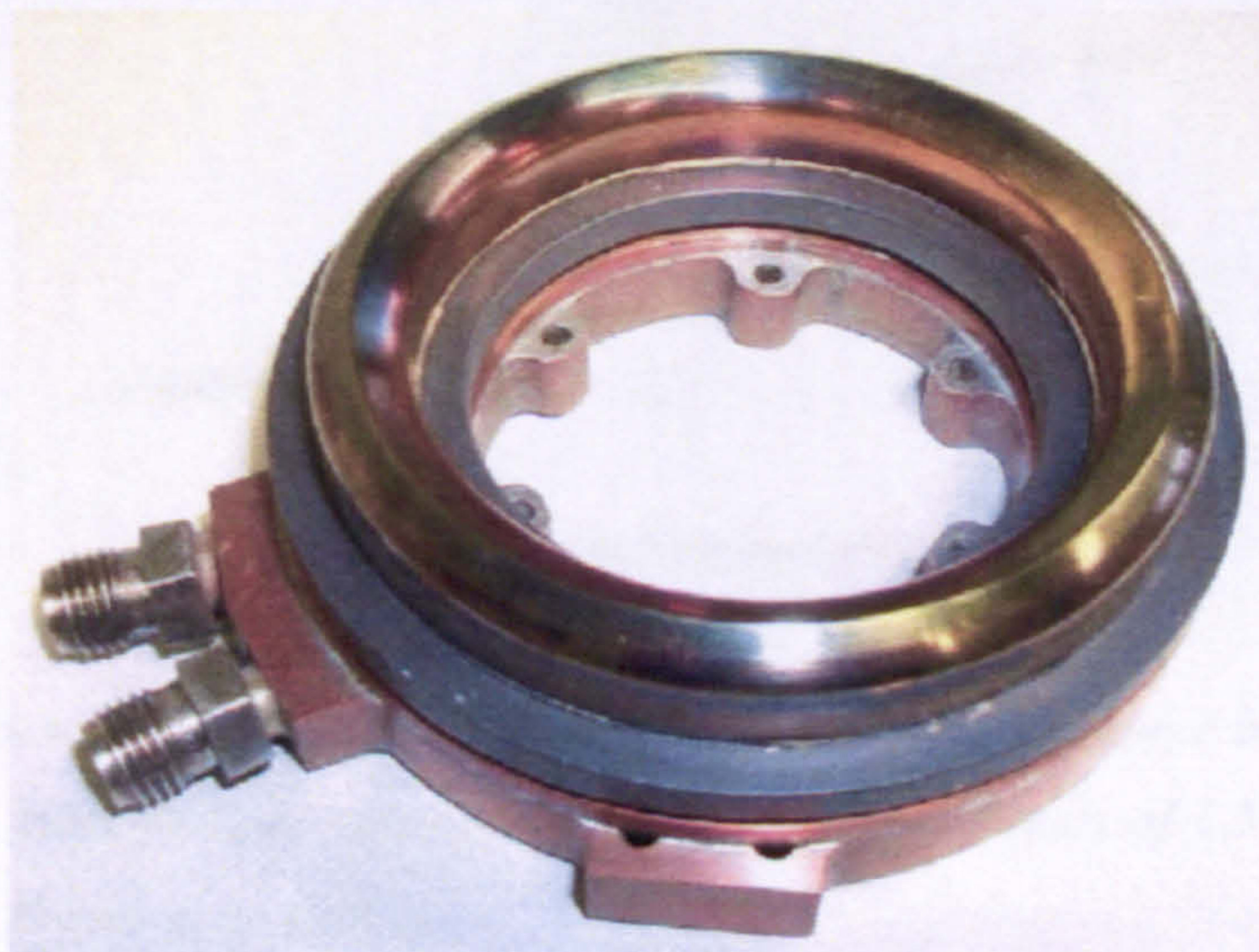


**Figure 2.21.** Photograph of the prototype ring anode design. An electrically insulating aluminium nitride ceramic (grey) separates the gold-plated anode from the water-cooled copper block below.



However, conventional X-ray sources experience a dramatic decrease in emission current in response to a reduction in accelerating voltage, significantly increasing integration times. To this end, a novel gold-plated anode with annular geometry is currently in development at the University of Leicester to increase photon yield at lower energies, shown in *Figure 2.21*.

The annular geometry of this *ring anode* maximises cathode area, resulting in a corresponding increase in primary X-ray flux. A circular thoriated tungsten filament is suspended above the anode, with primary X-rays generated by conventional means of electron bombardment. Fluorescent X-rays propagate back through the centre of the annulus, where they are imaged onto the CCD by the MCP relay optic. *Figure 2.22* shows the I-V characteristics of a prototype ring anode, with a 200 mA emission current recorded at 1 kV, a 200-fold increase over the current source. The principle of operation of the ring anode X-ray source is shown in *Figure 2.23*.

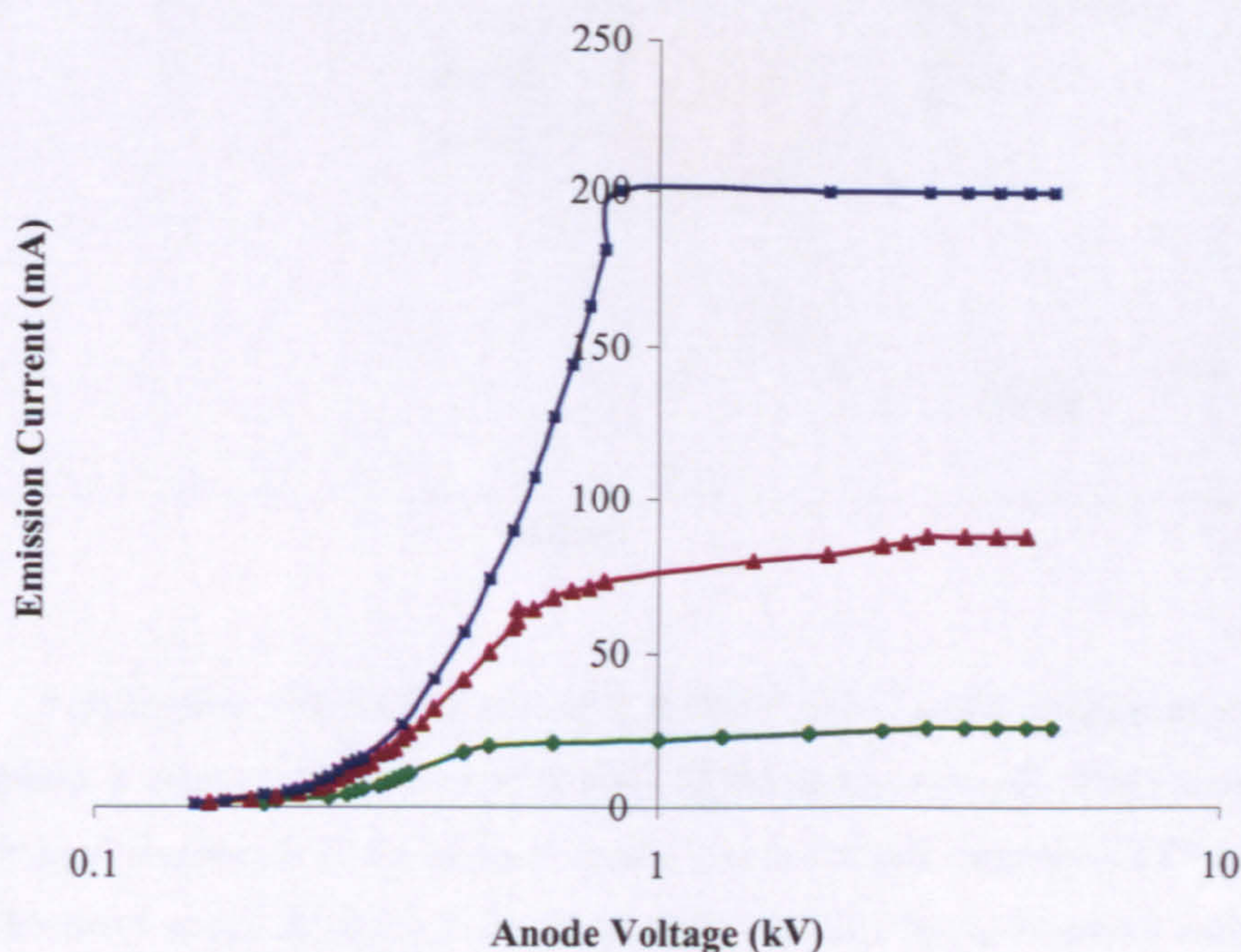


**Figure 2.22.** I-V characteristics of the prototype ring anode X-ray source based on preliminary testing. Diamonds, triangles and squares represent filament currents of 1.5 A, 1.6 A and 1.7 A respectively. From Fraser et al. (2002).

Primary X-ray generation by means of electron bombardment generates a significant amount of thermal energy in the system. Preliminary testing of a prototype ring anode source revealed



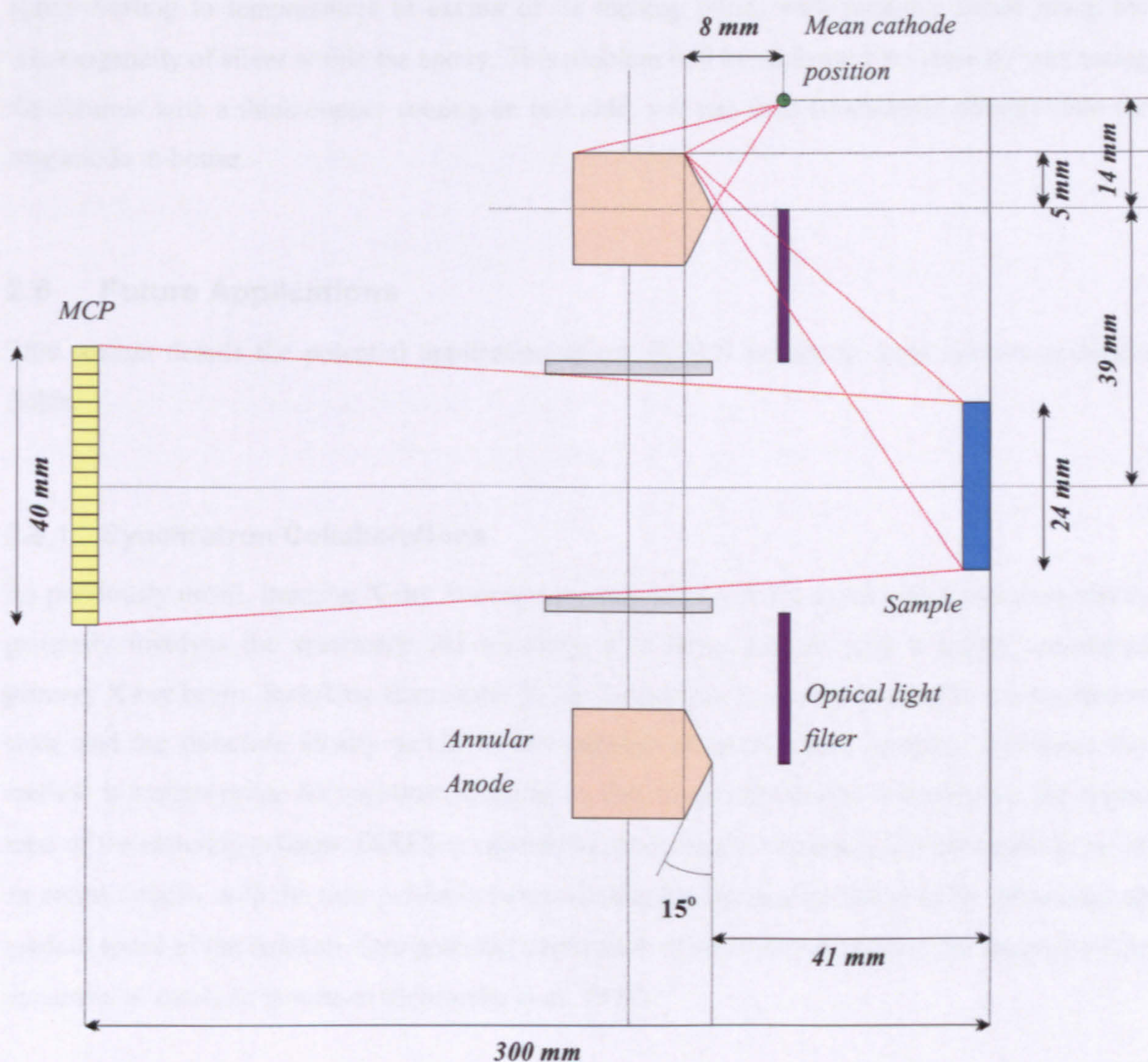


**Figure 2.23.** A schematic illustrating the ring anode X-ray source configuration. A circular filament (cathode) is suspended above and outside of the annular anode. Fluorescent X-ray flux propagates through the centre of the annular anode and is imaged onto the CCD using the MCP relay optic. The novel anode design will increase soft X-ray flux by (a) boosting emission current and (b) increasing the solid angle between anode and sample.

temperatures in excess of 200 °C at 2 kV measured at the support structure (incorporating both filament and optical light filters). A chilled water supply was placed in thermal contact with the ring anode itself using an intermediary ceramic, bonded with silver-loaded epoxy. A commercially produced aluminium nitride ceramic was selected due to its low-electrical and high-thermal conductivity properties. However during testing, the anode-ceramic bond failed, the



epoxy heating to temperatures in excess of its melting point, with probable cause being the inhomogeneity of silver within the epoxy. This problem will be addressed in future by purchasing the ceramic with a thick copper coating on one side; this can then be soldered directly onto the ring anode in-house.

## **2.6 Future Applications**

This section details the potential application of the IXRFS system to three diverse scientific fields.

### **2.6.1 Synchrotron Collaborations**

As previously noted, imaging X-ray fluorescence spectroscopy at a synchrotron radiation source generally involves the systematic 2D scanning of a target sample with a highly collimated primary X-ray beam. Resulting fluorescent X-ray images have a spatial resolution on the micron scale and are therefore ideally suited to the imaging of microscopic samples. However, this method is inappropriate for real-time imaging, as the image refresh rate is limited by the repeat time of the rastering process. IXRFS is capable of producing evolutionary 2D elemental maps of an entire sample, with the time period between subsequent images limited only by the maximum readout speed of the detector. One potential application of real-time imaging is the analysis of the dynamics of catalytic processes (Schroeder et al. 1997).

### **2.6.2 Botany and Marine Biology**

Elemental maps of botanical specimens are routinely generated using an SEM in conjunction with an Energy Dispersive X-ray microprobe analysis system (EDX), detailed in Heslop-Harrison, 1990. Samples as intricate as the reproductive system of maize can be successfully studied in this way (Heslop-Harrison and Reger, 1985), which are conventionally either frozen or dehydrated prior to analysis to prevent ion diffusion into the ambient vacuum. Whilst IXRFS is not currently suited to the study of microscopic specimens, there is scope for similar investigations on the macroscopic scale.

Compositional analysis of marine organisms is a widely-used method of observing the concentration of heavy metal pollutants in coastal environments. Sentinel aquatic molluscs such as *mussels* (Jeng et al. 2000), *limpets* (Cravo et al. 2002), *oysters* (Solis et al. 1996) and *marine*



*snails* (AbdAllah et al. 2002) have been used as pollution biomonitors worldwide. Analyses are commonly performed using Proton Induced X-ray Emission (PIXE). It may be possible to use IXRFS to image the characteristic *growth rings* seen in marine shells, potentially providing a continuous history of the heavy metal pollutants in the environment of the mollusc over its complete lifetime.

## 2.7 Conclusions

A new X-ray fluorescence spectrometer concept has been developed to the point that it is a useful laboratory tool in the non-destructive investigation of sample compositions. Two-dimensional elemental ratio maps (Mg/Si) of a Garnetiferous Anorthosite mineral were produced with sufficient spatial resolution to identify localised surface features. Each element believed to be present in the mineralogical structure was identified from a spectrum compiled from events contained within the imaged region. IXRFS is also applied in the field of instrument calibration; the Beagle 2 calibration target is imaged in its entirety, a total of ten component images mosaiced together to produce 2D elemental maps. All elements believed to be contained within both the spot paints and the target base itself were identified and imaged, each located in its expected position. Events were selected from an area (Spot 8) of one of the component exposures and compiled into an isolated events spectrum. Elements localised within the selected area appeared more prominent relative to a spectrum compiled from all events in the exposure and vice versa. The imaging capability of the instrument was key in the identification of a stainless steel based Cr (110) Bragg peak.

The sensitivity of IXRFS to different elements in a sample is fully calculable using the *fundamental parameters* approach, detailed in Tertian and Claisse (1982). Properties such as the system geometry, MCP efficiency (at all energies and grazing angles) source flux and detector QE (both as functions of photon energy) must be taken into account. The fluorescence yields of each spectral line must also be considered. In general, the sensitivity of IXRFS to a particular element depends critically on the presence of other, major elements; for example, in *Section 2.3*, the presence of the Si-K $\alpha$  peak in particular has the effect of swamping counts from neighbouring elements, shown in *Figure 2.12*. Background fitting is thus the key to deducing the ultimate sensitivity of any X-ray fluorescence spectrometer. This is beyond the scope of this thesis, yet should be considered in the near future.



Each image in the CCD plane recorded from IXRFS is a convolution of the cruxiform point spread function of the MCP optic with the target sample and the X-ray source. Image deconvolution was not performed in this work due to time constraints, yet should be investigated in the future.

The development of a novel annular anode X-ray source will increase emission current by a factor of over 200 times, enabling the imaging of low-Z element contamination on silicon wafers. It is currently foreseen that the technology will also be applied in the fields of botany and marine biology in the near future, with no further modifications to the experimental configuration being required.



## Chapter 3 MCP Optics for Lobster-ISS

### 3.1 Introduction

MCP optics have reached a level in their development where they are beginning to have real applications in X-ray astronomy, as discussed in *Chapter 1*. The particular astronomical application of MCP optics described in this thesis is the Lobster-ISS X-ray all sky monitor. In this chapter, the experimental focusing properties of both slumped and planar Lobster-ISS optics are investigated.

#### 3.1.1 Lobster-ISS as an X-ray All Sky Monitor

The X-ray sky is highly variable. The gaseous nebulae of supernova remnants and clusters of galaxies, estimated to contribute to <1% of the galactic source population and around 10% of the thousand brightest extragalactic sources respectively, are the only astrophysical objects to have shown negligible temporal variability in the X-ray band (Holt and Priedhorsky, 1987). All-Sky Monitors (ASMs) are telescopes with a large FOV which have the capability to map the X-ray sky at frequent intervals, providing a synoptic view of X-ray variability. A secondary use of ASMs is to provide a transient event alert facility to existing pointed telescopes, such as XMM-Newton (Jansen et al. 2001) and Chandra (Weisskopf et al. 2000), or for future missions such as Constellation-X (White and Tananbaum, 1999) or XEUS (Bavdaz et al. 2002) depending on the Lobster-ISS launch date, so that serendipitous discoveries can be studied in greater depth by more spectroscopically capable and sensitive, narrow-field instruments.

The most sensitive X-ray ASMs designed and/or flown to date are the Rossi X-ray Timing Explorer (RXTE), the MOnitoring X-ray Experiment (MOXE) and the Monitor of All-sky X-ray Image (MAXI). The ASM on RXTE (Bradt et al. 1991) remains in use almost ten years on from its launch in 1995, operating in the 2-10 keV energy band with a sensitivity of 8 mCrab in a one day observation, using a coded mask aperture to achieve an angular resolution of 15 x 3 square arcminutes. This is the most sensitive ASM in operation to date with most observable sources being galactic X-ray binaries. MOXE (In't Zand et al. 1994) was developed for the Russian-based Spectrum X-Gamma mission which is yet to fly due to funding difficulties. The MOXE design consists of an array of six X-ray pinhole cameras and has an angular resolution of 2.4 x 9.7 square degrees operating in the 2-25 keV energy band. In a 24 hour exposure, MOXE has a



detection threshold of 2 mCrab, a little less sensitive than MAXI (Matsuoka et al. 1999, Tomida et al. 2000) which has a projected one day sensitivity of 1.7 mCrab (Kawai et al. 1999). MAXI uses a combination of two large area, proportional counter-based Gas Slit Cameras (GSCs) to identify sources with an angular resolution of  $1.4 \times 1.4$  square degrees in the hard X-ray band (3-30 keV) and a single CCD-based Solid-state Slit Camera (SSC) to provide all-sky mapping and monitoring in the soft X-ray band (0.5-10 keV). MAXI is due to be launched in 2008 to 'Kibo', the Japanese Experiment Module (JEM) of the ISS (Kataoka et al. 2004).

Lobster-ISS is proposed to fly in the vicinity of MAXI, fixed to the neighbouring ESA Columbus module (*Figure 3.1*) and will use spherically slumped MCP focusing optics to provide a new generation of X-ray ASM with an unprecedented sensitivity and angular resolution.

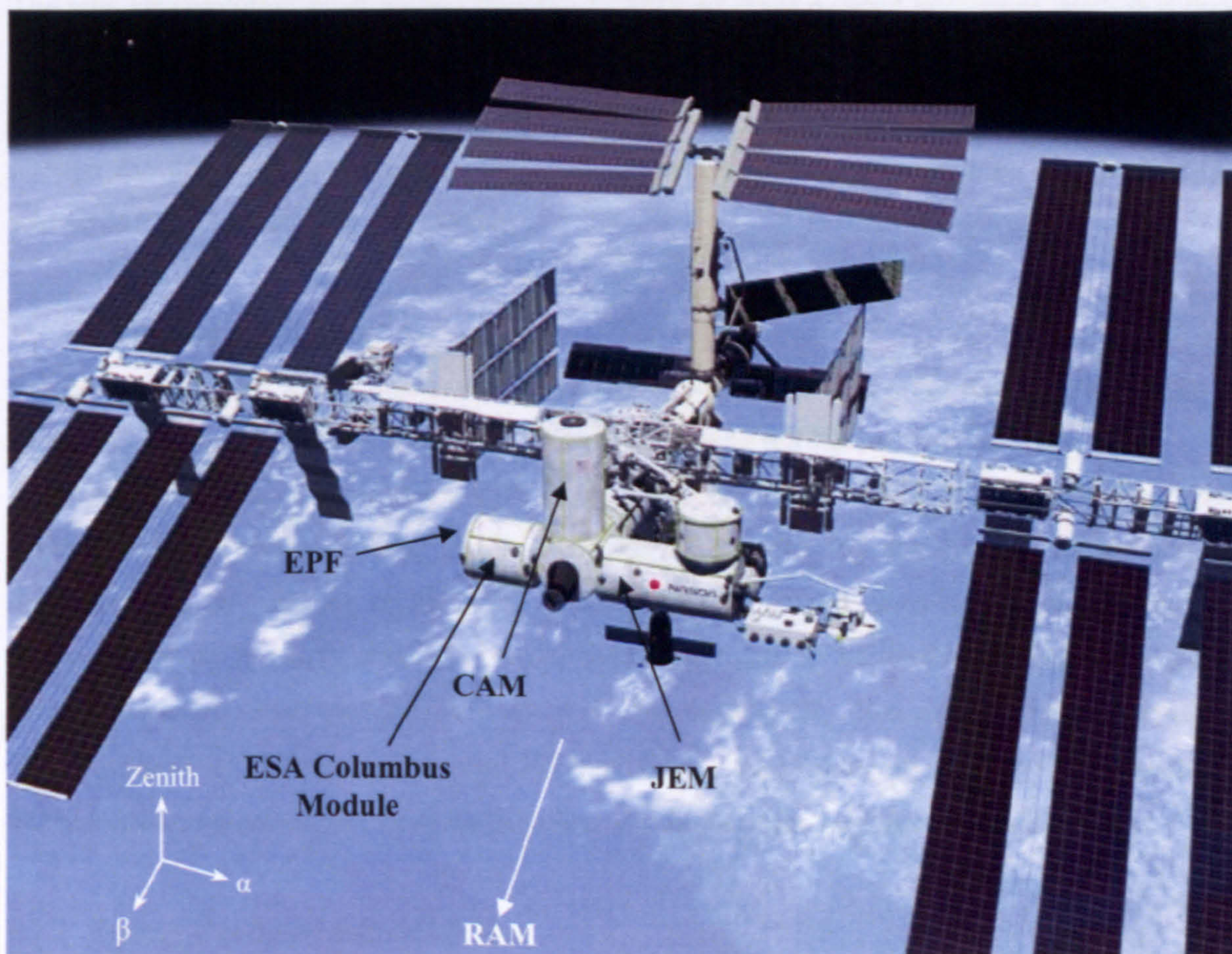


**Figure 3.1.** Artist's impression of the ISS showing the locations of the ESA Columbus module, the NASDA 'Kibo' or Japanese Experiment Module (JEM) and the Centrifuge Accommodation Module (CAM). The ESA Exposed Payload Facility (EPF) is located on the starboard edge of the ESA Columbus module.



Holt and Priedhorsky (1987) discuss the capabilities of the ideal X-ray ASM. These may be summarised as follows:

- **Overall Field of View**

The FOV of the ASM should be maximised and as near to  $4\pi$  steradians as possible – “the whole sky should be monitored unless the cost or complexity is prohibitive”.

*Lobster-ISS has an overall field of view of  $162^\circ \times 22.5^\circ$ ; the long axis of the FOV is orientated perpendicular to the direction of ISS motion (the RAM direction) and parallel to the  $\alpha$ -axis (Figure 3.2). Thus, Lobster-ISS uses the orbital motion of the International Space Station to map the X-ray sky.*

- **Angular Resolution**

The angular resolution must be less than the  $1^\circ$  FOV of other pointed telescopes, such that they may successfully locate the source in the event of a transient alert. An angular resolution of  $< 10$  arcmin is desirable.

*Lobster-ISS will have an order of magnitude improvement in angular resolution over both MAXI and MOXE, with a target of 4 arcminutes.*

- **Temporal Resolution**

For both galactic and extragalactic sources, a temporal resolution of order hours is acceptable to identify X-ray transients, with pointed instruments carrying out further detailed study.

*Lobster-ISS will map on average  $\sim 95\%$  of the X-ray sky every 90 minute ISS orbit (Bannister, 2004a), with any point on the sky being observed for between 400 and 1800 seconds per orbit depending on its position in the FOV (Pearson et al. 2003). Some areas of the sky are unobservable on a given orbit due to the orbital passage of Lobster-ISS through the South Atlantic Anomaly (SAA) and the presence of the Sun in the FOV. Also, due to design constraints on the volume of Lobster-ISS, a total FOV of  $162^\circ \times 22.5^\circ$  and not  $180^\circ \times 22.5^\circ$  results in unobservable regions of the sky at the extremes, (or in the polar regions) of the FOV.*

- **Energy Bandpass and Resolution**

Source monitoring with an ASM can be adequately accomplished using a single energy channel, with pointed instruments optimised for spectroscopy best employed to study isolated astronomical X-ray objects of interest. A single energy channel is especially appropriate near the detection threshold where spectral information is statistically insignificant.



*Lobster-ISS will perform continuous monitoring of the soft X-ray sky (0.1 – 3.5 keV) for the first time, providing an energy resolution of around 20% at 5.9 keV, corresponding to six FWHM spectral channels over the total band (Black et al. 2003).*

- **Sensitivity**

The instrument should be as sensitive as possible to maximise the number of extragalactic sources catalogued. An ultimate 1 day sensitivity of less than 1 mCrab is envisaged.

*Lobster-ISS is modelled to have a sensitivity of 0.32 mCrab in a one day observation through the use of focusing optics (Chapter 6); this is more than a factor of five times improvement over MAXI.*

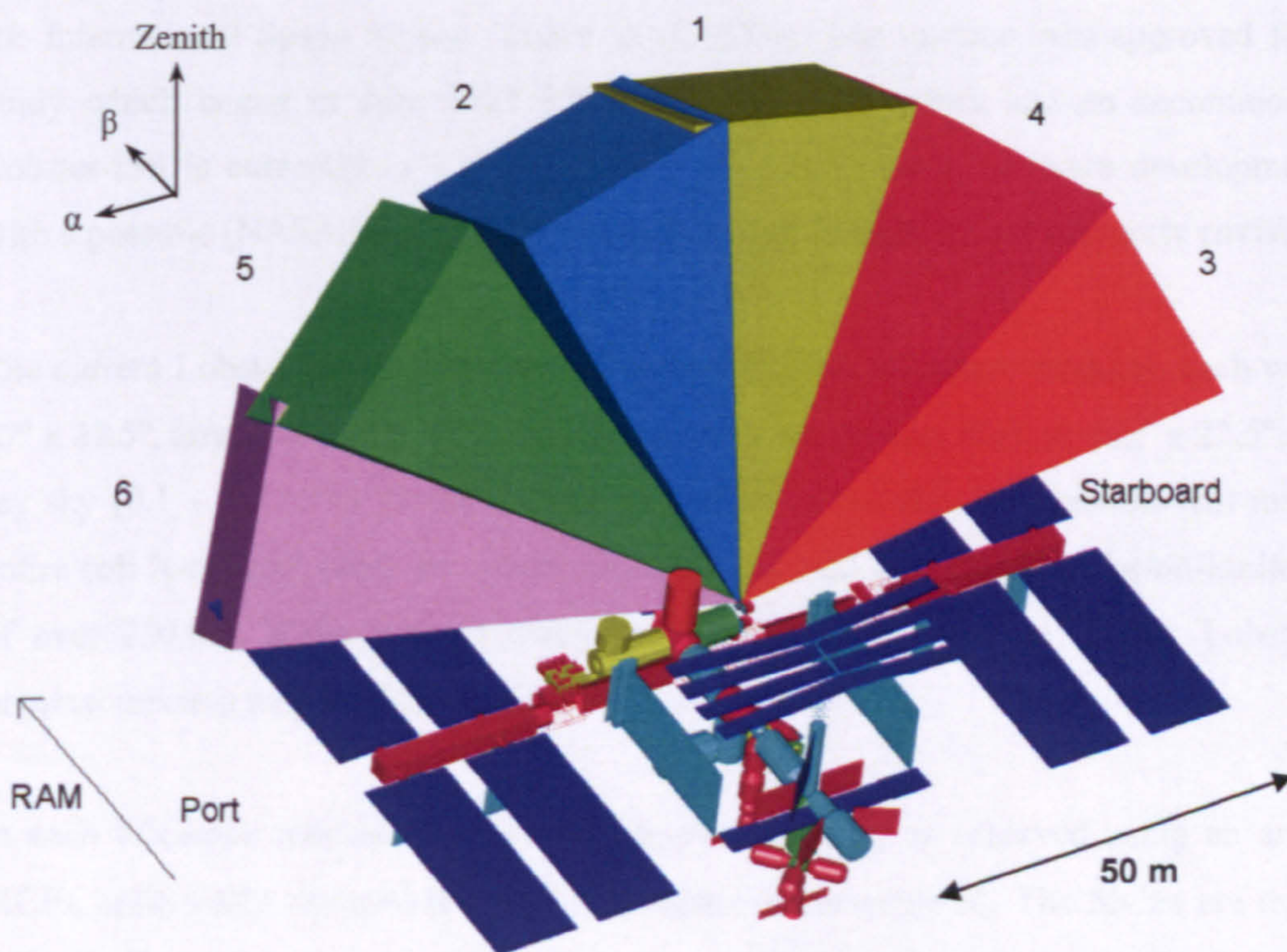


**Figure 3.2.** *Projected field of view of each of the 6 Lobster-ISS telescope modules (Smith et al. 2001). The telescopes are tilted 30° towards RAM (the direction of ISS motion) from the zenith direction, with modules 5 and 6 tilted a further 5° and 14° respectively towards RAM, to reduce obscuration by the nearby Centrifuge Accommodation Module (CAM).*



### 3.1.2 Development of the Lobster-ISS X-ray All Sky Monitor

The principle of operation of the eyes of certain crustaceans was deduced independently by Vogt (1975) and Land (1978) and applied to design an X-ray telescope by Angel (1979). MCPs as focusing optics were proposed by Wilkins et al. (1989) as a means of realising this “lobster eye” geometry, with Fraser et al. (1991) further considering their application on an X-ray ASM as a potential mini-satellite payload. Priedhorsky et al. (1996) undertook a detailed investigation into the astronomical applications of a lobster-eye telescope design, resulting in the submission of the LOBSTER concept to the NASA Small Explorer (SMEX) proposal round the following year (Priedhorsky et al. 1997). Although the SMEX science case was well-received, the proposal was rejected due to the technical immaturity of both the detector and optics. In 1996, funding in the form of an ESA Technology Research Programme (TRP) saw the further development of the MCP optics (Price, 2001) and an updated proposal was resubmitted in response to the ESA Call for Mission Proposals for the Flexi-Missions F2 and F3, as Lobster-ISS, an attached payload for the International Space Station (Fraser et al. 2000). The mission was approved for a Phase A study which began in July 2002 following technical reviews and an accommodation study. Lobster-ISS is currently in a Phase A extension, continuing hardware development activities, with a possible (NASA Space Shuttle) launch date of February 2010 currently envisioned.

The current Lobster-ISS design uses six identical X-ray telescope modules, each with a FOV of  $27^\circ \times 22.5^\circ$ , arranged so that Lobster-ISS has an instantaneous FOV of  $162^\circ \times 22.5^\circ$  of the soft X-ray sky (0.1 – 3.5 keV). Using the orbital motion of the ISS, Lobster-ISS will map almost the entire soft X-ray sky every 90 minute ISS orbit and will generate a confusion-limited<sup>iii</sup> catalogue of over 250,000 X-ray sources every two months (Pearson et al. 2003). Lobster-ISS has a nominal mission length of three years.

In each telescope module, Angel’s lobster-eye geometry is achieved using an array of 8 x 6 MCPs, spherically slumped to a 750 mm radius of curvature  $R_s$ . The MCPs are mounted on an AlBeMet<sup>®</sup> metal matrix composite (aluminium / beryllium) optic support<sup>iv</sup>, engineered with an equivalent slump radius to that of the optics. X-rays from infinity are thus focused onto a

---

<sup>iii</sup> Limited by the capability of the telescope to resolve individual sources; thus limited by the 4 arcmin angular resolution of Lobster-ISS.

<sup>iv</sup> AlBeMet alloy developed by Brush Wellman Engineered Materials, 17876 St. Clair Avenue, Cleveland, OH 44110, USA.



spherical detector plane, positioned at a radius  $\frac{R_s}{2}$  from the common origin. Thin-windowed gas proportional counters based on microwell geometry are mosaiced together in a pyramid configuration such that the detector plane geometry approximates the surface of a sphere (Black et al. 2003). Following X-ray absorption by the working gas (Xe), photoelectrons drift into one of a square array of microwells, where the presence of an electric field initiates an avalanche process, with the further ionisation of Xe atoms resulting in a detectable signal, with equal but opposite charges generated on the anodes and cathodes (*Figure 3.3*). The microwells are laser machined at the Laboratory for High Energy Physics, NASA / GSFC and have a nominal spatial resolution of 400  $\mu\text{m}$ , corresponding to an angular detector resolution of 4 arcminutes. All six telescope modules and their respective focal plane detectors will be directly mounted upon a single, triangular support structure.

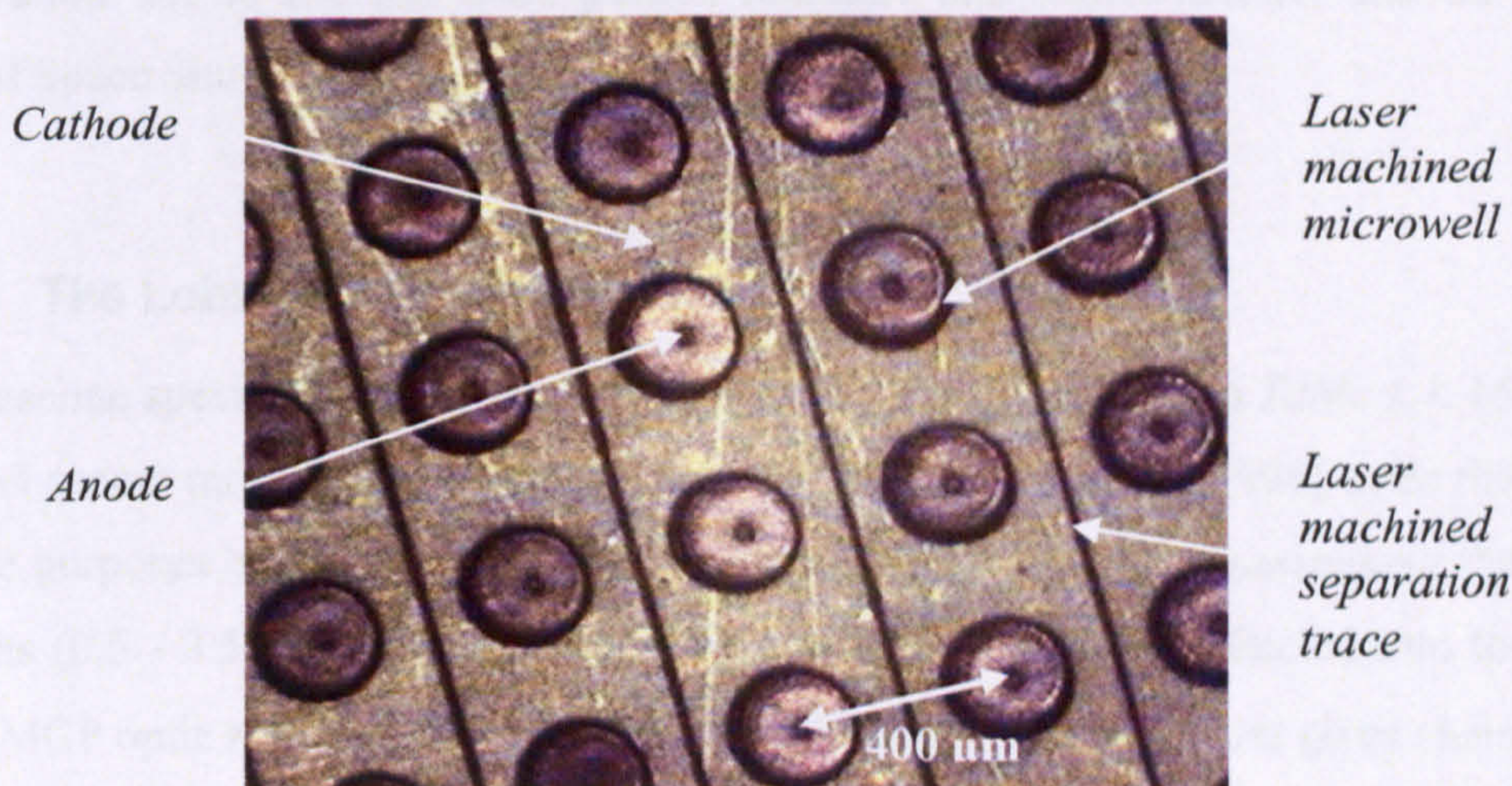


**Figure 3.3.** *The Lobster-ISS microwell detector. The cathodes are connected in rows separated by a UV laser machined trace, with the anodes connected in columns (on the underside of the detector).*

Lobster-ISS will also include a triplet of star trackers to provide direct instrument pointing information (Bannister et al. 2004). Generally, only one star tracker is required to be operational at a given time, with the remaining two redundant, required when the Sun nears the FOV of the operational star tracker. Thus, in the event of an X-ray transient alert for example, attitude reconstruction will enable the location of the source to an accuracy of one arcminute. To distinguish gamma ray bursts (GRBs) from other X-ray transients, a Gamma Ray Burst Monitor (GRBM) is included in the payload. When the GRBM detects an event, a realtime processing



sequence is initiated in which the recorded time and position of the event is used to search the X-ray telescope data for a previously undetected source. Data containing the nature and position of the event on the sky will then be rapidly downloaded via an uninterrupted ‘telescience’ link.

Sun and particle sensors cut the High Voltage (HV) to the microwell detector arrays when the Sun moves into the FOV and when the 51.6° ISS orbit passes through the high background particle fluxes associated with the South Atlantic Anomaly (SAA). Modules orientated such that they are unaffected by the immediate presence of the Sun in the FOV remain operational. A Detector Interface Unit (DIU) links both the Sun and particle sensors to the six telescope module-housed focal plane detectors.

A Computer Aided Design (CAD) based obscuration study (Smith et al. 2001) proposed the configuration of the six telescope modules shown in *Figure 3.2*, taking into account the FOV obscuration due to the ISS solar panels, radiators and superstructure, and the presence of a docked Space Shuttle orbiter.

### 3.1.3 The Lobster Micropore Optics

The baseline specifications for the Lobster MCP optics are shown in *Table 1.1*. MCP optics with channel aspect ratios of 50:1 were deduced by Priedhorsky et al. (1996) to be the most efficient for the purposes of Lobster-ISS; this conclusion was reached by maximising the ratio of input photons (0.5 - 3.5 keV) from a modelled Crab Nebula to those reflected into the central focus using MCP optic raytrace software. Selecting channel widths of 20  $\mu\text{m}$  gives channel lengths and thus a plate thickness of 1 mm, providing mechanical stability. A channel pitch of 24  $\mu\text{m}$  provides an open area fraction of 69%. In order to minimise the dimensions of each Lobster-ISS telescope whilst also taking into account the difficulty of manufacturing MCP optics to small slump radii, an  $R_s$  of 750 mm was selected to provide a focal length of 375 mm. Finally, the MCP optics are to be constructed from the Philips type 297 glass (*pseudo-molecule*:  $\text{Si}_{40}\text{O}_{98}\text{K}_8\text{Na}_7\text{Pb}_6\text{Bi}_2^v$ , *density*:  $3.3\text{ g cm}^{-3}$ ), used during the recent ESA TRP programme.

---

<sup>v</sup> A ‘pseudo-molecule’ is used solely to describe the composition of a substance in terms of the relative concentration of each element (by number) within that substance. It is not a physical molecule and is only used (for the purposes of this thesis) to describe the chemical content of a substance.



## 3.2 Experimental Instrumentation

The MCP focusing work performed in this chapter was conducted on two facilities developed at the University of Leicester. The first is the laboratory-based Vacuum Test Facility (VTF), used to test the point-to-point focusing of planar MCP optics. Slumped MCP optics are investigated in the Tunnel Test Facility (TTF), appropriately named due to its geographical location under the Department of Physics and Astronomy. Both facilities use the same MCP detector, whose specification is detailed in *Section 3.2.3*.

### 3.2.1 The Vacuum Test Facility

The VTF was initially developed in 1981 to test the rapidly developing field of MCP charge multipliers (Pearson, 1984) and currently resides in the Space Research Centre at the University of Leicester, UK. Since its conception, it has been heavily involved in MCP research for both optic and detector applications and was notably used as a means of first observing the characteristic cruxiform structure obtained when using square-packed, square pore MCPs as focusing optics (Fraser et al. 1993). A schematic and photograph of the VTF system are displayed in *Figures 3.4* and *3.5* respectively.

The structural body of the VTF is constructed from stainless steel, with the various chambers connected using a combination of conflat flanges and copper gaskets. The VTF has an operational pressure of  $10^{-7}$  -  $10^{-6}$  mbar, evacuated using a combination of roughing pump and TurboMolecular Pump (TMP). High vacuum is necessary primarily due to the operating requirements of the X-ray detector, where pressures of below  $\sim 5 \times 10^{-5}$  mbar are necessary to provide feedback-free operation and due to the high operating voltages required between electrodes.

A filter wheel located between source and optic positions contains four filters enabling the user to isolate different energy regimes without the need to break vacuum. At the same position, yet on the opposite side, a collimating hole, 1 mm in diameter may be inserted to perform pinhole camera-like operations. For the purposes of X-ray focusing, the collimating hole enables the user to illuminate a smaller region of an extended MCP optic. The detector mount may be translated  $\pm 50$  mm about the  $x$  and  $y$  axes and may be tilted by  $\pm 10^\circ$  about the horizontal axis (where the optical axis is along the  $z$ -axis, keeping with convention).



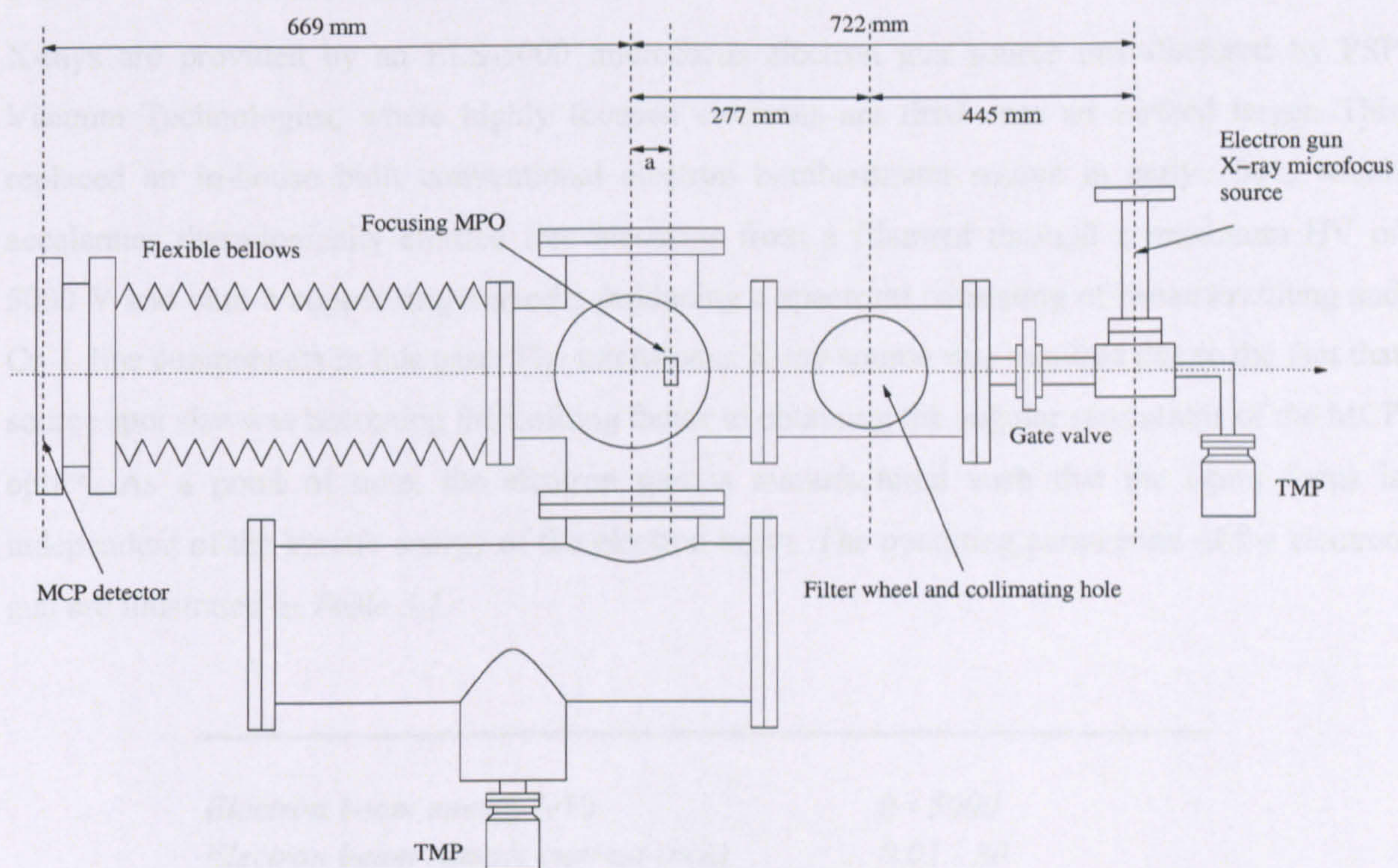


**Figure 3.4.** Schematic of the Vacuum Test Facility optimised for point to point soft X-ray focusing using planar MCP optics. In this instance,  $a = 26.5 \text{ mm}$  such that  $l_s = l_i = 695.5 \text{ mm}$ .

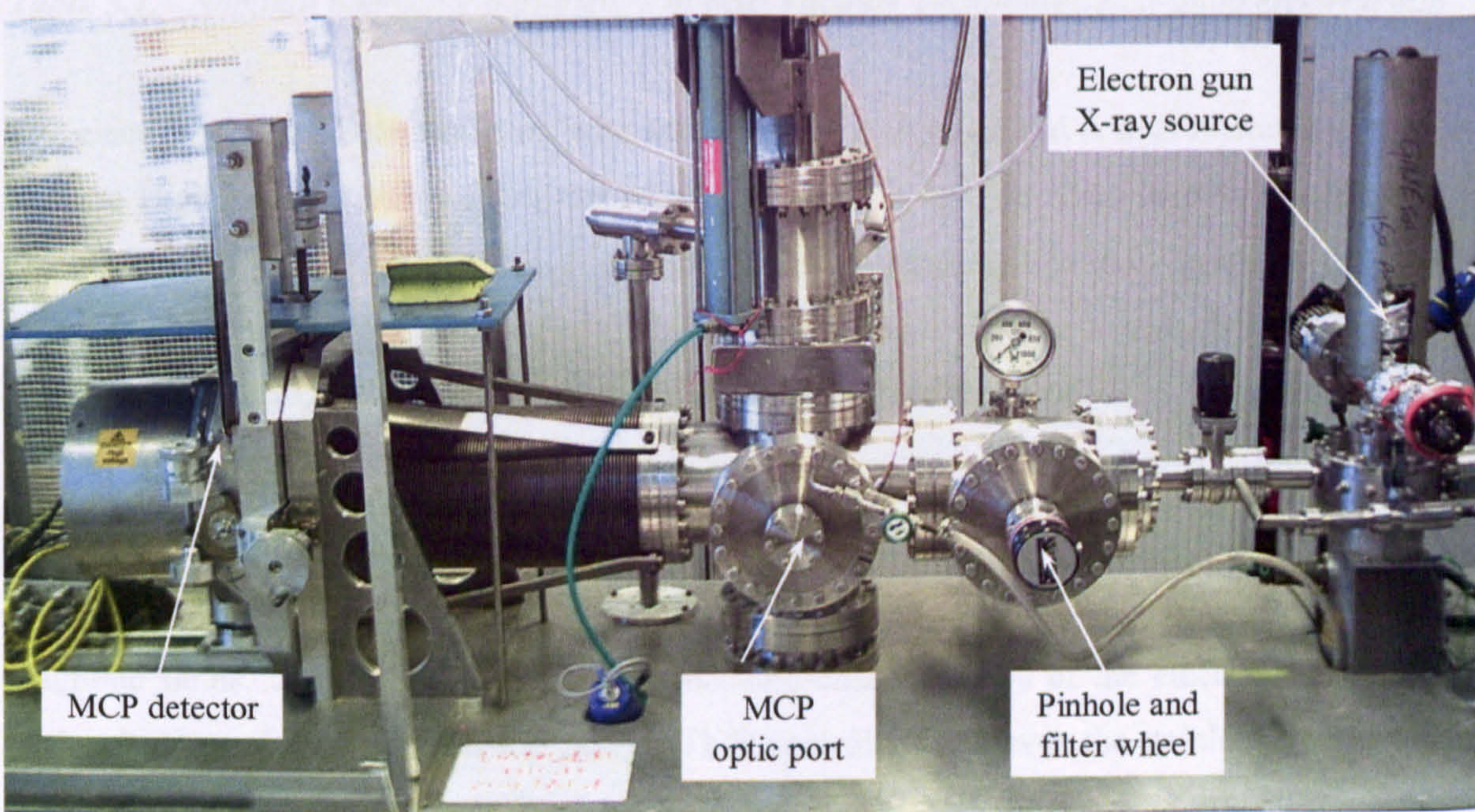


**Figure 3.5.** The Vacuum Test Facility (VTF).



3.2.1.1     *The Microfocus X-ray Source*

X-rays are provided by an ELS-5000 microfocus electron gun source manufactured by PSP Vacuum Technologies, where highly focused electrons are fired onto an earthed target. This replaced an in-house built conventional electron bombardment source in early 2001, which accelerates thermionically emitted free electrons from a filament through a maximum HV of 5000 V and onto a copper target anode, producing a spectrum consisting of bremsstrahlung and Cu-L line components in this case. The microfocus X-ray source was required due to the fact that source spot size was becoming the limiting factor in obtaining the angular resolutions of the MCP optics. As a point of note, the electron gun is manufactured such that the beam focus is independent of the kinetic energy of the electron beam. The operating parameters of the electron gun are illustrated in *Table 3.1*.

<i>Electron beam energy (eV)</i>	<i>0 - 5000</i>
<i>Electron beam sample current (mA)</i>	<i>0.01 - 30</i>
<i>Filament current (A)</i>	<i>0 - 2.8</i>
<i>Minimum source spot diameter (mm)</i>	<i>&lt; 25 mm [1 mA]</i>
	<i>&lt; 100 mm [30 mA]</i>

*Table 3.1. Nominal operating parameters of PSP Vacuum Technology ELS-5000 electron gun.*

The electron gun has been designed with surface science in mind and is thus intended to operate in Ultra High Vacuum (UHV). For this reason, the VTF is split into two distinct chambers by a combination of a gate valve and a 2 µm polycarbonate (Lexan) window, coated in 0.4 µm of aluminium to prevent surface charging. In this way, the polycarbonate window holds the pressure gradient, allowing the operating pressure of the source chamber to be 10<sup>-9</sup> - 10<sup>-8</sup> mbar when the gate valve is open.

The microfocus X-ray electron gun source is however particularly susceptible to external magnetic fields, which serve to affect the focusing characteristics of the electron beam. In the past, it has been found that Penning gauges, TMP controllers and even the stainless steel structure of the VTF itself have had an effect on beam focusing (Price, 2001). A mu-metal sheath now slides over the electron gun itself in an attempt to regulate external magnetic fields, yet focus is expected to be degraded at the (uncovered) target itself. The electron beam focus was optimised



to achieve a circular beam of minimum diameter of around  $\sim 150 \mu\text{m}$  at the target anode, which is tilted with a  $45^\circ$  take-off angle. The source diameter  $d_s$  was estimated by examining its diameter at the detector  $d_i$ , after having passed through the  $d_{pin} = 1 \text{ mm}$  diameter collimating hole (*Figure 3.6*). The dimensions of the collimating hole were subsequently removed using

$$d_s = \frac{l_s}{l_i}(d_i - d_{pin}) - d_{pin} \quad (3.1)$$

where, in this case,  $l_s$  and  $l_i$  are the lengths from source to pinhole (445 mm) and pinhole to detector (946 mm) respectively.

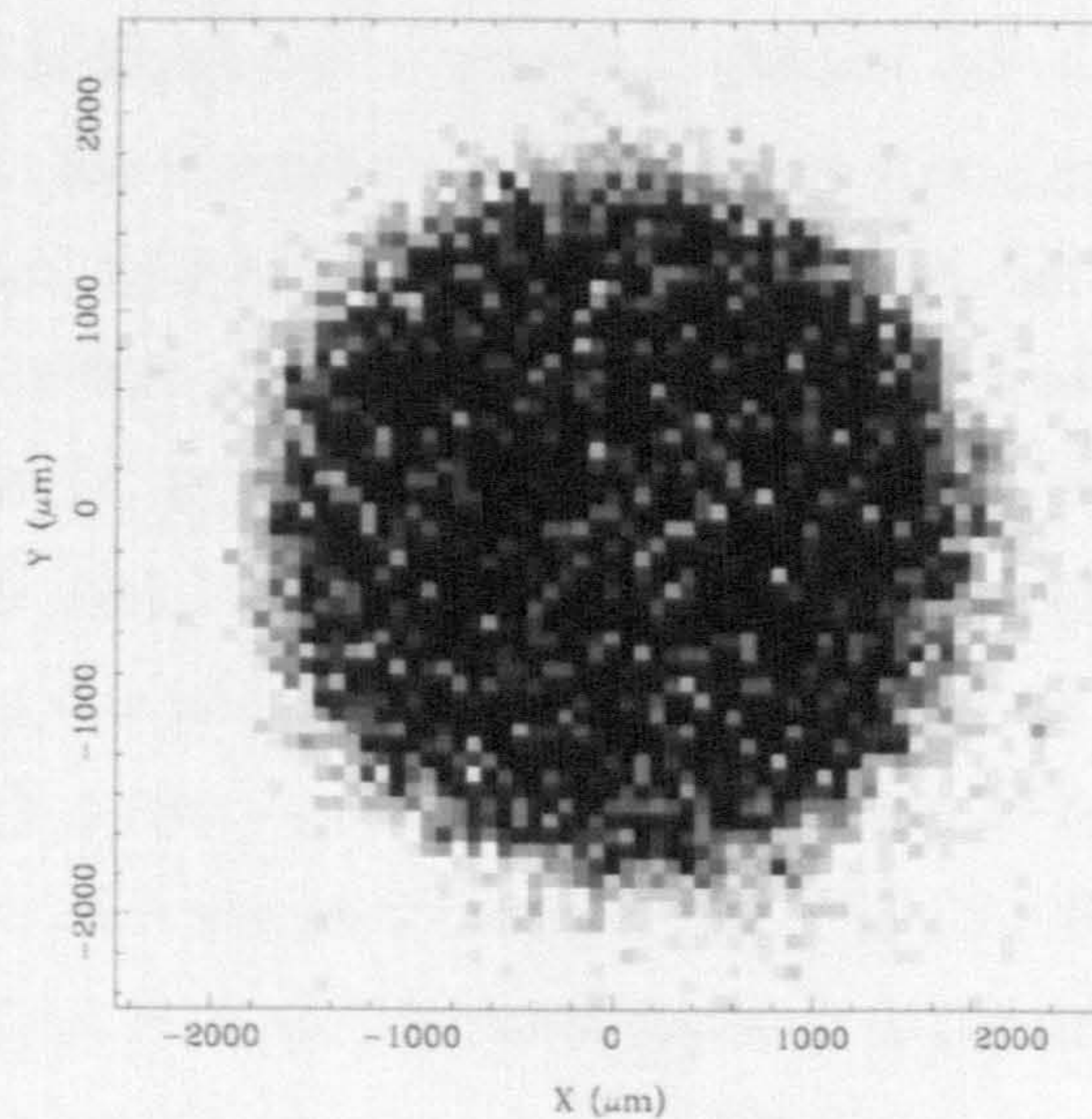


**Figure 3.6.** *Linearised intensity distribution of the microfocus source spot on the VTF detector. A collimating hole, 1 mm in diameter is installed between the source anode and detector. The electron beam is optimised such that it is incident on the centre of the Cu-coated anode and focused to the smallest possible spot size. A  $4 \mu\text{m}$  aluminium filter was inserted to isolate the desired Cu-L X-ray line (930 eV). A total 22037 counts comprise the image, collected a rate of 45 counts per second. The diameter of the imaged source  $d_i$  (defined as the diameter inside which 90% of the counts are contained) was measured to be  $\sim 3420 \mu\text{m}$ , corresponding to a source size  $d_s$  of  $\sim 150 \mu\text{m}$ .*



### 3.2.2 The Tunnel Test Facility

The TTF is a 20 metre X-ray beamline originally developed in the 1970s for the testing of collimated proportional counter detectors for Ariel-V and VI (Sanford, 1975) and has been repeatedly modified over the years to suit subsequent projects. Modifications included the addition of a large cylindrical ‘tank’ test chamber in the late 1970s, to house and test the EXOSAT Medium Energy Detector Array (MEDA) (Turner et al. 1981). A dimensioned schematic of the TTF is shown in *Figure 3.7*. Further modifications are currently being undertaken subsequent to this work to lengthen the beamline to approximately 27.5 m, extending the tank into a clean room (Pearson, 2005); in the future, MCP optics will be inserted and replaced in a clean environment.

Now primarily used for testing the focusing properties of MCP optics, ports along the length of the beamline may be used to position both planar and slumped optics, yet for the purposes of this thesis, only slumped optics are investigated in the TTF; as previously detailed, the MCP slump radius of Lobster-ISS optics is sufficiently small ( $R_s = 0.75$  m) that both optic and detector are positioned in the tank. Both tank and beamline are pumped down using one large liquid helium CTI Cryogenics Cryo-Torr 10 cryo-pump, achieving a TTF-wide operating pressure of  $\sim 10^{-6}$  mbar. The source chamber may be isolated from the rest of the system using a gate valve to enable maintenance work to be performed on the source without the need to vent the beamline. Vacuum is achieved in the source chamber by a combination of roughing (rotary) pump and TMP. The MCP detector is the same as that used on the VTF (*Section 3.2.3*), yet here mounted on a moveable carriage, which is capable of translating the detector along the optical axis in order to provide depth of focus measurements. The detector itself may traverse  $\pm 400$  mm from the 20 m point (located approximately mid-way inside the tank, along the optical axis).

A 5 kV soft X-ray electron bombardment source with a Cu-coated anode, constructed in-house is currently attached to the TTF for the purposes of this chapter. A  $0.4\text{ }\mu\text{m}$  aluminium filter is coupled to a 1 mm diameter pinhole to provide a calculated  $\sim 11$  arcsecond source size when viewed from the optic position (at the front of the tank in this case). The large distance between the X-ray source and optic in the TTF in comparison to that of the VTF means that incoming X-rays are almost perpendicular to the surface of the MCP optic, giving a more accurate representation of the ability of the optic to focus quasi-parallel X-rays.



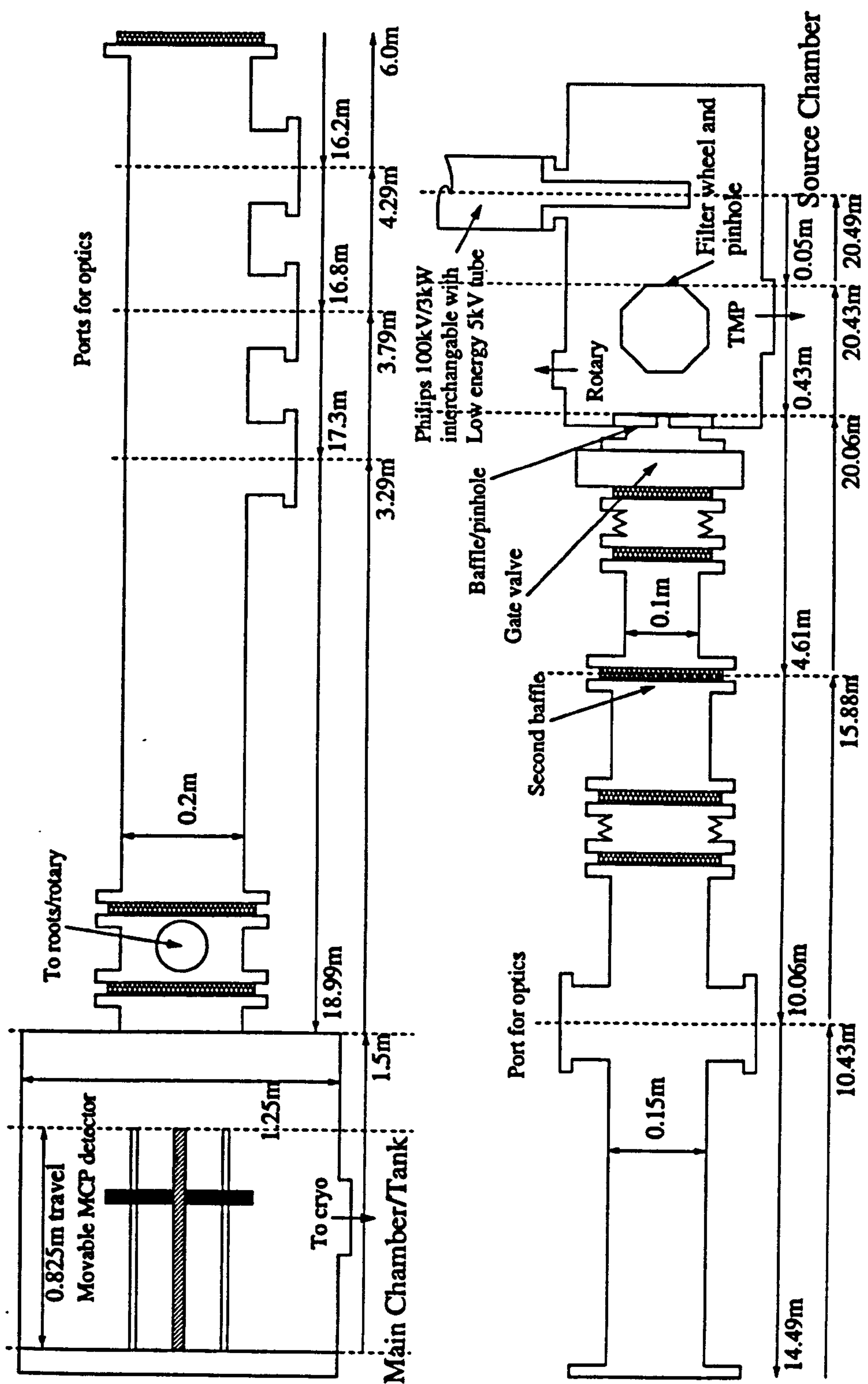


Figure 3.7. Dimensioned schematic of 20 m TTF beamline. Both MCP optic and detector housed in the tank test chamber of length 1.5m and diameter 1.25m. From Price (2001).



### 3.2.3 MCP Detector

On both test facilities, focal plane intensity distributions are recorded using a large area MCP detector with a resistive anode readout. The 100 x 100 mm<sup>2</sup> MCPs were originally developed for the High Resolution Camera (HRC) on AXAF (Zombeck et al. 1995), latterly renamed Chandra, with MCP detectors themselves now being used in applications as diverse as bioimaging (Lees and Hales, 2001; Richards and Lees, 2002). The MCPs are manufactured from low noise glass by Photonis SAS, with 120:1 12.5 µm diameter channels on a 15 µm pitch at a channel bias angle of 6°. Two identical MCPs are positioned in the chevron configuration (*Section 1.2.1*), with output encoded via charge division on the resistive anode.

Charge deposited on the resistive anode creates an analogue signal, read out by four charge sensitive pre-amps, one on each corner of the resistive anode. After passing through a filter amp, an 11 bit Analogue to Digital Converter (ADC) digitises the signal in preparation for its recording on an Acorn Archimedes computer. Further detail may be found in Brunton, 1994. The 2048 channel ADC provides a theoretical spatial resolution of 76 µm across the diagonal length of the 110 x 110 mm resistive anode. However, spatial distortions are associated with output from resistive anode readouts (Fraser and Mathieson, 1981). A mask containing a regular array of 24 x 24 100 µm pinholes, lying on a 4 mm pitch was fitted to the front of the detector and illuminated with soft X-rays. A “look-up” table was then created to map the observed pinhole coordinates onto the true event coordinates. This look-up or linearisation table was subsequently used to remove spatial errors from detector images (Lees and Pearson, 1997). The MCP detector has an active area of 93 x 93 mm<sup>2</sup>, set by the size of the rear electrode on the rear MCP.

### 3.2.4 MCP Holding Jigs

There are two holding jigs created to hold the MCP optics in both the VTF and TTF (*Figure 3.8*). The first, flange-based jig may be attached to both TTF and VTF through an 8 inch conflat flange, placed in the optics port at the midpoint of either VTF or TTF for the envisaged purpose of point to point focusing. The other jig is positioned in the tank test chamber on the TTF and was specifically designed for use with slumped MCP optics.

A combination of Poly-Chloro-Tetra-Fluoro-Ethylene (PCTFE) spacers and stainless steel leaf springs are used to secure the MCP optics into the jig head in both cases. Care must be taken when securing the MCPs to the respective jig head; over-tightening of the restraining bolts may



lead to MCP deformation or even fracture. The TTF tank jig sandwiches the MCP between concave and convex spacers, engineered to the radius of curvature of the MCP to be studied.

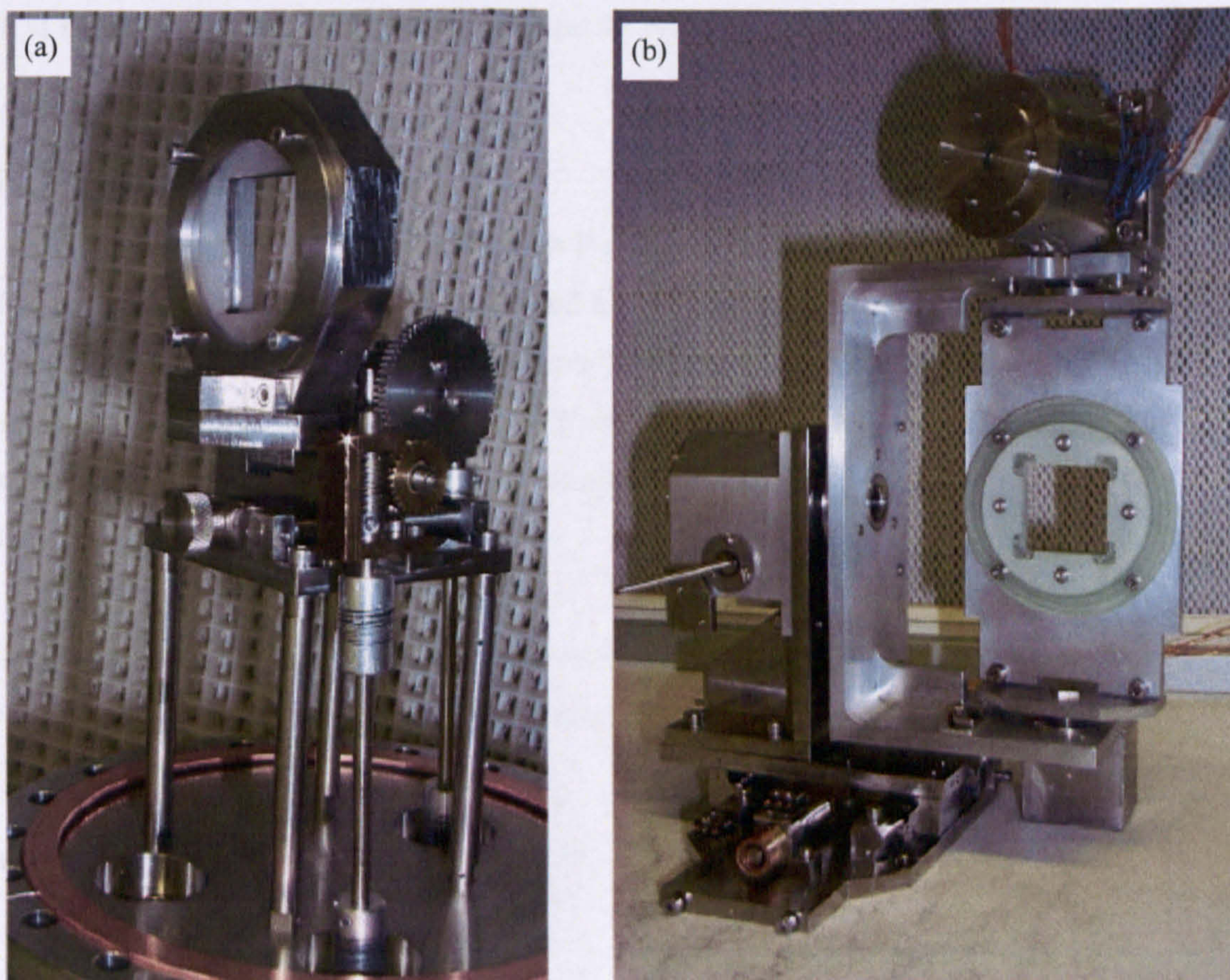


**Figure 3.8.** Two MCP optic holding jigs developed in-house. For the purposes of his thesis, the flange-based jig (a) was used in the focusing of planar MCP optics in the VTF, and the free-standing jig (b) was positioned in the TTF and used in the focusing of slumped MCP optics.

Each jig permits a certain degree of manipulation of the MCP optic in both  $x$  and  $y$  axes. In the case of the TTF tank jig, stepper motors permit a  $360^\circ$  tilt in both  $x$  and  $y$  axes if required, at an accuracy of  $40''$  / step (400 steps / motor revolution coupled with a  $1/80$  wormgear, Price, 2001). The flange-based jig is reported by Brunton (1994) to provide a tilt of  $-6^\circ$  to  $7^\circ$  about the  $x$ -axis at  $0.0066 \pm 0.0004^\circ$  / rotary drive turn and  $\pm 9^\circ$  in the  $y$ -axis at  $0.44 \pm 0.03^\circ$  / rotary drive turn. The jig head may also be translated along a short distance in the (optical)  $z$ -axis to fine-tune source and image distances for point to point focusing experimentation.



### 3.3 Soft X-ray Focusing by Lobster Optics

In this section, the focusing properties of both slumped and planar bare glass MCPs are investigated. Measurements of the quality of the MCP focus are expressed in terms of the Full Width at Half Maximum (FWHM) of the central focus.

#### 3.3.1 Slumped MCP Optics

Two slumped, bare glass MCPs procured from Photonis SAS with serial numbers HC001-A1 and HC001-A2 were manufactured to the nominal Lobster-ISS specification detailed in *Table 1.1*. Over a period of two months, depth of focus measurements were performed in the TTF to determine the angular resolution of each MCP optic. Angular resolutions for each MCP at best focus (where the detector is at a focal distance such that angular resolution is minimised in both axes) are shown in *Table 3.2*.

MCP	Date	Angular resolution (arcmin)		Comments
		x	y	
HC001-A1	07/01/2002	9.05	9.75	(a) Measurement 1
	17/01/2002	13.2	9.75	(b) Measurement 2
	21/02/2002	11.1	9.75	(c) After 48 hour 100 °C MCP bake-out
	01/03/2002	9.05	9.05	(d) After 48 hour 70% humidity immersion
HC001-A2	08/01/2002	11.1	11.1	Measurement 1

*Table 3.2. Angular resolutions of MCPs HC001-A1 and HC001-A2. Each angular resolution is at the position of best focus. Comments (a) to (d) refer to those images labelled in Figure 3.9.*

##### 3.3.1.1 HC001-A1

*Figure 3.9* shows four images from MCP HC001-A1 illuminated by Cu-L X-rays (930 eV). As *Table 3.2* demonstrates, the angular resolution of the MCP changes with time. Over a period of ten days, the angular resolution measured in the x-axis, at best focus (as shown in *Figure 3.9*) deteriorated from (a) 9.1 to (b) 13.2 arcmin. Prior to the initial measurement, HC001-A1 was stored in a low-humidity environment, remaining in the packaging in which it was delivered from the manufacturer. It was therefore initially believed that in the ten days between measurements, water had been adsorbed into the channel surfaces as previously reported by Price (2001),



degrading the focusing performance of the optic (by applying a surface tension to the reflecting surfaces and thus deforming the optic). In an attempt to remove the water from this optic, it was baked out at 100°C (under vacuum) over a two-day period. Subsequent focusing measurements revealed a partial improvement in angular resolution, reducing the  $x$  component to 11.1 arcmin (c), yet insufficient to restore the original focusing characteristics recorded on 07/01/2002. MCP HC001-A1 was then immersed for 48 hours in a 70% humidity environment in a further attempt to identify water adsorption as the factor behind the deterioration in its focal properties. Surprisingly, subsequent focusing measurements revealed the sharpest focus to date, with both  $x$  and  $y$  components achieving an angular resolution of 9.1 arcmin at best focus. Depth of focus measurements on this particular date are shown in *Figure 3.10*.

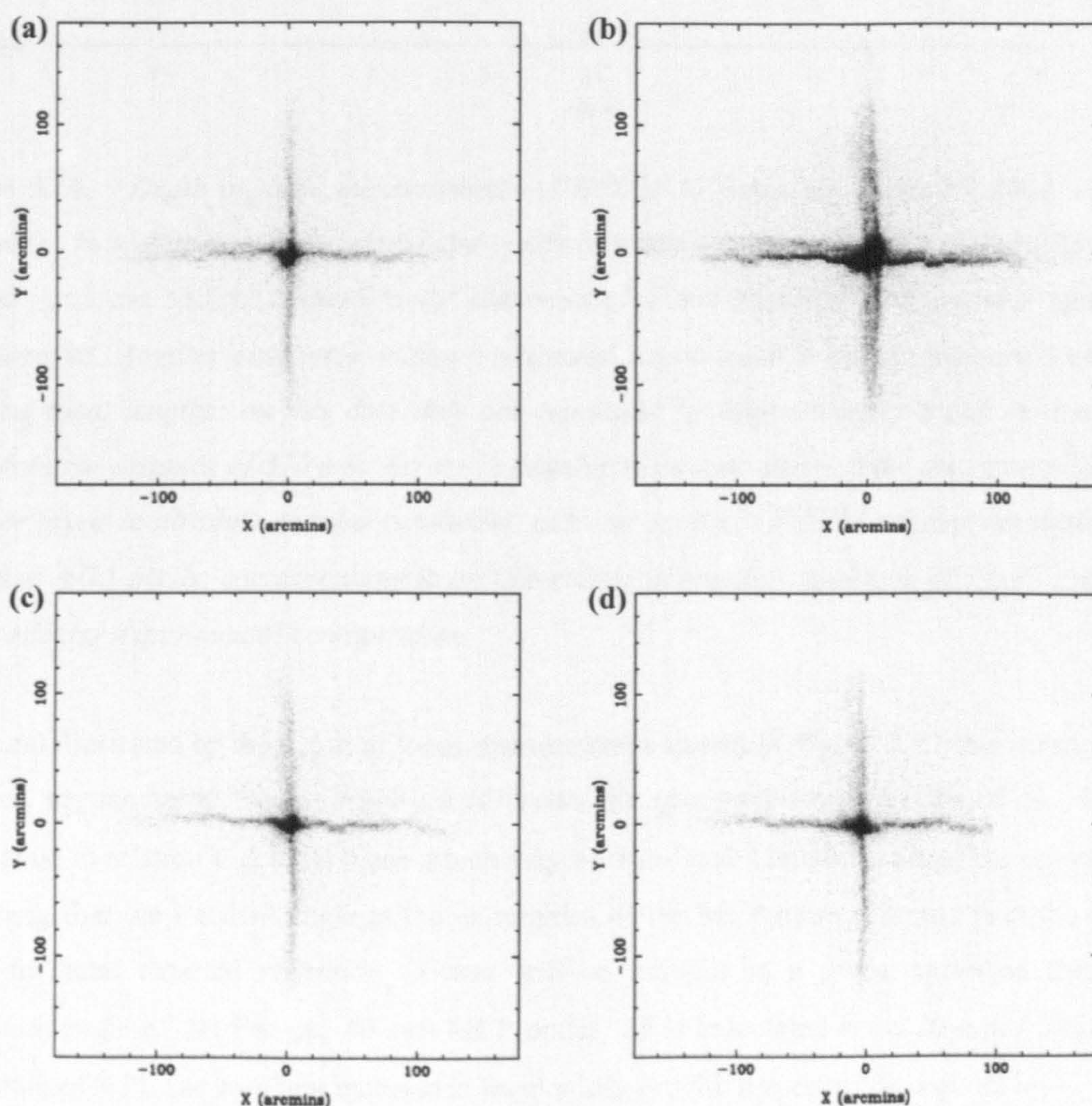


**Figure 3.9.** Focal plane distributions of HC001-A1 at best focus with Cu-L X-rays. Images (a) to (d) correspond to those angular resolution measurements in the 'Comments' field of Table 3.2.



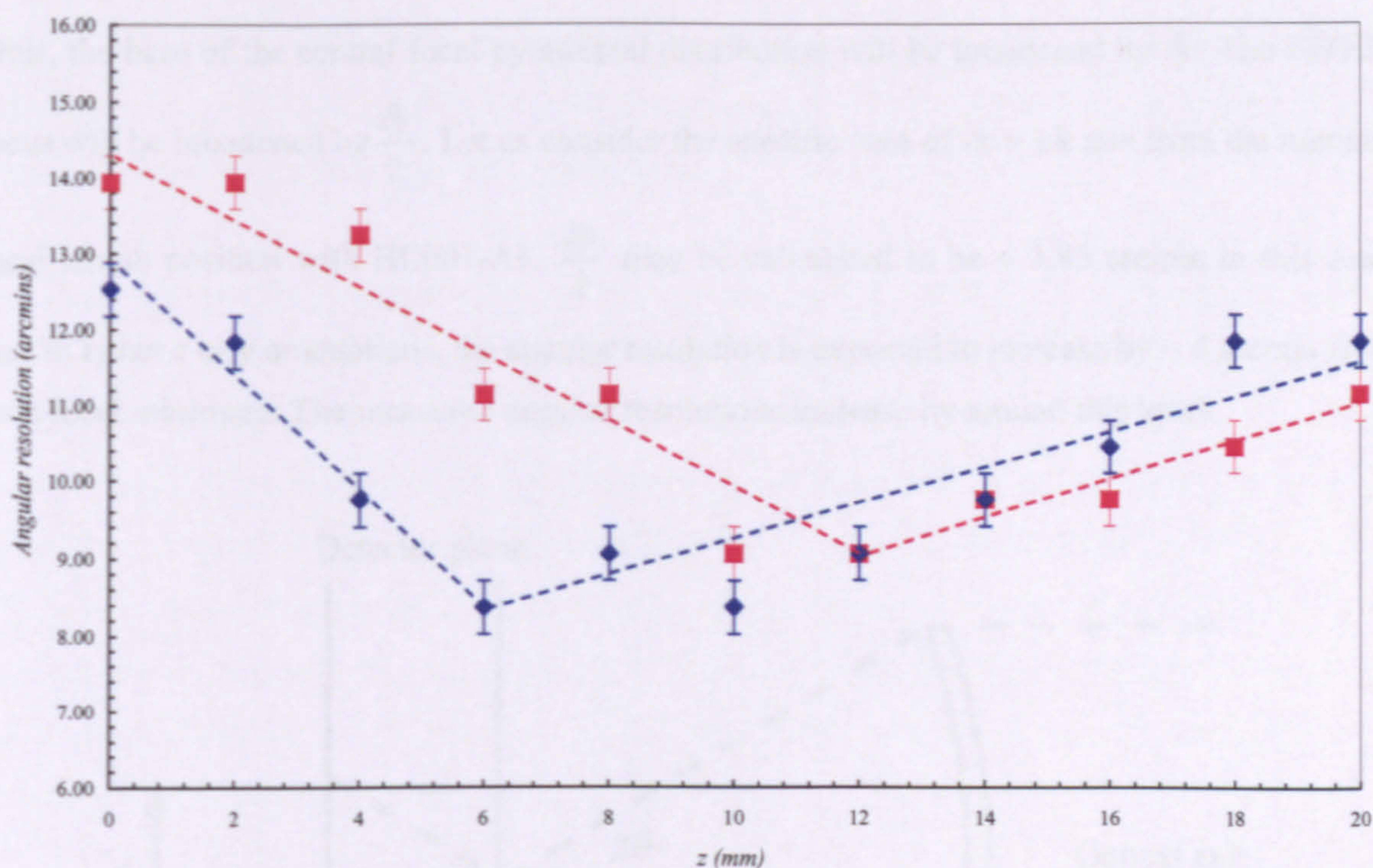


**Figure 3.10.** Depth of focus measurements of HC001-A1 taken on 1<sup>st</sup> March 2002. Angular resolutions in both the x-axis (squares) and y-axis (diamonds) (as orientated in Figure 3.9) of the central focus are shown. Optic-detector distances of 2 mm separate each angular resolution measurement. Angular resolution minima measured across both x and y axes are located at differing focal lengths; on this date they are separated by approximately 6 mm in a nominal optic-detector distance of 375 mm. Errors in angular resolution derive from the conversion from detector pixels to absolute angular resolution; detector errors in FWHM angular resolutions are quoted at  $\pm 0.5$  pixels, corresponding to an uncertainty in angular resolution of  $\pm 0.35$  arcmin in this particular experimental configuration.

The trend illustrated by the depth of focus measurements shown in Figure 3.10 may be supported by basic trigonometric theory; Figure 3.11 shows the geometric configuration of the slumped MCP optic in relation to a focal plane which may be translated a length  $\delta z$  along the optical axis. Assuming that the incident angle at the extremities of the MCP optic  $\theta$  is less than the critical angle for total external reflection, X-rays will be brought to a focus, reflected through a maximum angle of  $2\theta$ . For our 40 mm MCP optics,  $2\theta$  is calculated to be  $20 \text{ mm} / 375 \text{ mm} = 0.053 \text{ rad}$ , or  $3.1^\circ$ . The resultant increase in focal width  $\delta y$  with respect to  $\delta z$  is given by

$$\delta y = 4\theta\delta z \quad (3.2)$$



Thus, the base of the central focal pyramidal distribution will be broadened by  $\delta y$ . The FWHM focus will be broadened by  $\frac{\delta y}{2}$ . Let us consider the specific case of  $\delta z = \pm 8$  mm from the nominal focal length position with HC001-A1.  $\frac{\delta y}{2}$  may be calculated to be  $\sim 3.85$  arcmin in this case, thus in either  $x$  or  $y$  orientations, the angular resolution is expected to increase by  $\sim 4$  arcmin from each focal minimum. The measured angular resolutions increase by around this level.

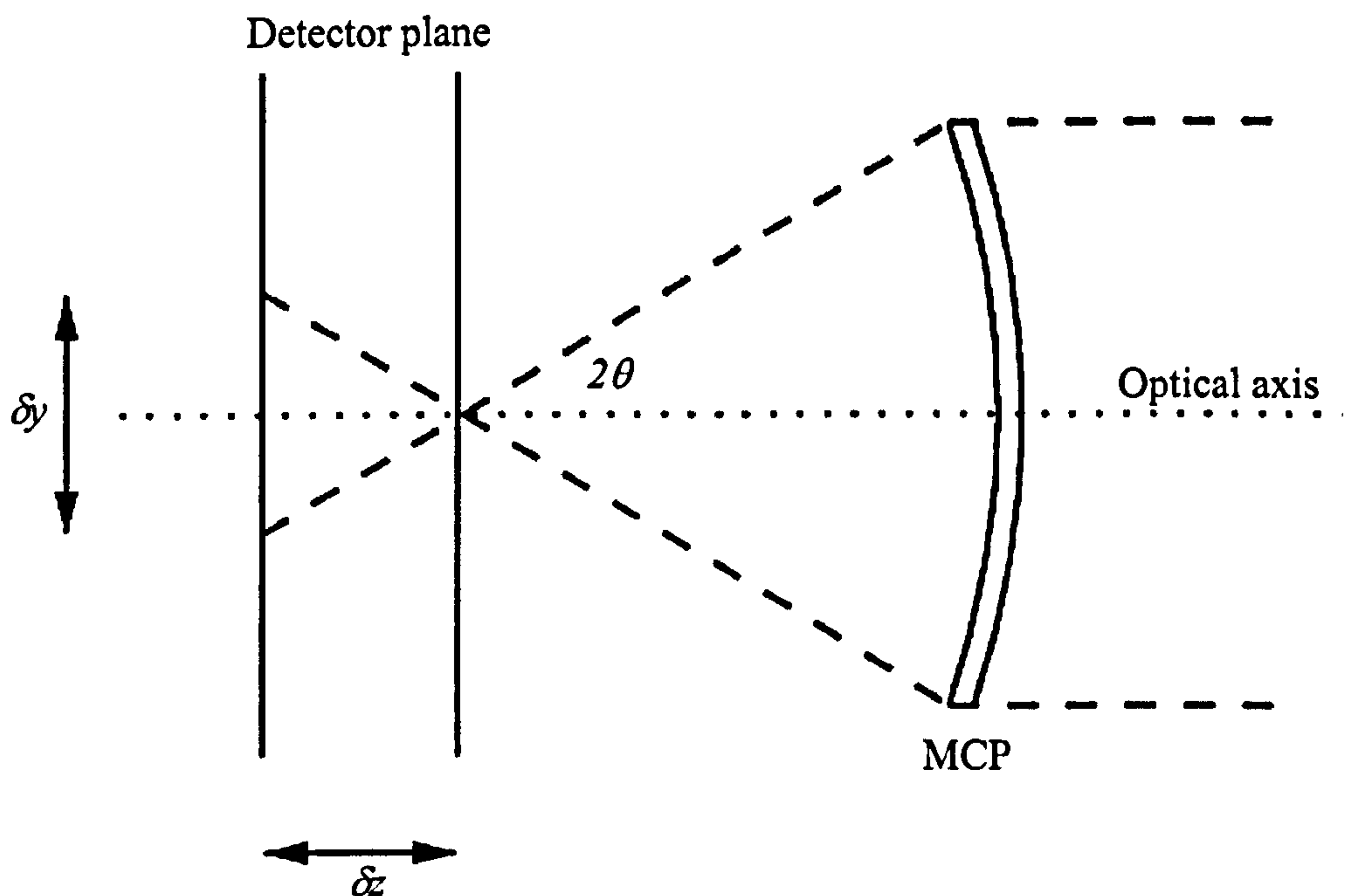


**Figure 3.11.** Focal spot broadening in an out-of-focus image. The focal plane is moved a distance  $\delta z$  from the focal point of the slumped MCP optic to an out-of-focus position. The base of the pyramidal resultant focus is increased by  $\delta y$ . The measured FWHM angular resolution is broadened by  $\frac{\delta y}{2}$ .

We infer that the temporal variation in angular resolution at best focus for HC001-A1 is not due to the adsorption of water into the MCP channel walls, but rather due to a geometrical deformation of the MCP optic, caused by uneven forces applied to the optic during focusing. This appears to be a demonstration of the susceptibility of these MCPs to mechanical deformation. The mechanism behind the fixing of the MCPs to the support structure of each Lobster-ISS module will surely present a complex technological challenge in future Phases B, C and D of



Lobster-ISS. It is currently envisaged that only three of the four MCP corners be fixed onto the beryllium alloy-based optic support, as MCP fracture may be prevented if the optic elements are not rigidly bonded to the support (Stevenson, 2004).

The form of the MCP deformation is best understood by referring to the depth of focus measurements shown in *Figure 3.10*. In this case, the contribution to the central focus from the horizontally orientated channel walls appears different to that from the vertically orientated channel walls; the best focus from each component occurs at a focal length 6 mm apart. In optics, this effect is known as astigmatism. This suggests that the MCP is deformed toroidally; that is to say that the radius of curvature  $R_s$  across one axis of the MCP was, on this date, 12 mm larger (or smaller) than across the other, as illustrated in *Figure 3.12*. Unfortunately, this conclusion could not be verified experimentally due to a lack of reliable in-house measuring techniques (e.g. surface profilometry) at the time.

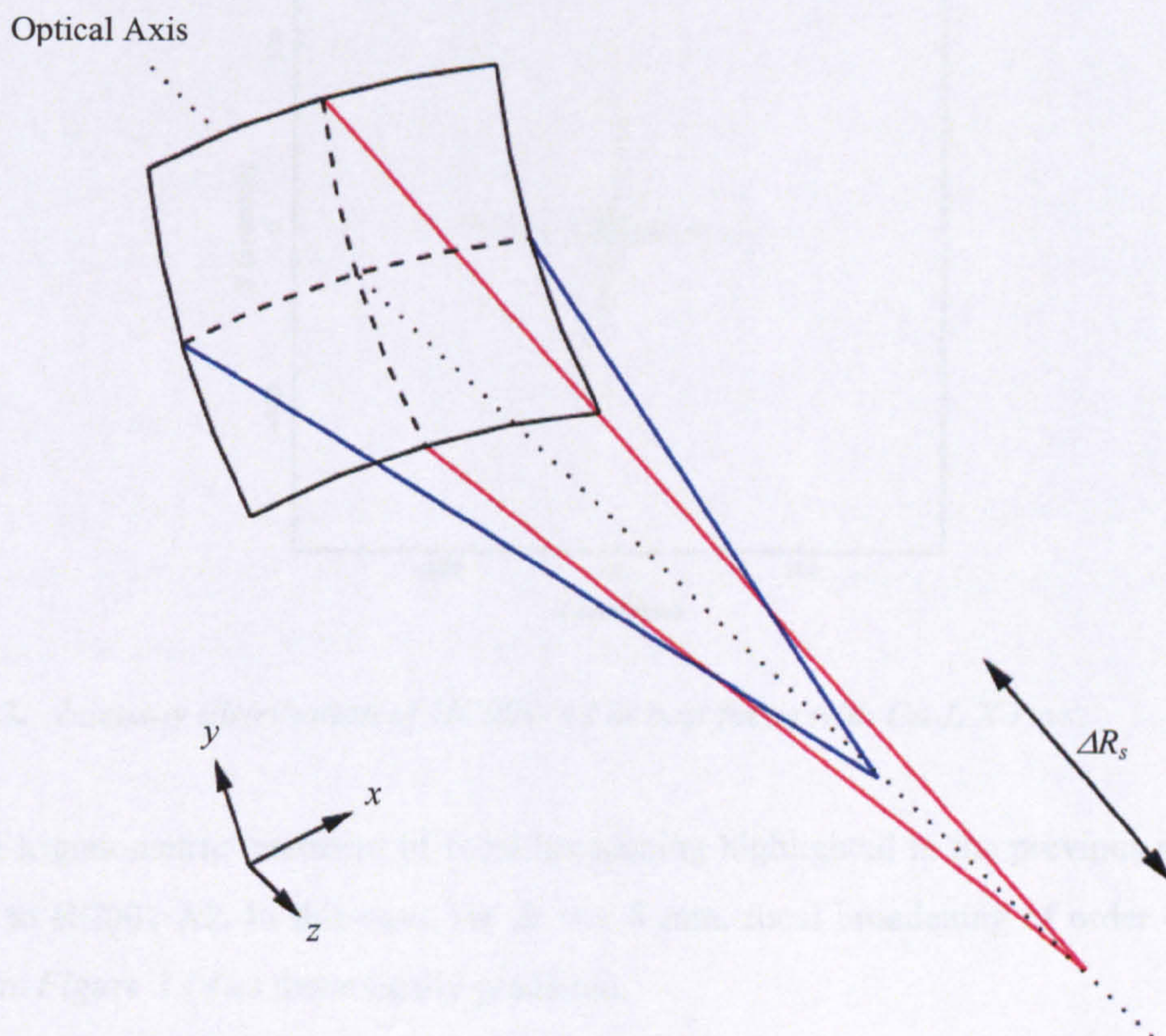


**Figure 3.12.** Toroidal deformation of an MCP optic. The radius of curvature  $R_s$  is different for the  $x$  and  $y$  components of the MCP as a result of the deformation. On 1<sup>st</sup> March 2002,  $\Delta R_s \sim 12$  mm, corresponding to the measured focal length difference of  $\sim 6$  mm between the two components.



### 3.3.1.2 HC001-A2

An initial analysis of MCP HC001-A2 on 8<sup>th</sup> January 2002 indicated a broader focus (11.1 arcmin across both  $x$  and  $y$  axes) at optimum detector distance compared with HC001-A1 (*Figure 3.13*). Depth of focus measurements of HC001-A2 from 8<sup>th</sup> January 2002 are shown in *Figure 3.14*. With these, the first (and only) depth of focus measurements taken, the focal width minima in the  $x$  and  $y$  orientations appear to coincide.

Further analysis of HC001-A2 at a later date was halted due to the MCP having fractured while in storage, thus preventing any study of MCP deformation on either axis over time as with HC001-A1. However, the breakage of MCP HC001-A2 in storage further highlights the fragility of the optics, discussed in the previous section.

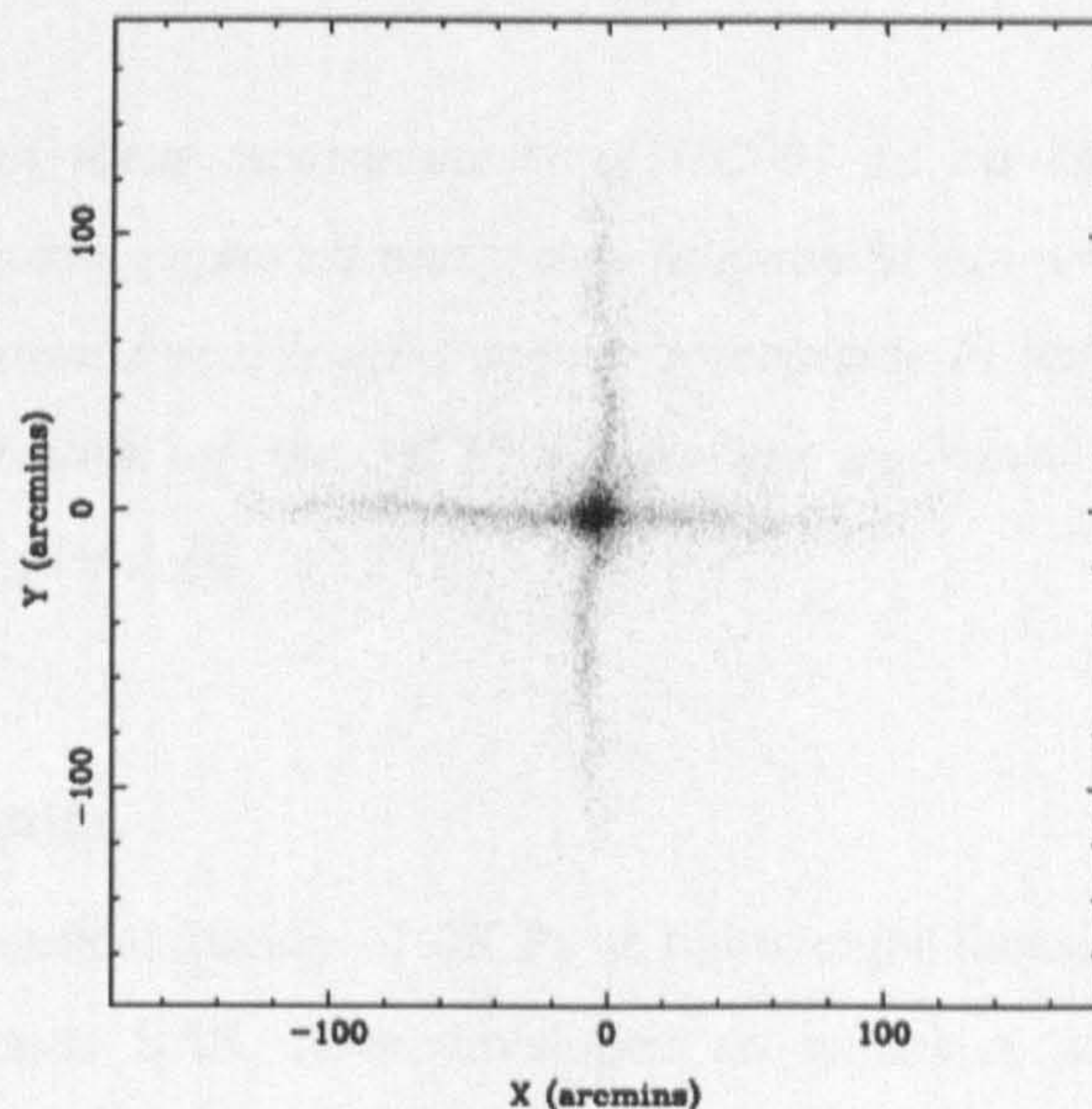


**Figure 3.13.** *Intensity distribution of HC001-A2 at best focus with Cu-L X-rays.*

The simple trigonometric treatment of focal broadening highlighted in the previous section may be applied to HC001-A2. In this case, for  $\delta z = \pm 8$  mm, focal broadening of order 4 arcmin is evident from *Figure 3.14* as theoretically predicted.



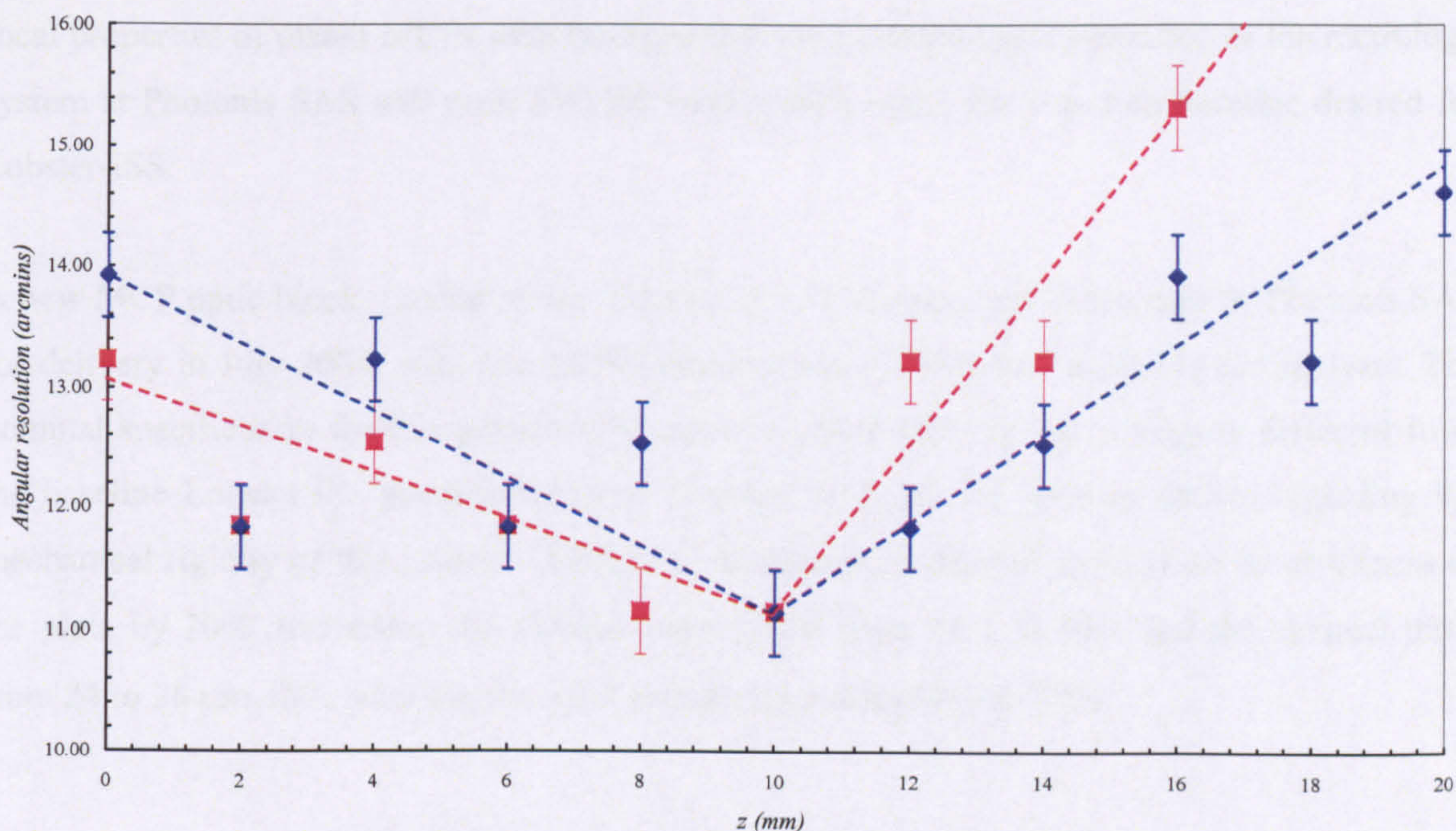


**Figure 3.14.** Depth of focus measurements of HC001-A2 on 8th January 2002. Angular resolutions in both the x-axis (squares) and y-axis (diamonds) (as orientated in Figure 3.13) of the central focus are shown. Focal lengths appear to coincide in both x and y axes, indicating minimal toroidal deformation of the MCP. Errors are explained by, and have equivalent magnitude to, those in Figure 3.10.

### 3.3.2 Planar MCP optics

In order to improve the optical quality of MCPs as lightweight focusing optics, ESA, with their industrial partners Photonis SAS, have developed an extensive metrology system used to automate and improve the MCP manufacturing process (Bavdaz et al. 2004a). An ‘on-line’ metrology system both monitors and controls the fibre drawing processes in real time. An ‘off-line’ metrology system then performs extensive measurements of the geometry of a sample of fibres post-production, a feed-back loop being implemented to optimise the drawing process and correct for those errors discovered for subsequent runs.

Prior to this work, the best focus reported from a square-packed, square pore MCP optic was of 500:1 format, with a measured FWHM square focus of 5.2 arcmin (Price, 2001). For a Lobster-spec 50:1 MCP optic, a best focus of 6.8 x 5.3 square arcmin was reported by Price et al. (2003b). In both cases the MCPs were illuminated with Cu-L X-rays (930 eV) on the VTF in its current configuration at the University of Leicester. This work continues the analysis of the soft X-ray



focal properties of planar MCPs with the hope that the ESA-led implementation of the metrology system at Photonis SAS will push FWHM focal widths under the 4 arcmin baseline desired for Lobster-ISS.

A new MCP optic block, funded by the University of Leicester, was fabricated by Photonis SAS for delivery in July 2004, with one MCP (serial number LF001-A1) available for analysis. The nominal specification for this particular Lobster block of MCP optics is slightly different from the baseline Lobster-ISS specification and is given in *Table 3.3*. Due to doubts regarding the mechanical rigidity of this Lobster block, the manufacturers decided to increase the thickness of the plate by 20%, increasing the channel aspect ratio from 50:1 to 60:1 and the channel pitch from 24 to 26  $\mu\text{m}$ , thus reducing the open area fraction from 69% to 59%.

<i>Side length (mm)</i>	<i>40 x 40</i>
<i>Channel width D (<math>\mu\text{m}</math>)</i>	<i>20</i>
<i>Channel length L (mm)</i>	<i>1.2</i>
<i>Channel pitch P (<math>\mu\text{m}</math>)</i>	<i>26</i>
<i>Channel aspect ratio (L:D)</i>	<i>60:1</i>
<i>Open area fraction (%)</i>	<i>59</i>
<i>Glass material</i>	<i>Philips type 297</i>

*Table 3.3. Specification of the planar MCP optic LF001-A1 manufactured by Photonis SAS. In this case, the specification was altered from the Lobster-ISS baseline (Table 1.1) due to manufacturing difficulties.*

Lobster optic LF001-A1 reveals immediate visual differences to its predecessors. A periodic pattern on the surface of the optic has been deliberately implemented during manufacturing in order to optimise the alignment of multifibres (Fairbend, 2004). A Nikon SMZ-U optical microscope was used in conjunction with a JVC TUV CCD video camera in the D.M. Taylor Clean Room at the Space Research Centre, University of Leicester to obtain magnified images of LF001-A1. *Figure 3.15* illustrates a characteristic ‘cross’ on each multifibre on alternate rows, with each cross intersecting slightly off-centre in both dimensions to ensure multifibres are stacked in the correct orientation during manufacture. The markings, dark brown in appearance,



are actually areas of the face of the multifibre that have been the subject of the hydrogen reduction process.

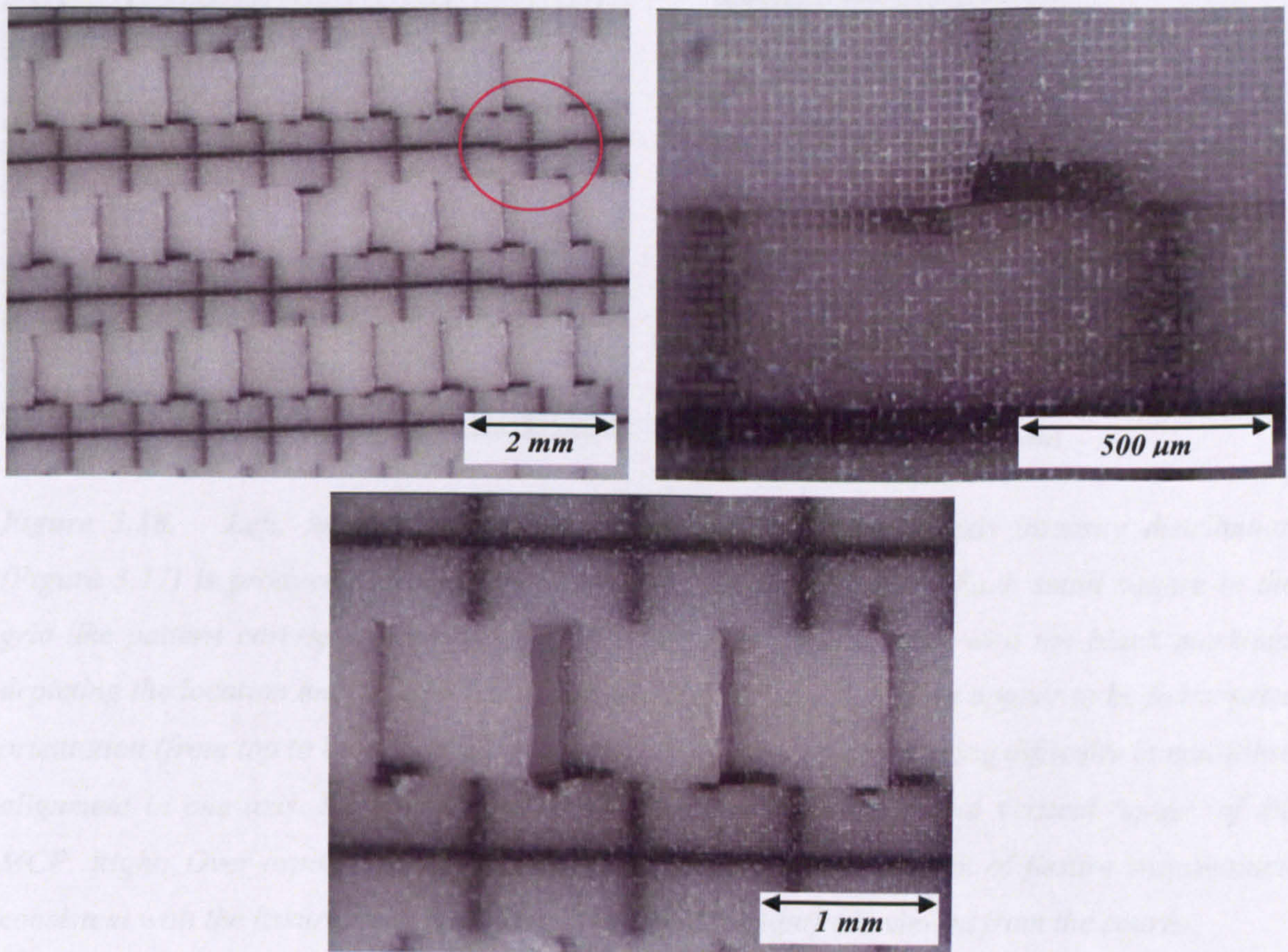


**Figure 3.15.** Images of LF001-A1 under an optical microscope. Upper left: Characteristic pattern used for multifibre alignment purposes at Photonis SAS. The pattern shown here is periodic over the entire 40 x 40 mm<sup>2</sup> structure. Unfortunately, the use of the patterns to correctly orientate multifibres is achieved with limited success as indicated. Upper right: At an increased magnification it appears that multifibres are poorly fused together. Lower: MCP “fissure”.

Holding the MCP up to a light on initial inspection, there also appeared to be a number of small, thin fissures or slits distributed over the extent of the MCP, visible to the naked eye and all in the same orientation. The fissures were mapped over the entire MCP structure using the optical microscope used previously and are shown in Figure 3.16. An optical microscope image of a more prominent fissure is illustrated in Figure 3.15.



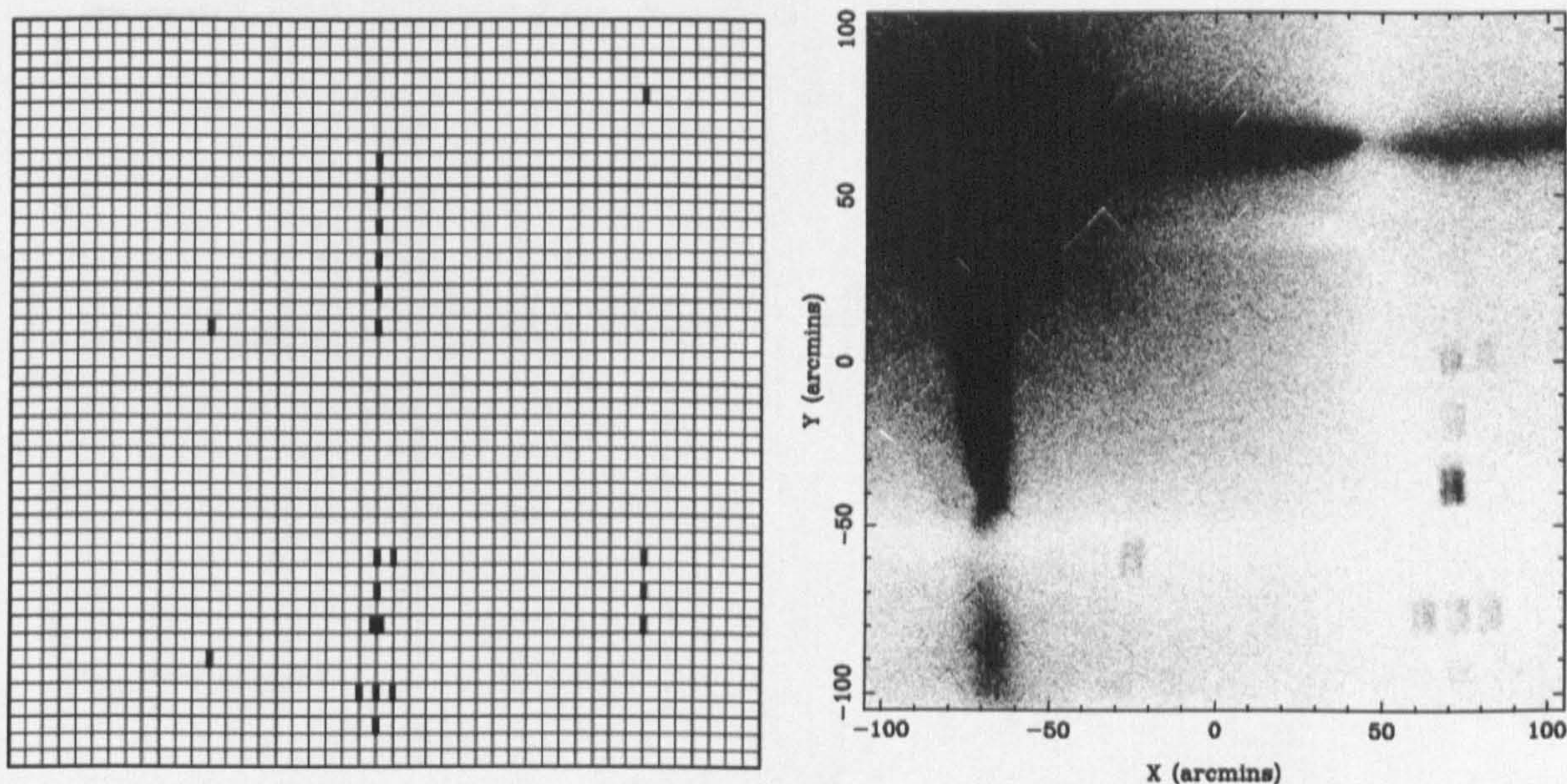


**Figure 3.16.** Left: MCP LF001-A1 orientated such that the on-axis intensity distribution (Figure 3.17) is produced through the focusing of soft Cu-L X-rays. Each small square in the grid-like pattern corresponds to one multifibre of 35 x 35 channels, with the black markings depicting the location and severity (or width) of the fissures. All fissures appear to be in the same orientation (from top to bottom as viewed here) revealing a manufacturing difficulty in multifibre alignment in one axis. Note the distribution of fissures down a central vertical 'spine' of the MCP. Right: Over-exposed region of off-axis focus, showing a pattern of fissure transmission consistent with the fissure map. Both diagrams (left and right) are viewed from the source.

Using the Vacuum Test Facility, LF001-A1 was illuminated on-axis with Cu-L (0.93 keV) soft X-rays and the subsequent best focus intensity distribution recorded from the MCP detector is illustrated in Figure 3.17. The vertically orientated cross-arm appears to be fragmented and smeared in the horizontal direction. It was initially thought that direct transmission through the fissures along the vertical central "spine" of the MCP was contributing to the structure of the vertically orientated cross-arm. For this reason, an off-axis image (also shown in Figure 3.17), with the MCP rotated approximately  $1.20^\circ$  about this central spine axis was taken to redirect the focus (on the detector) from any transmission pattern present as a result of the fissures. An overexposed image was required in order to identify the transmission pattern in the off-axis image, which may be matched to the lower part of the fissure map in Figure 3.16. The low fluxes associated with the transmission pattern suggest that it does not contribute significantly to the fragmented structure of the vertically orientated cross-arm in the on-axis image (Figure 3.17).



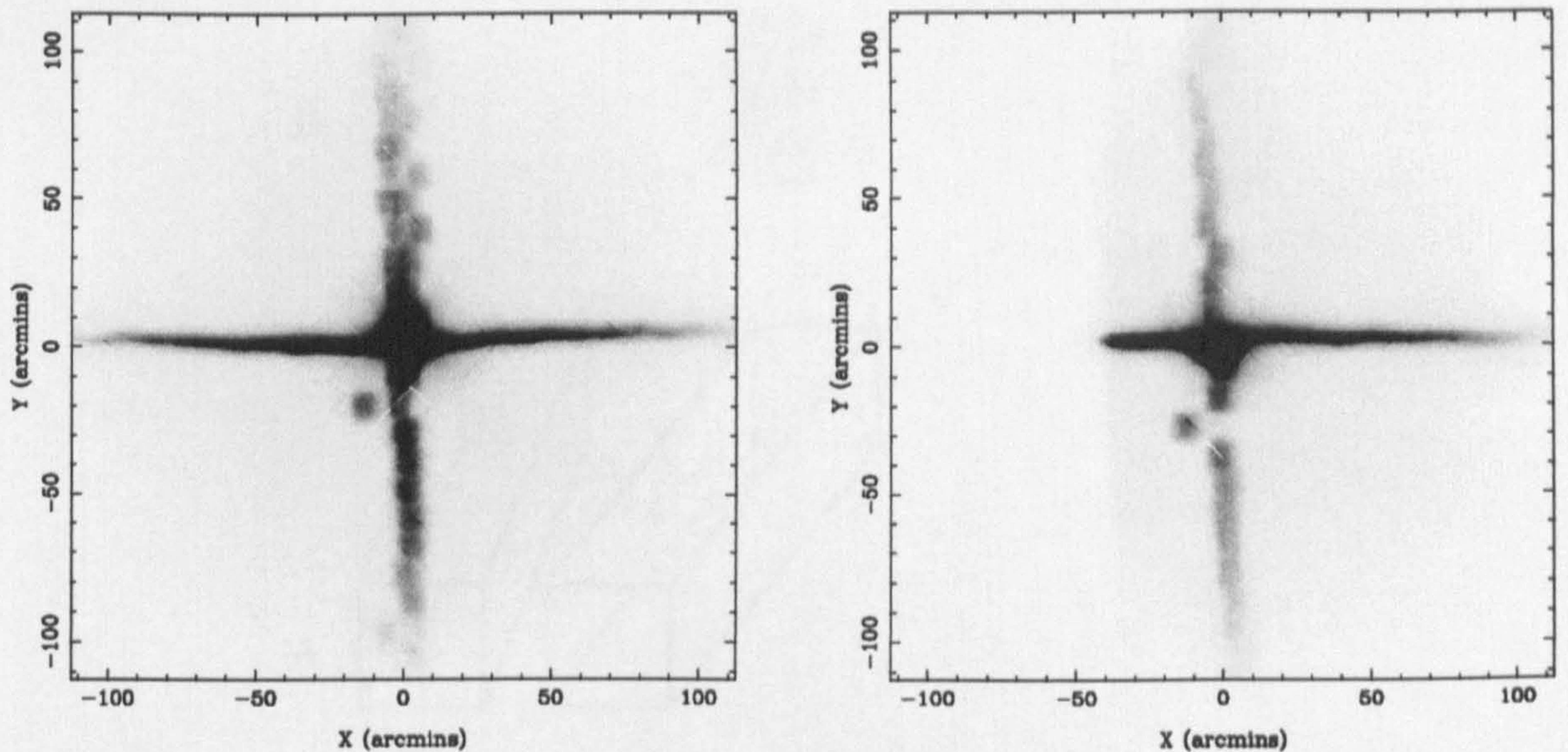


**Figure 3.17.** On-axis (left) and off-axis (right) cruxiform image structures provided by LF001-A1 at Cu-L (930 eV) X-rays. Images contain  $1.3 \times 10^7$  (left) and  $9.5 \times 10^6$  (right) counts, each collected in 20 hour exposures.

Horizontal and vertical FWHM focal width measurements of LF001-A1 yield an angular resolution of  $9.4 \times 7.5$  square arcmin respectively at best focus (optimum optic-detector distance), with similar FWHM (line) focal width measurements across the horizontally and vertically orientated cross-arms of 4.0 and 7.5 arcmin respectively. This compares slightly unfavourably with the previous best foci obtained for planar square pore, square-packed MCP optics outlined at the beginning of this section, and is a disappointing first result. However, the comparative focal widths of the line foci above infer that the MCP is more efficient at focusing soft X-rays in one orientation over the other. It appears that single reflections from the horizontally orientated walls on the MCP (*Figure 3.16*) are focused far more accurately than those from the vertically orientated walls, which are shown to produce the fragmented vertical cross-arm in *Figure 3.17*; each element of the vertical cross-arm is slightly horizontally displaced from its neighbours above and below. This is characteristic of multifibre misalignment in one axis (*Figure 3.18*).

In the case of LF001-A1, multifibres within the same horizontal row of the MCP (as shown in *Figure 3.16*) appear to be aligned in different directions relative to one another. The presence of the fissures provides scope for such misalignments; two rows of multifibres either side of a given fissure are orientated at an angle  $\phi$  from one another, providing the ‘double projections’ observed in the on-axis image in *Figure 3.17*.



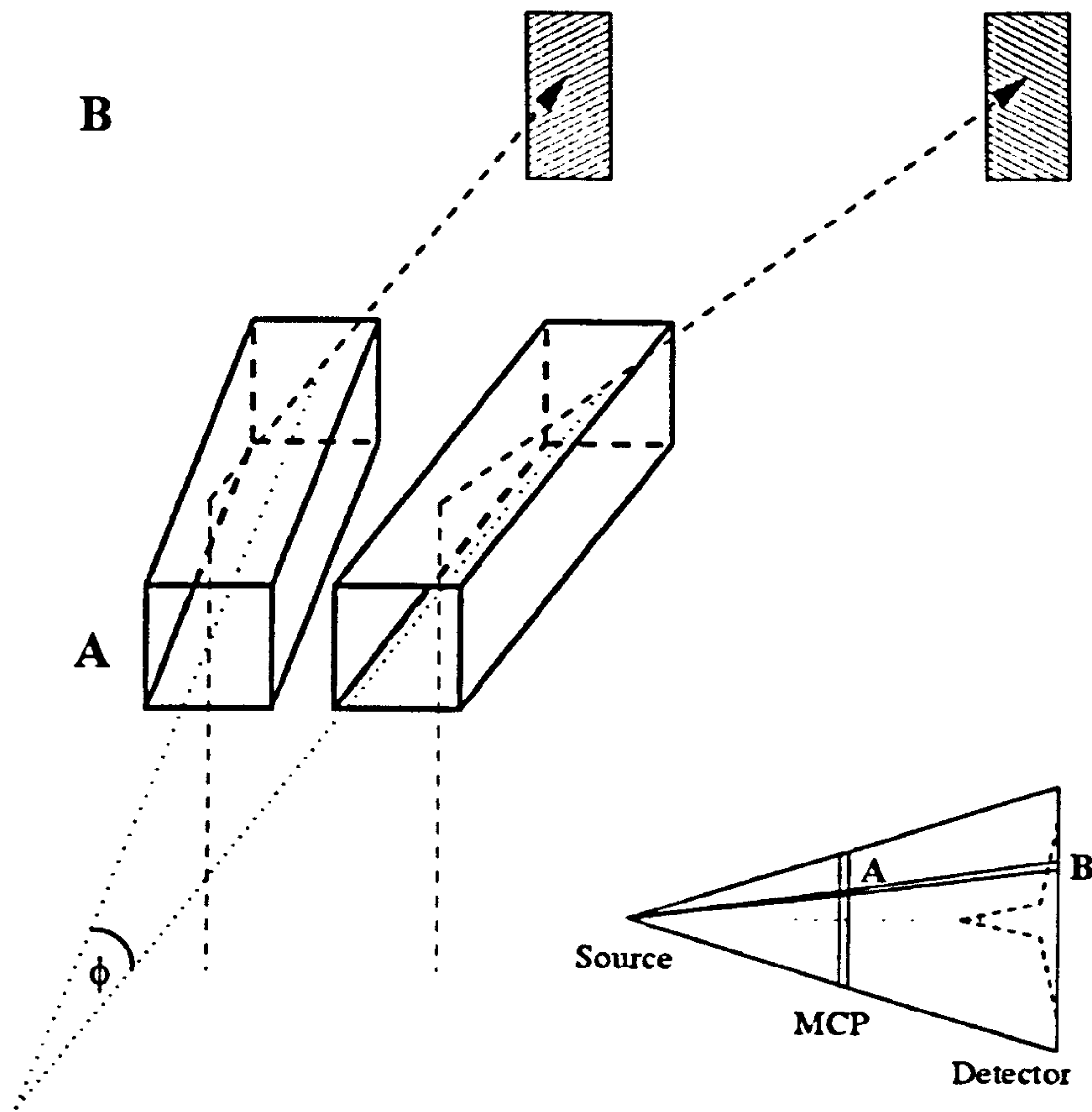


**Figure 3.18.** *Effect of multifibre misalignment on the cross-arm structure. Bottom right: The position of the source, on the optical axis joining the geometrical centres of MCP and detector. This configuration implies that each component of the vertical cross-arm (B) is focused by a unique row of multifibres (A). Main: If neighbouring multifibres are misaligned in the row plane by an angle  $\phi$ , the projection of the single reflections from each multifibre will occur a horizontal distance from one another on the detector (in this case).*

There is one gross example of this ‘row misalignment’ evident in the tilted image in *Figure 3.17*; a horizontal departure from the vertical cross-arm, underneath the central focus (as displayed). This misalignment with respect to the normal to the MCP surface may be estimated through the manipulation of simple trigonometry (*Figure 3.19*) using

$$\phi = \frac{x}{2l_i} \quad (3.3)$$

The row misalignment is estimated to be 5.81 arcmin using the method illustrated above. By means of comparison, recent measurements of the angular resolution of a *single multifibre* at



BESSY by Bavdaz (2004b) have yielded FWHM horizontal and vertical foci of 14.8 and 13.6 *arcsec*. The measurements were made on a single square pore, square-packed 50:1 multifibre made from Philips type 297 glass at Photonis SAS, with pore size 20  $\mu\text{m}$  on a 24.8  $\mu\text{m}$  pitch at 3 keV. These results demonstrate the potential of MCPs as focusing optics and represent a real advance, indicating *excellent alignment of fibres within each multifibre*. X-ray focusing using an *entire MCP* (as measured in our case) indicates that it is the *alignment of the multifibres, rather than individual fibres within each multifibre* that is currently limiting the angular resolution of MCP optics. This conclusion may in principle be verified by restricting the areas of the plate that are illuminated; this may be achieved by inserting the 1 mm pinhole (*Section 3.2.1*) or perhaps by creating a mask with a small aperture placed between source and MCP; translating the aperture in  $x$  and  $y$  across the MCP would enable us to build up a picture of which regions of the plate are responsible for each feature on the on-axis PSF in *Figure 3.17(a)* and thus even enable us to calculate a 2D multifibre misalignment ‘map’ over the MCP in  $x$  and  $y$ . Such a map would provide invaluable feedback to manufacturers Photonis SAS in their continuing efforts to optimise the multifibre alignment process.

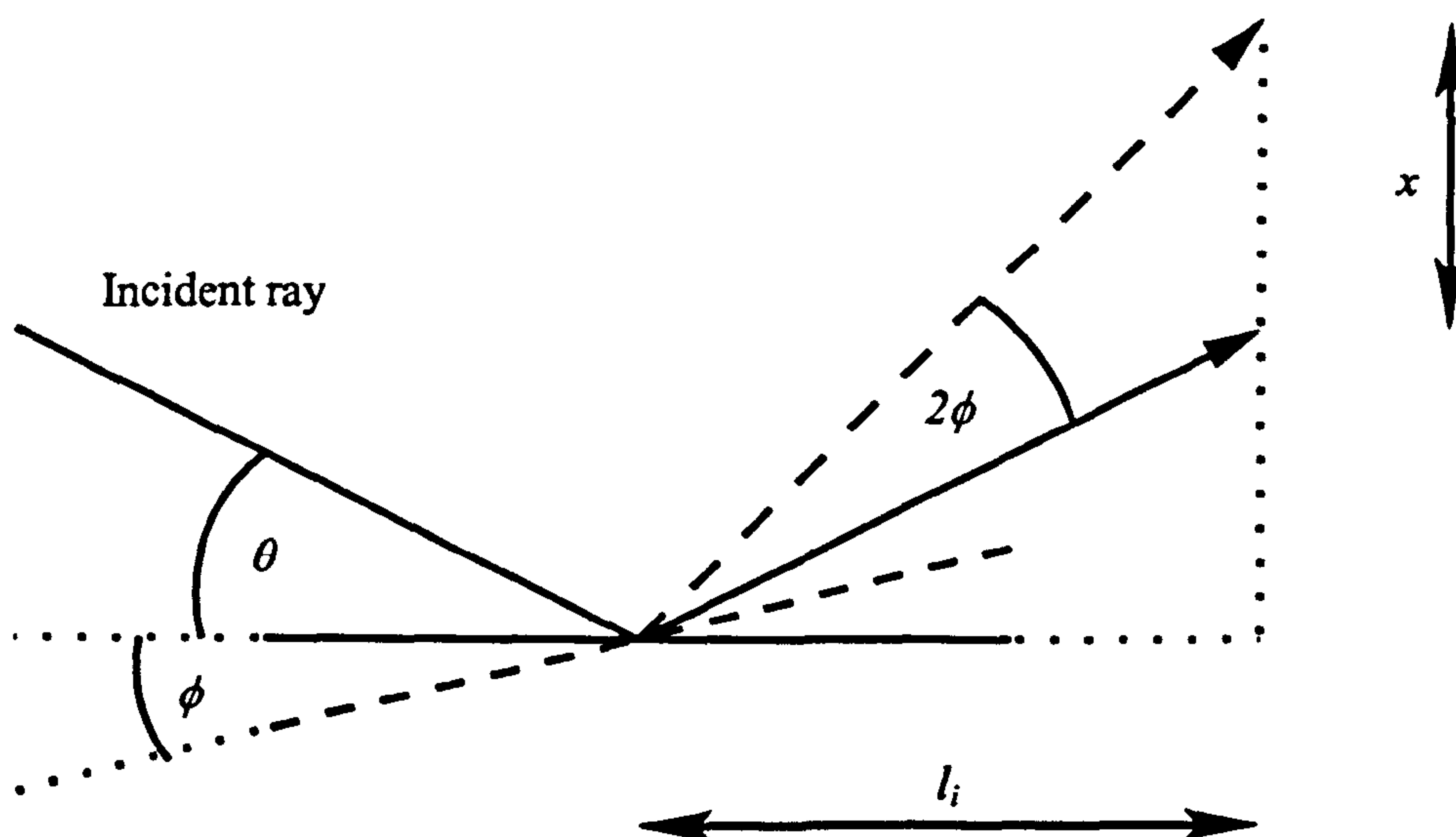


**Figure 3.19.** Geometric arrangement used to estimate MCP row misalignment. An incident ray (blue) with grazing angle  $\theta$  to the normally orientated multifibre (solid lines) is reflected and reaches the detector a distance  $x$  from a ray reflected from a multifibre misaligned at an angle  $\phi$  from the normal orientation.



With regard to MCP LF001-A1, after discussion with Fairbend (2004), it appears that multifibres of slightly differing dimensions were stacked together to form the block (some multifibres were non-square, with side dimensions as much as 3  $\mu\text{m}$  longer than wide over the nominal 910  $\mu\text{m}$ ). During the fusion process, it was envisaged that this 3  $\mu\text{m}$  may be ‘squeezed out’ to form a regular array of perfectly square multifibres. However, the multifibres were adjudged to have been so regular that their compressibility was minimal, leaving what we interpret as being fissures occurring in one orientation only.

### **3.4 Conclusions**

In this chapter, the focusing properties of slumped and planar MCP optics were investigated, with a view to their application on the Lobster-ISS all-sky monitor.

The angular resolution of slumped optic HC001-A1 at best focus appeared to change over time; there is no indication that water adsorption (into the reflecting surfaces of the MCP between the periods of experimentation) is responsible for this change. The change is believed to be due to the mechanical deformation of the MCP optic in the holding jig during experimentation. At best focus, we report an angular resolution of 9.1 x 9.1 square arcminutes (FWHM).

The ESA-funded development of an extensive metrology system at Photonis SAS has resulted in the manufacture of individual MCP multifibres capable of focusing soft X-rays to a measured angular resolution of < 15 arcseconds (Bavdaz, 2004b). We report the point to point focusing characteristics of planar MCP LF001-A1, (a product of the new metrology system) and measure an angular resolution of 9.4 x 7.5 square arcminutes (FWHM) at best focus. Soft X-ray transmission through ‘fissures’ in the MCP structure (located between neighbouring multifibres, in one orientation only) is observed. The disjointed structure of one of the cross-arms is attributed to the misalignment of rows of multifibres, separated by fissures.



## Chapter 4 Auger Electron Spectroscopy of MCP Optics

The application of a metal coating to the reflecting surfaces of MCP optics will theoretically improve the high energy and wide angle response of Lobster-ISS (*Section 1.4.2*). In this chapter, the Auger Electron Spectroscopy (AES) technique is used to characterise ruthenium and nickel MCP coatings, each deposited using different coating processes. Compositional analysis of one bare glass MCP optic is also performed.

### 4.1 The Coating Processes

In this thesis, MCP metal coatings are applied using the Electroless Nickel (EN) (*Ni coatings*) and Atomic Layer Deposition (ALD) (*Ru and Ir coatings*) techniques. What follows is a brief review of both coating processes.

#### 4.1.1 Electroless Nickel

‘Electroless’ plating is a chemical reduction process for depositing metals, similar to electroplating in that it can be run continuously to accumulate a thick coating. Metal is deposited only onto a pre-prepared surface, seeded with an appropriate catalyst, with the rate of deposition heavily dependent on the characteristic temperature of the process. The nature of the technique theoretically enables the coating to reproduce the surface characteristics of the substrate, even in “hard to get to” regions where electroplating may fail, thus minimising both surface roughness and variation in coating thickness. For MCPs, the process is carried out by Photonis SAS. A comprehensive overview of EN processing can be found in Brenner (1963) and Hibbard (1997).

The EN plating operations are carried out in three distinct stages:

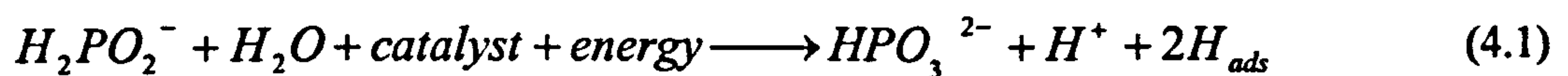
- Substrate pre-treatment
- Deposition of nickel-phosphorous alloy via an electrochemical growth process
- Heat treatment of sample to enhance coating durability and substrate-coating adhesion

The first stage of pre-treatment involves subjecting the substrate to a number of chemical solutions, which serve to clean the substrate surface and etch away any surface contaminants present. Next, the substrate is ‘sensitised’; immersion in a simple stannous chloride / hydrochloric acid solution attaches a monolayer of metallic atoms to the surface. This prepares

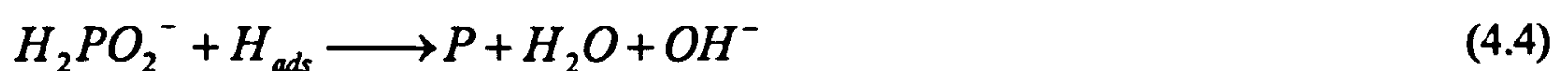


the substrate for the *seeding process*, which catalyses the surface in order to promote the subsequent auto-catalytic reaction. The seeding process involves immersing the substrate in an acidic, palladium chloride solution. A uniform distribution of the palladium-based catalyst is critical to the success of the EN process, as this is the surface that will be ‘reproduced’ by the subsequent coating (Fairbend, 2003).

The pre-treated substrate is then immediately immersed in the plating solution, an electrolyte made up of an ionic nickel salt, hypophosphite ions (the reducing agent, usually in the form of sodium hypophosphite) and a salt usually derived from an organic acid. The hypophosphite ions reduce the nickel salt in the presence of the catalysed surface, producing phosphorous as a by-product. No external electric current is applied, hence the ‘electroless’ process label. The two reactions that take place to make the electroless process possible are:



In both reactions (4.1) and (4.2), the hypophosphite ( $H_2PO_2^-$ ) is oxidised to an orthophosphite ( $HPO_3^{2-}$ ) at the catalysed substrate surface, producing adsorbed hydrogen atoms ( $H_{ads}$ ) and hydrogen gas ( $H_2$ ). It is the *adsorbed hydrogen* reacting with either the nickel salts or hypophosphite ions which produces the required nickel-phosphorous alloy (4.3), (4.4).



The nickel concentration, hypophosphite concentration, pH and operating temperature in the plating bath each affect the final EN alloy composition. Increased relative concentrations of nickel and phosphorus increase abundances of each respectively in the final alloy. Increasing the bath pH (normally 4 - 5) or increasing the bath temperature (normally 80 - 90°C) independently reduce the phosphorus content of the produced films. *Equation 4.1* implies that the bath of plating solution becomes progressively more acidic as the reaction continues; this would have the undesired effect of decreasing phosphorous content with film growth. The presence of the



organic acid however prevents the pH from falling, thereby stabilising the bath, while its concentration also determines the deposition rate of the desired nickel-phosphorous alloy. However, the most significant variable affecting deposition rate is the bath temperature, which varies almost exponentially (*Figure 4.1*).

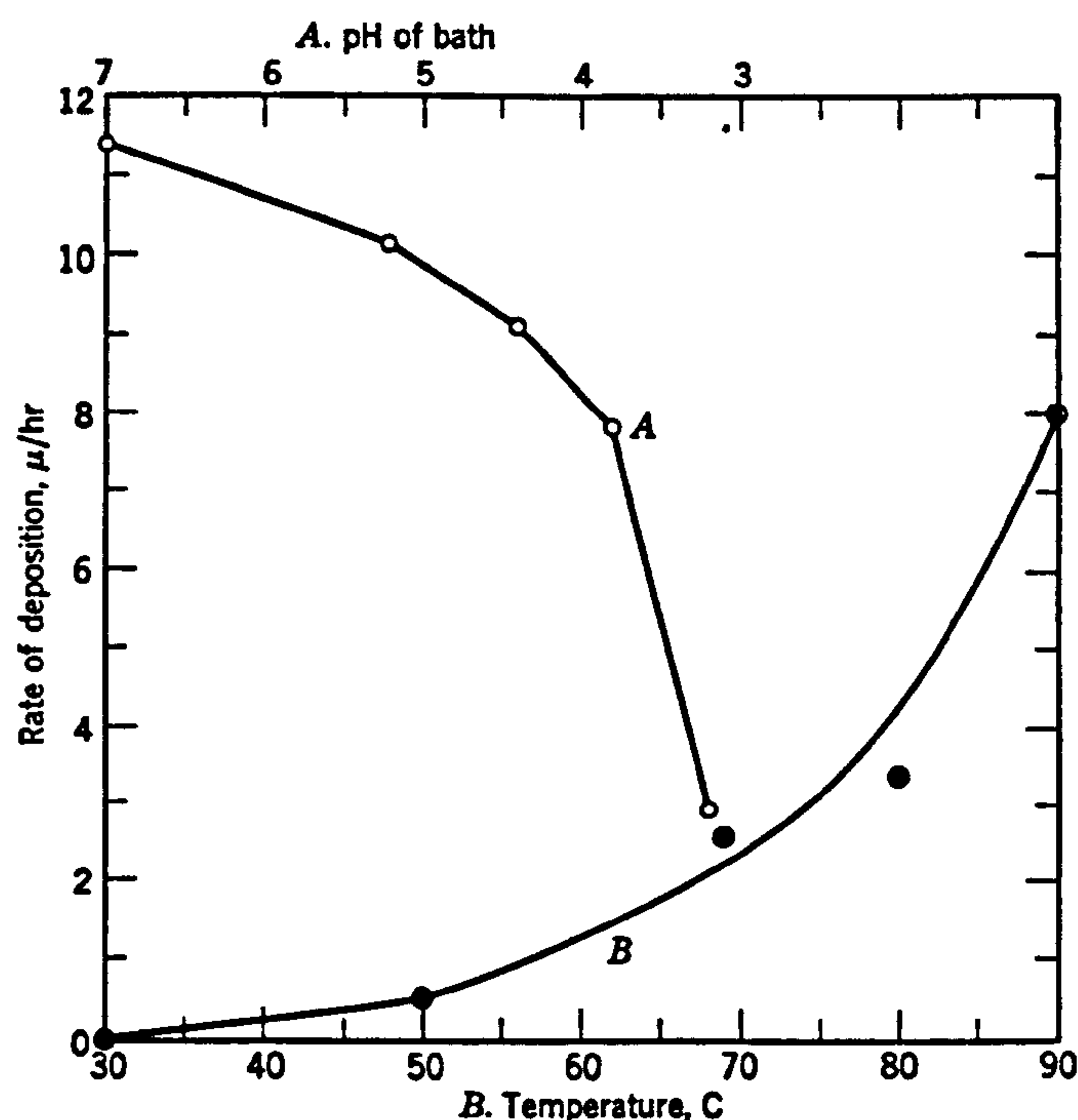


**Figure 4.1.** Variation in rate of Ni deposition with respect to bath temperature (B) and pH of plating solution (A). From Brenner (1963).

The reaction itself is very difficult to control, requiring constant monitoring of the nickel and hypophosphite concentration levels, pH and operating temperature. In addition, heavier elements contained within the MCP glass substrate, notably bismuth and lead, are catalytic poisons termed *inhibitors*, capable of suppressing the auto-catalytic reaction. Minimising the surface roughness of the coated substrate is central to the success of MCP X-ray optic focusing. Localisation of hydrogen (a by-product of the EN process) and other inhibitors adsorbed onto the catalytic surface may create a fragmented ‘cobblestone’ effect, with crevices appearing in the surface morphology (*Figure 4.2*). Increasing the relative quantity of phosphorous within the Ni-P alloy has the effect of reducing crevice depth, thereby improving surface roughness (if only on a scale of order 100 Å). The mass density of the Ni-P alloy applied to the MCPs is nominally 7.8 g cm<sup>-3</sup>, corresponding to around 10% phosphorus by weight (Fairbend, 2003) – significantly larger than



the standard 4 - 8% used in other industrial applications of the EN process such as for increasing the corrosion resistance of substrates prone to oxidation.

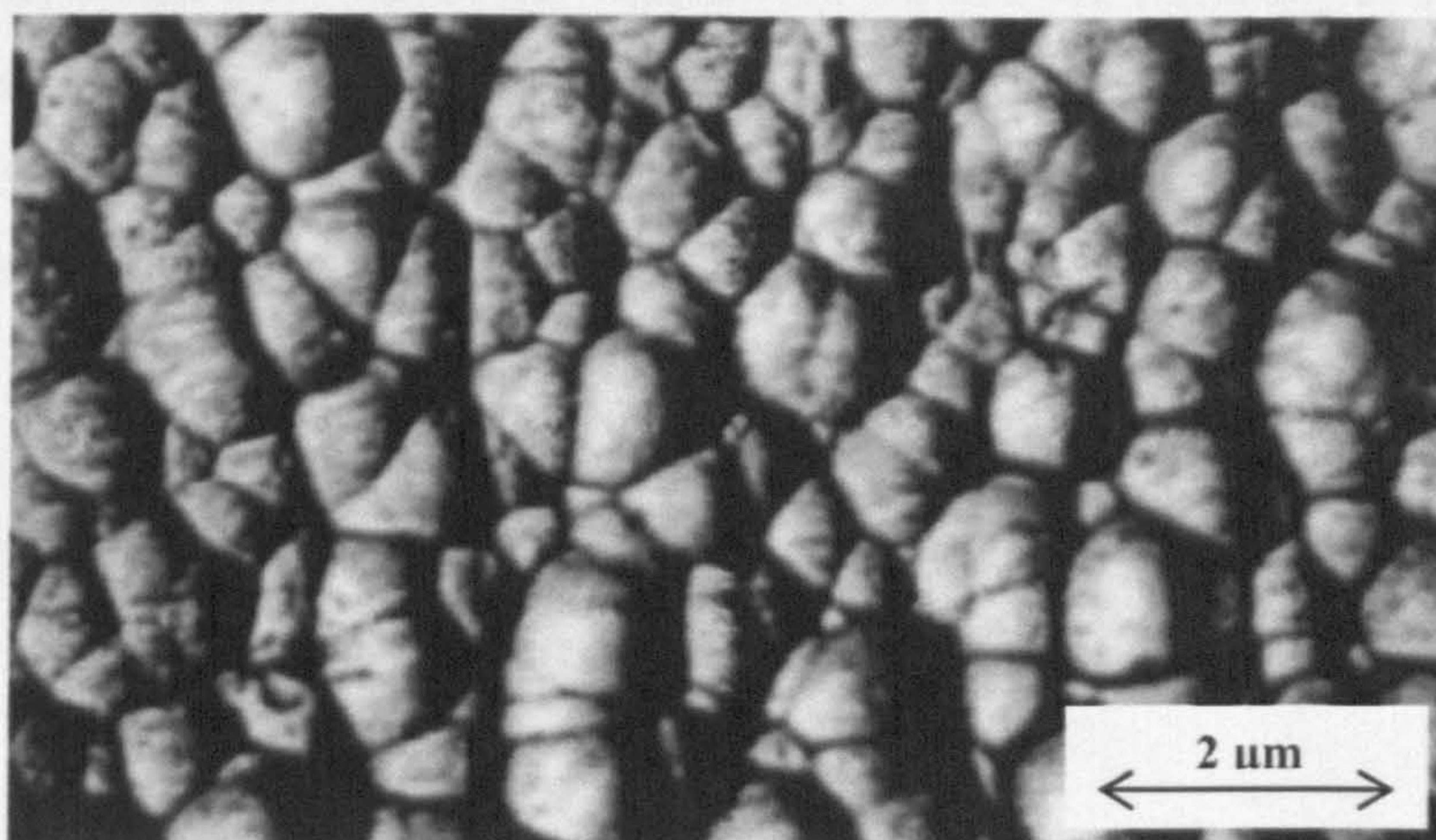


**Figure 4.2.** *Surface morphology of a typical electroless nickel deposit with low phosphorous content. Localised groups of inhibitors are adsorbed onto the catalytic surface, suppressing the growth of the Ni-P alloy during the chemical plating process. This creates a fragmented 'cobblestone' surface profile, with mounds ranging in size from 0.1 to 1 μm. Crevice depth is of order 100 Å. Increasing the phosphorus content of the alloy reduces crevice depth and relative mound height. Figure taken from Hibbard (1997).*

#### 4.1.2 Atomic Layer Deposition

The Atomic Layer Deposition process (ALD) provides a uniform, conformal coating through the alternating exposure of a substrate to two gaseous reactants. ALD is an alternative to Chemical Vapour Deposition (CVD) and was originally developed for applications in semiconductor microelectronics, magnetic storage media and catalysis (Lim et al. 2003). The ALD process has been successfully demonstrated for a variety of metal compounds, but for very few pure metals. This section follows the development of the ALD method by those at the Laboratory of Inorganic Chemistry, Department of Chemistry, University of Helsinki to coat Lobster-ISS specification MCP optics with pure ruthenium and iridium (Aaltonen et al. 2003a, 2004). The process has also been demonstrated for platinum (Aaltonen et al. 2003b) on flat borosilicate glass substrates, so platinum is also included in this overview of the ALD process.



The ALD process may be summarised as follows with reference to the experimental configuration shown in *Figure 4.3*:

1. The compounds from which the vapours are formed are termed *precursors*. A suitable vapour reactant is generated through the heating of each of the precursors. The vapour from precursor 1 is introduced into the process chamber (carried by an inert gas) and brought to the surface of the substrate to be coated.
2. The vapour reactant from precursor 1 is adsorbed onto the surface of the substrate forming a monolayer. The chamber is then purged with an inert gas removing the vapour reactant from precursor 1. The total exposure time of the substrate to a given vapour reactant is termed the *pulse time*.
3. The vapour reactant from precursor 2 is introduced into the process chamber and reacts with the monolayer to form a surface film. The chamber is again purged by an inert gas, removing the vapour reactant from precursor 2.

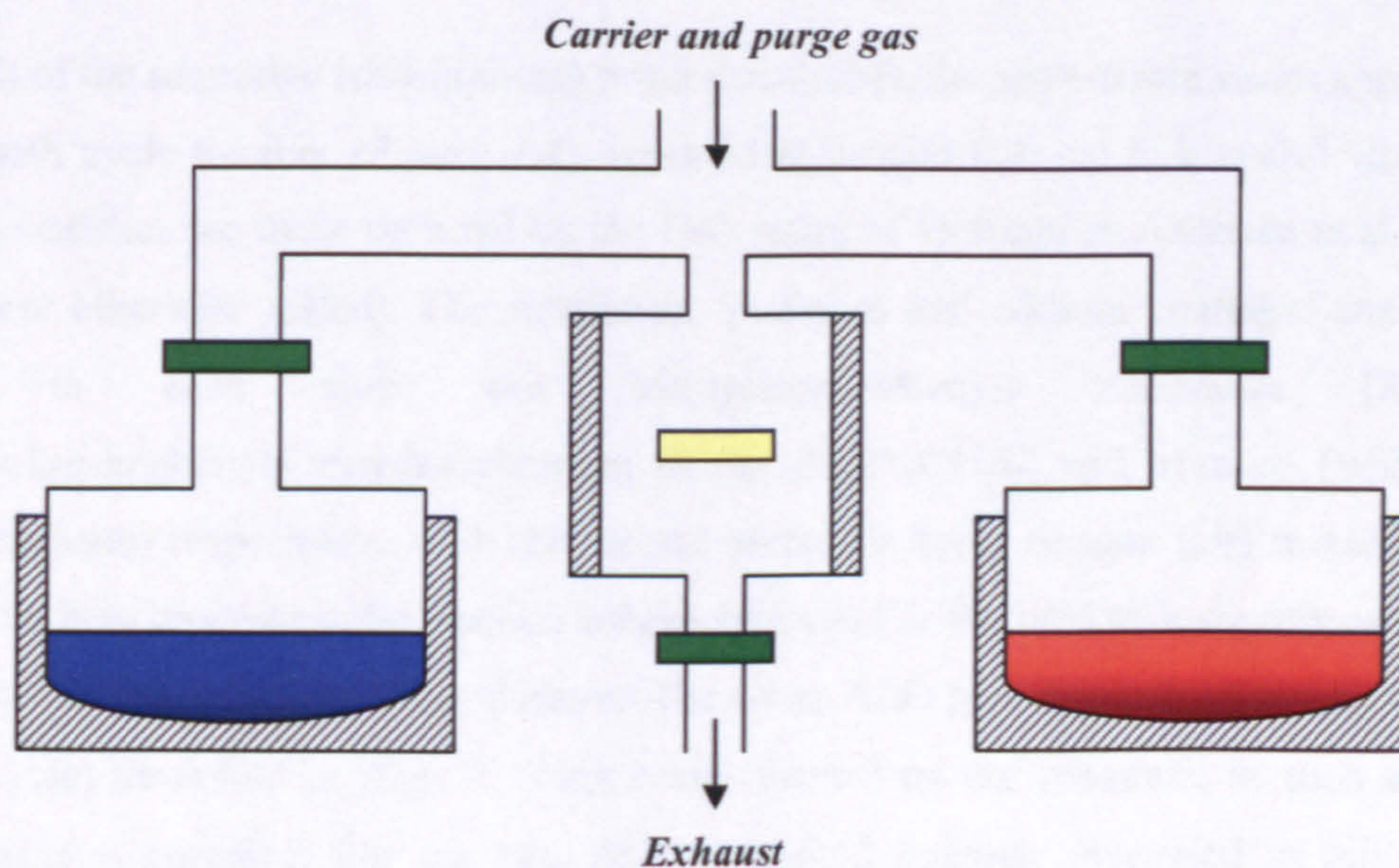


**Figure 4.3.** Typical experimental configuration used to perform the ALD process. The precursors (red, blue) are heated (shaded area) to produce vapour reactants which are introduced into the process chamber (centre) containing the substrate (yellow) through the use of automated high speed valves (green).



Stages 1-3 detail one complete *cycle* of the ALD method. The process is repeated for as many cycles are necessary to achieve the desired coating thickness.

The ALD process may produce uniform and conformal coatings, of a controlled thickness to a high degree of accuracy. This is achieved as a result of two ALD-specific process constraints; the surface reactions must be:

**(a) complementary**

*Both reactants must prepare the surface for the reaction with the other vapour, allowing the deposition cycle to be repeated.*

**(b) self-limiting**

*Providing the substrate is subjected to each reactant for a maximum or “saturating” pulse time, the thickness of material deposited per cycle is approximately constant. ALD may thus produce uniform coatings, even if the flow of reactants over the surface is non-uniform. Coating thickness is also easily controlled by the number of cycles performed.*

As a result of the saturative (self-limiting) property of ALD, the growth rate varies approximately linearly with cycle number (*Figure 4.4*), reported at around  $0.4 - 0.5 \text{ \AA cycle}^{-1}$  (this, and all following statistics are those reported by the University of Helsinki in Aaltonen et al. 2003a, b; 2004 unless otherwise stated). For ruthenium, platinum and iridium coatings, one precursor selected in each case was bis(cyclopentadienyl) ruthenium  $[\text{Ru}(\text{C}_5\text{H}_5)_2]$ , (methylcyclopentadienyl) trimethylplatinum  $[(\text{CH}_3\text{C}_5\text{H}_4)\text{Pt}(\text{CH}_3)_3]$  and  $\text{Ir}(\text{acac})_3$  (where acac = 2,4 pentanedione) respectively, with the second precursor being oxygen (air) in each case. For each of the three processes, the reaction mechanism used is the oxidative decomposition of the initial (non-oxygen) precursors stated above. For some ALD processes, the initial monolayer (in the first cycle) described in stage 2 is not easily formed on the substrate; in such an event, a seeding layer is required. For the two ALD deposited coatings discussed in this thesis, an aluminium oxide ( $\text{Al}_2\text{O}_3$ ) seeding layer is deposited (via ALD); such layers have been found to improve coating uniformity and reduce the formation of microscopic holes. Film growth rate is also a function of deposition temperature, regulated by the heaters surrounding the process chamber. Typical deposition temperatures range from  $200 - 400^\circ\text{C}$ .



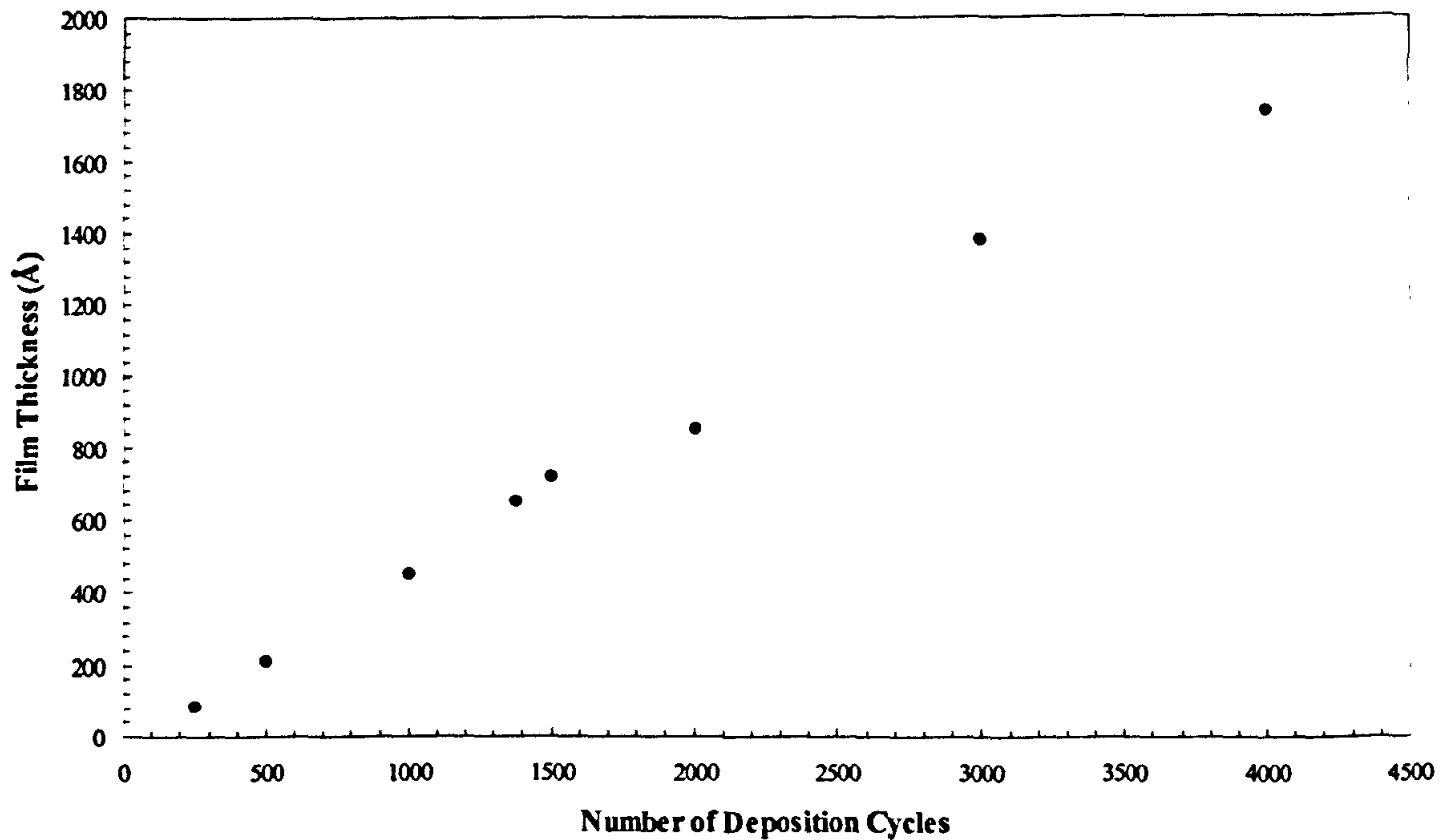


**Figure 4.4.** *Film thicknesses as a function of deposition cycle number for the ALD of iridium at a deposition temperature of 300 °C (Aaltonen et al. 2004).*

For applications in MCP optics, it is crucial that the coatings are mirror-like, with an RMS surface roughness  $\sigma$  of the order of 10 Å. Scanning Electron Microscope (SEM) and Atomic Force Microscope (AFM) images of a 500 Å thick Pt coating deposited using ALD are shown in *Figure 4.5*. Of the three coatings, previous studies have indicated that the iridium process offers the most promise in terms of reducing surface roughness. Promising measurements of  $\sigma \sim 10$  Å on a 200 Å thick Ir coating have been reported, whereas  $\sigma = 40 \pm 4$  Å for the 500 Å thick Pt coating would suppress the soft X-ray reflectivity significantly. These coatings however were performed on a 5 x 5 cm<sup>2</sup> borosilicate glass flat; achieving a 10 Å roughness on an MCP optic coating, given the geometry and channel aspect ratio (50:1 Lobster-ISS baseline) of the substrate may prove more complex. Uniform ALD coatings of cobalt have, however, been reported by Lim et al. (2003) into circular microchannels of diameter 20 µm for aspect ratios as high as 220:1.



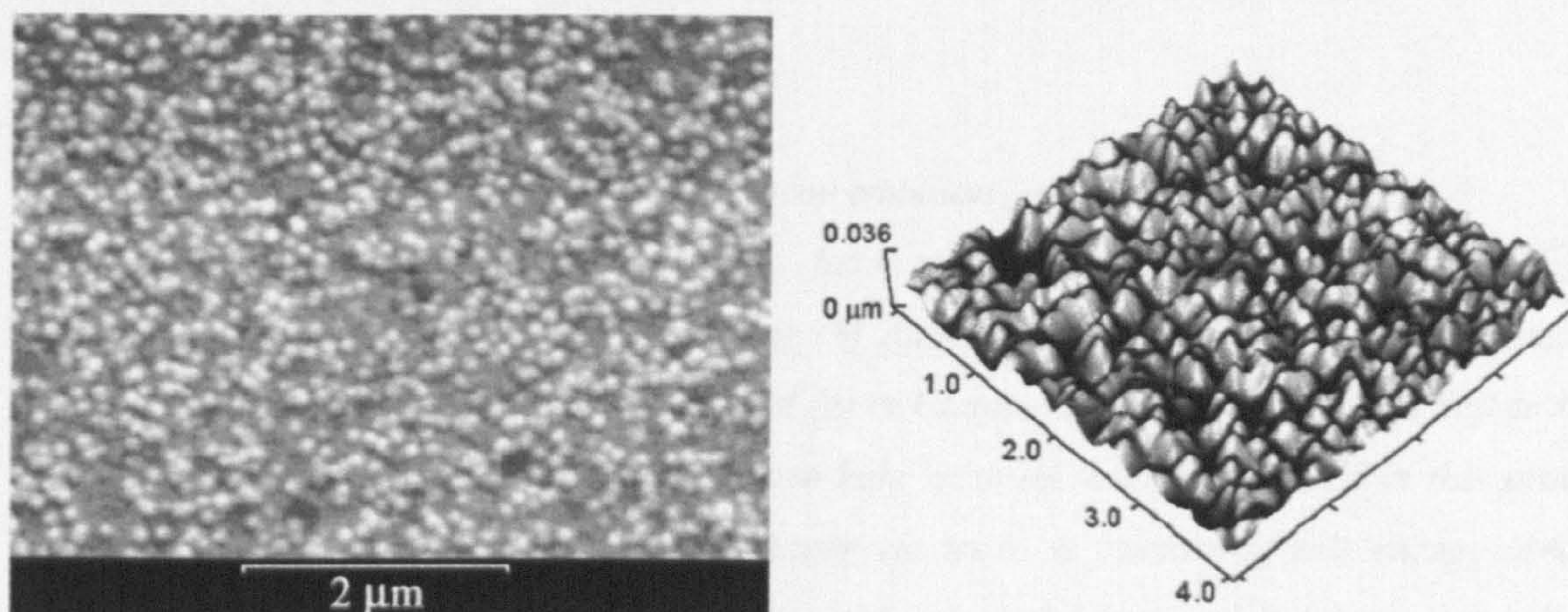


**Figure 4.5.** Atomic layer deposition of 500 Å thick platinum film onto an  $\text{Al}_2\text{O}_3$  seeded  $5 \times 5 \text{ cm}^2$  borosilicate glass substrate. The cobblestone effect discussed in Section 4.1.1 is again evident, as seen in SEM (left) and AFM (right) images. Images taken from Aaltonen et al. (2003b).

## 4.2 Depth Profiling of MCP Optics

It is important to understand the chemical composition of the MCP reflecting surfaces. The bulk MCP glass undergoes a series of chemical processes and heat treatments during manufacture (Section 1.4), resulting in a variation in glass composition with depth. In their bare glass form, it is desirable to obtain depth profiles of the MCP channel walls to improve our understanding of the elemental distribution within the optic surface. Depth profiling of metallised MCPs will allow us to characterise the films in terms of their uniformity and thickness, while also giving insight into the finer aspects of the coating procedure adopted; the observation of seeding layers at the metal/substrate interface for example.

### 4.2.1 Auger Electron Spectroscopy

AES is a widespread method used for the analysis of surfaces, thin films and interfaces. The physical basis of the technique may be summarised in two distinct stages:

#### 1. Atomic ionisation

*The Auger process is initiated by the removal of a core electron of binding energy  $E_i$ ; this is typically achieved by exposing a sample to a primary electron beam (normally of energy 2-10 keV). Such a primary electron beam has sufficient energy to eject core (K*



*shell) electrons from the lighter elements and electrons from higher core levels (L, M shells) of the heavier elements.*

## 2. *Atomic relaxation and Auger electron emission*

*The ionised atom will rapidly relax back to a lower energy state by one of two mechanisms; (a) x-ray fluorescence or (b) Auger electron emission. Here, we consider the latter mechanism, having discussed (a) in Chapter 2. An electron from a higher state (of binding energy  $E_2$ ) will fill the core hole, with the energy liberated in this process transferred to what is termed the 'Auger electron', a fraction of this energy used to overcome its binding energy ( $E_3$ ), with the remainder retained by the emitted Auger electron as kinetic energy.*

The Auger electrons are subsequently detected and their kinetic energies  $E_{AUGER}$  determined. The Auger electrons are emitted with an energy characteristic of the elements in the emitter – this is the basis of AES. Each element has unique values of  $E_{AUGER}$  based on the distinct atomic energy levels of the element. For a given element, it is possible to estimate the possible values of  $E_{AUGER}$ :

$$E_{AUGER} = (E_1 - E_2) - E_3 \quad (4.5)$$

An Auger transition is thus primarily characterised by  $E_1$ ,  $E_2$  and  $E_3$  and may be grouped into families of transitions based on the electron shell corresponding to each. For example, if a K shell electron is ejected from the atom, with an  $L_3$  electron taking its place during atomic relaxation, an Auger electron being ejected from the  $L_1$  shell, the Auger transition is formalised  $KL_3L_1$  or more generally as KLL. A more precise formulation is not possible due to  $E_2$  and  $E_3$  being indistinguishable from one another (Equation 4.5). For lighter elements, KLL is the most probable Auger transition, where LMM and MNN are more probable for the heavier elements. Tabulated values of  $E_{AUGER}$  may be found in Palmberg et al. (1972).

As the sampling depth of the AES technique is of the order 10 Å (Hill, 1976), it is particularly appropriate for use in depth profiling. Typically, argon ions are used to sputter the Auger sample volume, milling away surface layers during AES to measure elemental abundance as a function of time. Standard samples are used to estimate sputtering rates and thus provide a calibration between time and penetration depth.



## 4.2.2 Experimental Arrangements

AES measurements of one bare glass (HC001-A4), one ruthenium-coated (RU-1) and two nickel-coated (NI-1, NI-3) MCP optics were performed by D.D. Hall at the Loughborough Materials Characterisation Centre, Institute of Polymer Technology and Materials Engineering, University of Loughborough, using a JEOL JAMP-7100 Auger Microprobe at an operational pressure of  $P < 1 \times 10^{-8}$  mbar. The primary electron beam energy was set at 0.9 – 1.0 keV for the bare glass MCP (to reduce surface charging) and 3 keV for the metallised MCPs; the beam was incident upon a sample area (spot size) of approximately 1  $\mu\text{m}$  in diameter. The Auger microprobe was then rastered over an area of  $\sim 10 \times 10$  square microns. Depth profiling was carried out using a 3 keV Ar ion beam, sputtering an area of around 0.25  $\text{mm}^2$  onto a cross section of each MCP, each one analysed after the MCP was cleaved with a scalpel. Prior to analysis, the MCP sample surface was subject to a blast of pressurised air to remove any debris present as a result of the cleaving process.

## 4.2.3 Bare Glass MCP Optics

Previous authors have investigated the composition of bare glass MCPs as a function of depth, using AES [Hill, 1976; Siddiqui, 1977; Praček and Kern, 1993], Electron Spectroscopy for Chemical Analysis (ESCA) [Siddiqui, 1977] and Secondary Ion Mass Spectrometry (SIMS) [Then and Pantano, 1990]. The authors agree on a basic structure for the surface and subsurface of MCP intrachannel walls, shown in *Figure 4.6*. A very thin, alkali metal rich layer is reported on the channel surface, covering a thicker, silica rich layer, of thickness 100 – 500 Å. Lead is leached from this layer during the acid etching phase of MCP manufacture. Beneath, a thicker (0.1 – 10  $\mu\text{m}$ ) semiconducting region at bulk glass composition is a result of the hydrogen reduction process, reducing quantities of the lead oxide (present in the bulk glass) into metallic lead. However, as described in *Chapter 1*, the hydrogen reduction process is not used during the manufacture of MCP optics; its use in CEMs is to promote an increased secondary electron yield. In addition, of the published data above, only that of Hill (1976) is from experimentation performed on the Philips type 297 glass discussed in this chapter (Brock, 2005) (Corning 8161 lead silicate glass appears to have been widely used). Brunton et al. (1999) infer that the hydrogen reduction process has little impact on the surface and subsurface composition when considering MCPs as X-ray optics, using a two layer adaptation of the above model (neglecting the alkali metal monolayer) for the purpose of fitting X-ray reflectivity data.



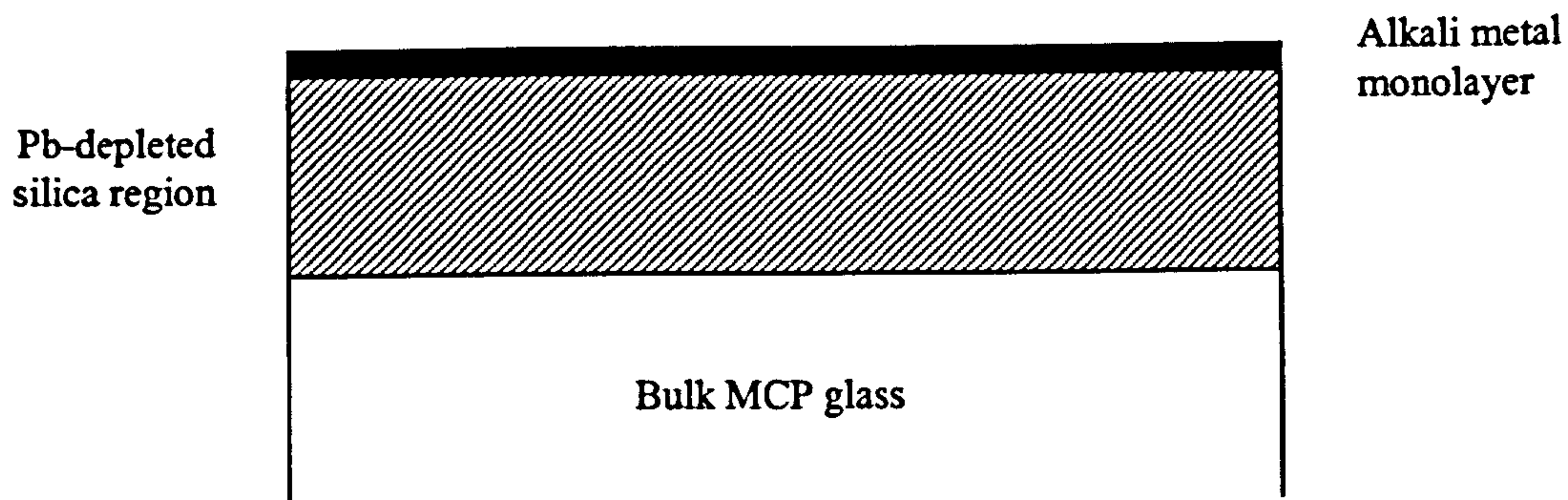


**Figure 4.6.** Surface structure of an MCP channel as suggested by Hill (1976), Siddiqui (1977), Then and Pantano (1990) and Praček and Kern (1993).

The bare glass sample analysed (S/N: HC001-A4) is a fragment of the same MCP ruthenium-coated by the University of Helsinki, using the ALD process (*Section 4.2.4.1*). Unfortunately, due to charging problems in the sample during AES, no depth profiles could be obtained. However, two Auger spectra, taken at depths of 100 Å and 2400 Å are shown in *Figure 4.7*.

The principal constituents of HC001-A4 at each depth are silicon and oxygen, with traces of carbon contaminant present at a depth of 100 Å. The presence of surface carbon is most likely attributable to the MCPs (all four tested in this chapter) being used for reflectivity analysis (*Chapter 5*); in that experiment, the vacuum chamber used was pumped down using a rotary pump, where the backstreaming of hydrocarbons from the pump's lubricant oils into the vacuum chamber is believed to be a major contributor to the carbon contamination. The exposure of the MCP optics to carbon-based atmospheric organics during both reflectivity and AES experimentation is also believed to be a cause. The presence of carbon on bare glass MCP channel surfaces has been reported previously by Hill (1976), Siddiqui (1997) and Praček and Kern (1993). Philips type 297 lead silicate glass may be described by the pseudo-molecule  $\text{Si}_{40}\text{O}_{98}\text{K}_8\text{Na}_7\text{Pb}_6\text{Bi}_2$ , yet there appear to be no detectable traces of potassium, lead or bismuth at either depth. Unfortunately, as mentioned in *Section 4.2.2*, due to sample charging problems, the primary electron beam energy was limited to  $\sim 1000$  eV, which is below the Na-K absorption edge (1070.8 eV) (Fuggle and Mårtensson, 1980); it was thus not possible on this occasion to verify the presence / absence of Na. The model in *Figure 4.6* suggests we would expect to find potassium and sodium to be highly concentrated at the surface, however, the absence of potassium, alongside those of lead and bismuth appears surprising at a depth of 2400 Å, far deeper than the silica-rich, lead-depleted layer, reported to be 500 Å at its deepest; according to



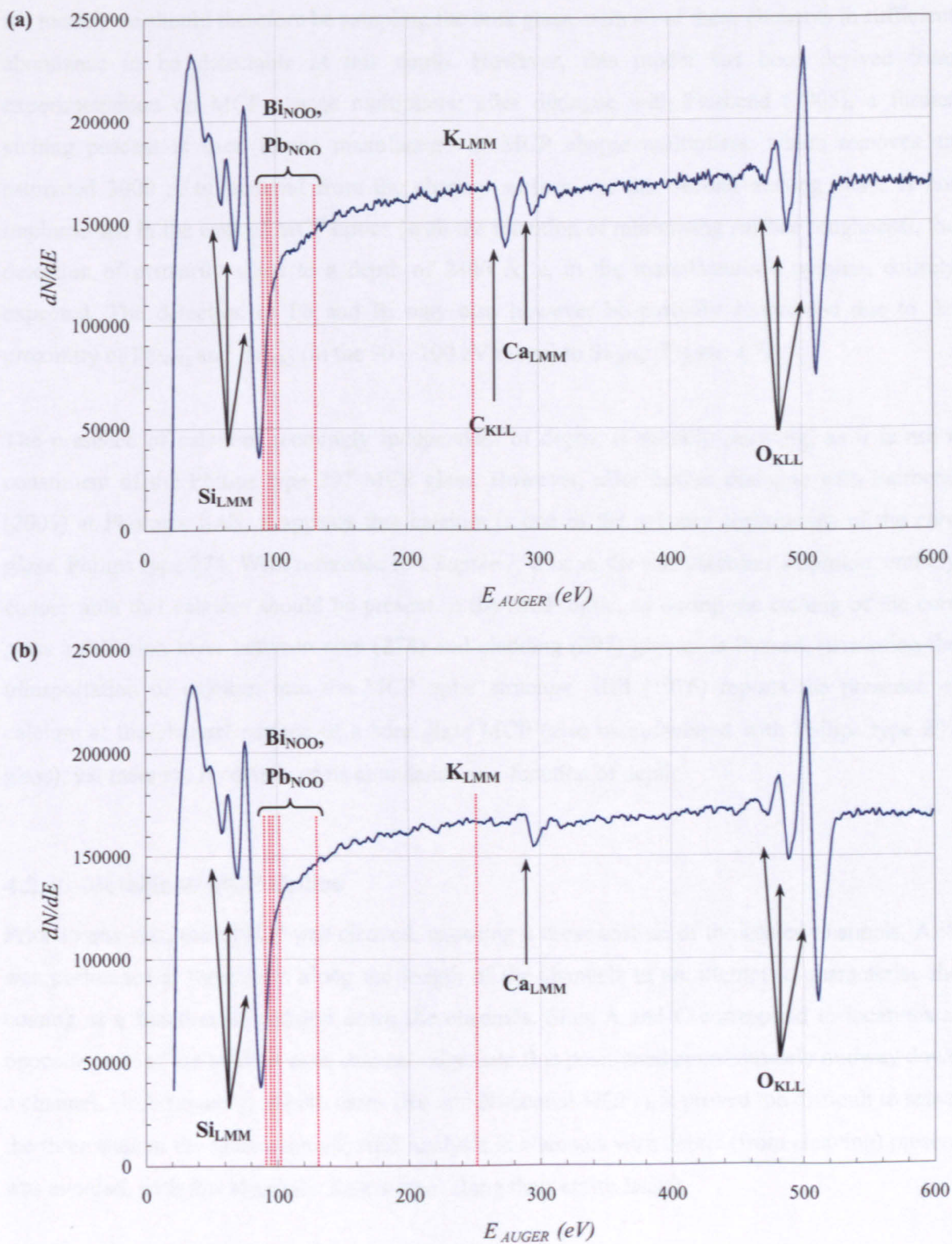


**Figure 4.7.** Auger spectra of bare glass MCP HC001-A4 from a position approximately midway down a channel, at depths of (a) 100 Å and (b) 2400 Å. The only appreciable difference in the spectra appears to be the presence of carbon subsurface contaminants in (a), not seen in (b). The expected  $E_{AUGER}$  positions of  $Pb_{NOO}$ ,  $Bi_{NOO}$  and  $K_{LMM}$  are labelled (Palmberg et al. 1972).



the model, we should therefore be sampling the bulk glass, with all of these elements in sufficient abundance to be detectable at this depth. However, this model has been derived from experimentation on MCP charge multipliers; after dialogue with Fairbend (2005), a further etching process is used in the manufacture of MCP charge multipliers, which removes an estimated 3000 Å of material from the channel surface. As this second etching phase is not implemented in the case of MCP optics (with the intention of minimising surface roughness), the detection of primarily silica to a depth of 2400 Å is, in the manufacturer's opinion, entirely expected. The detection of Pb and Bi may also however be partially suppressed due to the proximity of Pb<sub>N<sub>2</sub>O</sub> and Bi<sub>N<sub>2</sub>O</sub> (in the 90 – 100 eV range) to Si<sub>LMM</sub> (*Figure 4.7*).

The presence of calcium, seemingly independent of depth, is initially puzzling, as it is not a constituent of the Philips type 297 MCP glass. However, after further dialogue with Fairbend (2005) at Photonis SAS, it appears that calcium is one of the primary constituents of the *core glass*, Philips type 274. With reference to *Chapter 1*, it is, in the manufacturer's opinion, entirely conceivable that calcium should be present in the MCP optic, as during the etching of the core glass a diffusion layer between core (274) and cladding (297) glasses is formed, permitting the transportation of calcium into the MCP optic structure. Hill (1976) reports the presence of calcium at the channel surface of a bare glass MCP (also manufactured with Philips type 297 glass), yet there are no details of its abundance as a function of depth.

#### 4.2.4 Metallised MCP Optics

Prior to analysis, each MCP was cleaved, exposing a cross-section of the coated channels. AES was performed at three sites along the length of the channels in an attempt to characterise the coating as a function of position down the channels. Sites A and C correspond to locations at opposite ends of the MCP at each channel edge; site B is positioned approximately midway down a channel. Unfortunately, in both cases (Ru and Ni-coated MCPs), it proved too difficult to select the three sites in the same channel; AES analysis in channels with debris (from cleaving) present was avoided, with few channels 'debris-free' along their entire length.

##### 4.2.4.1 Ruthenium-coated MCP RU-1

Depth profiles at sites A, B and C are shown in *Figure 4.8*. The ALD ruthenium coating was reported to have a nominal thickness of 400 Å (Nenonen, 2004). An image of RU-1, after depth profiling at site B is shown in *Figure 4.9*.



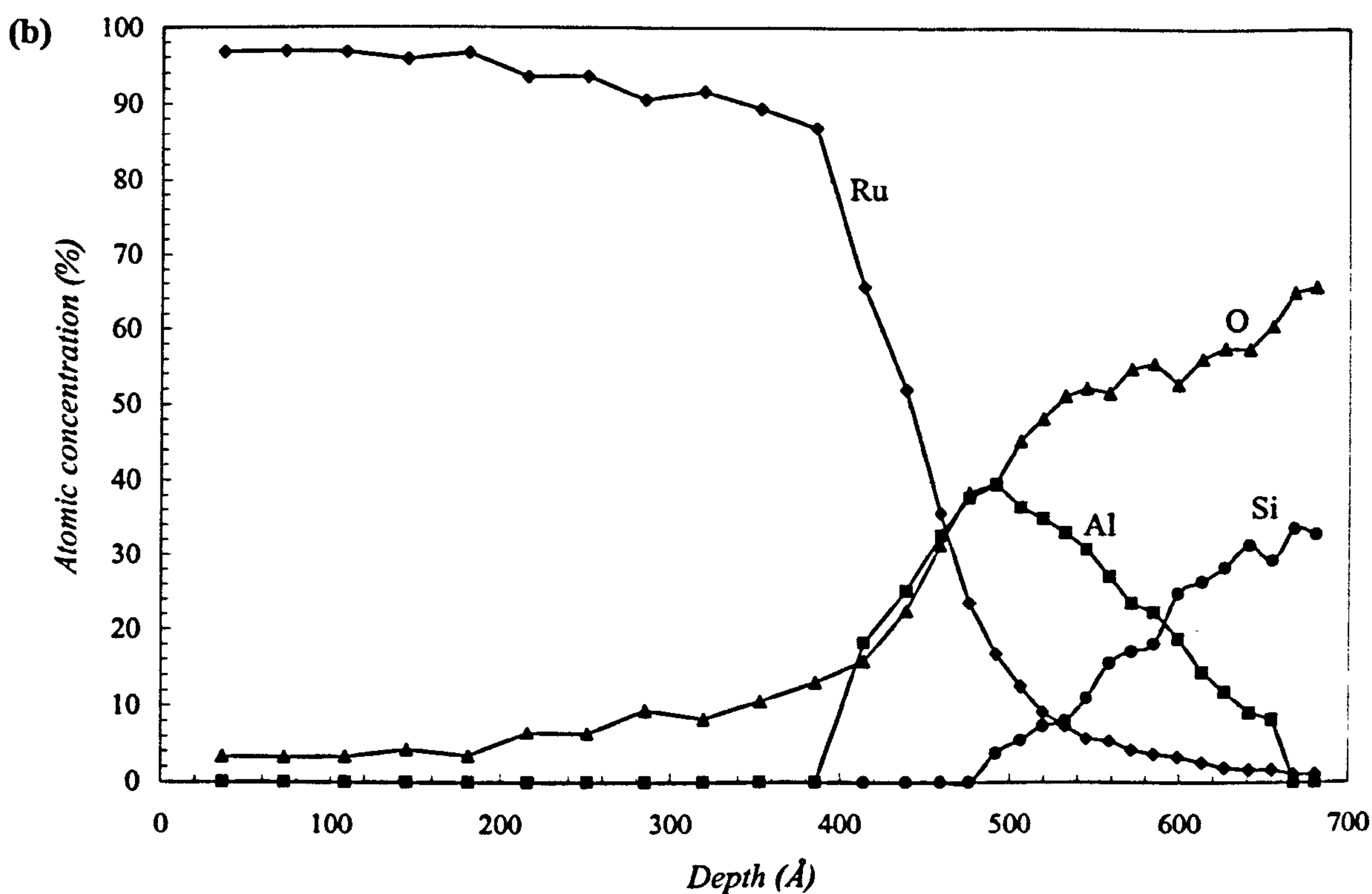
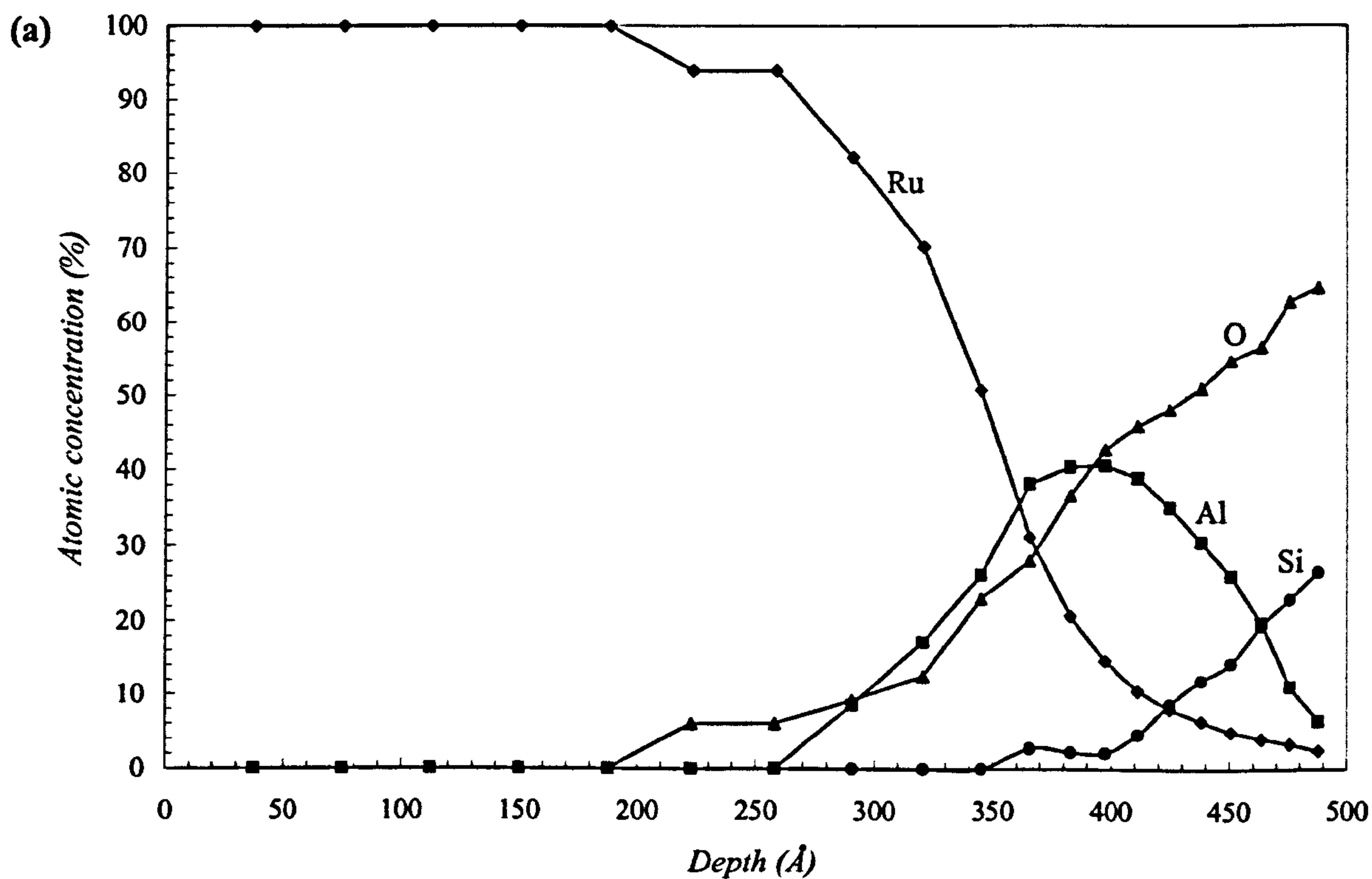


**Figure 4.8 (a,b).** Depth profiles of ruthenium-coated MCP RU-1 at (a) site A, and (b) site B indicating the relative atomic concentrations (by number) of ruthenium (diamonds), aluminium (squares), silicon (circles) and oxygen (triangles).



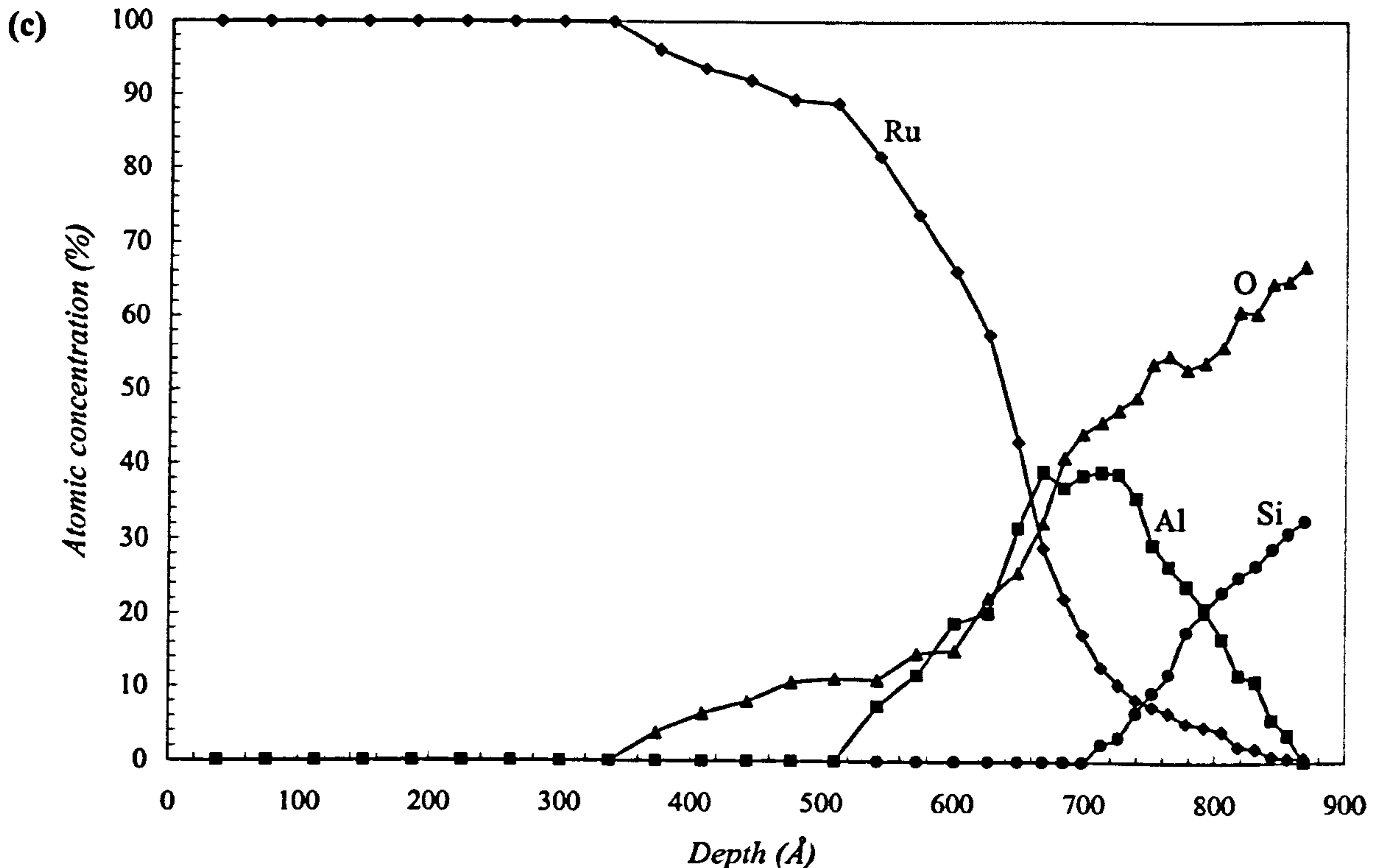


**Figure 4.8 (c).** Depth profiles of ruthenium-coated MCP RU-1 at site C, indicating the relative atomic concentrations (by number) of ruthenium (diamonds), aluminium (squares), silicon (circles) and oxygen (triangles).

Comparisons of ruthenium concentration as a function of depth at each of the three sites reveal a gradual change in the coating thickness from one side of the MCP to the other, along the length of the channels. *Figure 4.8 (a,b,c)* suggests a graded, rather than the more abrupt interface expected between the ruthenium and the observed aluminium oxide seeding layer (*Section 4.1.2*). This may suggest large variations in the surface morphology over the estimated 10 x 10 square micron active Auger area on the MCP. If this is the case, the ‘width’ of the interface (or depth over which the interface is measured to exist) should increase with penetration depth, as further errors in depth are introduced due to sputtering. *Figure 4.10* shows this to be the case, the ruthenium depth profiles at sites A, B and C fitted using a cumulative Gaussian function approximation to the profiles. The cumulative Gaussian function  $f(x, \mu, \sigma)$  takes the familiar form

$$f(x, \mu, \sigma) = \int_{-\infty}^x \frac{1}{\sigma\sqrt{2\pi}} e^{-\left[\frac{(x-\mu)^2}{2\sigma^2}\right]} dx \quad (4.6)$$



The function is modelled in Microsoft Excel, using the pre-defined NORMDIST statistical function. The form of the cumulative Gaussian function with respect to  $x$  (depth in this case) is that of an ogive, which was then inverted, scaled and translated such that the form of the curve resembled the modelled edge functions shown in *Figure 4.10*. The fit was then performed by trial and error, with mean depth  $\mu_d$  and standard deviation  $\sigma_d$  varied as free parameters.

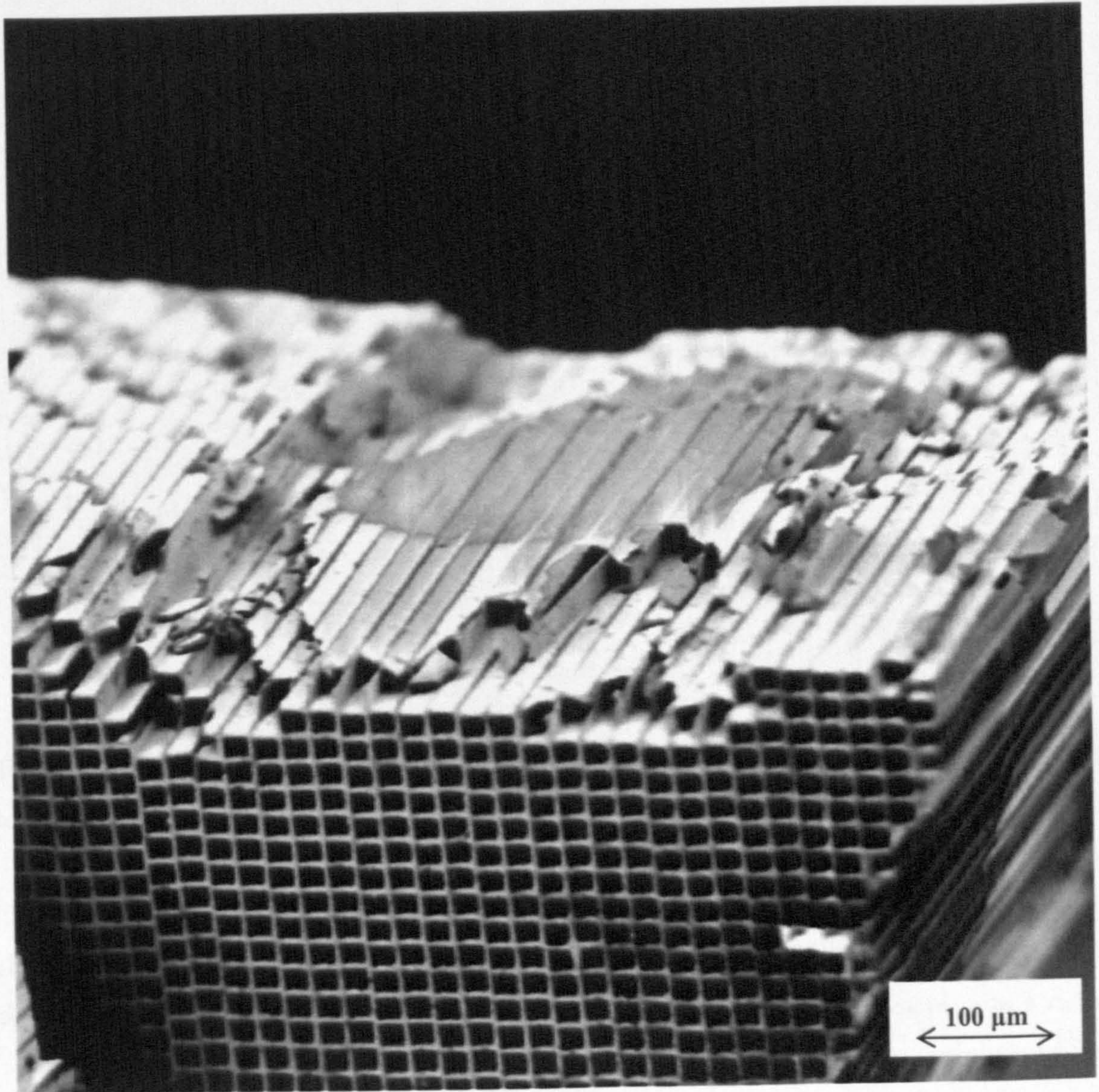


**Figure 4.9.** Image of RU-1 after depth profiling at site B at 90 X magnification. The sputtered, dark area is a crater, approximately 700 Å in depth.

We define the coating thicknesses at sites A, B and C using the modelled  $\mu_d$  values of  $323 \pm 39$  Å,  $422 \pm 60$  Å and  $627 \pm 90$  Å respectively (with a 1 sigma error). The coating process itself may



be responsible for the non-uniform thickness distribution of ruthenium along the channel length. The ALD technique in this case is reliant on the vapour reactants passing through the MCP channels in one direction only. As a result, it is likely that the coating process may occur preferentially on the near side of the optic, with the efficiency of the procedure decreasing with distance along the channel. Unfortunately there is no means of proving this theory with these data as the orientation of the MCP during coating was not documented.

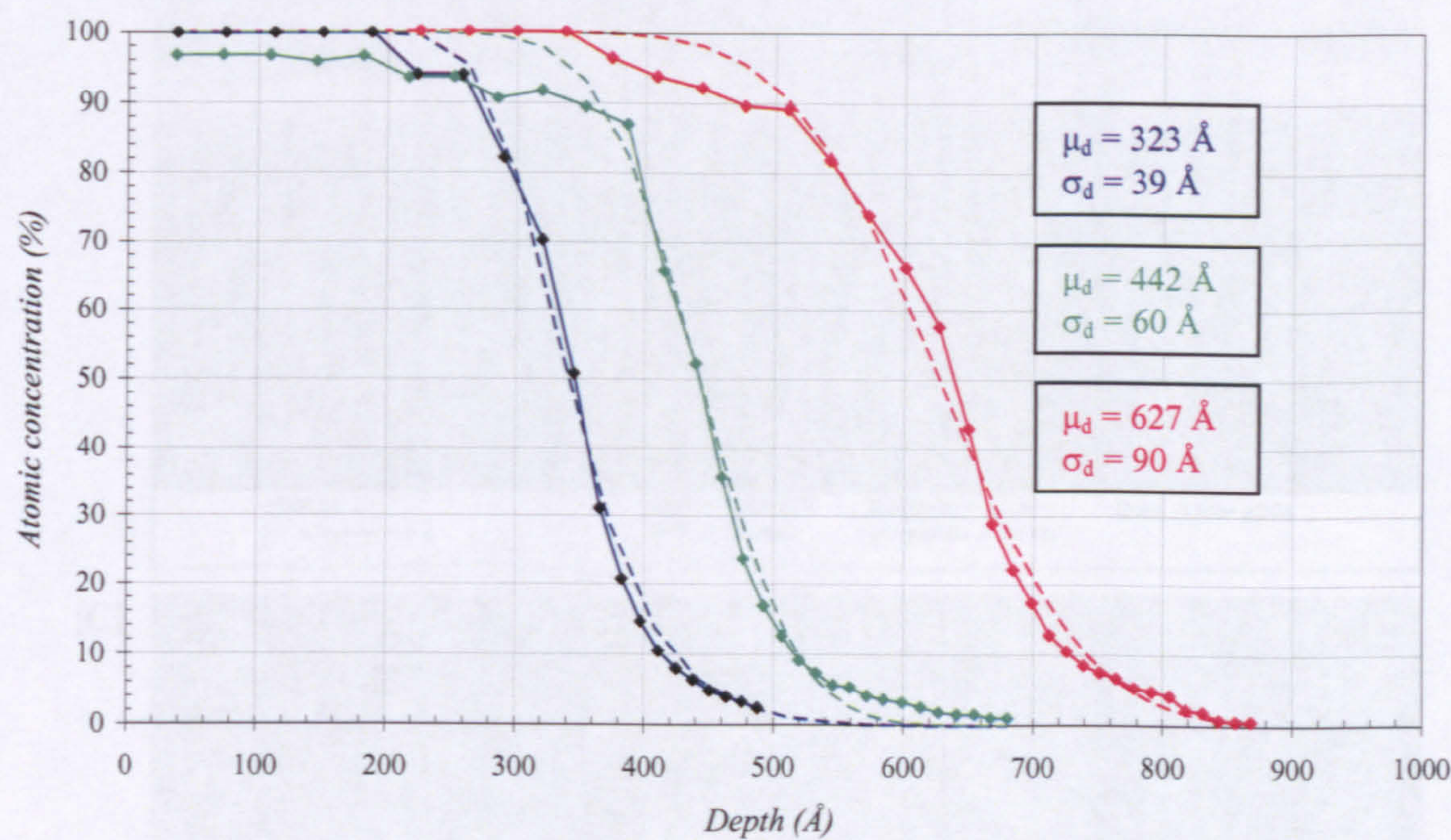


**Figure 4.10.** Depth profiles of ruthenium (solid lines) at sites A (blue), B (green) and C (red), together with fitted the respective fitted edge functions (dashed lines).

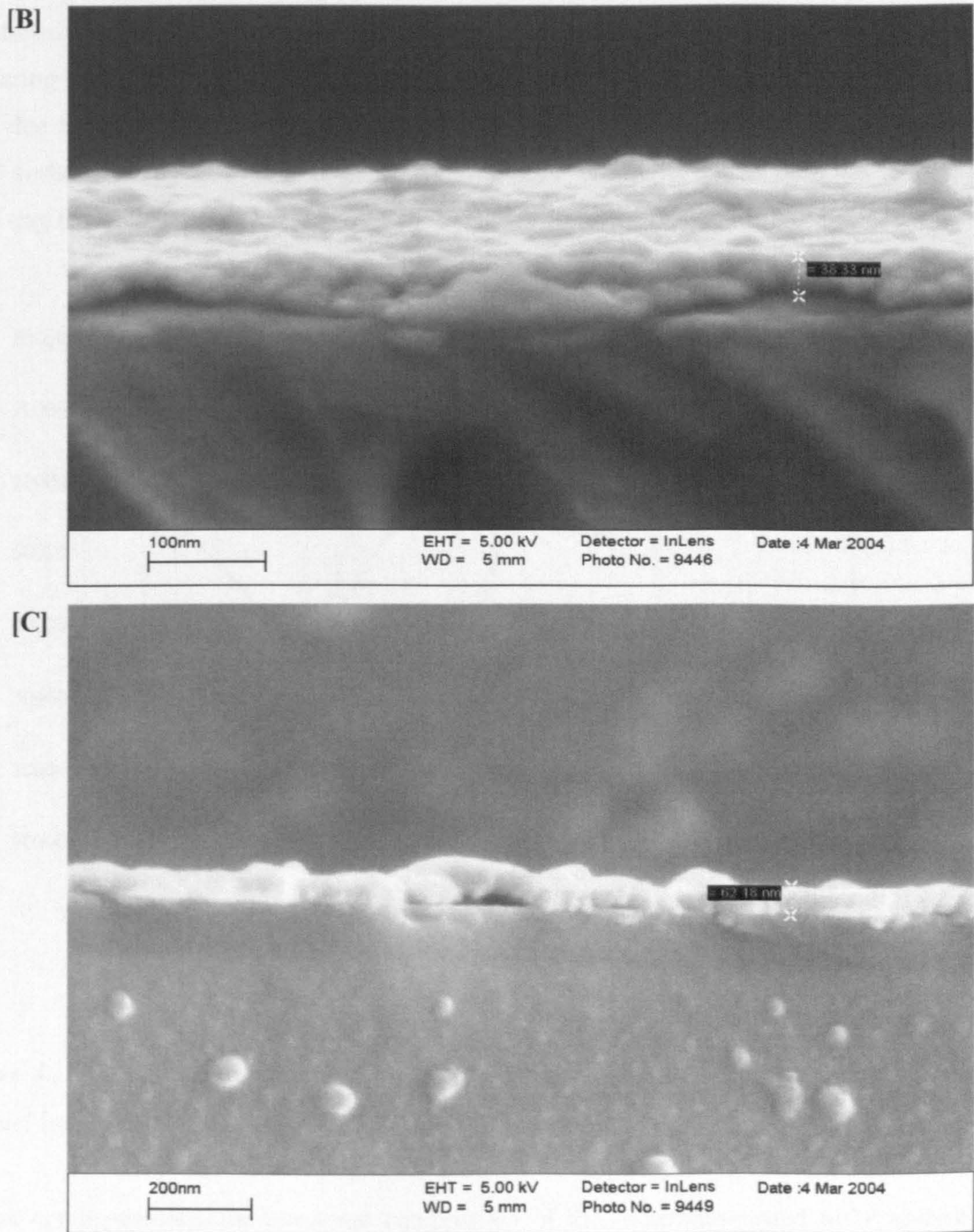
The thicknesses of the Al<sub>2</sub>O<sub>3</sub> seeding layer are estimated using the FWHM of the depth profiles (Figure 4.8); FWHM thicknesses of 135 Å, 175 Å and 185 Å at sites A, B and C respectively further lend weight to the argument, indicating that the measurements are taking place at a variety of depths simultaneously, possibly due to large variations in the RMS surface roughness of the sample. According to Nenonen (2005), the nominal thickness of the Al<sub>2</sub>O<sub>3</sub> layer was not documented during the ALD process, yet he anticipates our measured thicknesses of ~ 135 – 185 Å to be accurate.

Figure 4.11: SEM images of the MCP surface at sites A, B and C.

Images with an LEO 1530 VP Scanning Electron Microscope (SEM) were subsequently taken (by D.D. Hall at the University of Loughborough) in the positions corresponding to channel sites



B and C on the MCP (although in different channels to where the AES was performed in order to observe a surface region of the coating prior to sputtering), shown in *Figure 4.11*.



**Figure 4.11.** SEM images at sites B and C of the cleaved, ruthenium-coated MCP. The thickness of the ruthenium coating is estimated at 383 Å and 622 Å at sites B and C respectively.



The estimated coating thicknesses of 383 Å and 622 Å (*Figure 4.11*) are within error of our estimates of the ruthenium coating thickness at the same positions. Further inspection of *Figure 4.11(B)* shows the ruthenium coating has developed with island formation, characteristic of the ALD process (*Section 4.1.2*). The thickness of the ruthenium coating is shown to vary significantly on length scales of around 100 Å in *Figure 4.11*, further suggesting that at a nominal sputtering depth, a variety of actual depths may be sampled (over a range of order 100 Å) during AES due to the original surface morphology. Although not measured directly at this stage, the RMS surface roughness would appear to be varying on scales far greater than the 10 Å desired for X-ray focusing for Lobster-ISS.

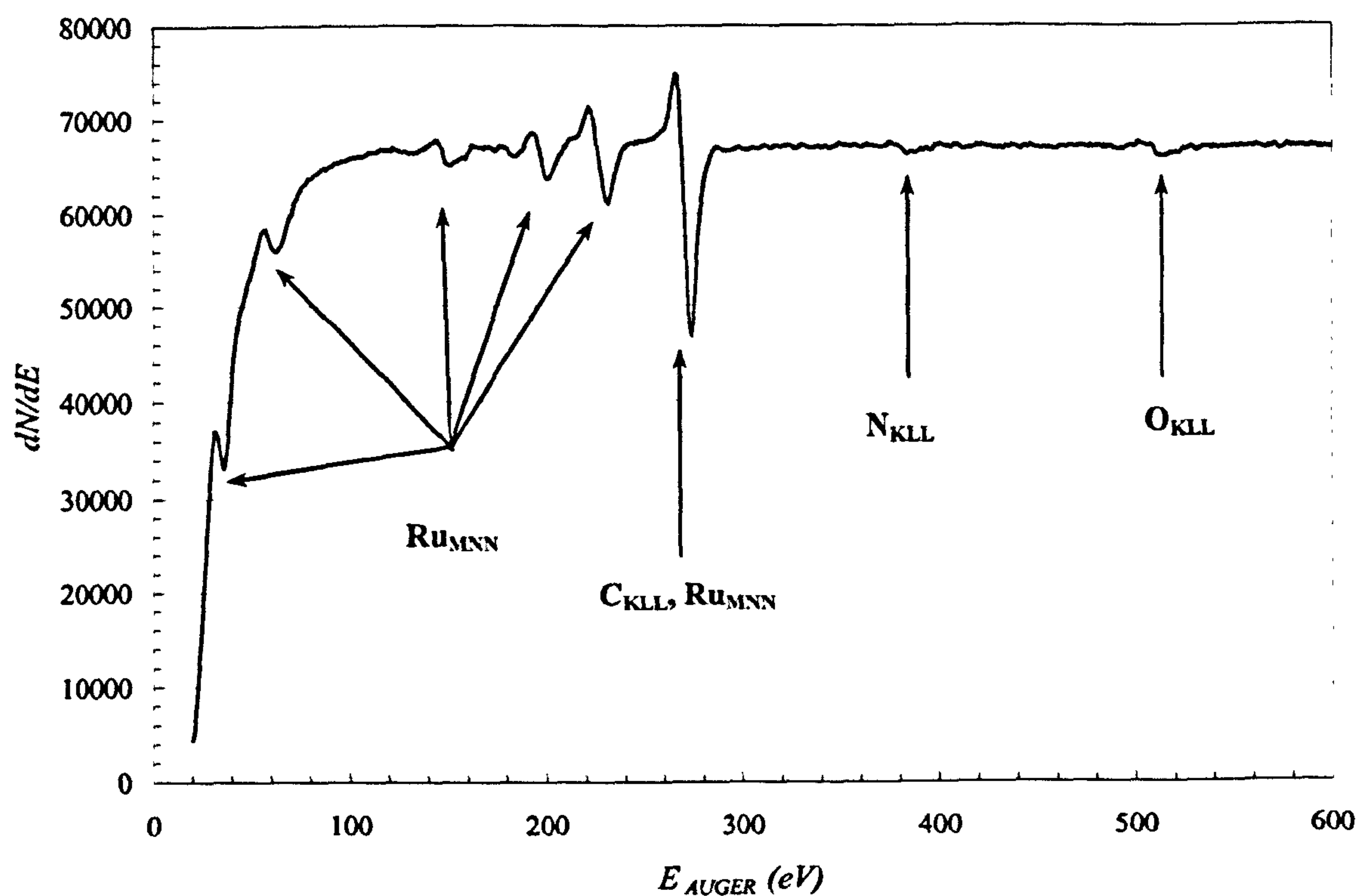


**Figure 4.12.** Auger spectrum of the surface of ruthenium-coated MCP RU-1, midway along the channel length (site B). Elements identified using Palmberg et al. (1972).

Before depth profiling, the elemental composition of the ruthenium-coated MCP surface was determined using AES at sites A, B and C to identify any surface contaminants. *Figures 4.12 and 4.13* inform of the presence of carbon (as seen with HC001-A4), nitrogen and oxygen (likely to be due to atmospheric adsorption). Carbon is the most abundant surface contaminant, its relative concentration on the ruthenium surface decreasing toward the centre of the channel. This may be



due to the relative inaccessibility of the centre of MCP channels for atmospheric contaminants in comparison to that at the channel ends.

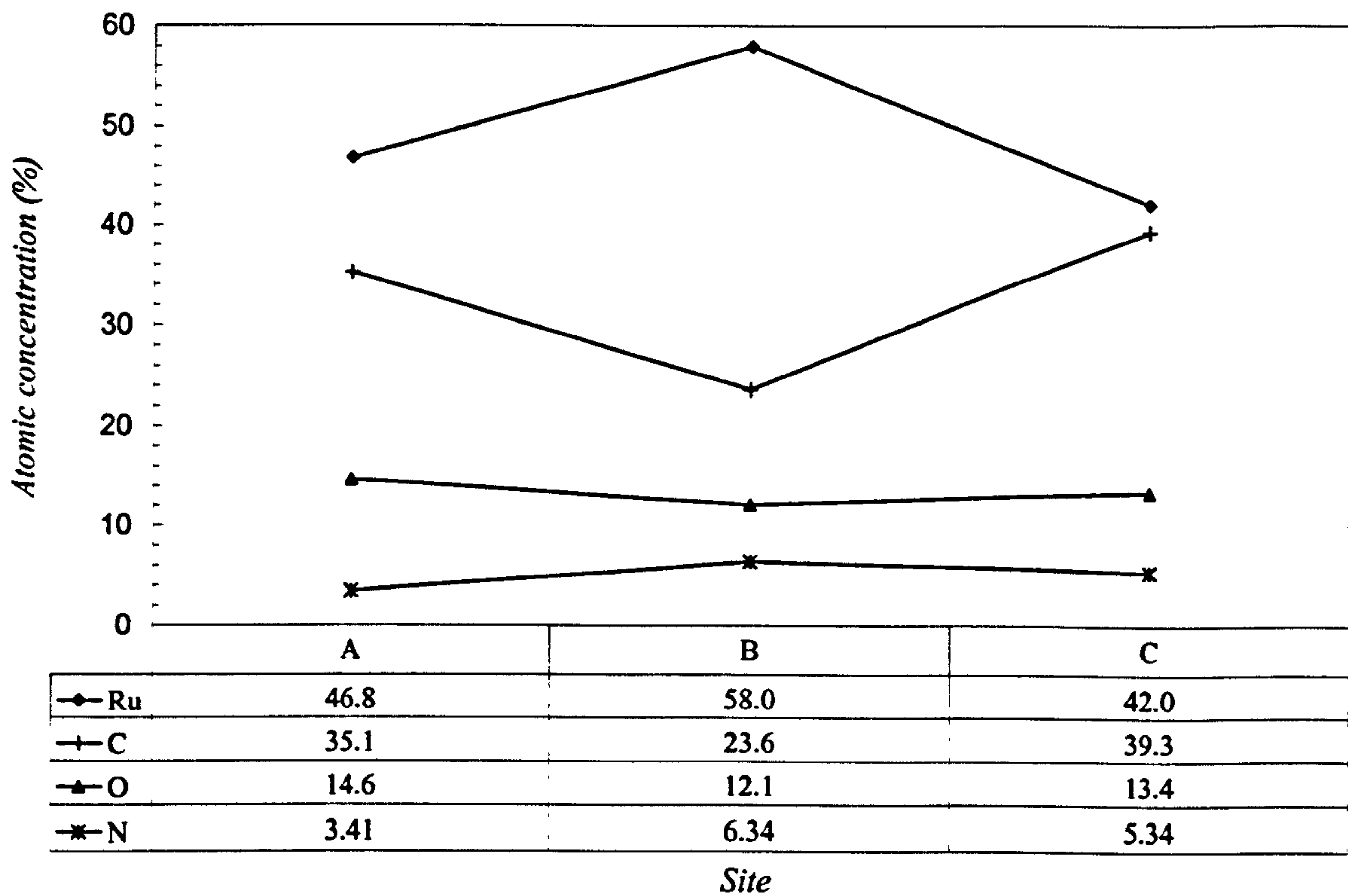


**Figure 4.13.** Surface atomic concentration (by number) of ruthenium, carbon, oxygen and nitrogen as a function of position along the channel. The relative concentration of carbon falls markedly midway down the channel (site B).

#### 4.2.4.2 Nickel-coated MCPs

The nominal nickel coating depths of the two samples available for analysis, hereafter referred to as NI-1 and NI-3, were identified by Photonis SAS to be 150 Å and 100 Å respectively. Unfortunately, little depth profiling data exists due to computer hardware problems at the University of Loughborough. Data recovered enables us to extract one near-surface depth profile of MCP NI-1, located at site C and shown in *Figure 4.14*. We keep to the convention that sites A and C will represent opposite ends of the MCP channels, with site B located midway down the channels.

At the surface, the composition of the nickel coating is similar to that of ruthenium, in that it accounts for around half of the coating material (by atomic number). However, in the case of



RU-1, very little other than pure ruthenium is detected from depths of 40-100 Å (this is certainly the case at the ends of the channel in *Figure 4.8(a,c)* which provide the best comparison [in terms of site] with the profile in *Figure 4.14*. At the surface, the other major constituent of the nickel coating is oxygen, an oxide layer perhaps forming on the surface due to the MCP being subject to atmospheric conditions during sample preparation; this would account for the approximately constant atomic concentration of oxygen in the first 10 Å (at around the 40% level).

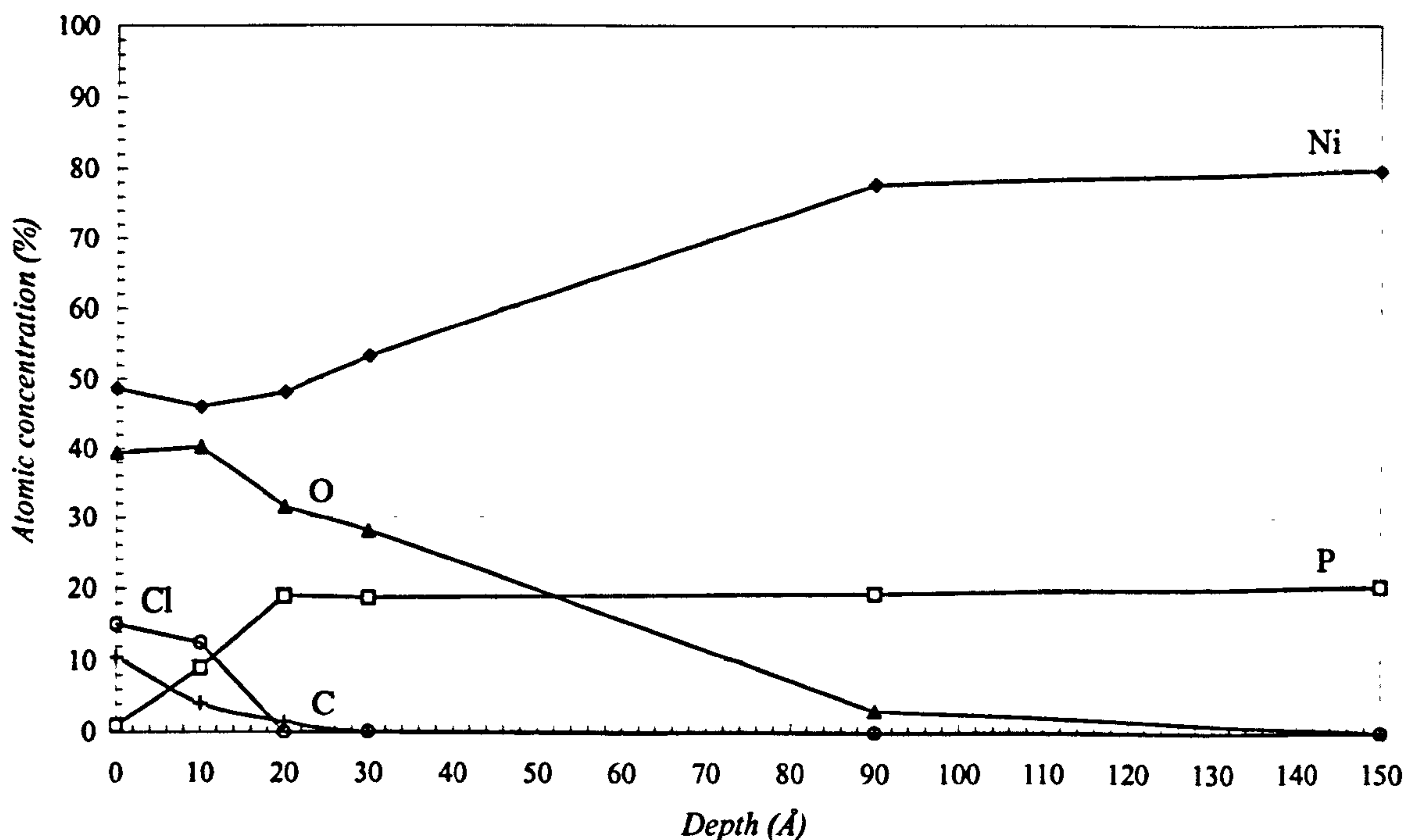


**Figure 4.14.** Surface depth profiles of nickel-coated MCP NI-1 at site C, indicating the relative atomic concentrations (by number) of nickel (diamonds), phosphorus (squares), carbon (crosses), chlorine (circles) and oxygen (triangles). In the case of chlorine, atomic concentrations are increased by a factor of 25 in order to better view the profile on this scale.

It is also conceivable that the EN coating process itself, which produces oxygen compounds in the form of orthophosphites ( $\text{HPO}_3^{2-}$ ), water ( $\text{H}_2\text{O}$ ) and negatively charged hydroxide ions ( $\text{OH}^-$ ), may be responsible for the distribution of oxygen *within* the coating. The relative atomic concentration of oxygen then falls with depth, with little evidence of it at a depth of 150 Å, at which point the coating comprises around 80% Ni, 20% P by atomic number. Using the atomic weights of P (30.97) and Ni (58.70) we find that this level of phosphorus approximately



corresponds to  $\left(\frac{30.97}{58.70}\right)20\% \approx 10.6\%$  by weight, impressively close to the 10% P by weight desired by Photonis SAS to minimise surface roughness (*Section 4.1.1*). This ratio however is significantly larger, almost doubling to 19.8% nearer the surface (a depth of 20 Å). Only trace amounts of phosphorus are found on the coating surface, yet this is expected to have little effect on the surface roughness, crevices and island structure having long taken form before this during the evolution of the coating. Surface contaminants in the form of chlorine and carbon are detected, yet disappear at depths of around 20 Å and 30 Å respectively. The origin of the chlorine (found to be present at the surfaces of both NI-1 and NI-3) is likely to be explained by the use of the stannous chloride and palladium chloride during the EN seeding process, the chlorine appearing to have migrated to the surface from the nickel / glass interface. An Auger spectrum taken from the surface of the opposite end of the channel, site A, is shown in *Figure 4.15*. The spectrum appears to characterise a coating indicative of that described in *Figure 4.14* (at site C), with chlorine, carbon, nickel, oxygen and phosphorus all present.

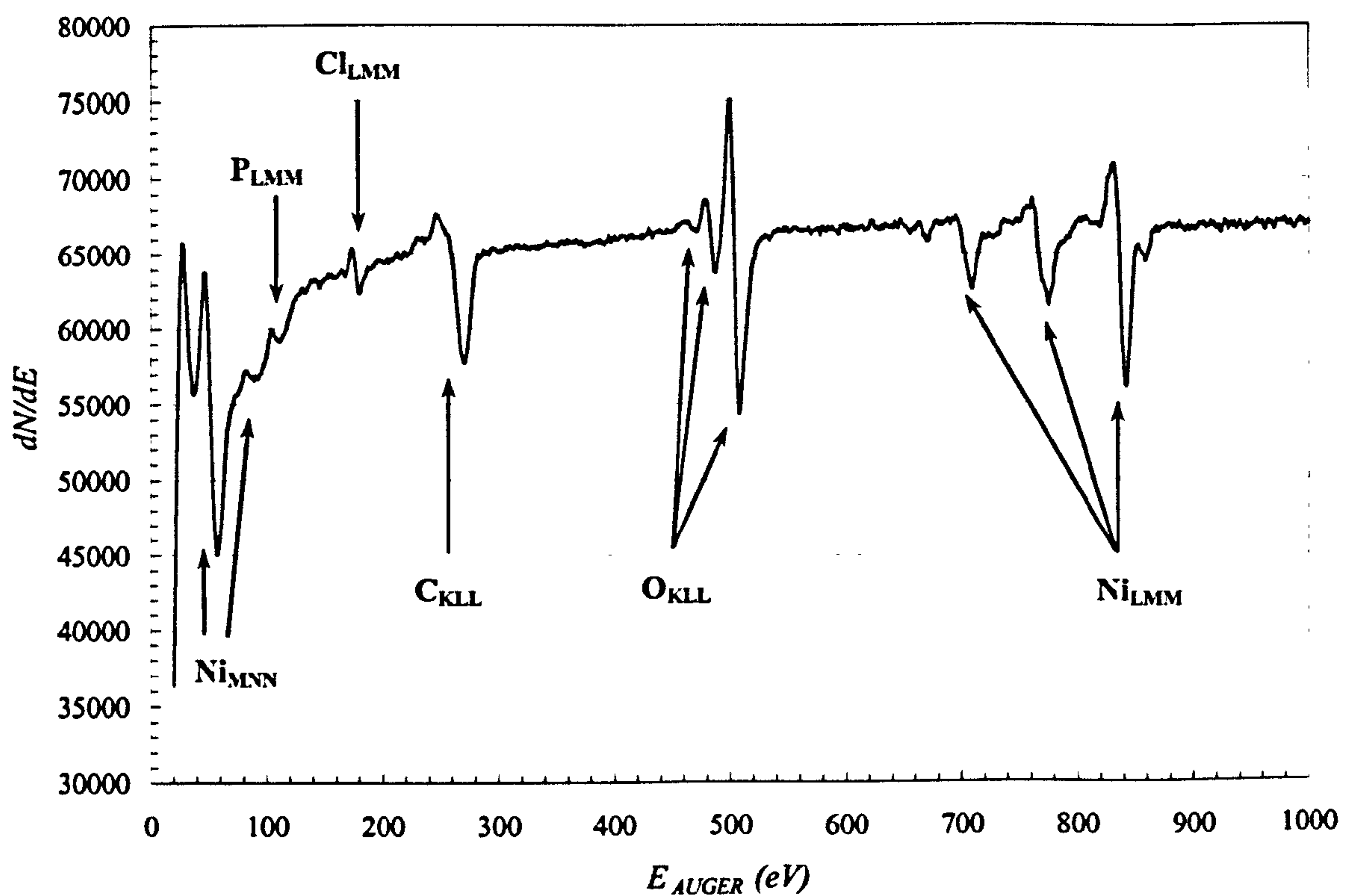


**Figure 4.15.** Auger spectrum of the surface of nickel-coated MCP NI-1 at site A. Elements identified using Palmberg et al. (1972).



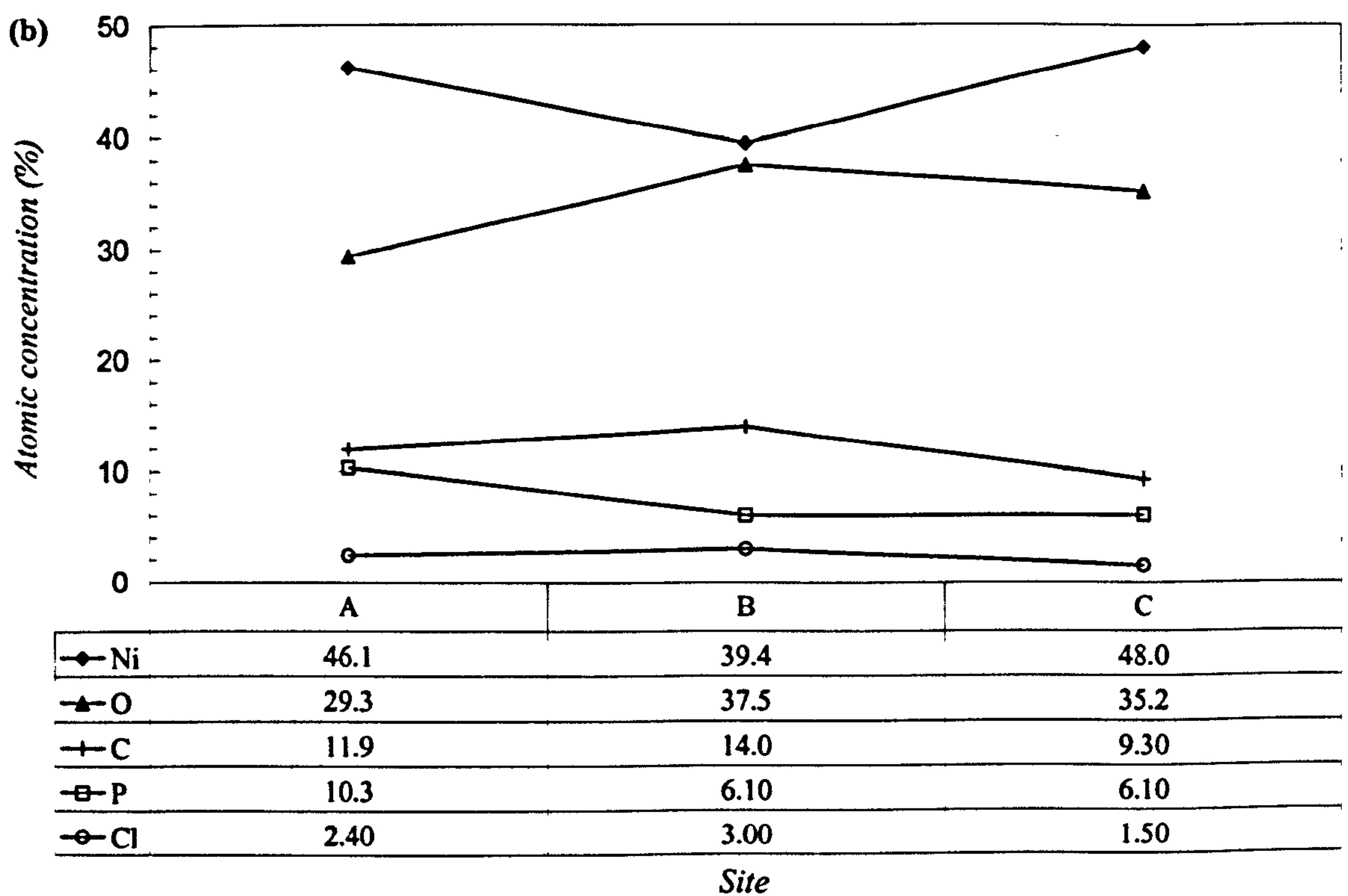
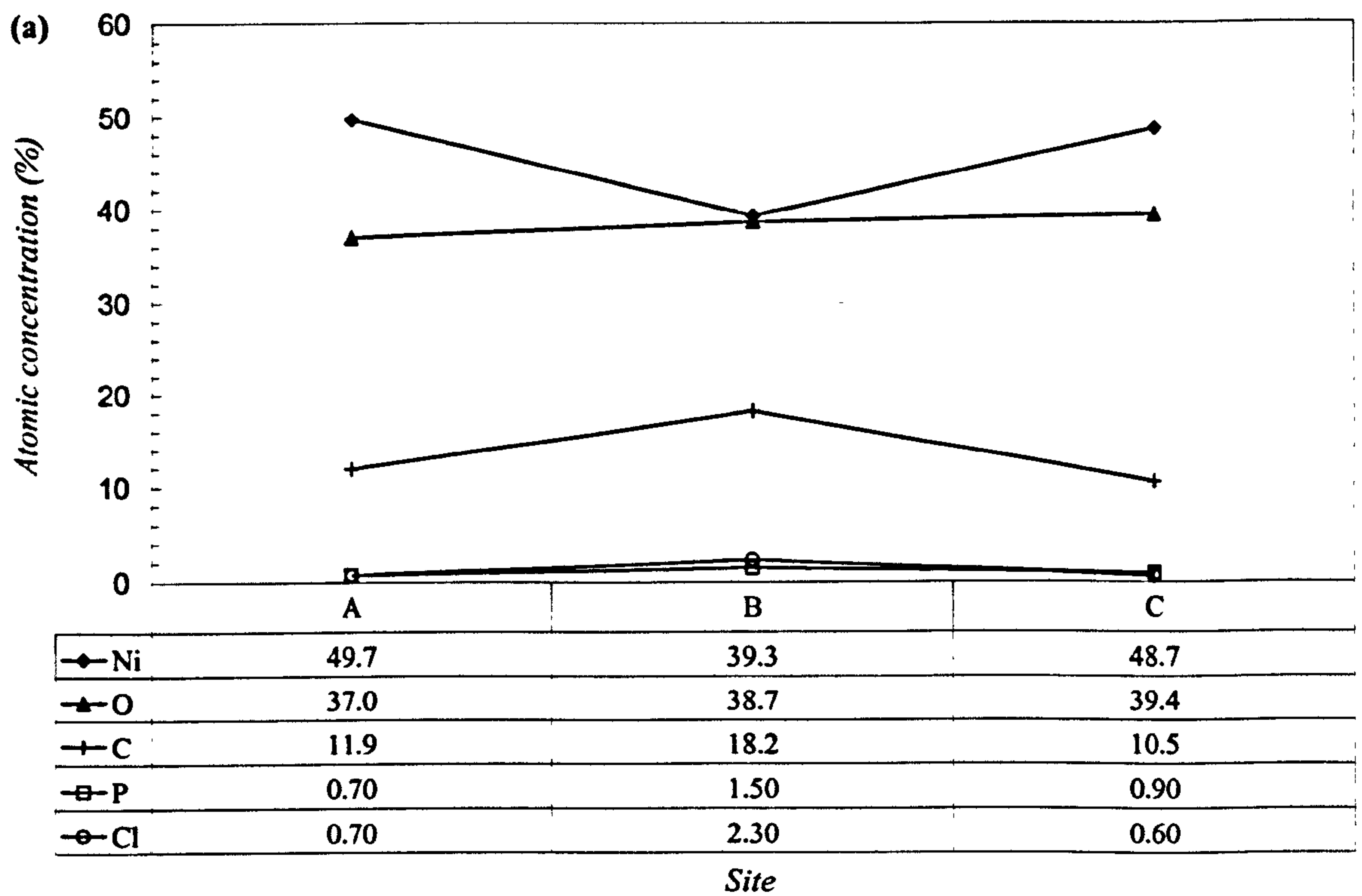


**Figure 4.16.** Surface atomic concentration (by number) of nickel, oxygen, carbon, phosphorus and chlorine as a function of position along the channel for (a) NI-1 and (b) NI-3. The relative atomic nickel concentration falls toward the midpoint of the channel in both MCPs.



Surface data exist for both NI-1 and NI-3, with the relative atomic concentrations (by number) of each element presented at sites A, B and C in *Figure 4.16*. Whereas the amount of surface nickel as a function of distance along the channel is estimated to be approximately uniform, it appears that, from both “edge” sites, A and C, the concentration of nickel falls towards the centre of the channel, at site B. This could be due to one of two reasons; firstly, because the level of surface carbon contamination increases towards the centre of the channel (which is not intuitive given the relative inaccessibility of site B), or secondly, because the capacity of the EN process to deposit a pure Ni-P film is reduced in a position midway down a channel. The increase in the atomic concentration of the majority of surface contaminants toward site B (C, Cl [NI-1] and C, Cl, O [NI-3]) appears to lend further weight to the argument in *both* nickel-coated MCPs.

### 4.3 Conclusions

In this chapter, the reflecting surfaces of one bare glass, one ruthenium-coated and two nickel-coated MCP optics were investigated using the AES technique.

#### 4.3.1 Bare Glass MCP [HC001-A4]

Silicon and oxygen appear to be the principal constituents of the MCP optic glass at measured depths of 100 Å and 2400 Å, with Pb, Bi and K not detected at either depth. Due to charging problems, it was not possible to confirm the presence nor absence of Na. MCP manufacturers Photonis SAS support the findings, anticipating a silica-rich layer surface layer ~ 3000 Å thick.

Calcium is detected at both measured depths of 100 Å and 2400 Å, its origin believed to have been the core glass; Ca is believed to have diffused into the MCP optic cladding glass during the etching phase of manufacture.

Carbon is detected at a depth of 100 Å and is adjudged to be a surface contaminant, the source of which is likely to be due to backstreaming hydrocarbons from a rotary pump used in reflectivity analysis (*Chapter 5*) and / or the exposure of the MCP to organics present in the atmosphere. Carbon is detected with each MCP optic tested, coated or uncoated.



### 4.3.2 Ruthenium-coated MCP [RU-1]

The thickness distribution of the ruthenium coating along the length of the MCP channel appears to change gradually, from  $627 \pm 90 \text{ \AA}$  at one end to  $323 \pm 39 \text{ \AA}$  at the other. This is thought to be due to the unidirectional vapour reactant flow in the ALD process.

The  $\text{Al}_2\text{O}_3$  seeding layer, used to start the ALD coating process was observed, with measured thicknesses of  $135 - 185 \text{ \AA}$  corresponding to the nominal thickness. SEM images and the non-abrupt nature of the coating interfaces ( $\text{Ru}/\text{Al}_2\text{O}_3$  and  $\text{Al}_2\text{O}_3/\text{SiO}_2$ ) suggest a surface roughness well in excess of the  $\sim 10 \text{ \AA}$  desired for MCP focusing.

Carbon, nitrogen and oxygen are evident on the surface of the ruthenium coating, with carbon contamination decreasing toward the midpoint of the channel, believed to be due to the relative inaccessibility of this area compared to the edges.

### 4.3.3 Nickel-coated MCPs [NI-1, NI-3]

One near surface depth profile of NI-1 taken at the edge of a channel suggests a Ni-P alloy thickness of at least  $150 \text{ \AA}$  (compared to the nominal thickness of  $150 \text{ \AA}$ ). Due to unforeseen circumstances, further data were lost, so the exact coating thickness cannot be determined.

Oxygen appears to constitute a large proportion of the coating nearer to the surface (40 % by atomic number), the concentration gradually falling with depth. It appears in negligible quantities at a depth of  $150 \text{ \AA}$ . At a depth of  $150 \text{ \AA}$ , phosphorus comprises 10.6 % (by weight) of the Ni-P alloy, compared to the Photonis SAS target of 10 %. This suggests the process is more effective when in its infancy, levels of phosphorus climbing closer to the surface. Very little phosphorus is observed on the Ni-P coating surface.

Surface contaminants of chlorine and carbon are detected, although neither is detected at depths greater than  $20 \text{ \AA}$  and  $30 \text{ \AA}$  respectively. The origin of the chlorine is thought to be due to the pre-treatment phases of the EN process; stannous chloride and palladium chloride are used to prepare the substrate before coating.

Surface studies suggest that the concentration of nickel falls towards the midpoint of a channel, due to the relative inaccessibility of this region (compared to the channel edges).



## Chapter 5 The Soft X-ray Reflectivity of MCP Optics

### 5.1 Introduction

The metallisation of the reflecting surfaces of MCP optics will theoretically improve their X-ray reflection efficiency at higher grazing angles by increasing the critical angle for total external reflection. Results were first reported by Peele et al. (1998); the motivation of that research, as here, was to improve the wide angle response and thus sensitivity of the Lobster-ISS ASM. *Figure 5.1* from Peele et al. (1998) indicates an increase in high grazing angle reflectivity at 2.0 keV for a nickel-coated plate compared to that of bare glass.

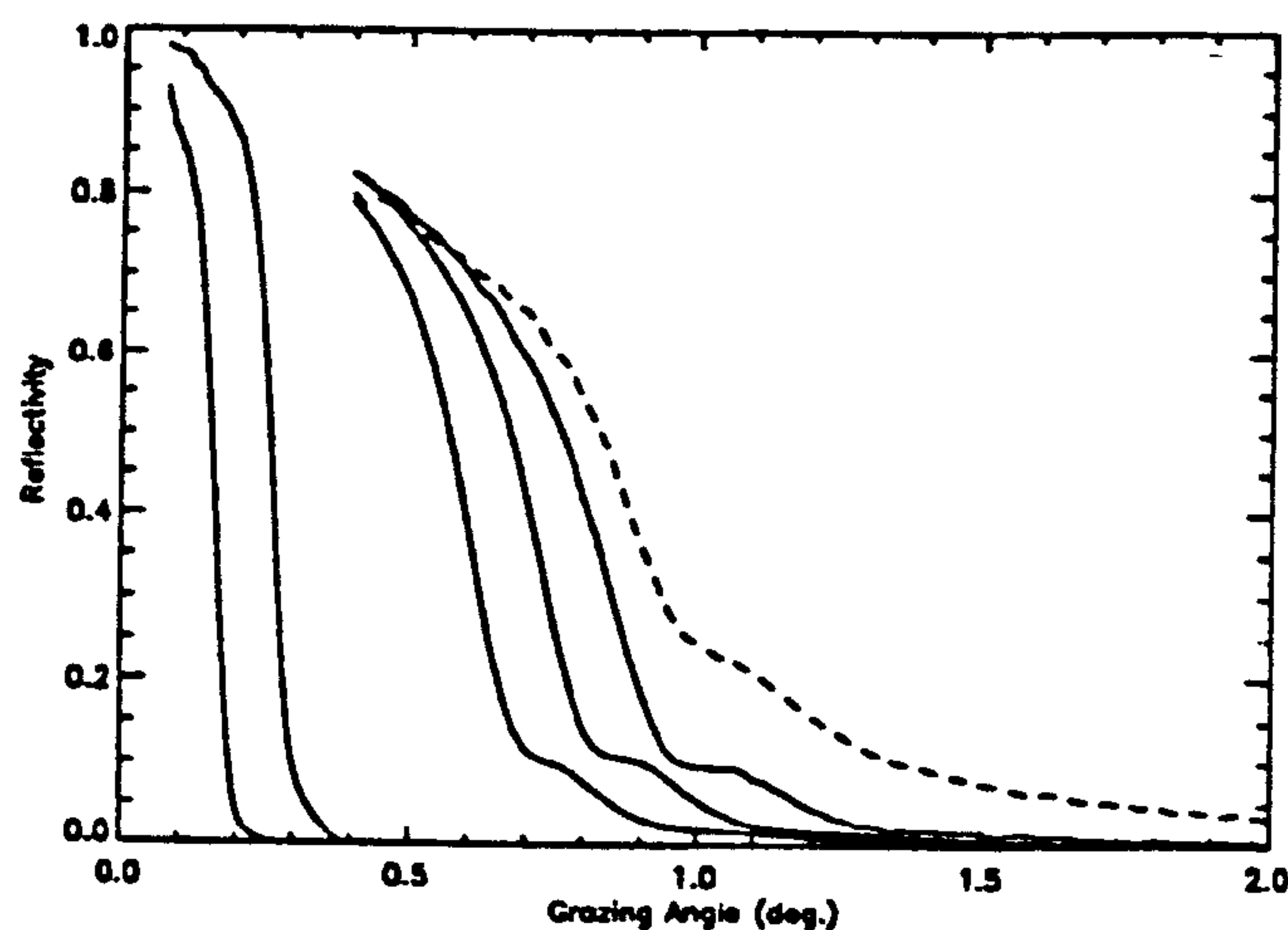


*Figure 5.1. Measured X-ray reflectivity as a function of grazing angle for a bare glass MCP at (from left to right) 12, 8, 2.8, 2.3 and 2.0 keV. The dashed line profiles a nickel-coated MCP and indicates the enhancement in reflectivity at grazing angles  $\theta > 0.6^\circ$  at 2.0 keV. From Peele et al. (1998).*

Martin (2000) reports a shortfall in reflectivity at lower grazing angles for the nickel-coated MCP in *Figure 5.1*. However, this shortfall is outweighed by the increase in reflectivity at higher grazing angles; an overall enhancement in reflectivity is observed, a conclusion derived by comparing the areas under each of the two (bare glass and nickel-coated) measured curves at 2.0 keV. This is the first evidence for the successful deposition of a nickel coating on MCP optics.

This chapter will examine the soft X-ray reflectivity of bare glass and metallised MCPs with experimental work carried out at the Daresbury SRS. The work should be viewed in conjunction



with the AES results of *Chapter 4*, which, in this chapter, are used to parametrise surface models of bare glass channel walls. The reflection properties of MCP optics coated with three different metals are investigated; nickel (deposited using the Electroless Nickel [EN] process), ruthenium and iridium (using Atomic Layer Deposition [ALD]).

## 5.2 X-ray Reflectivity Theory

The X-ray reflectivity of an MCP optic may be calculated using the atomic scattering factors  $f_1$  and  $f_2$ . Tabulated values of  $f_1$  and  $f_2$  as functions of energy are given by Henke et al. (1993). The atomic scattering factors used here are calculated using a database of atomic photoelectric cross-sections  $\sigma_p$  as a function of photon energy  $E$  (Cromer and Liberman, 1970) where

$$f_1(E) = Z^* + \frac{1}{\pi r_0 h c} \int_0^\infty \frac{\varepsilon^2 \sigma_p(\varepsilon)}{E^2 - \varepsilon^2} d\varepsilon \quad (5.1)$$

$$f_2(E) = \frac{E \sigma_p(E)}{2 r_0 h c} \quad (5.2)$$

where  $r_0$  is the classical electron radius ( $r_0 = 2.818 \times 10^{-5}$  Å),  $h$  is Planck's constant,  $c$  is the velocity of light in vacuo and  $\varepsilon$  denotes the X-ray energy for integration purposes.  $Z^*$  is a relativistic correction to the atomic number  $Z$ , with  $Z^*$  and  $Z$  only significantly different for the heavier elements. Henke et al. (1993) have deduced empirically that

$$Z^* = Z - \left( \frac{Z}{82.5} \right)^{2.37} \quad (5.3)$$

The complex dielectric constant  $K$  of the reflecting material is described in terms of two dielectric coefficients,  $\alpha$  and  $\gamma$ , which are small compared with unity in the soft X-ray region of interest (0.1–5 keV), such that

$$K = 1 - \alpha - i\gamma \quad \text{where} \quad \alpha = \frac{r_0 \lambda^2}{\pi} \sum_j n_j f_{1,j} \quad \text{and} \quad \gamma = \frac{r_0 \lambda^2}{\pi} \sum_j n_j f_{2,j} \quad (5.4 \text{ a,b,c})$$



where  $\lambda$  is the X-ray wavelength and  $n_j$  is the atomic number density of an element  $j$  in the reflecting material. In the case of *Equation 5.4(b,c)* we sum over all  $j$  to find the total contributions to  $\alpha$  and  $\gamma$  from each element. The reflectivity as a function of grazing angle  $\theta$  is derived using the Fresnel equations, for polarisation states  $\sigma$  and  $\pi$  (corresponding the electric field vector  $\underline{E}$  being parallel and perpendicular to the plane of reflection respectively). Henke (1981) states

$$R_{\sigma}(\theta) = \frac{4a^2(\sin\theta - a)^2 + \gamma^2}{4a^2(\sin\theta + a)^2 + \gamma^2} \quad (5.5)$$

and

$$\frac{R_{\pi}(\theta)}{R_{\sigma}(\theta)} = \frac{4a^2(a - \cos\theta \cot\theta)^2 + \gamma^2}{4a^2(a + \cos\theta \cot\theta)^2 + \gamma^2} \quad (5.6)$$

where

$$a^2 = \frac{1}{2} \left[ \sin^2\theta - \alpha + \sqrt{(\sin^2\theta - \alpha)^2 + \gamma^2} \right] \quad (5.7)$$

Finally, the reflectivity  $R(\theta)$  for an unpolarised incident X-ray beam is given by

$$R(\theta) = \frac{R_{\sigma}(\theta)}{2} \left( 1 + \frac{R_{\pi}(\theta)}{R_{\sigma}(\theta)} \right) \quad (5.8)$$

The critical angle for total external reflection  $\theta_c$  is defined as the square root of the dielectric coefficient  $\alpha$ ; It may be inferred from *Equations 5.140 and 5.141* in Michette and Buckley (1993) that  $\theta_c$  can be expressed as a function of the mass density of the reflecting material  $\rho$  and the wavelength of the incident radiation  $\lambda$ , where

$$\theta_c^2 = \frac{r_e \lambda^2}{\pi} \frac{\rho N_A}{A} f_1(\lambda) \quad (5.9)$$



where  $A$  is the atomic number of the element making up the reflecting surface and  $N_A$  is Avogadro's constant. The reflection efficiency, or reflectivity, of a perfectly smooth X-ray mirror at a given wavelength may be maximised by selecting a mirror material with as large a critical angle as possible; since  $\theta_c \propto \sqrt{\rho}$  it is desirable to select as dense a material as possible. The mass density of the Philips type 297 glass used to fabricate MCP optics is nominally  $3.3 \text{ g cm}^{-3}$ ; by applying a metal coating to the reflecting surfaces of the bare glass MCP, we can raise the critical angle of the surface and thus its reflectivity at higher grazing angles. The three metal coatings investigated in this chapter are nickel ( $\rho = 8.90 \text{ g cm}^{-3}$  for the bulk metal), ruthenium ( $\rho = 12.2 \text{ g cm}^{-3}$ ) and iridium ( $\rho = 22.5 \text{ g cm}^{-3}$ ).

### 5.3 Reflectivity Measurements at Daresbury SRS

All reflectivity data presented in this chapter were obtained on Beamline 3.4 at Daresbury SRS in three 'runs', in December 2001, December 2002 and November 2004. All of the MCPs were manufactured to the same specification, tabulated in *Chapter 1 (Table 1.1)*.

#### 5.3.1 Experimental Configuration

Beamline 3.4 uses a double crystal scanning monochromator based on InSb(111) crystals coupled with a  $500 \text{ \AA}$  chromium-coated plane pre-mirror to provide adequate high energy cut-off, resulting in a practical energy range of 1750 - 3500 eV. A toroidal mirror provides horizontal and vertical beam focusing. A pair of translational horizontal and vertical slits of widths 1 mm and 0.25 mm respectively, positioned between monochromator and experimental chamber were used to isolate the top of the cross-sectional beam, shaped like a frown. The MCP was mounted in a goniometric cradle, the upper of a two-axis rotation stage in the centre of the experimental chamber, which was evacuated to an operational pressure of 100 mbar. The optic was located between two He-filled (front and rear) Ion Chambers (ICs), each with  $3.5 \text{ }\mu\text{m}$  Mylar entrance and exit windows. The beam was incident upon the MCP via the front IC, which acted as a reference beam monitor. The rear IC provides a measure of the beam flux after interaction with the MCP optic. A diagram of the experimental arrangement is shown in *Figure 5.2*.

Initially, the MCP was positioned and rotated so as to provide maximum signal from the rear IC. This (maximum throughput) position was taken to correspond to a position of  $\theta = 0^\circ$  grazing angle. The goniometer was then commanded to tilt the MCP in increments of  $\Delta\theta = 0.02^\circ$  about



the  $y$ -axis, with both front and rear IC currents recorded after each. Due to the finite beam width, the rotation of the MCP subsequently splits the incident X-ray beam into two components, a reflected and unreflected (or transmitted) beam. The positions of both 'component' beams were observed using a light-shielded, intensified CCD camera positioned at the rear of the experimental chamber; a P43 (Gadox) phosphor screen was located behind the rear IC. Two such "angle-scans" are required to calculate reflectivity profiles; the first records the combined flux from both reflected and unreflected beams, the second records flux from the reflected beam only. For the latter angle-scan, a "beamstop" is inserted between the MCP and rear IC in order to block the unreflected flux. The minimum grazing angle at which measurements were deemed to be accurate is conservatively estimated at  $0.3^\circ$ , geometrically limited by the minimum angle at which both component beams may be resolved at the beamstop.

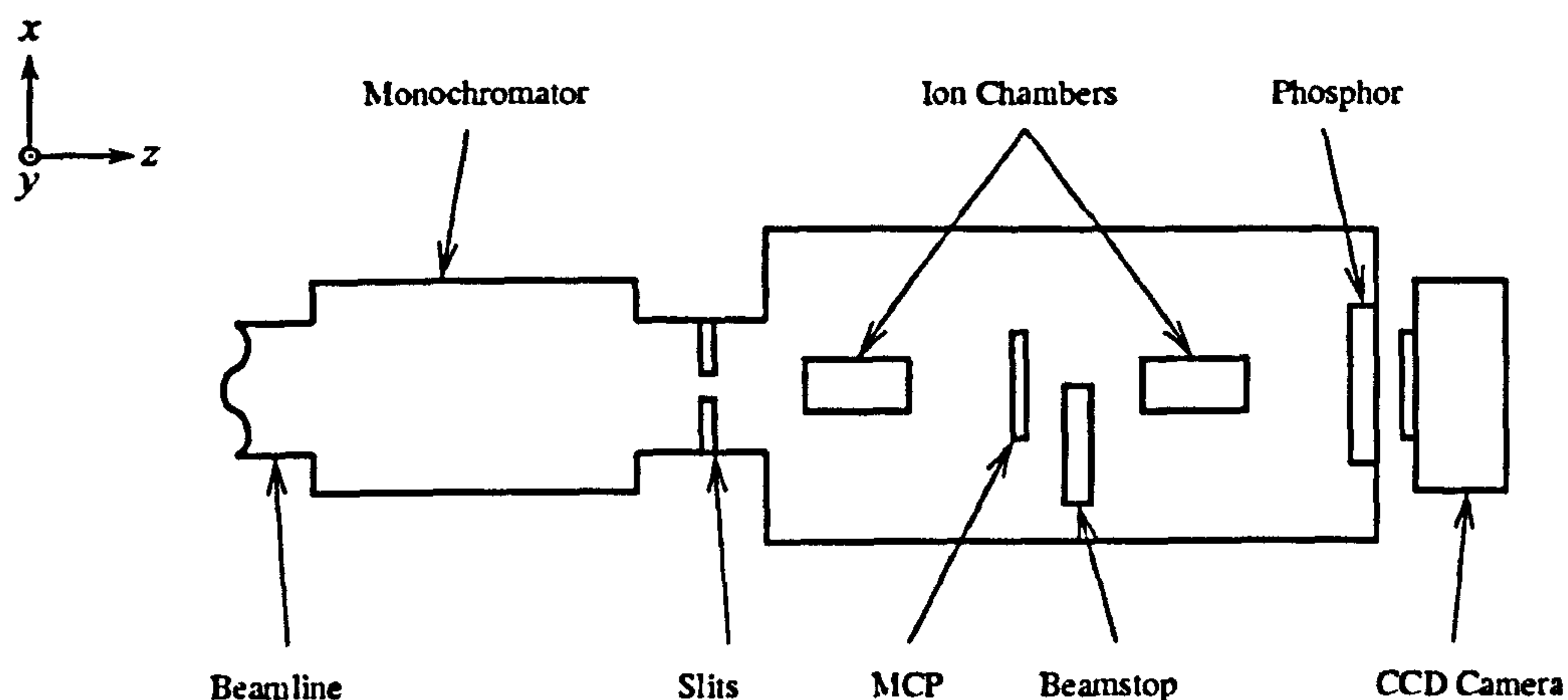


**Figure 5.2.** *Experimental arrangements of Beamline 3.4 at the Daresbury SRS, used to obtain the reflectivity measurements of MCP optics presented in this work.*

The MCP reflectivity  $R$  is calculated using the following method:

$$A_{open}F_0 = \frac{F_r}{R} + F_u \quad (5.10)$$

where  $F_0$  is the flux incident upon the MCP and  $A_{open}$  is the MCP open area fraction; thus the product of  $A_{open}$  and  $F_0$  on the left-hand side of Equation 5.10 is the incident flux entering the



MCP channels.  $F_r$  and  $F_u$  are the reflected and unreflected (or transmitted) fluxes respectively. As the recorded IC currents are directly proportional to the incident flux passing through them,

$$kA_{open}I^F = \frac{I_r^R}{R} + I_u^R \quad (5.11)$$

where  $I^F$  is the front IC current,  $I_r^R$  is the rear IC current contribution due to the reflected beam only and  $I_u^R$  is the rear IC current contribution due to the unreflected beam only. IC efficiencies are factored out of *Equation 5.11* through the constant  $k$ , which scales all currents measured in the front IC to that of the rear, also accounting for any absorption between the ICs; i.e. with no MCP present,  $k = \frac{I_r^R}{I^F}$ . Our two angle-scan datasets provide  $I_r^R$  and the sum of both  $I_r^R$  and  $I_u^R$ , denoted as  $I_{r+u}^R$  for convenience. Dividing through by  $I^F$ , *Equation 5.11* may be re-written:

$$kA_{open} = \frac{I_r^R}{RI^F} + \frac{I_{r+u}^R}{I^F} - \frac{I_r^R}{I^F} \quad (5.12)$$

We define quantities  $IR$  and  $IRU$  such that

$$IR = \frac{I_r^R}{kI^F A_{open}} \quad \text{and} \quad IRU = \frac{I_{r+u}^R}{kI^F A_{open}} \quad (5.13 \text{ a,b})$$

where  $IR$  is the fraction of flux entering the MCP that is reflected, and  $IRU$  the fraction of flux entering the MCP that is either reflected or unreflected. The reflectivity of the MCP may thus be expressed in terms of the measurable quantities  $IR$  and  $IRU$ , as

$$R = \frac{IR}{IR - IRU + 1} \quad (5.14)$$

where  $IR$  and  $IRU$  are both generated as a function of grazing angle  $\theta$ , with the product of  $k$  and  $A_{open}$  determined empirically by the value of  $IRU$  at  $\theta = 0^\circ$  grazing incidence.  $A_{open}$  (defined in this context as the probability that an X-ray incident upon the MCP will enter a channel) is constant as a function of grazing angle. A program named '*REFLECT*' was written by the author in the IDL programming language to extract the reflectivity profiles  $R(\theta)$ .



### 5.3.2 X-ray Reflectivity Modelling

The MCP channel surface properties may be modelled by fitting theoretical reflectivity profiles to those observed experimentally. The IMD computer program was purpose-written by Windt (1998) to perform work of this nature and was used by the author throughout this chapter. For the purposes of modelling the X-ray reflectivity from a multilayered surface, we consider the progress of a photon incident on an interface separating layers  $u$  and  $v$ . IMD models a multilayer stack of  $N$  homogeneous layers and  $N+1$  interfaces, where the  $u^{\text{th}}$  layer has a thickness  $d_u$ , and complex index of refraction  $n_u$ . Windt (1998) then calculates the nett Fresnel amplitude reflection coefficient  $r_u$  for the  $u^{\text{th}}$  layer as follows:

$$r_u = \frac{r_{uv} + r_v e^{2i\xi_u}}{1 + r_{uv} r_v e^{2i\xi_u}} \quad (5.15)$$

where

$$\xi_u = \frac{2\pi d_u n_u \sin \theta_u}{\lambda} \quad (5.16)$$

and where  $r_v$  is the nett Fresnel amplitude reflection coefficient of the  $v^{\text{th}}$  layer. *Equation 5.15* is applied recursively, starting at the lower-most layer (the substrate) in order to calculate the net Fresnel amplitude reflection coefficient  $r$  for the entire multilayer stack. The reflectivity  $R$ , the measure of the reflected intensity is simply given by  $R = |r|^2$ .

IMD incorporates a surface and interface roughness model based on the classical scalar theory of Beckmann and Spizzichino (1963), as interpreted by Cowley and Ryan (1987). Prior to its application in *Equation 5.15*, the Fresnel amplitude coefficient of reflection  $r_{uv}$  is modified by a Debye-Waller type factor containing the RMS surface roughness  $\sigma_{uv}$  at the interface between layers  $u$  and  $v$ , through

$$r_{uv}^* = r_{uv} \exp \left[ -\frac{1}{2} \left( \frac{4\pi\sigma_{uv}}{\lambda} \sin \theta_u \right)^2 \right] \quad (5.17)$$



The instrumental resolution  $\delta\theta$  was taken into account by IMD by convolving the modelled reflectivity profile  $R(\theta)$  with a Gaussian (whose profile is estimated to describe the beam shape, Brunton et al. 1997) of FWHM  $\delta\theta$ . With an MCP installed at normal incidence to the beam, the beam width measured at the beamstop has contributions from beam divergence and MCP channel misalignments. The instrumental resolution for this investigation was measured in this way and is estimated at  $\sim 0.075^\circ$  throughout this investigation.

### 5.3.3 Bare Glass MCPs

Two bare glass MCP optics were investigated, with serial numbers HC001-A4 (analysed prior to the AES measurements performed in *Chapter 4*) and HC001-A8/1, hereafter referred to as A4 and A8/1 respectively. Each was manufactured to the specification given in *Table 1.1*.

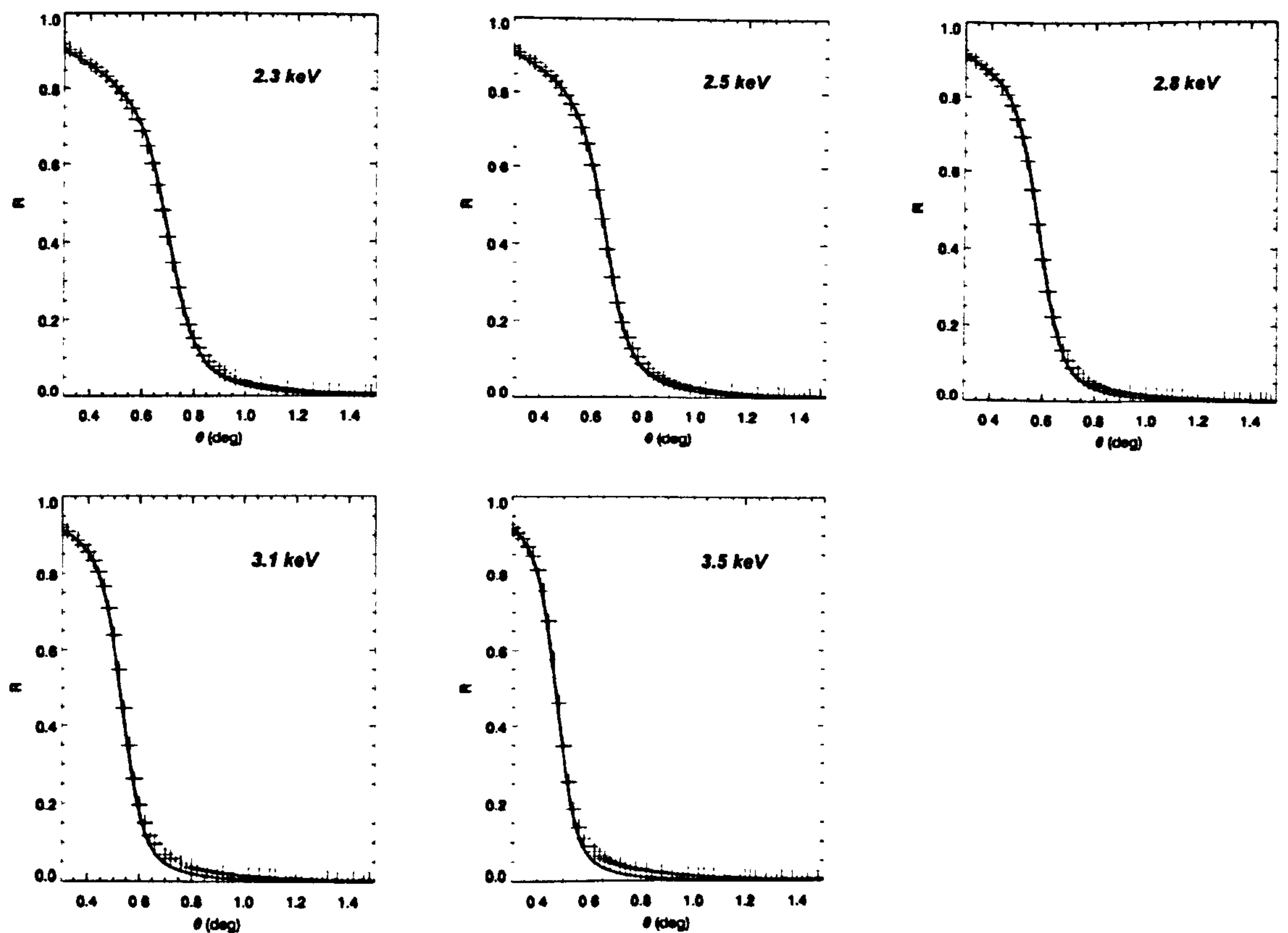


**Figure 5.3.** Reflectivity of MCP A4 as a function of grazing angle  $\theta$  at X-ray energies of 2.3, 2.5, 2.8, 3.1 and 3.5 keV. Experimental data (crosses) are plotted alongside fitted curves generated using a simple substrate-only model, parametrised with an O:Si ratio of 7:2,  $\rho = 1.920 \text{ g cm}^{-3}$  and  $\sigma = 9 \text{ \AA}$ .



$R(\theta)$  curves for MCPs A4 and A8/1 are shown in *Figures 5.3 and 5.4*, respectively. AES measurements of A4 in *Chapter 4* suggest that the channel surface may be modelled with a silicon and oxygen composition up to a depth of at least 2400 Å. Indeed, Fairbend (2005) suggested (on behalf of the manufacturers Photonis SAS) that he would fully expect a silicon and oxygen composition to a depth of around 3000 Å. Theoretical reflectivity curves were thus initially modelled as a silica-like ( $\text{Si}_x\text{O}_y$ ) substrate, with atomic concentration of Si and O, bulk substrate density and RMS surface roughness specified as free parameters during the fitting process. The fits shown in *Figures 5.3 and 5.4* support the AES analysis and validate this ‘substrate-only’ model with both MCPs A4 and A8/1. The ‘best fit’ modelled parameters are tabulated in *Table 5.1* for both MCPs.

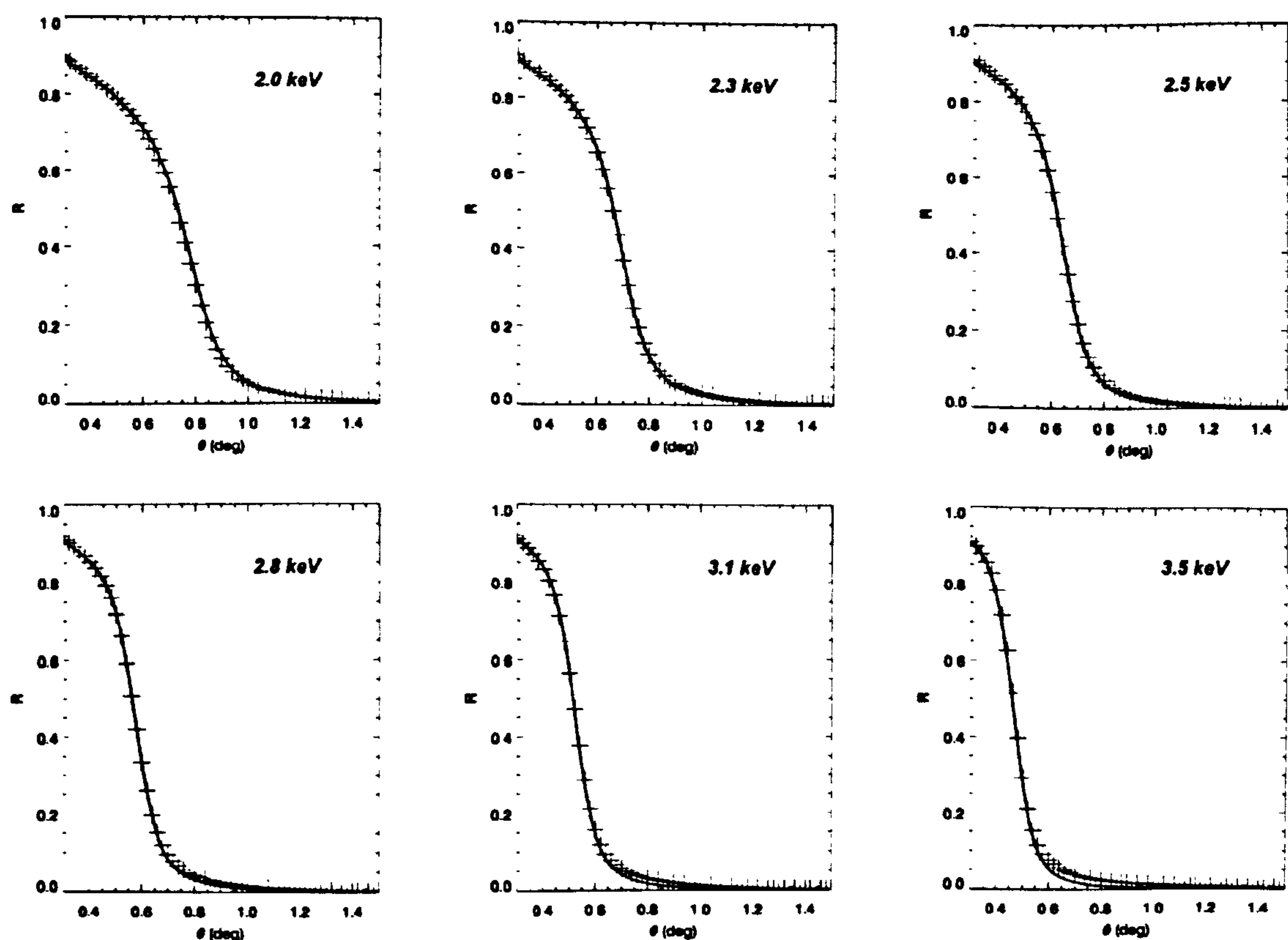


**Figure 5.4.** Reflectivity of MCP A8/1 as a function of angle at X-ray energies of 2.0, 2.3, 2.5, 2.8, 3.1 and 3.5 keV. Experimental data (crosses) are plotted together with fitted curves generated using a simple substrate-only model, parametrised with an O:Si ratio of 3:1,  $\rho = 1.860 \text{ g cm}^{-3}$  and  $\sigma = 11 \text{ Å}$ .



The modelled fits suggest that both bare glass MCPs A4 and A8/1 are very similar in their composition; indeed, they are both cuts from the same MCP optic block. For both MCPs, the oxygen concentration appears to be slightly higher than that of standard bulk silica  $\text{SiO}_2$ , with the relative concentrations at 3 and 3.5 times that of silica for A8/1 and A4 respectively. RMS surface roughnesses  $\sigma$  of 9 Å [A4] and 11 Å [A8/1] appear reasonable in the context of previous reports (Peele et al. 1998, Brunton et al. 1999).

MCP	A4	A8/1
<i>Atomic concentration O / Si</i>	$3.50 \pm 0.5$	$3.00 \pm 0.5$
<i>Mass density <math>\rho</math> (<math>\text{g cm}^{-3}</math>)</i>	$1.92 \pm 0.02$	$1.86 \pm 0.02$
<i>RMS surface roughness <math>\sigma</math> (Å)</i>	$9 \pm 4$	$11 \pm 4$

**Table 5.1.** *Values of parameters derived from fitting reflectivity curves of bare glass MCP optics A4 and A8/1.*

However, both authors (Peele et al. 1998, Brunton et al. 1999) report the presence of ‘Kiessig fringes’ in their  $R(\theta)$  profiles. Kiessig fringes (Kiessig, 1931) are apparently anomalous reflectivity values caused by the interference of rays reflected from a layered mirror; for example, for certain combinations of grazing angle, X-ray energy and layer thickness, X-rays may penetrate through a surface layer, reflect from an interface beneath, then penetrate back through the surface layer, and, at the detector, subsequently interfere with rays that have reflected from the surface layer only. The observation of Kiessig fringes is therefore an indicator of a layered reflecting surface, with Brunton et al. (1999) modelling the sub-surface structure of bare glass MCP channel walls to fit with previously reported models (described in *Section 4.2.3*). However, in both Peele et al. (1998) and Brunton et al. (1999), the MCPs investigated were manufactured from Corning 8161 ( $\text{Si}_5\text{O}_{12}\text{KPb}$ ,  $\rho = 4.0 \text{ g cm}^{-3}$ ) lead silicate glass by Nova Scientific Inc.; this investigation is the first to measure  $R(\theta)$  profiles of MCP optics manufactured from Philips type 297 glass ( $\text{Si}_{40}\text{O}_{98}\text{K}_8\text{Na}_7\text{Pb}_6\text{Bi}_2$ ,  $\rho = 3.3 \text{ g cm}^{-3}$ ) by Photonis SAS. The absence of Kiessig fringes from any of the measured reflectivity profiles of MCPs A4 and A8/1 (in *Figures 5.3* and *5.4* respectively) indicates that the reflecting surfaces are not layered for both MCPs, concurring with the surface models used to obtain the fits in each case.



### 5.3.4 Nickel-coated MCPs

A total of twelve nickel-coated MCP optics were investigated in December 2001 and December 2002, each coated by Photonis SAS using the EN process to varying specifications. Two coating parameters were varied by the manufacturer in an attempt to find an optimum configuration; the characteristic temperature of the bath  $T_B$  in which the MCPs were immersed, and the total immersion time  $t_{IMM}$ . Sometimes the process was completed twice or more for a single MCP optic; for example, in the case of an MCP being coated twice, for 15 seconds each time, we refer to the coating as  $t_{IMM} = 15+15$ . MacDermid Inc., the manufacturer of the proprietary coating solutions used by Photonis SAS, estimate a 50 Å coating thickness for every 15 seconds of immersion time at  $T_B = 84$  °C. Each MCP is identified by its truncated serial number; ‘HC001-A8/3’ becoming ‘A8/3’.

$R(\theta)$  profiles for each nickel-coated MCP at 2.5 keV are shown in *Figure 5.5*. The MCPs are grouped by the characteristic temperature of the bath in which they were coated, where  $T_B = 84$  °C (*Figure 5.5(a)*), 80 °C (*Figure 5.5(b)*) and < 78 °C (*Figure 5.5(c)*). Each set is compared with bare glass MCP A4 and two theoretical reflectivity curves, denoted NI [A] and NI [B]. Details of the NI [A] and NI [B] models are shown in *Table 5.2*.

<i>Model</i>	NI [A]	NI [B]
<i>Coating material</i>	Ni	Ni
<i>Thickness (Å)</i>	200	200
<i>Density (g cm<sup>-3</sup>)</i>	7.8	7.8
<i>RMS surface roughness (Å)</i>	10	23

**Table 5.2.** Coating parameters used to define models NI [A] and NI [B]. Each coating is modelled on an A4-like substrate of bulk density  $\rho = 1.920$  g cm<sup>-3</sup> and O / Si = 3.5 with an interface roughness of 10 Å. MacDermid Inc. estimate that the nickel is deposited at a reduced density of 7.8 g cm<sup>-3</sup>.



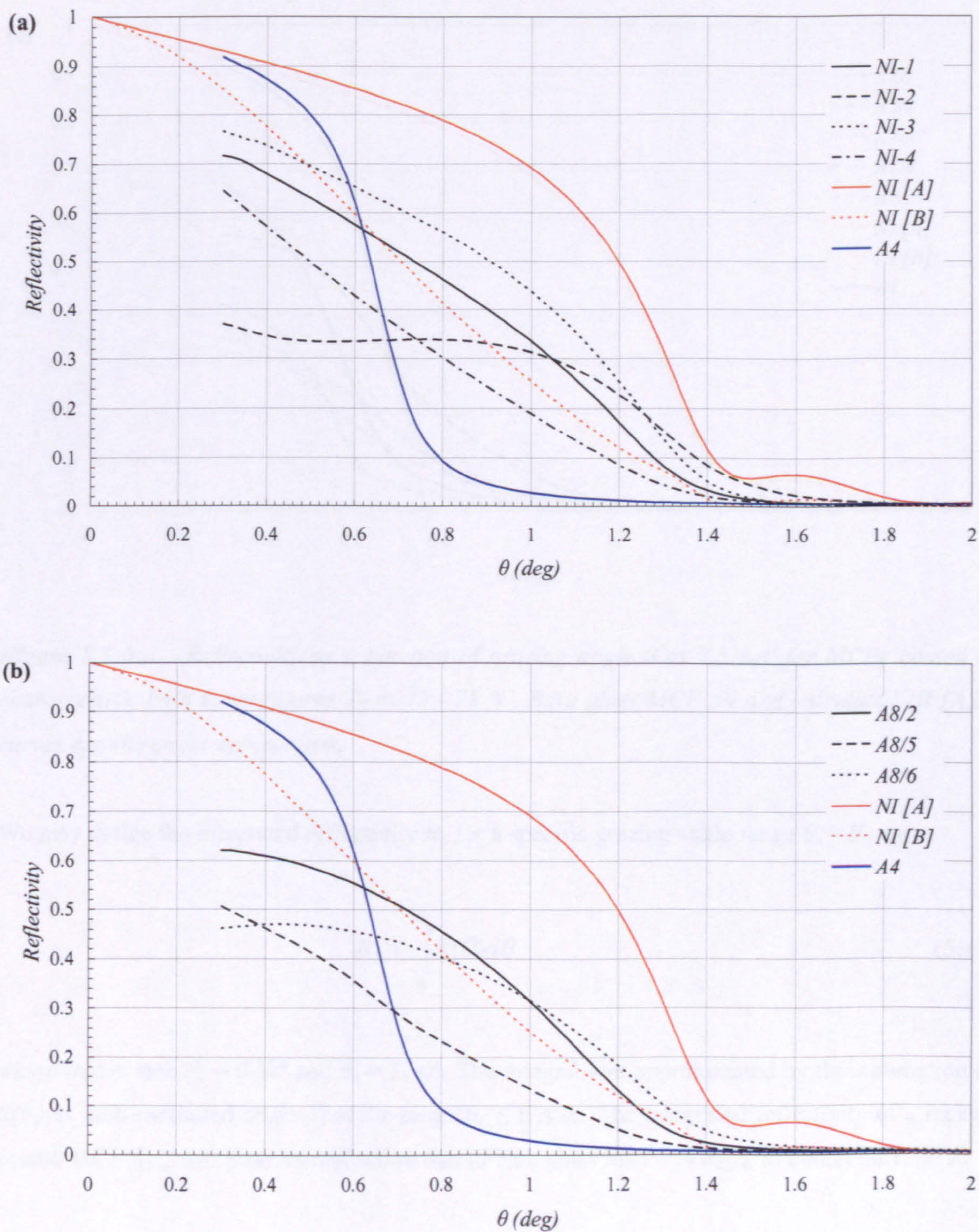


**Figure 5.5 (a ,b).** Reflectivity as a function of grazing angle  $\theta$  at 2.5 keV for MCPs coated at characteristic bath temperatures  $T_B$  of (a) 84 °C and (b) 80 °C. Measured bare glass MCP A4 and calculated NI [A,B] curves are shown for comparison.



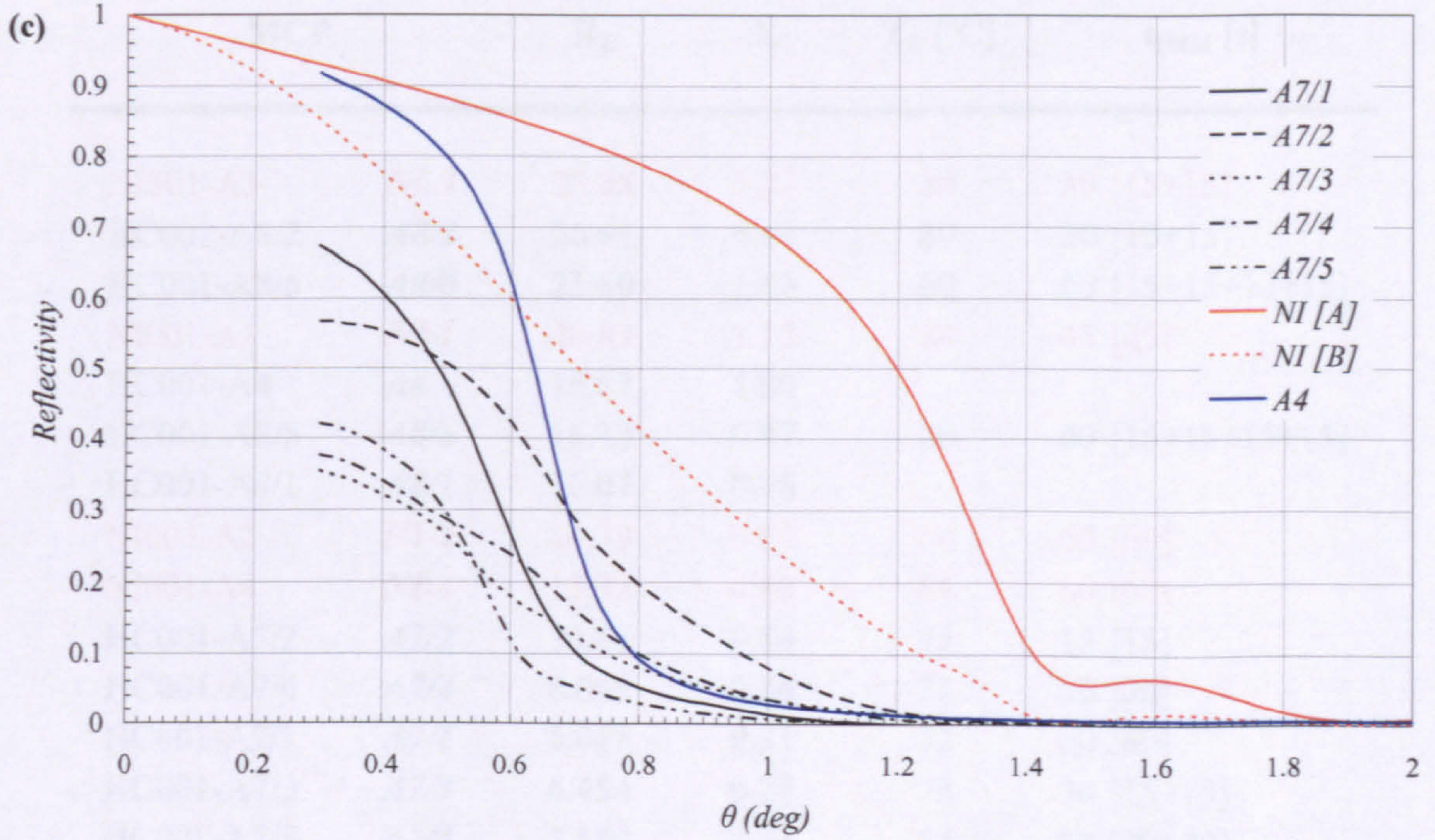


**Figure 5.5 (c).** Reflectivity as a function of grazing angle  $\theta$  at 2.5 keV for MCPs coated at characteristic bath temperatures  $T_B$  of 72 - 78 °C. Bare glass MCP A4 and calculated NI [A,B] curves are shown for comparison.

We may define the integrated reflectivity  $R_\Sigma$  for a specific grazing angle range  $\theta_n - \theta_l$ , by

$$R_\Sigma = \int_{\theta_l}^{\theta_n} R(\theta) d\theta \quad (5.18)$$

where in our case  $\theta_l = 0.30^\circ$  and  $\theta_n = 2.00^\circ$ . The integral was approximated by the summation of  $R(\theta_i)$  at each measured angle  $\theta_i$  in the range  $\theta_l \leq \theta \leq \theta_n$ . The integrated reflectivity of a nickel-coated MCP  $R_{\Sigma, Ni}$  was then normalised to that of bare glass MCP A4  $R_{\Sigma, A4}$ , to obtain the ratio  $X$ :

$$X = \frac{R_{\Sigma, Ni}}{R_{\Sigma, A4}} \quad (5.19)$$

which provides a quantitative measure with which to compare the nickel-coated and bare glass MCP optics. Table 5.3 lists the MCPs in terms of  $X$ , in descending order.



MCP		$R_{\Sigma}$	X	$T_B$ [°C]	$t_{\text{IMM}}$ [s]
NI001-A3	<b><i>NI-3</i></b>	28.88	1.73	84	30 [15+15]
HC001-A8/2	<b><i>A8/2</i></b>	26.91	1.61	80	30 [15+15]
HC001-A8/6	<b><i>A8/6</i></b>	23.89	1.43	80	60 [15+15+15+15]
NI001-A1	<b><i>NI-1</i></b>	20.89	1.25	84	45 [45]
HC001-A4	<b><i>A4</i></b>	16.67	1.00		
HC001-A8/5	<b><i>A8/5</i></b>	16.12	0.97	80	60 [15+15+15+15]
HC001-A8/1	<b><i>A8/1</i></b>	16.07	0.96		
NI001-A2	<b><i>NI-2</i></b>	14.79	0.89	84	60 [60]
NI001-A4	<b><i>NI-4</i></b>	13.32	0.80	84	60 [60]
HC001-A7/2	<b><i>A7/2</i></b>	10.61	0.64	75	15 [15]
HC001-A7/4	<b><i>A7/4</i></b>	6.048	0.36	78	30 [30]
HC001-A7/1	<b><i>A7/1</i></b>	5.088	0.31	72	60 [60]
HC001-A7/3	<b><i>A7/3</i></b>	4.454	0.27	75	30 [15+15]
HC001-A7/5	<b><i>A7/5</i></b>	3.550	0.21	75	60 [30+30]

**Table 5.3.** Nickel-coated and bare glass MCPs investigated at the Daresbury SRS. MCP serial numbers are shown with their abbreviations (bold-italic). MCPs are sorted by their integrated reflectivity  $R_{\Sigma}$  at 2.5 keV over the  $0.30^{\circ} - 2.00^{\circ}$  grazing angle range. MCPs are colour-coded by coating bath temperatures  $T_B$  of 84 °C (red) 80 °C (green) and 72-78 °C (blue). Bare glass MCPs A4 and A8/1 are shown in black.

The nickel-coated MCP optics may be split into two distinct groups; MCPs with  $T_B \geq 80$  °C (hereafter named **group 1**) have larger  $R_{\Sigma}$  than those coated in lower temperature baths (**group 2**). The rate of reaction of the EN process is a near exponential function of bath temperature (Section 4.1.1); it is possible that at higher  $T_B$ , hydrogen is more easily adsorbed onto the channel surface (Equation 4.1); in this case the nickel salts ( $\text{Ni}^{2+}$ ) would form a substantially thicker nickel layer in the same amount of time as if the process was performed at a lower  $T_B$  (Equation 4.3). Of the four MCPs coated at  $T_B \leq 78$  °C (Figure 5.5 (c)), only one, A7/2, shows any significant increase in high angle reflectivity at 2.5 keV.

For all bath temperatures, it appears that  $R_{\Sigma}$  may be maximised by minimising  $t_{\text{IMM}}$ . In both groups, better reflectivity profiles were achieved by coating processes using the shortest total immersion times (of 30 s [**group 1**] and 15 s [**group 2**]). The EN process uses an autocatalytic



reaction, the coating thickness gradually increasing with time. However, it is vital to the success of the procedure that the substrate is as clean and smooth as possible before commencing, hence the emphasis on substrate pre-treatment (*Section 4.1.1*). This is because the EN process will, in theory, reproduce the surface morphology of the substrate; in practice, inhibitors may promote island formation in the coating, which will grow more pronounced with time. Rougher coating surfaces as a result of longer immersion times may be responsible for the poorer reflectivity profiles observed. In anticipation of this, Photonis SAS elected to restart the process in some MCPs after 15 or 30 second intervals, as many as three more times; a new seeding layer may promote growth in ‘creviced’ areas of the coating during the subsequent immersion, where it had halted previously. Further investigation is required to deduce whether this is the case, as these ‘repeated’ coatings are responsible for the poorest integrated reflectivity values in **group 2**, yet in **group 1**, 15+15 immersions (at both 84 °C and 80 °C) provided the best two reflectivity profiles (observed with NI-3 and A8/2 respectively). In light of the above, a specification of  $T_B \geq 84$  °C and  $t_{IMM} \approx 15$  s should be investigated as a potential best combination of coating parameters.

In addition, we observe a variety of reflectivity profiles resulting from similar coating specifications; indeed, MCP pairs [NI-2, NI-4] and [A8/2, A8/5] have equivalent nominal coating specifications, yet markedly different  $R(\theta)$  profiles (*Figure 5.5 (a,b)*). If nickel-coated MCPs are to be used as X-ray mirrors, the consistency of the EN process must improve.

Of the twelve nickel-coated MCPs analysed, only four appear to have significantly improved their efficiency as reflectors at 2.5 keV over bare glass MCP optics (i.e.  $X > 1$ ). *Figure 5.5(a,b)* suggests that in each of these four cases, the critical angle is larger than that of a bare glass optic. However, although the coating boosts reflectivity at larger grazing angles, there appears to be a shortfall in reflectivity at the lower angles, as first reported by Martin (2000). It may be shown using *Equations 5.5 – 5.8* that for a perfect reflector, as  $\theta \rightarrow 0$ ,  $R(\theta) \rightarrow 1$ . In the case of *Equation 5.6* this can be shown clearly by multiplying numerator and denominator by  $\tan^2 \theta$ , such that

$$\frac{R_{\pi}(\theta)}{R_{\sigma}(\theta)} = \frac{4a^2(a \tan \theta - \cos \theta)^2 + \gamma^2 \tan^2 \theta}{4a^2(a \tan \theta + \cos \theta)^2 + \gamma^2 \tan^2 \theta} \quad (5.20)$$

and as  $\theta \rightarrow 0$ ,  $\cos \theta \rightarrow 1$  and  $\tan \theta \rightarrow 0$ , so



$$\lim_{\theta \rightarrow 0} R_{\sigma}(\theta) = 1 \quad \text{and} \quad \lim_{\theta \rightarrow 0} \frac{R_{\pi}(\theta)}{R_{\sigma}(\theta)} = 1 \quad \text{and thus} \quad \lim_{\theta \rightarrow 0} R(\theta) = 1 \quad (5.21 \text{ a,b,c})$$

In fact, the shortfall in reflectivity occurs across the entire measured angle range at 2.5 keV compared to the theoretically generated NI [A]. This shortfall occurs to varying degrees in different MCPs; for example, in the case of NI-2, *Figure 5.5 (a)* clearly indicates the presence of nickel, yet  $R(\theta)$  is approximately constant for  $0.3^{\circ} \leq \theta \leq 1^{\circ}$ , with  $R(\theta)$  tending toward  $\sim 0.4 - 0.5$  as  $\theta \rightarrow 0$ , whereas for NI-3,  $R(\theta) \rightarrow \sim 0.8$ , which is non-ideal in both cases. This low angle shortfall is not observed experimentally for bare glass MCP optics (*Figures 5.3 and 5.4*). In order to explain this effect, it is necessary to analyse the experimental data in further detail. A total of three MCPs will be investigated; bare glass MCP A4, and nickel-coated MCPs NI-2 (with poor low-angle reflectivity) and NI-3 (which exhibits the best low angle reflectivity of all of the nickel-coated MCPs).

As stated in *Section 5.3.1*, experimental  $R(\theta)$  profiles are generated from two parameters,  $IR$  and  $IRU$ .  $IR$  is the fraction of incident X-ray flux entering the MCP that is reflected from the MCP channel walls *and detected* in the rear IC.  $IRU$  is the fraction of both reflected and unreflected components of the incident X-ray flux entering the MCP and detected in the rear IC. The two ratios are related by

$$IRU(\theta) = IR(\theta) + IU(\theta) \quad (5.22)$$

where  $IU$  is the detected fraction of incident X-ray flux entering the MCP and not interacting with the MCP channel walls; the unreflected or transmitted component only. In order to understand whether the coating has in some way affected the MCP channel geometry, we calculate  $IU$  as a function of angle from the experimentally obtained  $IR(\theta)$  and  $IRU(\theta)$ . With reference to *Figure 5.6*,  $IU(\theta)$  may be modelled theoretically as  $IU_{theo}(\theta)$ , where for an MCP of channel aspect ratio  $L:D$ ,

$$IU_{theo}(\theta) = \frac{x_1}{D}; \quad D = x_1 + x_2 \quad \text{and} \quad x_2 = L \tan \theta \quad (5.23 \text{ a,b,c})$$

and hence



$$IU_{theo}(\theta) = 1 - \frac{L}{D} \tan \theta \quad (5.24)$$

where for the purposes of this investigation  $L:D = 50:1$  (nominally).  $IU_{theo}(\theta)$  is compared with measured profiles of  $IU(\theta)$  for MCPs A4, NI-2 and NI-3 in *Figure 5.7*.

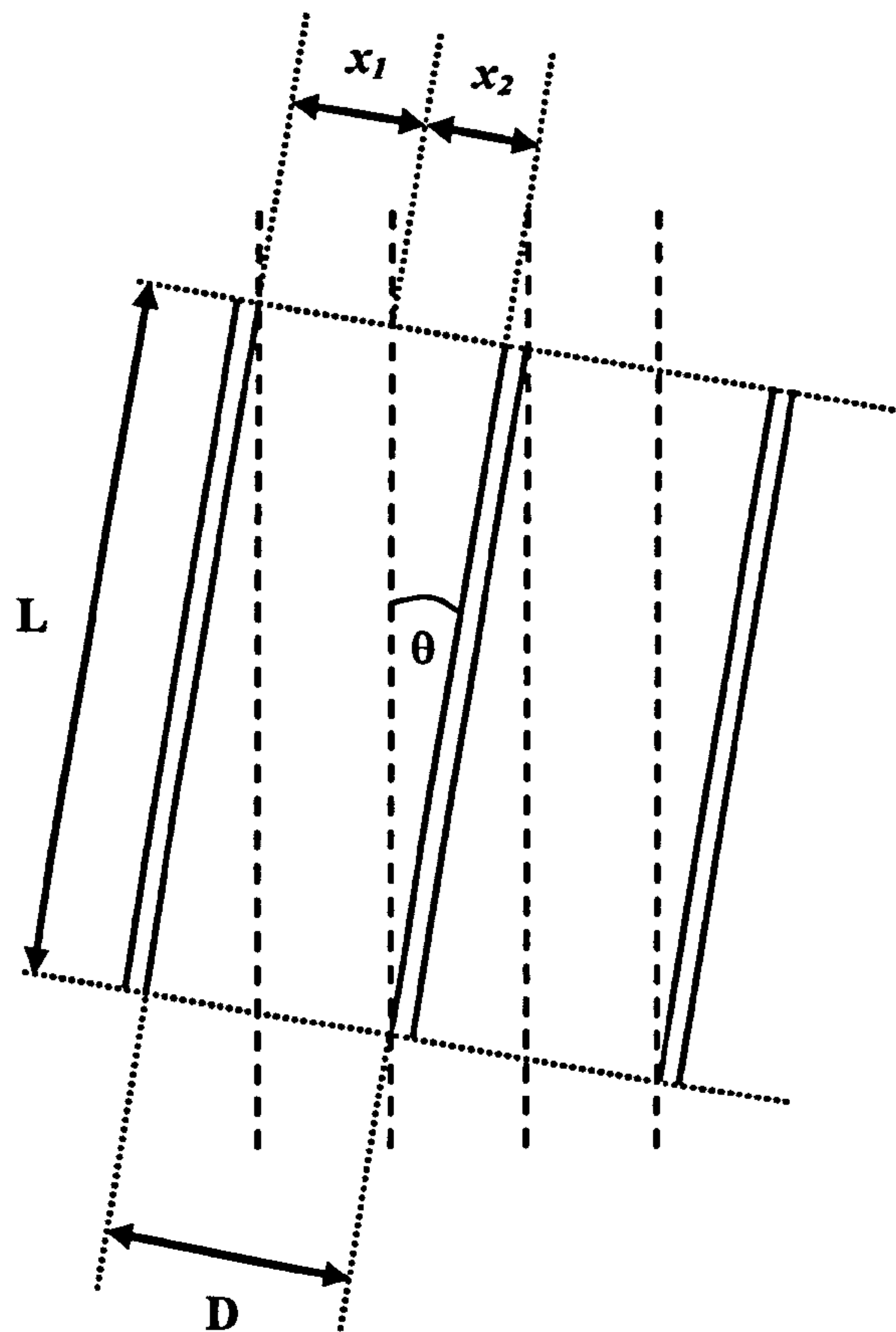


*Figure 5.6. Cross-section of an MCP optic (of channel aspect ratio  $L:D$ ) rotated an angle  $\theta$  relative to the incident X-ray beam (dashed lines).*

All three MCPs conform closely to  $IU_{theo}(\theta)$ , with  $IU$  approximately tending toward zero as  $\theta \rightarrow$  the transmission angle  $\theta_T$  (as expected). This result would appear to indicate that there are no significant channel blockages as a result of the coating process as the expected fraction of incident X-rays transmitted through each MCP as a function of angle is observed in each of the three cases. In other words, the shortfall in reflectivity observed across the measured grazing angle range cannot be attributed to a shortfall in the transmitted flux.



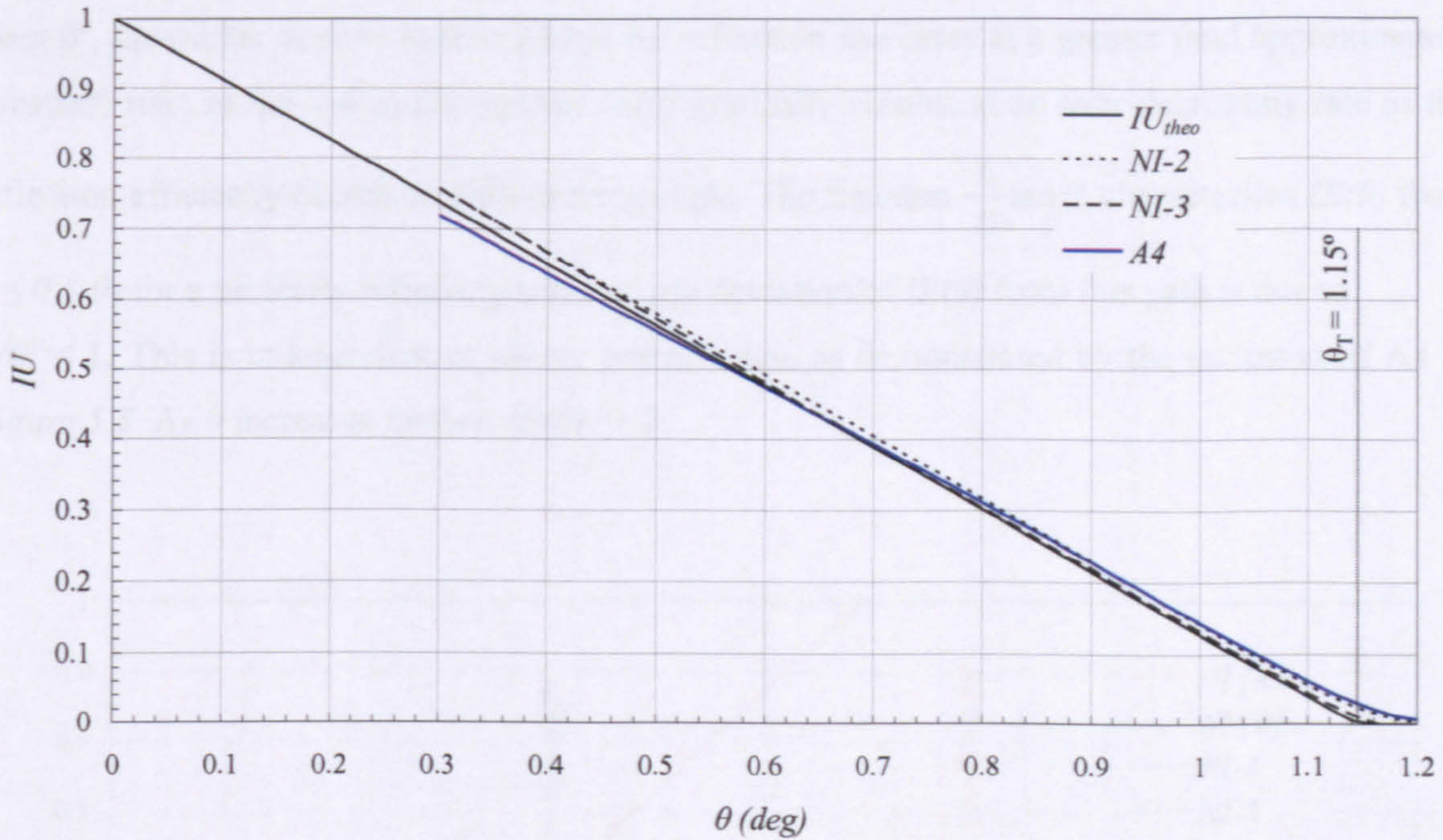


**Figure 5.7.**  $IU(\theta)$  for nickel-coated MCPs NI-2, NI-3 and bare glass MCP A8/1. In each case,  $IU \rightarrow \sim 0$  as  $\theta \rightarrow \theta_T$ .

The shortfall in reflectivity observed in all nickel-coated plates must therefore be explained by a shortfall in  $IR$ , a significant fraction of the reflected flux being undetected by the rear IC. This may be verified by comparing profiles of  $IR(\theta)$  for NI-2 and NI-3 against theoretically generated profiles  $IR_{NI[A,B]}(\theta)$  using the NI [A] and NI [B] models. The fraction of X-rays incident on the reflecting surface of an MCP optic as a function of grazing angle is given by  $\frac{L}{D} \tan \theta$ , following the arguments leading up to Equation 5.24.  $IR_{NI[A,B]}(\theta)$  is thus given by

$$IR_{NI[A,B]}(\theta) = R_{NI[A,B]}(\theta) \frac{L}{D} \tan \theta \quad (5.25)$$

where  $R_{NI[A,B]}(\theta)$  are the theoretical reflectivity profiles for the NI [A] and NI [B] models.

Figure 5.8 confirms the shortfall in  $IR$  across the extent of the measured grazing angle range  $0.30^\circ \leq \theta \leq 2.00^\circ$ , observed in both nickel-coated MCP optics NI-2 and NI-3. The form of  $IR(\theta)$  may be explained by considering the channel geometry shown in Figure 5.6. The  $IR(\theta)$  function is the product of the reflectivity and the proportion of the X-ray beam incident on the reflecting



surfaces. Although the reflectivity for a monochromatic X-ray beam decreases as  $\theta$  increases from  $0^\circ$ , the mirror surface area available for reflection increases at a greater (and approximately constant) rate; in the low angle regime,  $IR(\theta)$  gradually climbs, at an ever-decreasing rate as the reflection efficiency decreases with grazing angle. The function  $\frac{L}{D} \tan \theta$  characterises  $IR(\theta)$  from  $0 \leq \theta \leq \theta_T$  for a perfectly reflecting surface; any deviation of  $IR(\theta)$  from this path is due to  $R(\theta) < 1$ . This is independent of mirror composition, as demonstrated by the inclusion of A4 in Figure 5.8. As  $\theta$  increases further,  $IR(\theta) \rightarrow 0$ .

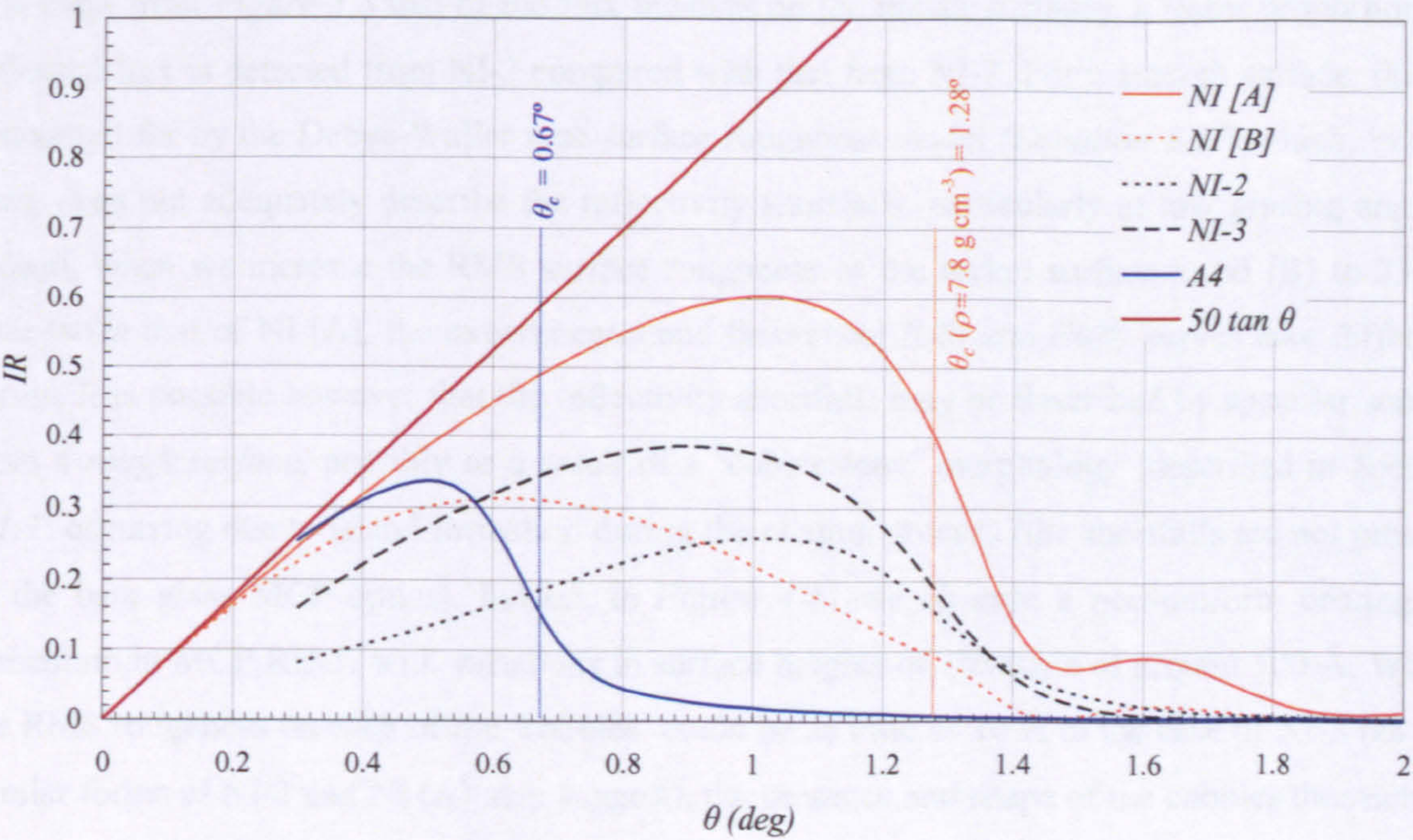


**Figure 5.8.**  $IR$  as a function of  $\theta$  for nickel-coated MCPs NI-2 and NI-3 at 2.5 keV, compared with the theoretical  $IR_{NI[A,B]}$ . MCP A4 is included for comparison with bare glass MCP optics. Critical angles are calculated for  $IR_{NI[A,B]}$  (orange dashed line) and A4 (blue dashed line). The maximum rate of increase of  $IR$  with respect to  $\theta$  [ $50 \tan \theta$ ] is also shown (brown).

For a mirror created from a non-absorbing medium,

$$\begin{aligned}
 R(\theta) &= 1 & 0 \leq \theta \leq \theta_c \\
 R(\theta) &< 1 & \theta > \theta_c
 \end{aligned}$$



and thus  $\theta_c$  may be estimated from profiles of either  $R(\theta)$  or  $IR(\theta)$ . However, a non-absorbing medium is unphysical, and thus it is not possible to accurately deduce  $\theta_c$  from the inspection of one of the aforementioned profiles. The critical angles at 2.5 keV for NI [A,B] and A4 (the latter based on the modelled fits in *Section 5.3.3*) may be calculated using *Equations 5.9* and *5.4(b)* respectively (where  $\theta_c \approx \sqrt{\alpha}$  at X-ray energies); these values are labelled in *Figure 5.8*. The experimentally observed declines in the  $IR(\theta)$  profiles of both NI-2 and NI-3 have similar forms to that of  $IR_{NI[A]}(\theta)$  and we thus may propose that the nickel is deposited at a reduced bulk density, as suggested by AES measurements in *Chapter 4* (in the case of NI-3).

It is clear from *Figure 5.8* that of the flux incident on the mirror surfaces, a lesser proportion of reflected flux is detected from NI-2 compared with that from NI-3. For a smooth surface, this is accounted for by the Debye-Waller type surface roughness model (*Equation 5.17*) which, in this case, does not adequately describe the reflectivity shortfalls, particularly at low grazing angles. Indeed, when we increase the RMS surface roughness of the nickel surface in NI [B] to 23 Å, over twice that of NI [A], the experimental and theoretical  $R(\theta)$  and  $IR(\theta)$  curves take different forms. It is possible however that the reflectivity shortfalls may be described by specular scatter from a *rough surface*, possibly as a result of a ‘cobblestone’ morphology (described in *Section 4.1.1*) occurring due to island formation during the coating process (the shortfalls are not present in the bare glass MCP optics). Indeed, in *Figure 4.11* we observe a non-uniform coating of ruthenium in MCP RU-1, with variations in surface heights on the scale of around 100 Å. While the RMS roughness on each of the ‘cobbles’ could be as little as 10 Å in the case of NI-3 (as the similar forms of NI-3 and NI [A] may suggest), the presence and shape of the cobbles themselves may be responsible for the observed loss in reflected flux. It is believed that in this *rough surface limit*, a combination of specular reflection from the cobbles and photoelectric absorption is responsible for the shortfall in reflected flux (*Figure 5.9*). The fall in reflected flux from *sparsely populated, isolated cobbles* could be accounted for by a ‘loss factor’, whose magnitude is dependent on the proportion of X-rays incident on the cobbles as opposed to the smooth surface. Unfortunately, in our case, the close proximity of the cobbles to one another (*Figure 4.11*) can result in multiple interactions of an X-ray between neighbouring cobbles; modelling the reflected flux observed at the rear IC from our MCP coating-based cobblestone surfaces is therefore non-trivial and beyond the scope of this thesis.

As the coatings performed on all MCPs in this chapter are of the order 100 – 700 Å thick (700 Å observed in *Chapter 4* in the case of RU-1), changes to the  $L:D$  of the MCPs as a result of the



coating thickness are insignificant and would not be observable in the  $IU(\theta)$  profiles in Figure 5.7.

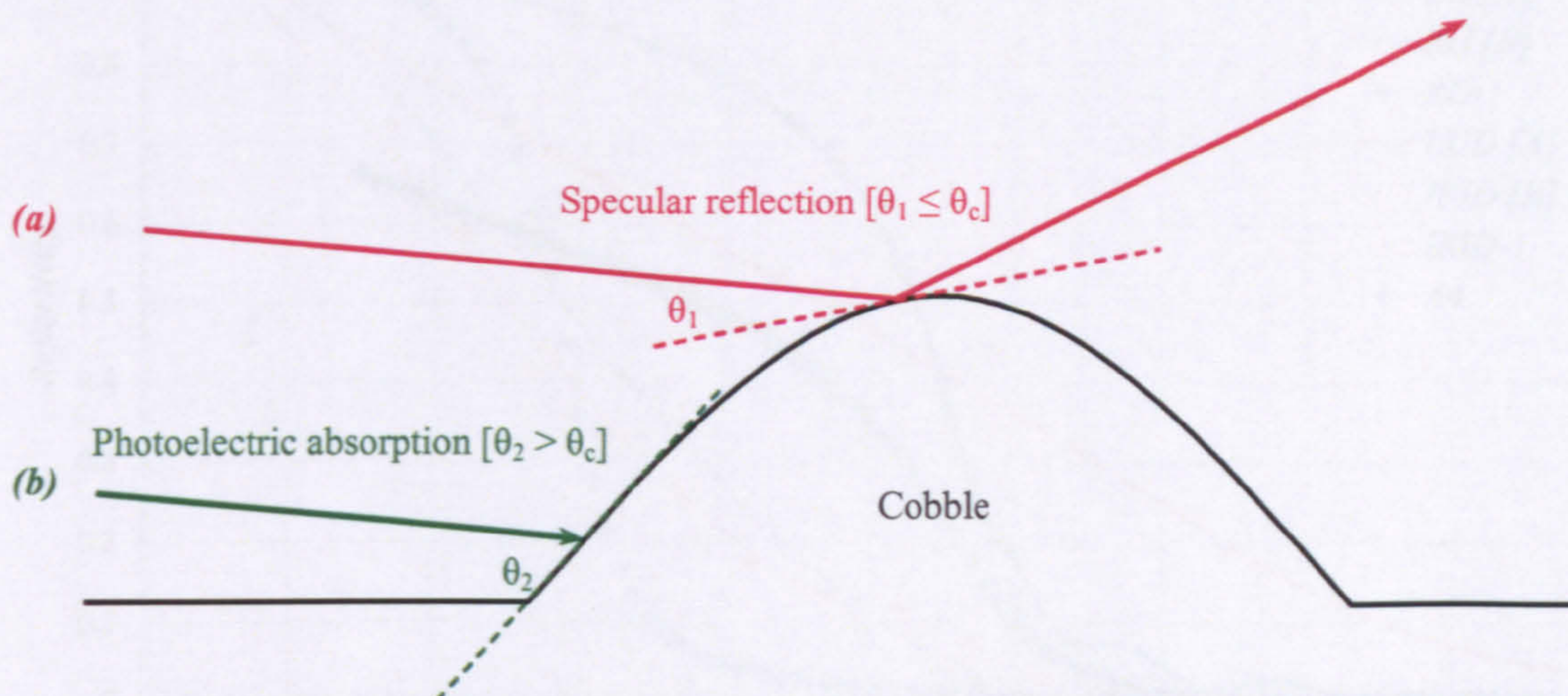


**Figure 5.9.** *Specular reflection and photoelectric absorption of X-rays incident on a rough surface with a ‘cobblestone’ morphology. The grazing angle is a function of the position on the cobble at which interaction occurs. (a) Specular reflection occurs when  $\theta \leq \theta_c$ ; however, as the plane of reflection is not necessarily parallel to the channel surface, the reflected ray may further reflect from the channel walls before emerging from the MCP. (b) Where  $\theta > \theta_c$  the ray is absorbed by the cobble before it reaches the flat surface. This effect is known as shadowing. The loss in reflected flux observed at the rear IC may be explained by both of these cases.*

### 5.3.5 Ruthenium and Iridium-coated MCPs

The bare glass optic A4 was cut into 16 square MCPs, each of area  $1 \text{ cm}^2$ . Two of these smaller MCP optics were sent to the University of Helsinki for coating (by the ALD method), one with iridium (hereafter referred to as IRID-1) and the other with ruthenium (RU-1). The nominal coating thickness in each case was  $400 \text{ \AA}$ , investigated in the case of RU-1 in Chapter 4. IRID-1 was studied at the Daresbury SRS in November 2004; on this run, the experimental configuration was slightly altered in an attempt to maximise the grazing angle range over which reflectivity measurements were made. The ICs were substituted by wire meshes, which ultimately provided very low signal to noise ratios. Statistical fluctuations in the reflectivity data were smoothed by grouping the data into grazing angle bins of width  $0.1^\circ$ . Due to time constraints on this particular run, reflectivity measurements of IRID-1 were only performed at 2.8, 3.1 and 3.5 keV. For this reason, in this section we concentrate on comparative measurements made at 2.8 keV.



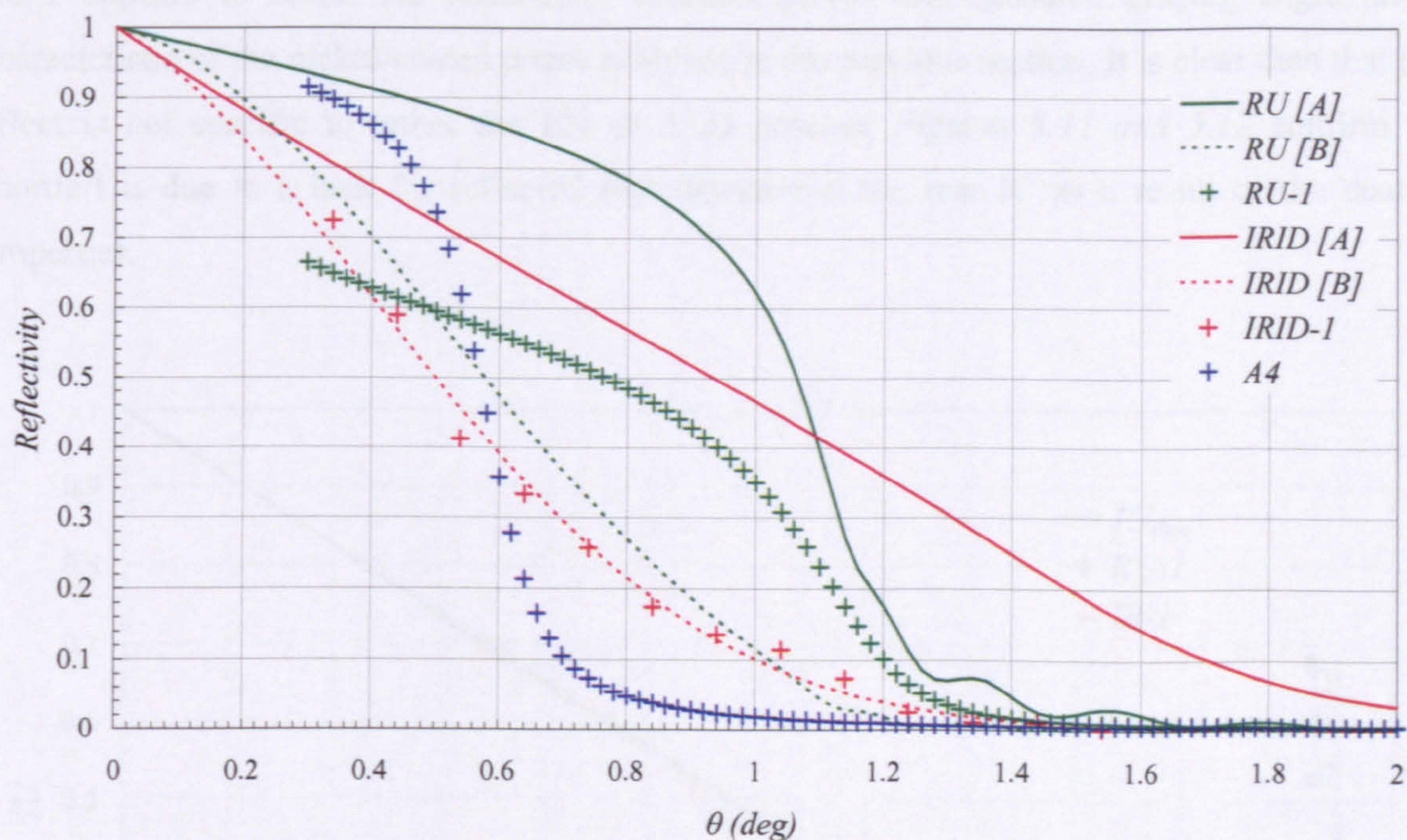


**Figure 5.10.** Reflectivity as a function of grazing angle  $\theta$  at 2.8 keV for MCPs RU-1 and IRID-1. Modelled reflectivity profiles of RU [A,B], IRID [A,B] and measured bare glass MCP A4 are also plotted for comparison.

Reflectivity profiles of RU-1 and IRID-1 as a function of grazing angle at 2.8 keV are shown in Figure 5.10. Modelled  $R(\theta)$  of iridium and ruthenium-coated MCP optics (hereafter referred to as IRID [A,B] and RU [A,B] respectively) are also shown for comparison. Details of the IRID [A,B] and RU [A,B] models are shown in Table 5.4.

Model	IRID [A]	IRID [B]	RU [A]	RU [B]
Coating material	Ir	Ir	Ru	Ru
Thickness ( $\text{\AA}$ )	400	400	400	400
Density ( $\text{g cm}^{-3}$ )	22.5	22.5	12.2	12.2
RMS surface roughness ( $\text{\AA}$ )	10	26	10	26

**Table 5.4.** Coating parameters used to define models IRID [A,B] and RU [A,B]. Each coating is modelled on an A4-like substrate of bulk density  $\rho = 1.920 \text{ g cm}^{-3}$  and  $O / Si = 3.5$  with an interface roughness of  $10 \text{ \AA}$ .



RU-1 appears to suffer the reflectivity shortfall across the measured grazing angle range, characteristic of the nickel-coated plates analysed in the previous section. It is clear then that this effect is not specific to either the EN or ALD process; *Figures 5.11 and 5.12* confirm the shortfall is due to a lack for reflected flux detected at the rear IC as a result of the coating properties.

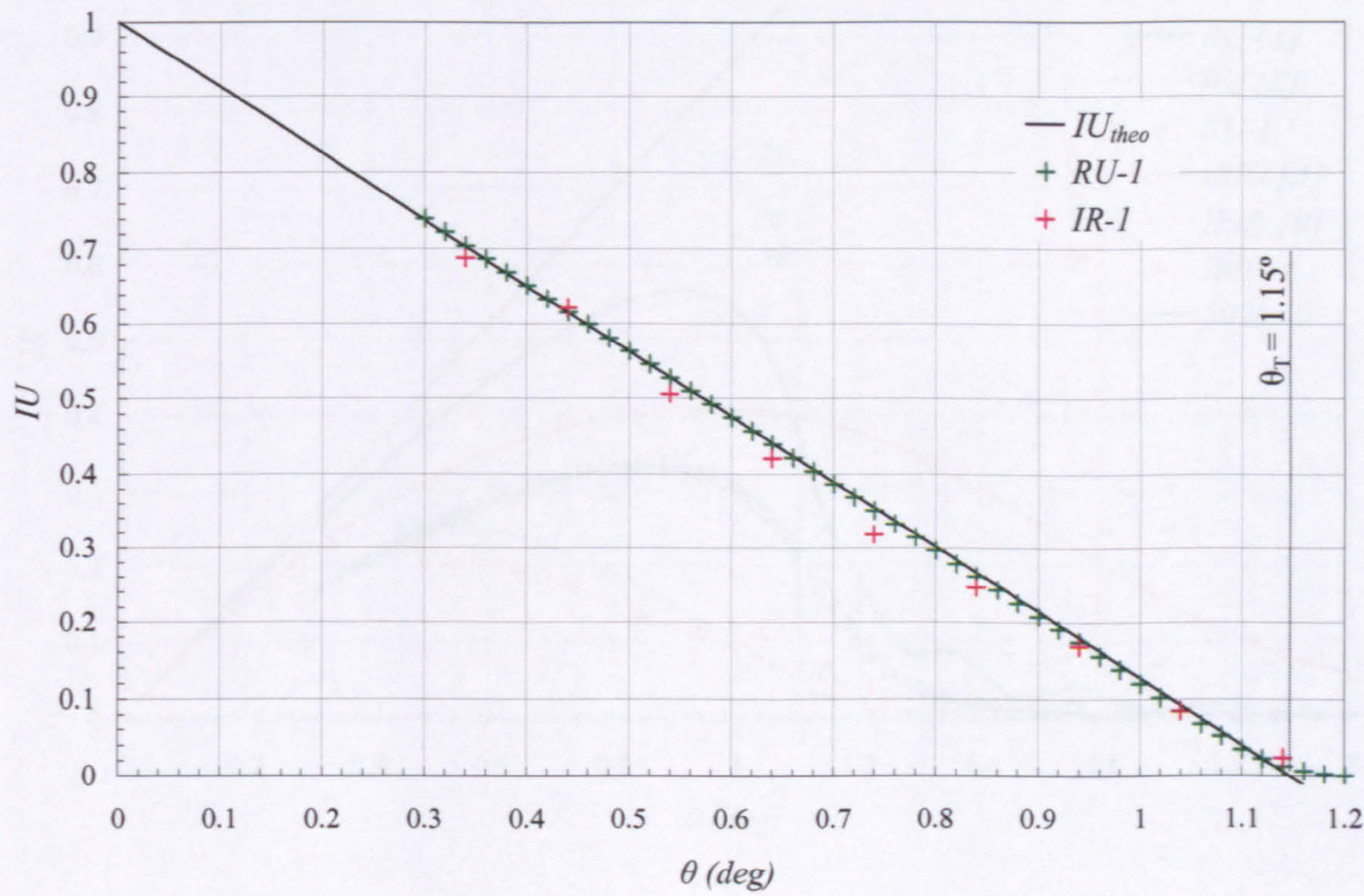


**Figure 5.11.** *IU as a function of grazing angle  $\theta$  for ruthenium and iridium-coated MCPs RU-1 and IRID-1. In each case,  $IU \rightarrow \sim 0$  as  $\theta \rightarrow \theta_T$ .*

The  $R(\theta)$  and  $IR(\theta)$  profiles of MCP IRID-1 in *Figures 5.10 and 5.12* are greatly suppressed compared to those theoretically generated using the IRID [A] model, although  $IU(\theta)$  closely conforms to the theoretical transmission through a 50:1 MCP (*Figure 5.11*). However, in this case, it appears that  $R(\theta) \rightarrow 1$  as  $\theta \rightarrow 0$ ; a fit to the IRID-1  $R(\theta)$  profile was generated at 2.8 keV using a model hereafter referred to as IRID [B]. IRID [B] is in fact almost identical to IRID [A], the only difference being an increase in modelled RMS roughness on the surface of the iridium coating; for IRID [B],  $\sigma = 26 \text{ \AA}$ , compared to  $\sigma = 10 \text{ \AA}$  of IRID [A]. Further experimental  $R(\theta)$  data from IRID-1 at 3.1 and 3.5 keV is fitted with the IRID [B] model in *Figure 5.13*. The  $R(\theta)$  and deduced  $IR(\theta)$  profiles of IRID [B] are plotted in *Figures 5.10 and 5.12* and would seem to provide a far better description of the IRID-1 iridium coating than those of IRID [A]. Referring to



the hypothesis made at the conclusion of *Section 5.3.4*, it may be possible that in the case of IRID-1, the cobblestone surface structure is not in evidence. In this case, if the ALD process could be optimised to reduce the RMS surface roughness of future iridium coatings, it may be able to provide the first metallised MCPs suitable for optical applications such as Lobster-ISS.

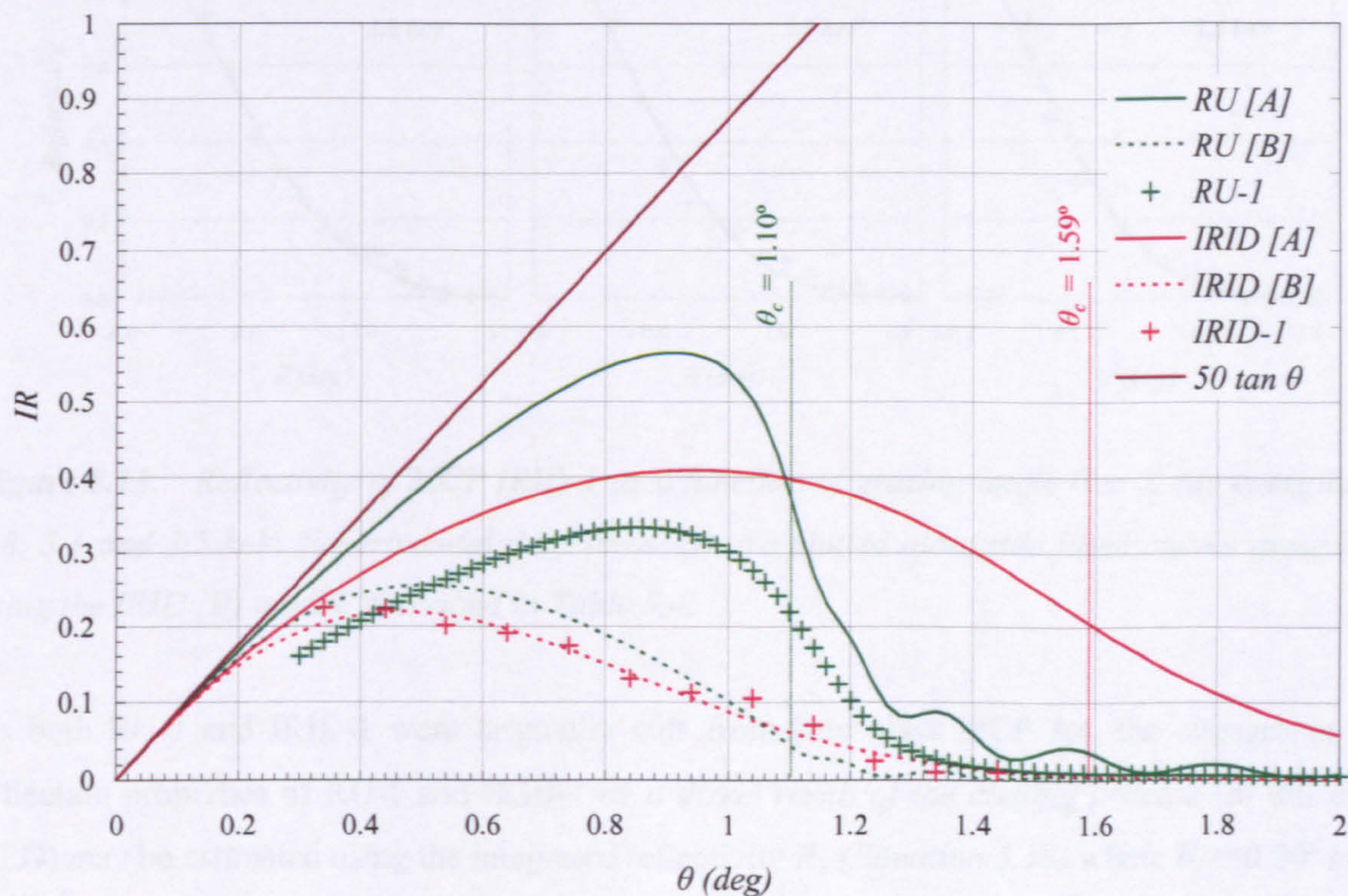


**Figure 5.12.** *IR as a function of grazing angle  $\theta$  for MCPs RU-1 and IRID-1 at 2.8 keV, compared with the theoretical models RU [A,B] and IRID [A,B]. Critical angles are calculated for RU [A,B] (green dashed line) and IRID [A,B] (red dashed line). The maximum rate of increase of IR with respect to  $\theta$  [ $50 \tan \theta$ ] is also shown (brown).*

A model RU [B] incorporates the same surface roughness as IRID [B],  $\sigma = 26 \text{ \AA}$  and is displayed for comparison with RU-1 in *Figures 5.10* and *5.12*. In this case, it is clear that  $\sigma_{\text{RU-1}} < \sigma_{\text{IRID-1}}$ . Critical angles for RU [A,B] and IRID [A,B] at 2.8 keV are calculated to be  $1.10^\circ$  and  $1.59^\circ$  respectively using *Equation 5.9*. The RU-1 profile in *Figure 5.12* would appear to be of the same form as that of RU [A] at the critical angle, which may suggest that the ruthenium has been deposited at approximately bulk density. This is not inconsistent with the AES depth profiles obtained from RU-1 in *Chapter 4*, which showed a relatively contaminant-free coating; of course, any low-Z element contamination would have the effect of reducing the bulk density of the coating. Although both  $R(\theta)$  and  $IR(\theta)$  of IRID-1 (shown in *Figures 5.10* and *5.12* respectively)



are negligible at  $\theta = \theta_c$ , we may infer from the IRID [B] fit that the iridium has been deposited at approximately bulk density.

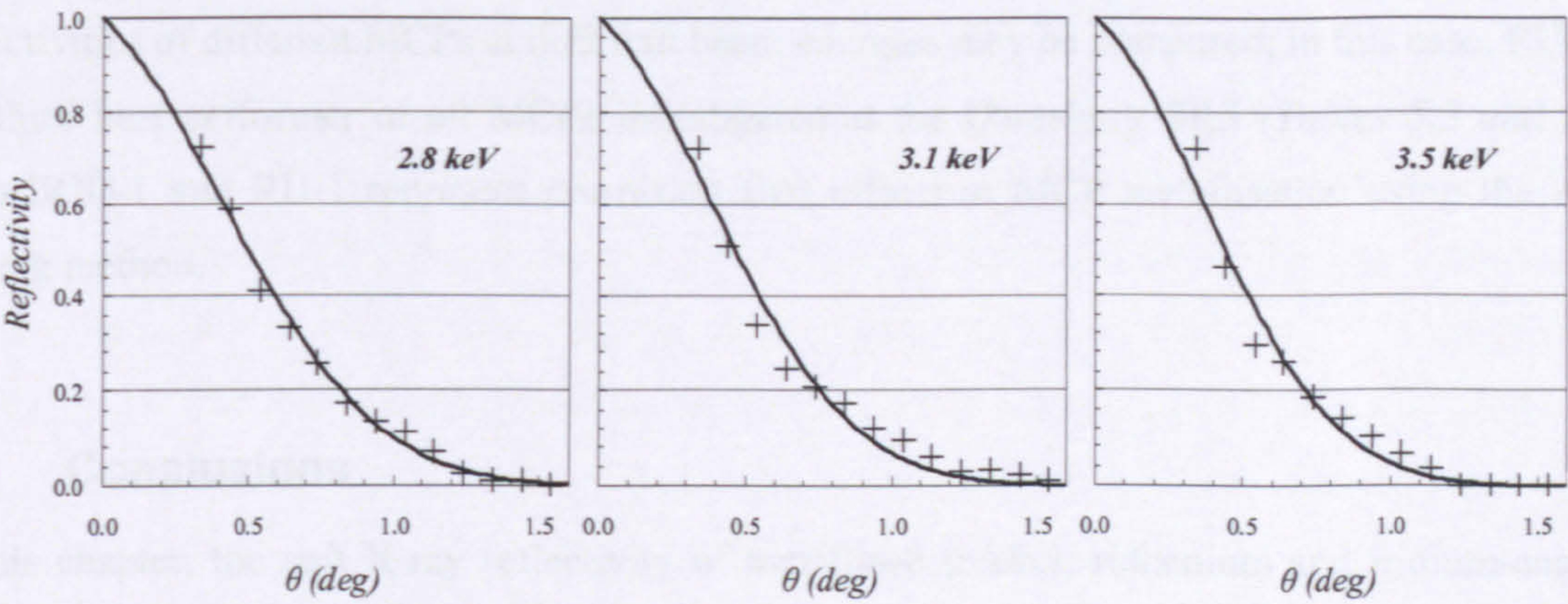


**Figure 5.13.** Reflectivity of MCP IRID-1 as a function of grazing angle  $\theta$  at X-ray energies of 2.8, 3.1 and 3.5 keV. Experimental data (crosses) are plotted alongside fitted curves generated using the IRID [B] model, described in Table 5.4.

As both RU-1 and IRID-1 were originally cuts from bare glass MCP A4, the changes in the reflection properties of RU-1 and IRID-1 as a direct result of the coating process (in this case ALD) may be estimated using the integrated reflectivity  $R_\Sigma$  (Equation 5.18) where  $\theta_i = 0.30^\circ$  and  $\theta_n = 2.00^\circ$  (as in Section 5.3.4). Values of  $R_\Sigma$  and  $X$  (Equation 5.19) for MCPs RU-1 and IRID-1 at 2.8 keV are shown in Table 5.5.

MCP	$R_\Sigma$	$X$
RU-1	21.99	1.59
IRID-1	14.25	1.03
A4	13.79	1.00

**Table 5.5.** Integrated reflectivities  $R_\Sigma$  of ruthenium-coated [RU-1], iridium-coated [IRID-1] and bare glass [A4] MCP optics at 2.8 keV. The ratio  $X$  (the integrated reflectivity normalised to that of bare glass MCP A4) is also shown. In the case of IRID-1,  $R_\Sigma$  was multiplied by a factor of 5 after the summation as the raw data was binned from  $\Delta\theta = 0.02^\circ$  to  $\Delta\theta = 0.1^\circ$  due to poor statistics.



The high RMS surface roughness of IRID-1 has suppressed  $R_{\Sigma}$  such that it is barely more efficient as a soft X-ray reflector than it was prior to its coating over the  $0.30^{\circ} \leq \theta \leq 2.00^{\circ}$  range; however *Figure 5.10* shows that the iridium has augmented  $R$  for  $\theta > 0.6^{\circ}$ . RU-1 is the more effective reflector at 2.8 keV, despite the low angle shortfall in  $R$ . Using the ratio  $X$ , integrated reflectivities of different MCPs at different beam energies may be compared; in this case, RU-1 is the third best performer of all MCPs investigated at the Daresbury SRS (*Tables 5.3 and 5.5*). Both IRID-1 and RU-1 represent promising first efforts at MCP metallisation using the ALD coating method.

## 5.4 Conclusions

In this chapter, the soft X-ray reflectivity of metallised (nickel, ruthenium and iridium-coated) and bare glass MCP optics was investigated.

### 5.4.1 Bare Glass MCPs [A4 and A8/1]

Reflectivity profiles as a function of grazing angle for bare glass MCPs A4 and A8/1 were fitted using similar intrachannel surface models, summarised in *Table 5.1*. As suggested from AES measurements (*Chapter 4*), in both cases the bare glass MCPs may be modelled as a silica-like, oxygen rich substrate. Modelled RMS surface roughnesses of 9 – 11 Å are consistent with previous measurements.

### 5.4.2 Nickel-coated MCPs

Reflectivity profiles of 12 nickel-coated MCP optics coated at different bath temperatures  $T_B$  and for different immersion times  $t_{IMM}$  were investigated, with higher bath temperatures [80 – 84 °C] appearing to provide the largest integrated reflectivity  $R_{\Sigma}$  over the measured grazing angle range. Minimising  $t_{IMM}$  appears to similarly provide larger  $R_{\Sigma}$ , but to a lesser degree. Only 4 of the 12 nickel-coated MCP optics significantly improved their efficiency as reflectors at 2.5 keV, in each case raising the critical angle for total external reflection.

Reflectivity shortfalls (compared to theory) in all 12 MCPs are observed over the extent of the measured grazing angle range  $0.30^{\circ} \leq \theta \leq 2.00^{\circ}$ . This is shown to be due to a shortfall in the reflected flux detected experimentally. Specular reflection from and absorption by a cobblestone



surface morphology of the coating is believed to be the cause. There appears to be no significant evidence of channel blockages due to the coating process.

#### **5.4.3 Ruthenium and Iridium-coated MCPs [RU-1 and IRID-1]**

Reflectivity shortfalls reported in nickel-coated MCPs are similarly observed in ruthenium-coated MCP RU-1, indicating that the shortfall is independent of coating process. No significant evidence of channel blockages in either RU-1 or IRID-1 was found. Tentative observation of the reflectivity profile of RU-1 indicates the coating is deposited at approximately bulk density, as would be expected from the purity of the coating determined as a function of depth in *Chapter 4*. The ruthenium coating applied to bare glass MCP A4 is determined to have improved the soft X-ray reflection efficiency by around 60 % over the measured  $0.30^\circ \leq \theta \leq 2.00^\circ$  range (RU-1).

Low grazing angle reflectivity shortfalls are not observed in MCP IRID-1; this is believed to imply that a relatively uniform iridium coating has been deposited, with island formation (and thus absorption) occurring to a lesser extent. A model of the MCP intrachannel reflecting surfaces was used to generate theoretical reflectivity profiles of IRID-1 as a function of grazing angle, which were fitted to those observed experimentally at 2.8, 3.1 and 3.5 keV; the RMS surface roughness was deduced to be of the order 26 Å, as opposed to an estimated 10 Å for RU-1. The iridium is modelled to have been deposited on MCP IRID-1 at bulk density. If the roughness can be reduced, there is great hope that the ALD (iridium) coating process may be capable of metallising MCP optics for use with Lobster-ISS.



## Chapter 6 The Projected Capabilities of Lobster-ISS

The metallisation of MCP optics will theoretically improve the high energy and wide angle response of Lobster-ISS. The Lobster-ISS Instrument Definition Document (IDD) (Bannister et al. 2004b) currently baselines a nickel coating, based on preliminary work undertaken on nickel-coated MCPs and the relative ease of application to MCPs in comparison to alternative electroplating methods. As discussed in previous chapters, alternative coatings (ruthenium, iridium and platinum) are now available; an assessment of the scientific return from Lobster-ISS for each MCP coating is therefore required in order to make an informed decision on whether the baseline optic coating selection should be changed. This chapter analyses the performance of each coating with regard to the astrophysical phenomena that Lobster-ISS will observe.

In order to model the performance of Lobster-ISS, we need a quantitative understanding of how the different metal coatings affect the MCP optic efficiency, and hence the telescope as a whole; for our purposes, this is performed using a piece of raytrace software named MCPTRACE. MCPTRACE was conceived by Brunton (1994) and subsequently developed by Price (2001) in order to model the observed defects associated with the first generation of MCP optics. What follows is a brief description of the principles of operation of the model, with a particular emphasis on the work in this chapter. Further detail may be found in Price (2001).

### 6.1 MCPTRACE: A Microchannel Plate X-ray Optic Raytrace Model

For the purposes of this thesis, rays are modelled from an infinite source, whose dimensions and shape are set such that they are equivalent to that of the focusing MCP, and are modelled with zero divergence. Incident rays are traced to the surface of the optic (slumped in this case) using simple vector algebra, each ray described using

$$\mathbf{r} = \mathbf{a} + t\mathbf{b} \tag{6.1}$$

where  $\mathbf{a}$  is a specified cartesian origin and  $\mathbf{b}$  is a unit vector direction, with position vector magnitude scaled by  $t$ . The origin of the system in the case of slumped MCP optics is located on the optical axis, at the position behind the optic where perpendicular vectors from the surface of the optic coincide (*Figure 6.1*).



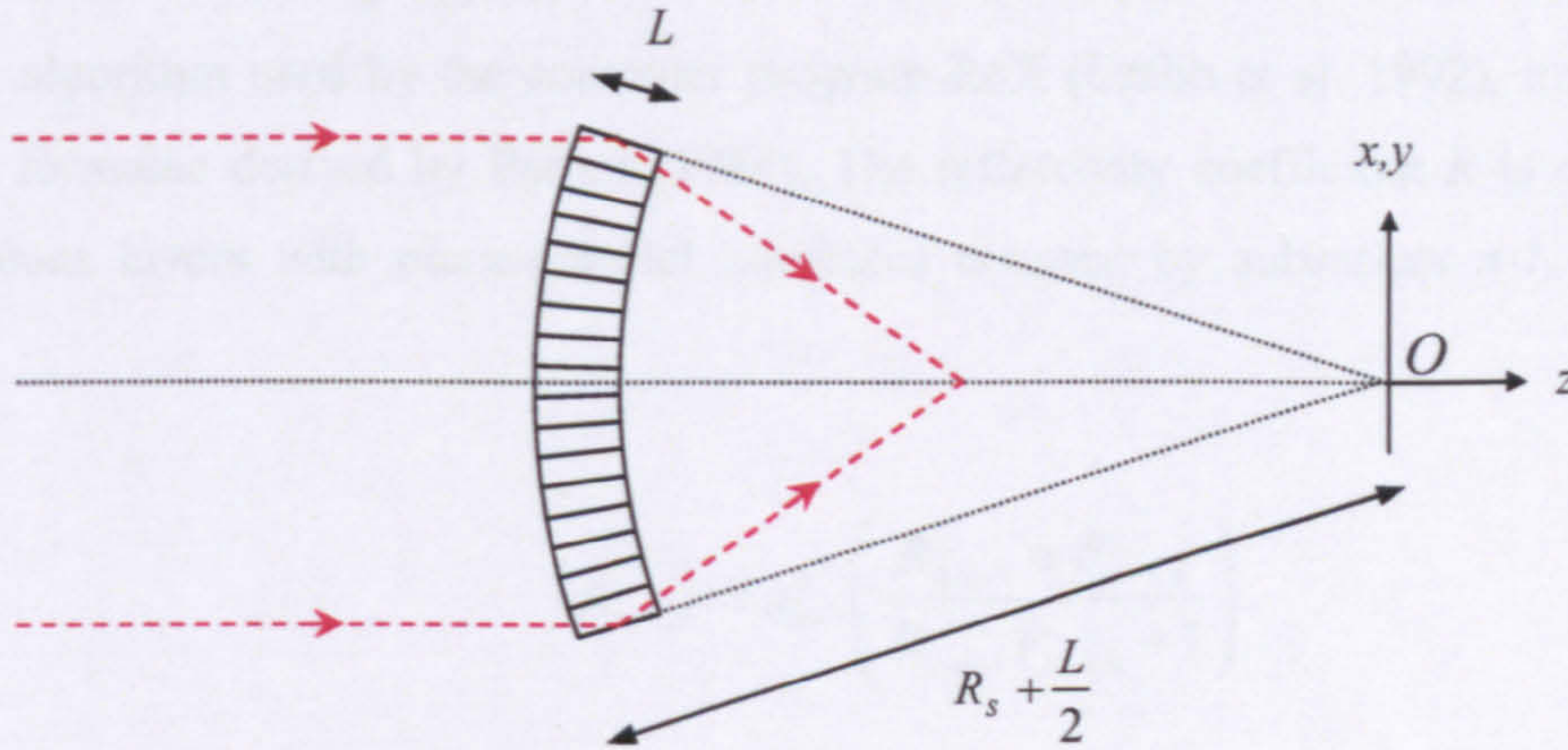


**Figure 6.1.** Geometric configuration of raytrace model for the purposes of this chapter, with the origin labelled  $O$ , located at the centre of curvature of the slumped MCP optic.

Based on this origin, ray interaction occurs where the following condition is satisfied:

$$\mathbf{r} \cdot \mathbf{r} = R_s^2 \quad (6.2)$$

At this juncture, the ray may either strike the inter-channel web, or enter a channel, where the probability of the latter is governed by the MCP open area fraction  $A_{open}$ . In the case of the former, the ray may be absorbed or transmitted through the web to a neighbouring channel using the method detailed in *Section 6.1.2*. If a ray gains entry to a particular channel, the coordinates are recorded and this channel becomes the optical axis of the system. The grazing angle at which the rays interact with the channel is determined only by the position at which the ray strikes the MCP and the radius of curvature of the slumped optic  $R_s$ , due to the incident rays all arriving parallel to one another, modelled from infinity.

The ray may now either be reflected from, absorbed by, or transmitted through the channel wall.

### 6.1.1 Reflection

When a ray is incident upon a channel surface, the probability of reflection, or reflectivity of the surface is calculated. Based on this reflectivity, a Monte Carlo process determines whether the ray is reflected or not. For the purposes of this work, the MCP channel surface is modelled as a



bi-layer; a metal coating applied over the MCP substrate. MCPTRACE incorporates the reflection algorithm used by the computer program ReX (Crabb et al. 1992), implementing the recursion formulae derived by Parratt (1954). The reflectivity coefficient  $R$  is calculated for  $n$  homogeneous layers with plane-parallel interfaces denoted by subscripts  $n-1$ ,  $n$  and  $n+1$  as follows:

$$R_{n-1,n} = a_{n-1}^4 \left( \frac{R_{n,n+1} + F_{n-1,n}}{R_{n,n+1} F_{n-1,n} + 1} \right) \quad (6.3)$$

where

$$F_{n-1,n} = \frac{f_{n-1} - f_n}{f_{n-1} + f_n} \quad (6.4)$$

and

$$f_n = (\theta^2 - \alpha_n - i\gamma_n)^{1/2} \quad (6.5)$$

The real and imaginary decrements from unity of the complex dielectric constant are denoted by  $\alpha$  and  $\gamma$  respectively and are calculated by a separate program, XOPT (Pearson et al. 2000). The grazing incidence angle of the X-ray is denoted  $\theta$ . The amplitude reduction factor  $a_n$  is defined at half the perpendicular layer depth  $d_n$  and is given by

$$a_n = \exp\left(-i \frac{\pi}{\lambda} f_n d_n\right) \quad (6.6)$$

Surface roughness is implemented using the scalar theory of Beckmann and Spizzichino (1963). The Fresnel coefficient is modified by the Debye-Waller factor such that

$$F'_{n-1,n} = F_{n-1,n} e^{-\frac{1}{2} \left( \frac{4\pi\sigma \sin(\theta)}{\lambda} \right)^2} \quad (6.7)$$

Where  $\sigma$  is the RMS surface roughness and  $\lambda$  is the X-ray wavelength.



### 6.1.2 Transmission

When a ray interacts with a channel surface and is not reflected (whether through striking the inter-channel web on the MCP face or the channel walls themselves) MCPTRACE calculates the probability of ray transmission through a thickness  $t$  of the MCP lead glass substrate using Beer's law (*Equation 6.8*) to determine whether the ray may eventually emerge into a channel.

$$\frac{I}{I_0} = e^{-\mu} \quad (6.8)$$

The linear absorption coefficient  $\mu$  may be written in terms of the wavelength and complex refractive index  $n = 1 - \delta - i\beta$  such that (Henke, 1981)

$$\mu = \frac{4\pi\beta}{\lambda} \quad (6.9)$$

In the X-ray region, the complex dielectric constant, defined  $K = 1 - \alpha - i\gamma$  is related to the refractive index  $n = 1 - \delta - i\beta$  as  $n = \sqrt{K}$ . Accordingly,  $\alpha \approx 2\delta$  and  $\gamma \approx 2\beta$  and thus we may express the linear absorption coefficient  $\mu$  ( $\text{\AA}^{-1}$ ) in *Equation 6.9* in terms of the imaginary complex dielectric coefficient  $\gamma$  and photon energy  $E$  (keV) as

$$\mu = \frac{2\pi\gamma E}{12.4} \quad (6.10)$$

In the event of specular reflection from the channel wall, a new ray is created at the vector position of reflection  $\mathbf{c}$ , of the form

$$\mathbf{r} = \mathbf{c} + s\mathbf{d} \quad (6.11)$$

where  $s$  is a scalar and  $\mathbf{d}$  is a unit vector describing the direction of the reflected ray. *Figure 6.2* shows that  $\mathbf{d}$  is calculated from the unit vector normal to the wall  $\hat{\mathbf{n}}$  and incident ray direction  $\mathbf{b}$  such that

$$\mathbf{d} = 2\hat{\mathbf{n}}\cos\phi_i + \mathbf{b} \quad (6.12)$$



where  $\phi_i$  is the angle of incidence. The ray is subsequently traced in this way until it emerges from the channel. For a total  $N_0$  rays, the number of rays traced to have an odd-odd, even-odd, odd-even and even-even number of reflections is recorded in an output file, along with those absorbed by the MCP web matrix, for a given input spectrum.

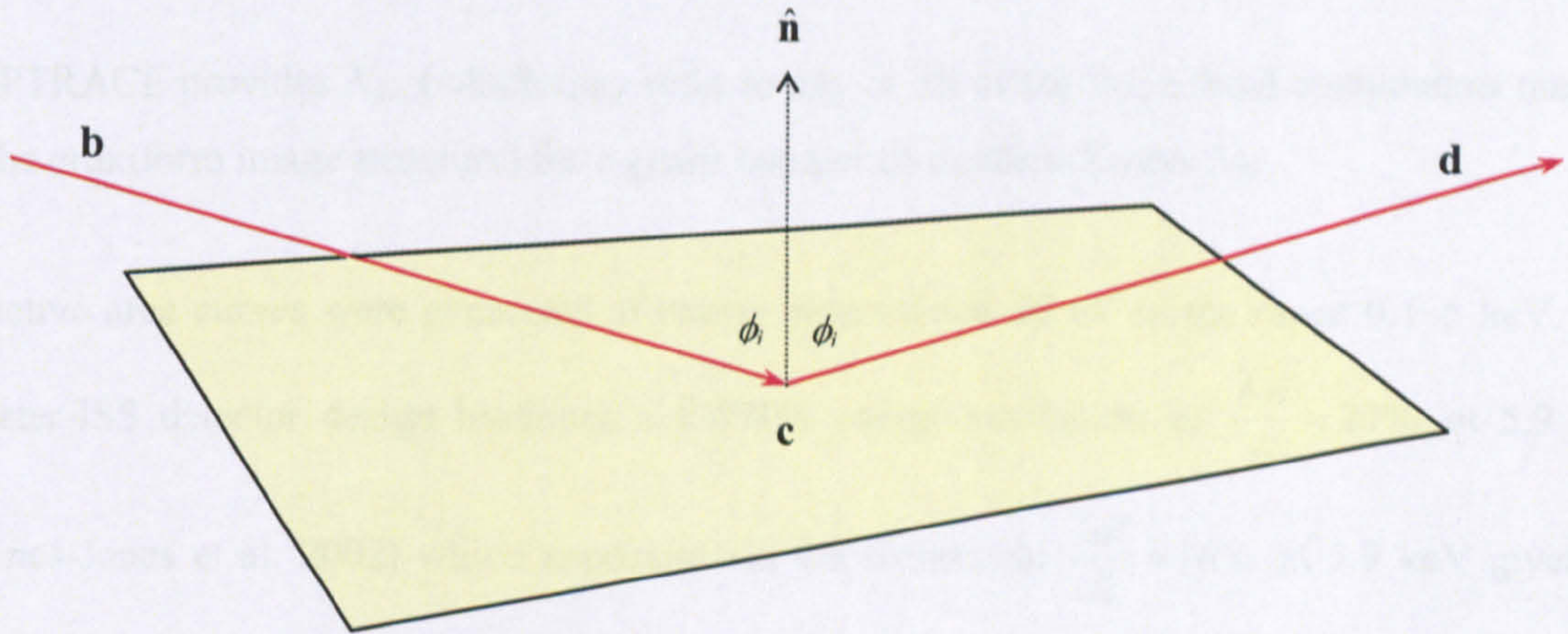


**Figure 6.2.** Specular reflection from a channel surface. An incident ray with vector direction  $\mathbf{b}$  is reflected from a plane (defined by a unit normal vector  $\hat{\mathbf{n}}$ ) at a position  $\mathbf{c}$ . The reflected ray propagates in a vector direction  $\mathbf{d}$ .

## 6.2 Effective Area of Lobster-ISS

The effective area  $A_{eff}$  of a telescope is a measure of its overall efficiency, taking into consideration parameters such as the collecting area of the optic, the transmission of the detector windows and the quantum efficiency of the focal plane detector. The calculation of  $A_{eff}$  provides a means of directly comparing different types of telescope operating within the same energy range, notwithstanding detector spatial and energy resolution effects. In the case of Lobster-ISS, the effective area of one module may be expressed as

$$A_{eff}(E) = \frac{N_{foc}(E)}{N_0} A_{geo} T_{win}(E) C_{Xe}(E) \quad (6.13)$$



Where	$A_{eff}$	=	Effective area (cm <sup>2</sup> )
	$E$	=	Photon energy (keV)
	$N_0$	=	Number of photons incident on telescope
	$N_{foc}$	=	Number of photons focused by MCP optic
	$A_{geo}$	=	Geometric area of a single Lobster-ISS optic module (cm <sup>2</sup> )
	$T_{win}$	=	Transmission through detector window
	$C_{Xe}$	=	Absorption of Xe-based counter gas at 1.5 atm

MCPTRACE provides  $N_{foc}$  (which may refer to any or all of the three focal components making up the cruxiform image structure) for a given number of incident X-rays  $N_0$ .

Effective area curves were generated at energy intervals of 50 eV in the range 0.1–5 keV. The Lobster-ISS detector design baselines a FWHM energy resolution of  $\frac{\Delta E}{E} \approx 20\%$  at 5.9 keV

(Deines-Jones et al. 2002) which approximates the theoretical  $\frac{\Delta E}{E} \approx 16\%$  at 5.9 keV given by

$\frac{\Delta E}{E} \approx \frac{0.4}{\sqrt{E}}$  (Fraser, 1989). The empirically generated figure of  $\frac{\Delta E}{E} \approx 20\%$  at 5.9 keV above

corresponds to  $\Delta E \approx 200$  eV at the lowest operating energy  $E \approx 250$  eV (*Figure 6.5.*). For the purposes of this work, MCPTRACE performs raytracing for a specified monochromatic energy, starting at 100 eV, and repeating for all energies at 50 eV intervals to a final 5 keV.  $N_{foc}$  (whether corresponding to true, line or diffuse focus) is then extracted from the output files generated from each of the 100 runs. Each run raytraced  $N_0 = 1 \times 10^6$  events.

In the current design, each Lobster-ISS optic module has a FOV of  $27^\circ \times 22.5^\circ$ , which at a radius of curvature of 750 mm, corresponds to an optic area  $A_{geo}$  of  $35.3 \times 29.5 = 1040$  cm<sup>2</sup>. For simplicity,  $A_{geo}$  was modelled using a square MCP of side  $\sqrt{1040} = 32.3$  cm. All modelled MCP parameters are summarised in *Table 6.1*.



<b><i>MCP size (mm)</i></b>	<b><i>323 x 323</i></b>
<b><i>Channel diameter D (μm)</i></b>	<b><i>20</i></b>
<b><i>Channel pitch P (μm)</i></b>	<b><i>24</i></b>
<b><i>Channel length L (μm)</i></b>	<b><i>1000</i></b>
<b><i>L:D</i></b>	<b><i>50:1</i></b>
<b><i>A<sub>open</sub></i></b>	<b><i>69%</i></b>
<b><i>R<sub>s</sub> (mm)</i></b>	<b><i>750</i></b>
<b><i>Coating thickness (Å)</i></b>	<b><i>250</i></b>
<b><i>Channel RMS surface roughness (Å)</i></b>	<b><i>10</i></b>
<b><i>Channels / multifibre</i></b>	<b><i>55 x 55</i></b>
<b><i>Packing format</i></b>	<b><i>SQUARE</i></b>
<b><i>MCP glass</i></b>	<b><i>Philips type 297</i></b>

**Table 6.1.** *MCP raytrace parameters used to generate effective area curves. All coatings are assumed to have bulk densities. The bare glass MCP has been modelled as an oxygen-enriched, 'silica-like' substrate with an O:Si concentration of 3:1 (by number) of density  $\rho = 1.860 \text{ g cm}^{-3}$  and RMS surface roughness  $9 \text{ Å}$  based on the reflectivity fits of MCP A8/1 achieved using experimental data in Chapter 5 (Figure 5.4).*

The five metal coatings to be investigated are nickel, iridium, ruthenium, platinum and gold. The development of coating techniques specific to microchannel plate optics (Ni, Ir, Ru, Pt) has taken place only in the past five years. This chapter contrasts their theoretical performance with that of gold, (used, for example, to coat the mirrors of XMM-Newton) and with the uncoated, bare glass MCP optic.

In order to determine the thickness of the coating to be modelled, we refer to the work of Henke et al. (1982), which suggests that at the critical angle for total external reflection  $\theta_c$ , the depth  $d_{1/e}$  (the  $\frac{1}{e}$  depth of a material through which 36.8% of rays are transmitted) is given by

$$d_{1/e} = \frac{\lambda}{2\pi\sqrt{2}\gamma} \quad (6.14)$$

For the purposes of reflection, the modelled penetration depth must be large enough such that a minimum of rays are transmitted through the coating. Any reflected ray observed is assumed to have been reflected at the depth  $d_{1/e}$  and is thus transmitted through the coating upon entering and



exiting the coating. For this reason, we double  $d_{1/e}$ , which will provide the minimum thickness of a material through which a maximum of 13.5% of rays are transmitted (the baseline for selecting the nominal coating thickness). Converting X-ray wavelength to energy  $E$ , the minimum coating thickness  $z$  (in Angstroms) is given by

$$z = \frac{12.4}{\pi E \sqrt{2\gamma}} \tag{6.15}$$

with the constant of proportionality selected such that energy  $E$  is given in keV. For all five coatings, a nominal thickness of 250 Å (Figure 6.3) satisfies the baseline conditions previously outlined over an energy range of 100 - 5000 eV.

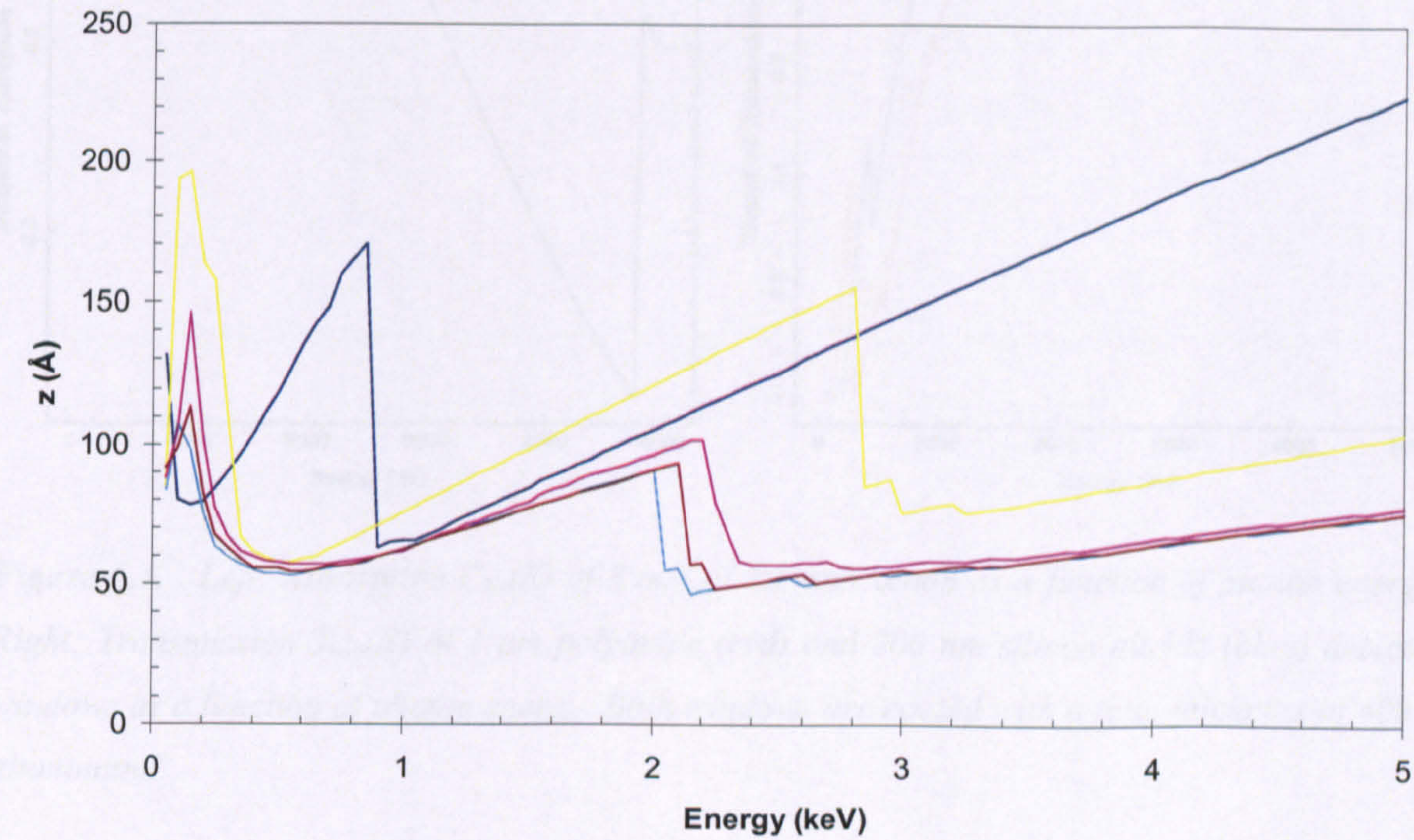


**Figure 6.3.** Variation in minimum coating thickness  $z$  at the critical angle for total external reflection with respect to photon energy for nickel (dark blue), ruthenium (yellow), iridium (turquoise), gold (magenta) and platinum (brown) coatings deposited at bulk density.  $L$  (Ni, Ru),  $M$  (all) and  $N$  (Ir, Pt, Au) shell absorption edges are present in the 0.1 - 5 keV waveband.

The baseline detector windows for Lobster-ISS are currently 1 µm polyimide (C<sub>22</sub>H<sub>10</sub>N<sub>2</sub>O<sub>5</sub>) coated with 400 Å aluminium, 200 Å on each side (Jahoda et al. 2000). As an alternative to



polyimide, a 200 nm silicon nitride ( $\text{Si}_3\text{N}_4$ ) window is currently under investigation (Fraser and Pearson, 2004), which, in conjunction with 400 Å of aluminium, theoretically provides 40% higher transmission below 1.8 keV and whose rigidity and low porosity may even eliminate the need for a gas replenishment system (Black et al. 2003). The X-ray transmission  $T_{\text{win}}$  of each of the proposed detector windows as a function of energy was calculated using *Equations 6.8 and 6.10* (with complex constants deduced from theoretically calculated atomic cross-sections of electron orbitals, given by Cromer and Liberman, 1970) with both polyimide and silicon nitride detector windows modelled at their bulk mass densities.

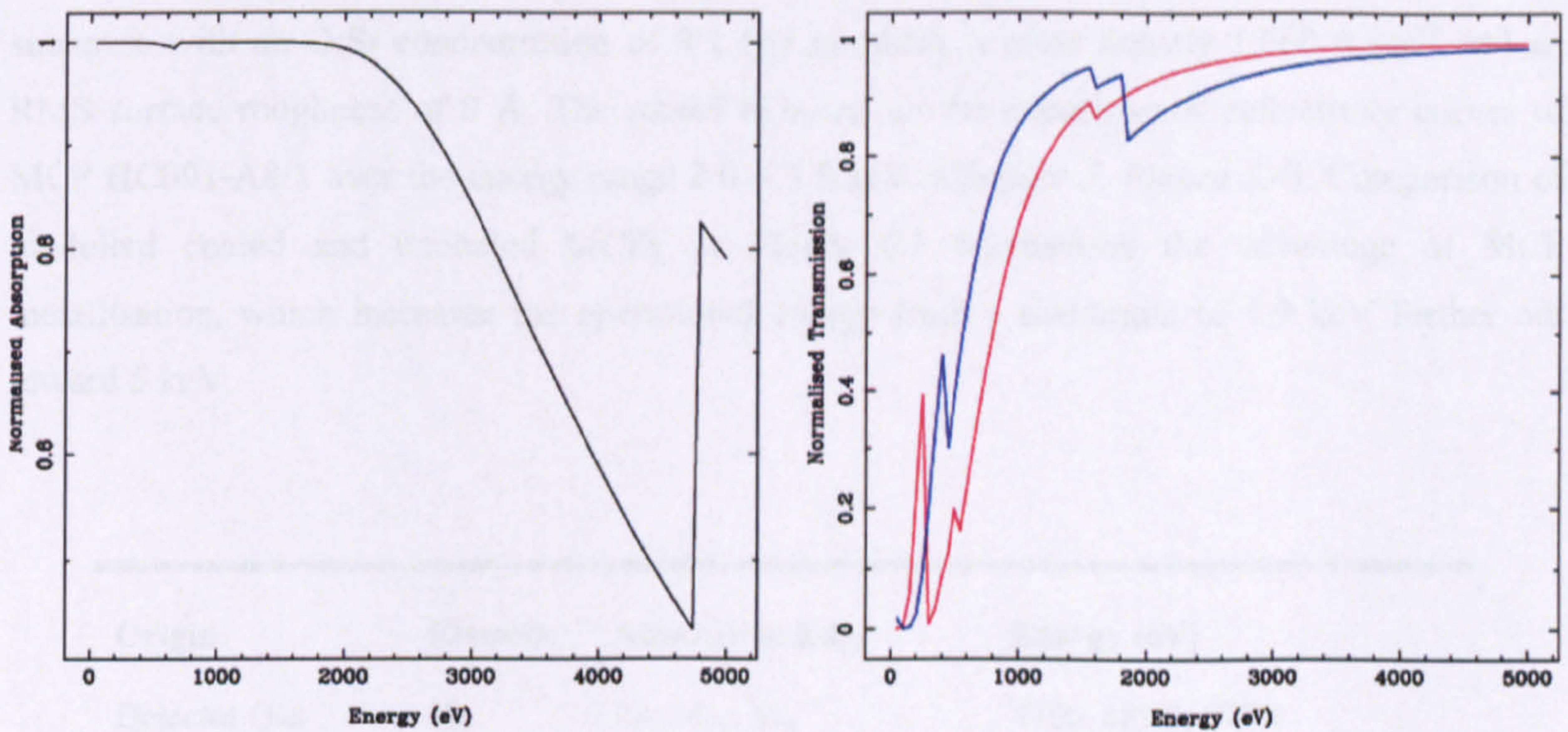


**Figure 6.4.** Left: Absorption  $C_{\text{Xe}}(E)$  of 3 mm of 1.5 atm xenon as a function of photon energy. Right: Transmission  $T_{\text{win}}(E)$  of 1  $\mu\text{m}$  polyimide (red) and 200 nm silicon nitride (blue) detector windows as a function of photon energy. Both windows are coated with a total thickness of 400 Å aluminium.

As discussed in *Chapter 3*, the Lobster-ISS microwell detectors have a quantum efficiency which may be modelled by the absorption of a baseline 1.5 atm of xenon gas. For Lobster-ISS, the concentration (by number) is 95% Xe working gas, mixed with a  $\text{CO}_2$  quench gas (5%). The presence of  $\text{CO}_2$  has a negligible effect on the absorption properties of the gas and is thus neglected. The absorption  $C_{\text{Xe}}(E)$  was deduced from  $1 - T_{\text{Xe}}(E)$  where the transmission is modelled using the same method as for the detector windows above. The mass density of xenon at Standard Temperature and Pressure is  $5.5 \text{ kg m}^{-3}$  (Lide, 1993) and assuming that the gas is ideal and at room temperature, the density was scaled by 1.5 times as  $P \propto \rho$  for an ideal gas, such



that  $\rho_{Xe,P=1.5\text{ atm}} = 8.25 \times 10^{-3} \text{ g cm}^{-3}$ . The absorption coefficient  $\mu(E)$  was estimated as above using this derived mass density of xenon. The nominal detector depth is 3 mm as detailed by Black et al. (2003). In both window transmission and xenon absorption cases,  $\mu(E)$  was calculated using the computer program XOPT (Willingale et al. 2000, Pearson et al. 2000). The calculated functions  $C_{Xe}(E)$  and  $T_{win}(E)$  used in the generation of the effective area curves are shown in *Figure 6.4*.

Lobster-ISS effective area as a function of energy and MCP optic coating are shown in *Figure 6.5*. All observed absorption edges for *Figures 6.3, 6.4 and 6.5* are shown in *Table 6.2*. A useful comparison shown is with a typical bare glass MCP optic, modelled as an oxygen-enriched silica substrate with an O:Si concentration of 3:1 (by number), a mass density  $1.860 \text{ g cm}^{-3}$  and an RMS surface roughness of 9 Å. The model is based on the experimental reflectivity curves of MCP HC001-A8/1 over the energy range 2.0 – 3.5 keV (*Chapter 5, Figure 5.4*). Comparison of modelled coated and uncoated MCPs in *Figure 6.5* emphasises the advantage of MCP metallisation, which increases the operational energy from a maximum of 1.9 keV further out toward 5 keV.

Origin	Element	Absorption Edge	Energy (eV)
Detector Gas	Xe	L <sub>III</sub> , M <sub>IV</sub> , M <sub>V</sub>	4786, 689.0, 676.4
Detector Windows and MCP Optic	C	K	284.2
	N	K	409.9
	O	K	543.1
	Al	K	1559.6
	Si	K	1839
MCP Coatings	Ni	L <sub>I</sub> , L <sub>II</sub> , L <sub>III</sub>	1008.6, 870.0, 852.7
	Ru	L <sub>I</sub> , L <sub>II</sub> , L <sub>III</sub>	3224, 2967, 2838
	Ir	M <sub>I</sub> , M <sub>II</sub> , M <sub>III</sub> , M <sub>IV</sub> , M <sub>V</sub>	3174, 2909, 2551, 2116, 2040
	Pt	M <sub>I</sub> , M <sub>II</sub> , M <sub>III</sub> , M <sub>IV</sub> , M <sub>V</sub>	3296, 3027, 2645, 2202, 2122
	Au	M <sub>I</sub> , M <sub>II</sub> , M <sub>III</sub> , M <sub>IV</sub> , M <sub>V</sub>	3425, 3148, 2743, 2291, 2206

**Table 6.2.** Absorption edges (*Figures 6.3, 6.4 and 6.5*) (Bearden and Burr, 1967; Cardona and Ley, 1978; Fuggle and Mårtensson (1980).



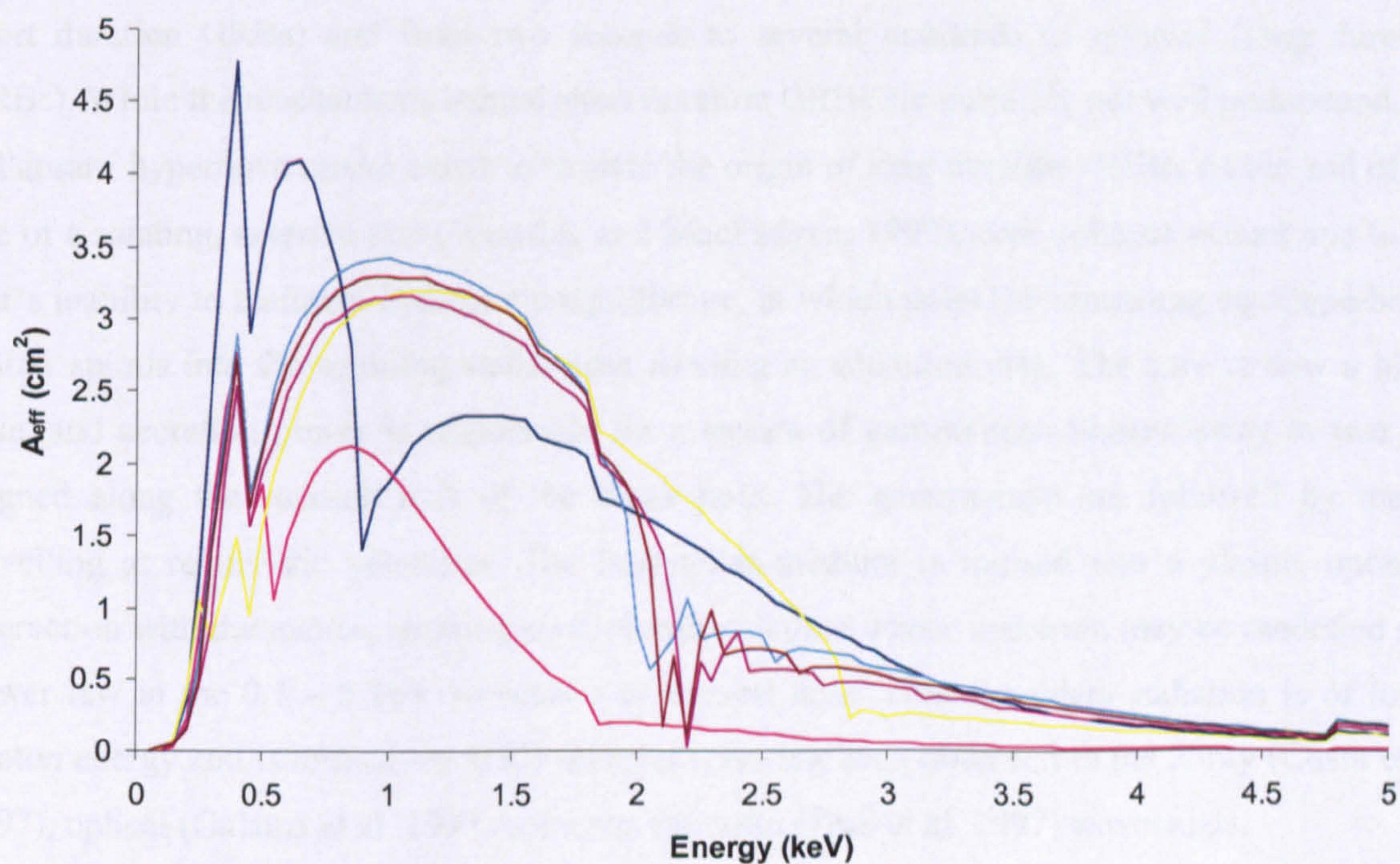
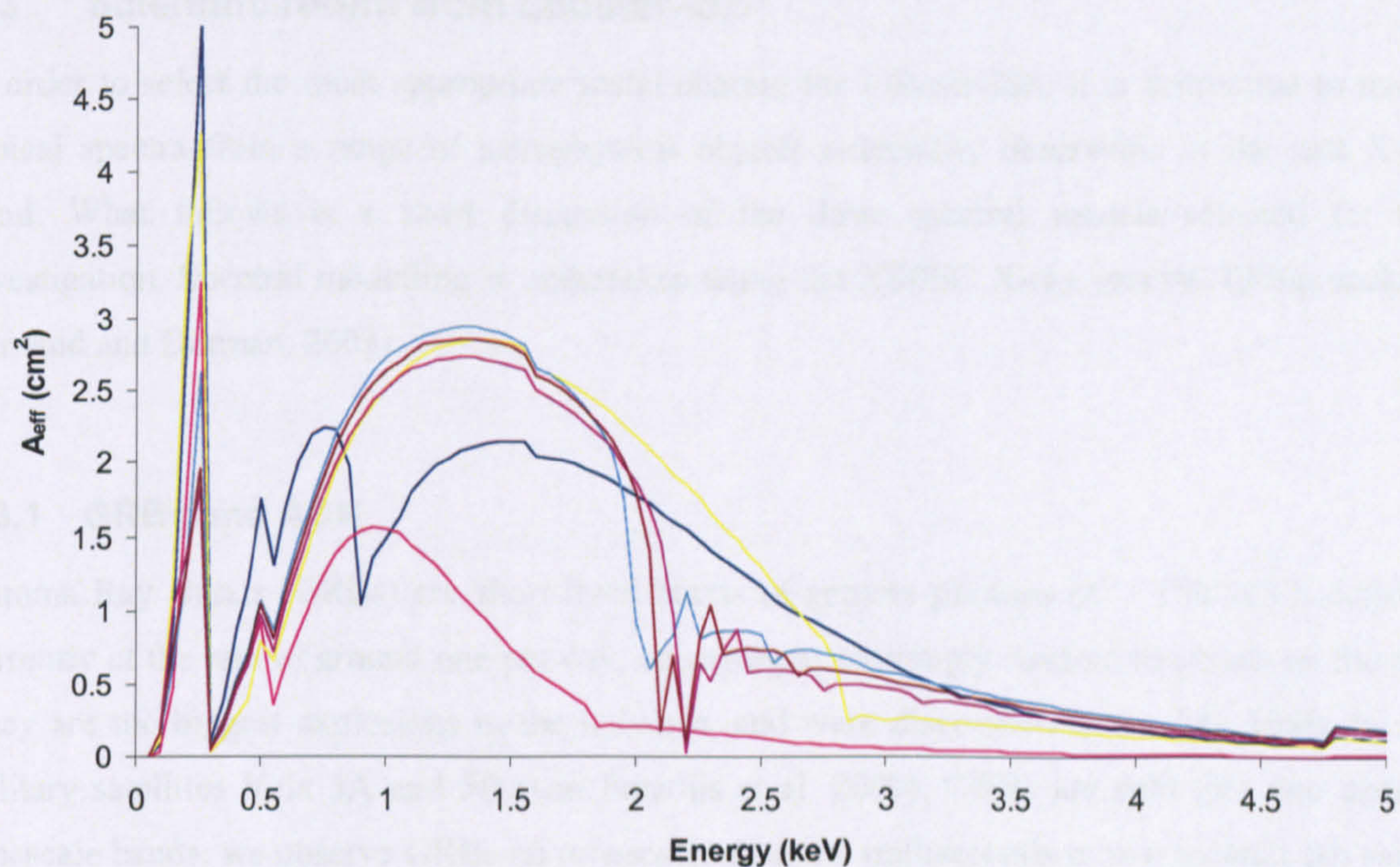


**Figure 6.5.** *Lobster-ISS true focus effective area as a function of X-ray energy with  $1\ \mu\text{m}$  polyimide (top) and  $200\ \text{nm}$   $\text{Si}_3\text{N}_4$  (bottom) detector windows. MCP optics are metallised with  $250\ \text{\AA}$  of nickel (dark blue), ruthenium (yellow), iridium (turquoise), gold (magenta) and platinum (brown). Lobster-ISS modelled with a bare glass MCP (pink) is shown for comparison.*



### 6.3 Scientific return from Lobster-ISS

In order to select the most appropriate metal coating for Lobster-ISS, it is instructive to model typical spectra from a range of astrophysical objects potentially observable in the soft X-ray band. What follows is a short discussion of the three spectral models selected for this investigation. Spectral modelling is undertaken using the XSPEC X-ray spectral fitting package (Arnaud and Dorman, 2003).

#### 6.3.1 GRBs and AGN

Gamma Ray Bursts (GRBs) are short-lived bursts of gamma photons ( $E > 100$  keV), detected currently at the rate of around one per day, occurring at seemingly random locations on the sky. They are the biggest explosions in the universe, and were discovered in the late 1960s by US military satellites Vela 5A and 5B (van Paradijs et al. 2000). GRBs are split into two distinct timescale bands; we observe GRBs on timescales of a few milliseconds to two seconds (so called short duration GRBs) and from two seconds to several hundreds of minutes (long duration GRBs). While the mechanisms behind short duration GRBs are currently not well understood, the collapsar / hypernova model exists to explain the origin of long duration GRBs. At the end of the life of a rotating, massive star (Woosley and MacFadyen, 1999), core collapse occurs due to the star's inability to maintain hydrostatic equilibrium, at which point the remaining envelope-based matter spirals into the spinning stellar core forming an accretion disk. The core is now a black hole, and accretion power is responsible for a stream of gamma-rays blasted away in two *jets* aligned along the rotation axis of the black hole. The gamma-rays are followed by matter travelling at relativistic velocities. The interstellar medium is ionised into a plasma upon its interaction with the matter, emitting synchrotron radiation whose spectrum may be modelled as a power law in the 0.1 – 5 keV waveband of interest here. This secondary radiation is of lower photon energy and is termed the GRB afterglow, having been observed in the X-ray (Costa et al. 1997), optical (Galama et al. 1997) and even the radio (Frail et al. 1997) wavebands.

The majority of galaxies are thought to host a largely inactive SuperMassive Black Hole (SMBH), where  $M_{SMBH} \approx 10^6 - 10^9 M_{SUN}$ ; however 1-10% of galaxies have bright cores, termed Active Galactic Nuclei (AGN) (Fabian et al. 2000). AGN are the most luminous sources in the universe with bolometric luminosities ranging from  $10^{40}$  to  $10^{48}$  erg s<sup>-1</sup>, and thus are excellent probes of the early universe, having been detected to redshifts of  $z \approx 6$  (Mathur et al. 2002). Matter orbiting the SMBH forms an accretion disk; viscous forces dissipate the initial angular



momentum of the orbiting matter leaving it to fall into the SMBH. Thermal bremsstrahlung radiation generated in the accretion disk is hypothesised to interact with a postulated hot coronal plasma above the surface of the more central regions of the accretion disk, where inverse Compton scattering modifies UV / optical photons to those in the X-ray band (Czerny and Elvis, 1987; Haardt and Maraschi, 1993) and is thought to be the mechanism behind the ‘soft X-ray excess’, commonly observed in AGN spectra (Page et al. 2004). The broad spectrum produced from the Comptonised X-ray radiation may be modelled to first approximation as a power law over the energy range of interest (0.1 – 5 keV) (O’Brien, 2004).

The power law adopted in this investigation for GRBs and AGN is modelled in XSPEC and takes the form

$$S_s(E)dE = K_{1keV} E^{-\Gamma} \quad (6.16)$$

where:	$S_s$	=	Source photon flux	(photon cm <sup>-2</sup> s <sup>-1</sup> keV <sup>-1</sup> )
	$K_{1keV}$	=	Spectral scaling parameter	(photon keV <sup>-1</sup> cm <sup>-2</sup> s <sup>-1</sup> at 1 keV)
	$\Gamma$	=	Photon index of power law	
	$E$	=	Photon energy	(keV)

For the purposes of this investigation, spectral models for both GRBs (Rol et al. 2005) and AGN (Nandra and Pounds, 1994) take the form  $K_{1keV} = 1$  photon keV<sup>-1</sup> cm<sup>-2</sup> s<sup>-1</sup> at 1 keV and  $\Gamma = 1.9$ .  $K_{1keV} = 1$  is simply a scaling factor that will be modified over the course of the investigation.

### 6.3.2 Stellar Coronae

The first evidence for the existence of extra-solar X-ray stellar coronae was presented by Catura et al. (1975). After a rocket flight in 1974, the star Capella was observed to show significant X-ray flux in the 0.2 – 1.6 keV waveband and was subsequently modelled to have a plasma electron temperature of around  $8 \times 10^6$  K and an X-ray luminosity of  $10^{31}$  erg s<sup>-1</sup>, the latter four orders of magnitude greater than that of the Sun (Güdel, 2004). The mechanisms pertaining to radiative energy generation are still poorly understood, yet EUV and X-ray emission from stellar atmospheres are widely accepted to originate in the corona, where plasma is confined within dynamic, closed magnetic loop structures, which themselves are believed to be generated through “dynamo action” (Bowyer et al. 2003). The X-ray emission from the solar corona is due to both



bremsstrahlung and line emission (Ness et al. 2004); solar models are currently the basis for the modelling of X-ray emission from other stellar coronae.

The spectral form of stellar coronae is modelled as an optically thin plasma, using the MEKAL code (Phillips et al. 1999, Kaastra and Mewe, 2000), applied in XSPEC. The spectra generated are typical of previously modelled sources, parameterised for this investigation with a plasma temperature  $kT = 1$  keV (*Capella*, Brinkman et al. 2000), a hydrogen density of  $1 \times 10^{10}$  atoms  $\text{cm}^{-3}$  (*Capella*, Ness et al. 2004, *Procyon*, Ness et al. 2001) and redshift  $z = 0$  (for galactic sources).

### 6.3.3 Cold Absorbers

Galactic interstellar dust in sufficient quantity is responsible for the suppression of low energy X-ray flux between emission and detection due to photoelectric absorption. The dust is modelled in XSPEC as a neutral (cold) hydrogen column of atomic density  $n_H$  using the Winconsin ABSorption (WABS) model (Morrison and McCammon, 1987), given by

$$C(E) = e^{-[n_H \sigma_p(E)]} \quad (6.17)$$

where  $\sigma_p(E)$  is the photoelectric cross-section and  $C(E)$  is the energy dependent absorption coefficient.  $C(E)$  is then multiplied with each of the above model input spectra  $S_S(E)$  to model a source spectrum subject to cold absorption. Two extremes of cold absorption will be investigated for both input spectra;  $n_H = 1 \times 10^{19}$  atoms  $\text{cm}^{-2}$  and  $n_H = 1 \times 10^{21}$  atoms  $\text{cm}^{-2}$ .

## 6.4 Modelling the Sensitivity of Lobster-ISS

Two types of effective area are calculated in order to determine the response of Lobster-ISS to point source and background photons (Priedhorsky et al. 1996). Using MCPTRACE, it is possible to estimate the effective area for each of the true, line and diffuse foci as a function of energy (*Figure 6.6*). In order to estimate the count rate  $N_{foc}(E)dE$  (photon  $\text{s}^{-1}$ ) from point sources expected in the true or line focus we multiply the relevant effective area distribution  $A_{eff}$  ( $\text{cm}^2$ ) by the source spectrum  $S_S(E)$  (photon  $\text{cm}^{-2} \text{s}^{-1} \text{keV}^{-1}$ ) generated in XSPEC such that

$$N_{foc}(E)dE = A_{eff}(E)S_S(E)dE \quad (6.18)$$



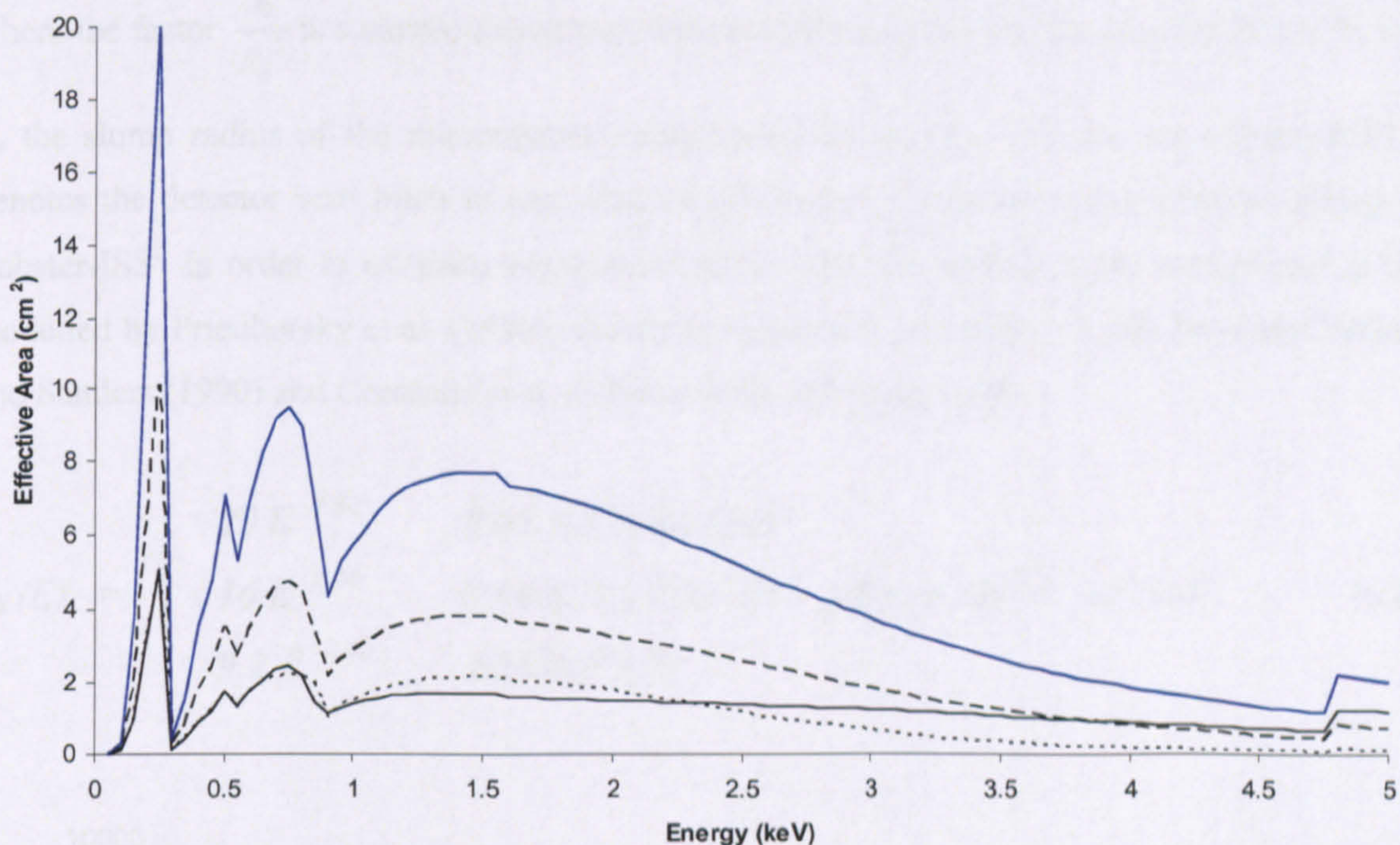


**Figure 6.6.** Effective areas  $A_{\text{eff}}$  for the true (dotted line), line (dashed line) and diffuse (solid line) foci as function of photon energy for the baseline lobster specification (Ni-coated MCPs, polyimide windows). The total effective area  $A_{\text{TOT}}$  is the sum of all three components (blue line).

The second effective area to be defined is  $A_{\text{TOT}}(\text{cm}^2)$ , which is the capability of the telescope to focus photons by any means (true, line and diffuse) and corresponds to the total active area of the telescope. The count rate at the detector  $N_{\text{TOT}}(E)dE$  (photon  $\text{s}^{-1}$ ) is given by

$$N_{\text{TOT}}(E)dE = A_{\text{TOT}}(E)S_S(E)dE \quad (6.19)$$

The response of Lobster-ISS to the diffuse X-ray background must take account of all focal components as it is projected onto the detector through all three mechanisms. The background rate per unit area at the detector  $n_b(E)dE$  (photon  $\text{pixel}^{-1} \text{s}^{-1}$ ) from a diffuse background spectrum  $S_B$  (photon  $\text{cm}^{-2} \text{s}^{-1} \text{sr}^{-1} \text{keV}^{-1}$ ) is defined as

$$n_b(E)dE = \frac{4}{R_s^2} P^2 A_{\text{TOT}}(E)S_B(E)dE \quad (6.20)$$



where the factor  $\frac{4}{R_s^2}$  is a simple conversion from steradians to  $\text{cm}^2$  on the detector ( $\text{sr cm}^{-2}$ ), with  $R_s$  the slump radius of the microchannel plate optics in cm ( $R_s = 75$  cm for Lobster-ISS).  $P$  denotes the detector well pitch in cm, where a pitch of  $P = 0.04$  cm is currently baselined for Lobster-ISS<sup>i</sup>. In order to estimate background rates  $n_b(E)$ , the diffuse X-ray background is that modelled by Friedhorsky et al. (1996), shown in *Figure 6.7*, according to data from McCammon and Sanders (1990) and Comastri et al. (1994) (Peele, 2004), given by

$$S_B(E) = \begin{array}{ll} 20 E^{-1.89} & 0.05 \leq E \leq 0.44 \text{ keV} \\ 16 E^{-2.16} & 0.44 \leq E \leq 2.23 \text{ keV} \\ 9.2 E^{-1.47} & 2.23 \text{ keV} \leq E \end{array} \text{ photon cm}^{-2} \text{ s}^{-1} \text{ sr}^{-1} \text{ keV}^{-1} \quad (6.21)$$

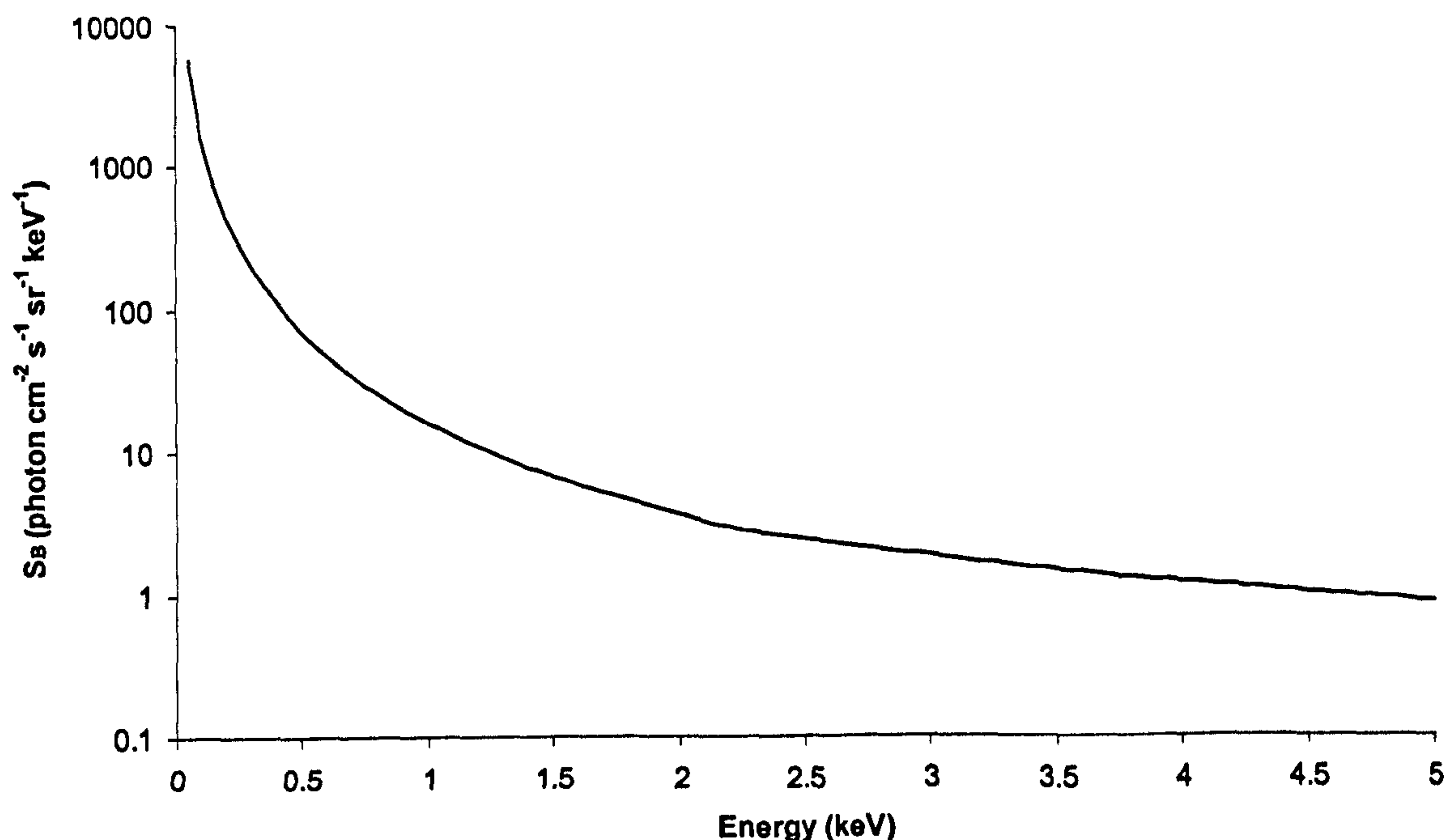


**Figure 6.7.** The diffuse X-ray background modelled as a function of photon energy.

<sup>i</sup> The Lobster-ISS microwell detector is not a pixellated detector; the readout signal is a continuous measure of position. Although the spatial resolution of the detector has been measured at 250  $\mu\text{m}$  (Black et al. 2003), the spatial resolution of Lobster-ISS is dominated by that of the MCP optics, with the Full Width at Zero Maximum (FWZM) angular resolution corresponding to a spatial resolution of  $\sim 400$   $\mu\text{m}$  due to the pyramidal photon distribution in the central focus; so for the purposes of this investigation, we treat signal and background events as occurring within units of square area  $P$ , hereafter referred to as ‘pixels’.



The image of a point source on the detector will occupy a square area  $A$  on an assumed flat detector calculated using basic geometry as

$$A = \left( \frac{R_s}{2} \right)^2 (\Delta\theta)^2 \quad (6.22)$$

where  $\Delta\theta$  is the angular resolution of the telescope in radians (a goal of 4 arcmin or  $1.16 \times 10^{-3}$  rad is envisaged for Lobster-ISS; this figure is assumed for modelling in this chapter). For Lobster-ISS,  $A = 1.90 \times 10^{-3} \text{ cm}^2$ , which is larger than the detector pixel area of  $1.6 \times 10^{-3} \text{ cm}^2$ , thus it can not be assumed that (for the true focus) every event will wholly take place in one detector pixel. For the purposes of this investigation, the worst case scenario of each event taking place over 4 detector pixels is assumed, which will provide conservative sensitivity calculations. When examining a combination of true and line foci, the event is assumed to occur over a total of 146 pixels based on the theoretical area of the projection of the point source at the detector. The extent of the crossarms on the detector is based on the maximum transmission angle of the MCP  $\theta_T$  and the optic-detector distance  $\frac{R_s}{2}$ . The angular extent of the cross arms is  $2\theta_T \sim 2.3^\circ$ . The central focus and crossarms occupy an area of  $0.23 \text{ cm}^2$  on the detector, corresponding to 146 pixels. Over an integration time  $t$  (s), the total number of background photons  $N_B$  detected in the energy range 0.1 – 5 keV may be represented as

$$N_B = tN_p \int_{0.1}^5 n_b(E) dE \quad (6.23)$$

where  $N_p$  is the total number of pixels across which an event is measured; i.e.  $N_p = 4$  when the true focus only is used in collecting source counts, with  $N_p = 146$  for true and line focus. All integrals in this section are evaluated numerically, through the summation of 100 energy bins, each of width  $dE = 50 \text{ eV}$  from 0.1 – 5 keV.

The Lobster-ISS total detector background is dominated by the diffuse X-ray background, estimated using *Equations 6.20 – 6.23* at the rate of  $0.68 \text{ photon cm}^{-2} \text{ s}^{-1}$  (0.1 – 5 keV). The particle background, in contrast is of order  $10^{-3} \text{ count cm}^{-2} \text{ s}^{-1}$  assuming (for the Lobster-ISS focal plane detector) a ROSAT PSPC particle event rejection efficiency of 99.5% (Fraser 1989, Mason and Culhane 1983).



Over an integration time  $t$  (s), the total number of source photons  $N_s$  detected in the energy range 0.1 – 5 keV may be represented as

$$N_s = t \int_{0.1}^5 N_{\text{src}}(E) dE \quad (6.24)$$

The detection significance of the source flux  $\sigma$  is given by

$$\sigma = \frac{N_s}{\sqrt{N_s + N_b}} \quad (6.25)$$

For the purposes of this investigation, an event is said to be detected if  $\sigma \geq 5$  (corresponding to a 99.99997% confidence). The number of source counts  $N_{s,5\sigma}$  required as a function of  $N_b$  over a given time period for a  $5\sigma$  detection is thus given by

$$N_{s,5\sigma} = \frac{25 + \sqrt{625 + 100N_b}}{2} \quad (6.26)$$

where a minimum of 25 photons is required for a  $5\sigma$  detection. Each input source spectrum is scaled by a factor  $F = \frac{N_s}{N_{s,5\sigma}}$  such that the condition for a  $5\sigma$  detection in Equation 6.26 is satisfied. The limiting energy flux  $G_{LIM}$  ( $\text{erg s}^{-1} \text{ cm}^{-2}$ ) or sensitivity of Lobster-ISS is thus defined by:

$$G_{LIM} = \frac{1.60 \times 10^{-9}}{F} \int_{0.1}^5 E S_s(E) dE \quad (6.27)$$

where  $1 \text{ erg} = 6.24 \times 10^8 \text{ keV}$  or  $1 \times 10^{-7} \text{ J}$ .

Sensitivity  $G_{LIM}$  is often expressed in units of Crabs, pertaining to the limiting energy flux we measure at Earth from the Crab Nebula. The Crab Nebula source spectrum  $S_C$  ( $\text{photon cm}^{-2} \text{ s}^{-1} \text{ keV}^{-1}$ ) is modelled by Priedhorsky et al. (1996) as



$$S_C(E) = 10E^{-2.05} \exp[-(0.7E^{-2.47})] \quad (6.28)$$

where interstellar absorption is approximated by the exponential term. In this waveband, the limiting energy flux  $G_C$  ( $\text{erg cm}^{-2} \text{ s}^{-1}$ ) is estimated using the following relation

$$G_C = 1.60 \times 10^{-9} \int_{0.1}^5 ES_C(E) dE \quad (6.29)$$

where 1 Crab is found to correspond to a measured energy flux of  $2.36 \times 10^{-8} \text{ erg cm}^{-2} \text{ s}^{-1}$  from 0.1 – 5 keV.

## 6.5 Discussion

The limiting X-ray (0.1 – 5 keV) energy flux  $G_{LIM}$  ( $\text{erg cm}^{-2} \text{ s}^{-1}$ ) incident on Lobster-ISS required for a  $5\sigma$  detection of the modelled input sources outlined in *Section 6.4* is a measure of the sensitivity of the telescope. In this section,  $G_{LIM}$  is presented as a function of selected foci, exposure time, detector window, input source and galactic cold absorption in order to indicate the most appropriate metal coating for the Lobster-ISS MCP optics (*Table 6.3*). Results from this investigation are based on the average 400 s exposure / ISS orbit; the exposure time per orbit does however vary (up to 1800 s / ISS orbit) depending on the position of the source in the FOV (*Chapter 3*).

A potential concern is whether counts detected from both line and true foci from point sources of interest (as opposed those from the true focus alone) are necessary to improve the sensitivity of Lobster-ISS. In such an event, deconvolution algorithms are required to redistribute counts from the line focus into the true focus for imaging purposes (Peele, 2000). In the case of both true and line foci (hereafter denoted  $T+L$ ), the total background over a constant integration time is 146 / 4 times larger than in the case of the single true focus (hereafter denoted  $T$ ), due to the geometric projection of the foci onto the detector (as discussed in the previous section). For the initial orbits, for all combinations of MCP optic coating, detector window and input spectra,  $G_{LIM}(T+L) < G_{LIM}(T)$ ; the enhanced effective area from both true and line foci increasing the number of detected photons despite the 146 / 4 factor increase in background counts. However, it may be shown that the time evolution of  $G_{LIM}$  is described by



$$G_{LIM}(t) = \frac{1.60 \times 10^{-9} \int_{0.1}^5 E S_S(E) dE}{2 \int_{0.1}^5 A_{eff}(E) S_S(E) dE} \left( \frac{1}{t} \right) \left[ \sigma^2 + \left( \sigma^4 + \frac{16 \sigma^2 P^2 N_P t}{R^2} \int_{0.1}^5 A_{TOT}(E) S_B(E) dE \right)^{\frac{1}{2}} \right] \quad (6.30)$$

Examination of Equation 6.30 for a given MCP coating, detector window and input spectra reveals that the component in the square bracket is responsible for the “dampening effect” of the time evolution of  $G_{LIM}$  (Figure 6.8). The  $N_P$  term has the capacity to flatten the gradient of the time evolution curves, with increasing effect with increased  $N_P$  (the larger the number of pixels an event takes place over, the higher the background for that event and the higher the limiting flux at a given exposure time). Hence, after a number of orbits  $N_{ORB}$  we expect

$G_{LIM}(T) < G_{LIM}(T+L)$ ; at this juncture, it is no longer appropriate to include photons from the line foci as the background now dominates in this region of the detector. The variation in  $N_{ORB}$  as a function of MCP coating, detector window and source spectra are displayed in Table 6.4.

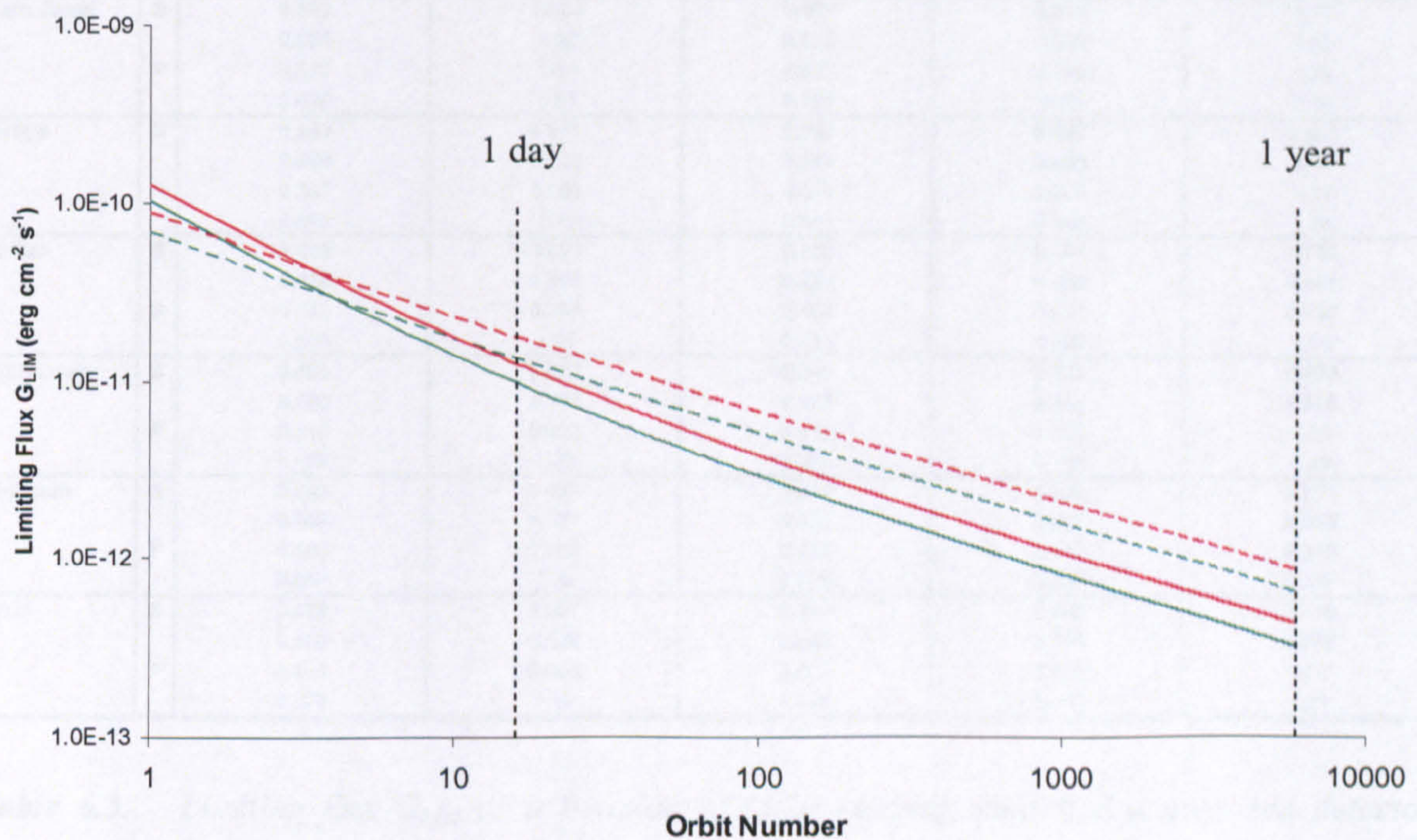


**Figure 6.8.** Time evolution of limiting flux  $G_{LIM}$  for nickel coated MCP optics in combination with a polyimide (red) or silicon nitride (green) detector windows. Dashed lines indicate the contribution of both line and true foci to  $G_{LIM}$ , with solid lines denoting contributions from the true focus only.



		$G_{\text{LIM}} [\times 10^{-13} \text{ ergs cm}^{-2} \text{ s}^{-1}]$				
		AGN/GRB (min)	AGN/GRB (max)	Coronal (min)	Coronal (max)	Crab Nebula
Bare Glass	S	1.58	2.59	1.46	1.55	4.88
		<b>3.06</b>	<b>5.04</b>	<b>2.98</b>	<b>3.21</b>	<b>9.16</b>
	P	1.54	4.81	1.86	2.37	6.87
		<b>2.99</b>	<b>9.16</b>	<b>3.78</b>	<b>4.90</b>	<b>12.5</b>
Nickel	S	1.15	1.77	1.29	1.46	3.21
		<b>2.26</b>	<b>3.49</b>	<b>2.57</b>	<b>2.92</b>	<b>6.39</b>
	P	1.14	3.16	1.61	2.27	4.22
		<b>2.25</b>	<b>6.26</b>	<b>3.21</b>	<b>4.60</b>	<b>8.44</b>
Iridium	S	1.31	1.61	1.02	0.97	2.33
		<b>2.57</b>	<b>3.16</b>	<b>2.02</b>	<b>1.92</b>	<b>4.58</b>
	P	1.38	2.45	1.24	1.34	2.89
		<b>2.71</b>	<b>4.82</b>	<b>2.46</b>	<b>2.67</b>	<b>5.69</b>
Ruthenium	S	1.40	1.67	1.06	0.97	2.16
		<b>2.78</b>	<b>3.34</b>	<b>2.12</b>	<b>1.95</b>	<b>4.37</b>
	P	1.15	3.10	1.39	1.73	3.46
		<b>2.28</b>	<b>6.30</b>	<b>2.79</b>	<b>3.52</b>	<b>7.07</b>
Platinum	S	1.34	1.62	1.03	0.97	2.33
		<b>2.63</b>	<b>3.19</b>	<b>2.05</b>	<b>1.94</b>	<b>4.61</b>
	P	1.41	2.48	1.26	1.35	2.91
		<b>2.78</b>	<b>4.88</b>	<b>2.50</b>	<b>2.70</b>	<b>5.74</b>
Gold	S	1.40	1.65	1.05	0.98	2.34
		<b>2.75</b>	<b>3.25</b>	<b>2.10</b>	<b>1.96</b>	<b>4.63</b>
	P	1.40	2.65	1.31	1.45	3.09
		<b>2.76</b>	<b>5.24</b>	<b>2.61</b>	<b>2.91</b>	<b>6.13</b>

		$G_{\text{LIM}} [\times 10^{-11} \text{ ergs cm}^{-2} \text{ s}^{-1}]$				
		AGN/GRB (min)	AGN/GRB (max)	Coronal (min)	Coronal (max)	Crab Nebula
Bare Glass	S	0.549	0.903	0.507	0.539	1.70
		<b>0.651</b>	<b>1.07</b>	<b>0.632</b>	<b>0.682</b>	<b>1.95</b>
	P	0.513	1.60	0.622	0.790	2.29
		<b>0.630</b>	<b>1.93</b>	<b>0.797</b>	<b>1.03</b>	<b>2.63</b>
Nickel	S	0.350	0.537	0.392	0.442	0.973
		<b>0.468</b>	<b>0.722</b>	<b>0.531</b>	<b>0.605</b>	<b>1.32</b>
	P	0.337	0.929	0.475	0.669	1.24
		<b>0.463</b>	<b>1.29</b>	<b>0.661</b>	<b>0.946</b>	<b>1.74</b>
Iridium	S	0.426	0.524	0.333	0.316	0.759
		<b>0.539</b>	<b>0.662</b>	<b>0.424</b>	<b>0.402</b>	<b>0.961</b>
	P	0.442	0.788	0.400	0.431	0.930
		<b>0.566</b>	<b>1.01</b>	<b>0.515</b>	<b>0.558</b>	<b>1.19</b>
Ruthenium	S	0.480	0.571	0.363	0.333	0.738
		<b>0.590</b>	<b>0.708</b>	<b>0.449</b>	<b>0.414</b>	<b>0.925</b>
	P	0.340	0.917	0.412	0.512	1.02
		<b>0.469</b>	<b>1.30</b>	<b>0.575</b>	<b>0.725</b>	<b>1.46</b>
Platinum	S	0.443	0.536	0.342	0.322	0.771
		<b>0.554</b>	<b>0.671</b>	<b>0.431</b>	<b>0.407</b>	<b>0.969</b>
	P	0.460	0.805	0.410	0.440	0.945
		<b>0.583</b>	<b>1.02</b>	<b>0.525</b>	<b>0.566</b>	<b>1.20</b>
Gold	S	0.472	0.557	0.357	0.332	0.790
		<b>0.580</b>	<b>0.686</b>	<b>0.443</b>	<b>0.414</b>	<b>0.978</b>
	P	0.451	0.853	0.422	0.466	1.00
		<b>0.578</b>	<b>1.10</b>	<b>0.547</b>	<b>0.608</b>	<b>1.28</b>

**Table 6.3.** Limiting flux  $G_{\text{LIM}}$  as a function of MCP coating, modelled source and detector window after 1 year (top) and one day (bottom). Bracketed comments min and max refer to the level of cold absorption modelled in each source spectra ( $1 \times 10^{19}$  and  $1 \times 10^{21}$  atom  $\text{cm}^{-2}$  respectively). Contributions to  $A_{\text{eff}}$  from the true focus only (black) and a combination of both true and line foci (blue) are also shown, with silicon nitride (bold text) and polyimide (standard text) detector windows denoted S and P respectively.



$N_{ORB}$  is found to range from 3 or 4 orbits (Ni and Ru, polyimide) to 10 orbits (bare glass, silicon nitride), or to a maximum of  $N_{ORB} = 7$  orbits for coated MCPs. This means that with the baseline nickel-coated MCPs and polyimide detector windows, any event occurring on a timescale of under 4.5 hours (assuming a 90 minute ISS orbit) would be best observed using data from a combination of true and line foci. For alternative coatings (Pt, Ir, Au) the timescale is as long as 10.5 hours.

Coating	W	$N_{ORB}$				
		AGN/GRB (min)	AGN/GRB (max)	Coronal (min)	Coronal (max)	Crab Nebula
Bare Glass	S	9	9	7	7	10
	P	7	8	6	6	9
Nickel	S	5	5	5	5	5
	P	4	4	4	4	3
Iridium	S	7	7	6	6	6
	P	6	6	6	6	6
Ruthenium	S	7	7	7	7	7
	P	4	4	4	4	3
Platinum	S	7	7	7	7	7
	P	6	6	6	6	6
Gold	S	7	7	7	7	7
	P	6	6	6	6	6

**Table 6.4.** Variation in the number of modelled, complete orbits  $N_{ORB}$  as a function of modelled source spectrum, MCP optic coating and detector window  $W$  (for silicon nitride  $S$  and polyimide  $P$ ). At the conclusion of  $N_{ORB}$ ,  $G_{LIM}(T) < G_{LIM}(T+L)$ . Any given point on the sky is observed for a modelled 400 s per orbit.

It is also apparent that  $N_{ORB}(\text{polyimide}) \leq N_{ORB}(\text{silicon nitride})$ , independent of source spectra or MCP coating. This suggests the polyimide detector window has a greater transparency to the diffuse X-ray background than that of silicon nitride. This is shown in *Figure 6.9* and explained with reference to *Figure 6.5*. The background peaks for polyimide and silicon nitride detector windows occur around 200 and 350 eV respectively, explained with reference to the K-shell absorption edges for polyimide (284.2 eV, C-K) and silicon nitride (409.9 eV, N-K). As the modelled diffuse X-ray background photon flux (*Figure 6.7*) falls with increasing energy (in the 0.1 – 5 keV waveband) the polyimide is the more transparent of the two windows to this background. Furthermore, there is a significant contrast in  $N_{ORB}$  in the case of the ruthenium MCP optic coating for the two modelled detector windows, which ranges from  $N_{ORB,RU}(\text{polyimide}) = 3, 4$  to  $N_{ORB,RU}(\text{silicon nitride}) = 7$ , irrespective of modelled source (*Figure 6.9*). The response of the ruthenium effective area curve below the polyimide-based C-K edge is almost completely



suppressed by the N-K edge with a silicon nitride window configuration, reducing its capacity to focus the diffuse X-ray background and increasing  $N_{ORB}$  in this case.

Time evolution of  $G_{LM}$  as a function of MCP optic coating is shown in *Figure 6.10*. In the case of the Crab Nebula, ruthenium appears to be the coating of choice after 1 year, provided a silicon nitride detector window is used, achieving an ultimate limiting flux of  $2.16 \times 10^{-13} \text{ erg cm}^{-2} \text{ s}^{-1}$  (*Table 6.3*). However, as suggested previously, in conjunction with a polyimide detector window, signal to noise ratio falls, resulting in a limiting flux of  $3.46 \times 10^{-13} \text{ erg cm}^{-2} \text{ s}^{-1}$  (an increase of 60.2%). Far more consistent is the performance of the heavier metals, iridium, platinum and gold, where  $G_{LM}$  varies with respect to detector window by 24.0%, 24.9% and 32.1% respectively. For the purposes of Lobster-ISS, should technological progress dictate a change in baseline detector window, the selection of Ir, Pt or Au as baseline coatings would mean the resulting optic performance would be less dependent on this change. Furthermore, in the case of these heavier metals,  $G_{LM}(\text{Ir}) < G_{LM}(\text{Pt}) < G_{LM}(\text{Au})$ , independent of detector window and modelled source after one year, suggesting iridium to be the MCP optic with greatest potential.

The limiting flux in the 1 day observational limit for the baseline Lobster-ISS specification, (Ni-coating, polyimide detector windows) again using the Crab Nebula as the benchmark modelled source, is 0.527 mCrab. This is a factor of five times greater than the previously modelled  $G_{LM}(1 \text{ day}) = 0.1 \text{ mCrab}$  (Priedhorsky et al. 1996), (hereafter denoted PPN) yet remains a factor of three times more sensitive than that advertised of MAXI, where  $G_{LM}(1 \text{ day}) \approx 1.7 \text{ mCrab}$ . Discrepancies between this model and that of PPN may be explained by a combination of two major factors. Firstly, in order to estimate background flux, PPN use the projected area  $A$  of a point source at the detector, rather than the four ‘pixels’ of background flux (true focus only) used here, which improves the PPN sensitivity (*Equation 6.30*). Secondly, the detection criteria adopted by PPN differ to that stated in *Equation 6.25*, PPN adopting the less stringent (yet equally valid) criteria of  $\sigma = \frac{N_s}{\sqrt{N_B}}$  in combination with a minimum of 5 photons (Priedhorsky, 2004). Under the PPN criteria, the baseline Lobster-ISS specification achieves  $G_{LM}(1 \text{ day}) = 0.16 \text{ mCrab}$  as according to PPN to within a factor of 2.

An iridium MCP optic coating in conjunction with the polyimide is modelled to further increase Lobster-ISS sensitivity to  $G_{LM}(1 \text{ day}) = 0.395 \text{ mCrab}$ , and with a silicon nitride window, to  $G_{LM}(1 \text{ day}) = 0.322 \text{ mCrab}$ .



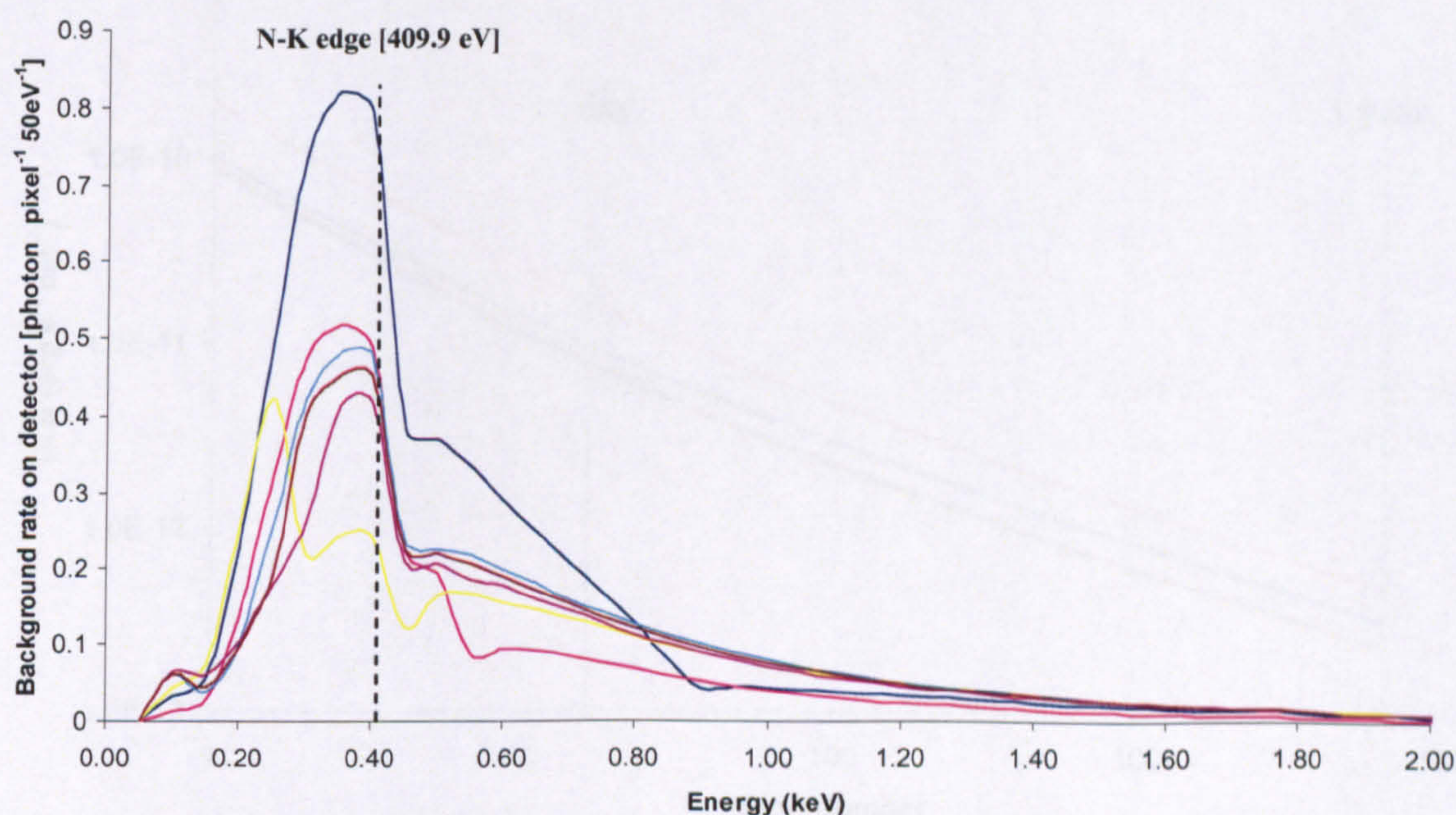
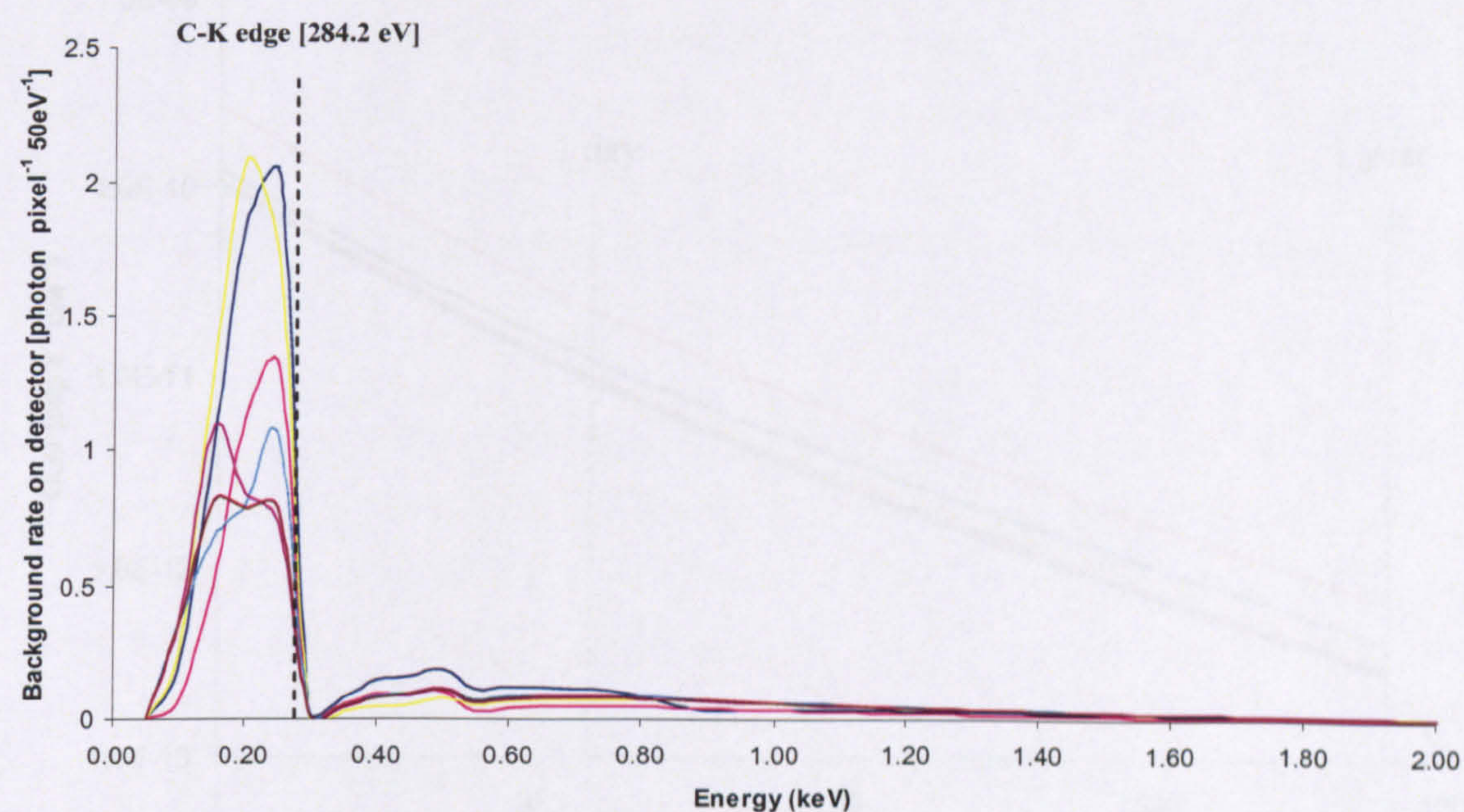


**Figure 6.9.** Distribution of the total diffuse X-ray background photons detected per pixel per 50 eV energy bin after a total integration time of 6400s (16 orbits, 1 day). Background photon counts are displayed as a function of energy for nickel (dark blue), ruthenium (yellow), iridium (turquoise), gold (magenta) and platinum (brown) coated MCP optics for polyimide (top) and silicon nitride (bottom) detector windows. Bare glass MCP rates are also displayed for comparison (pink).



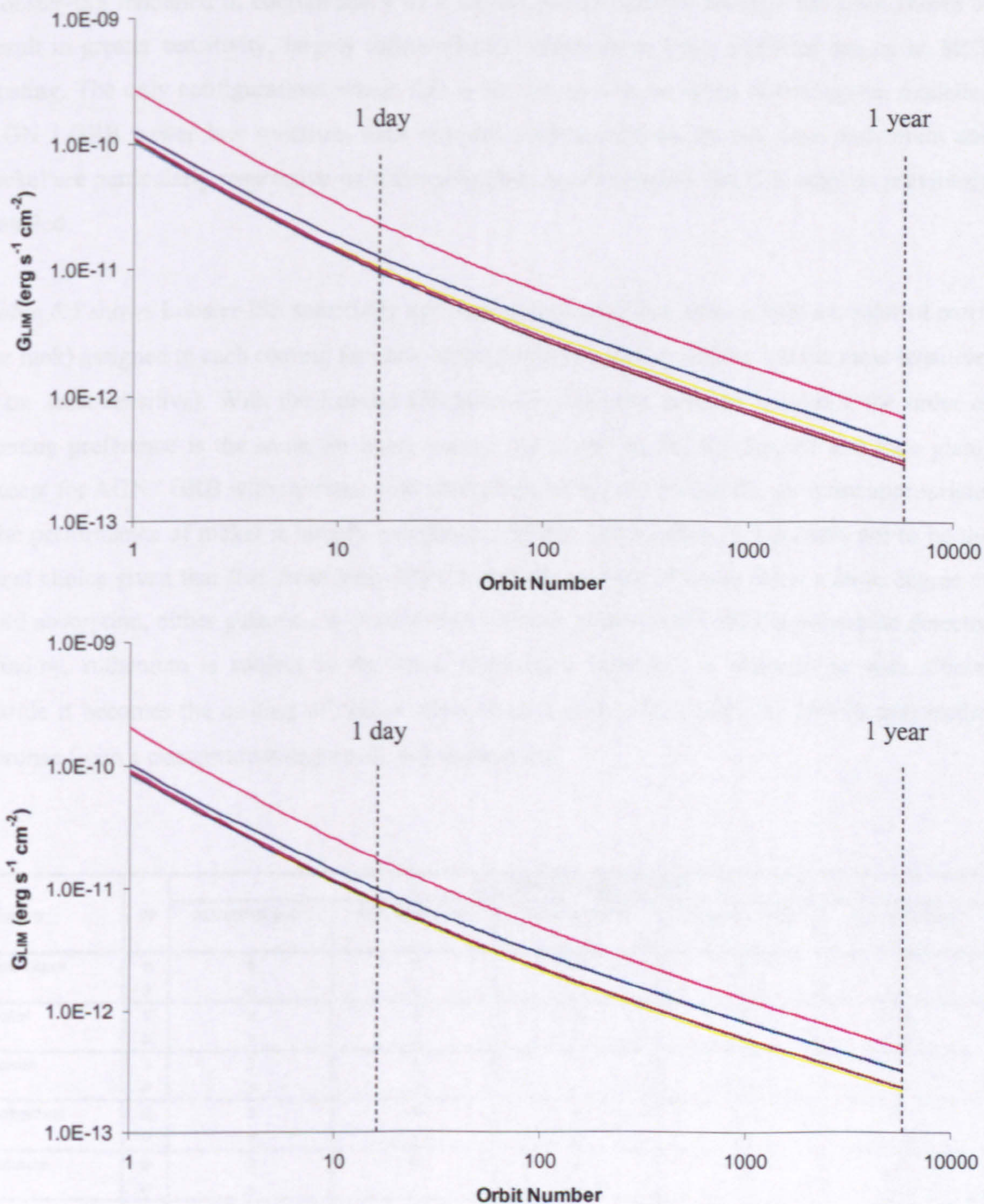


**Figure 6.10.** Time evolution of  $G_{LIM}$  from a Crab-like source as a function of nickel (dark blue), ruthenium (yellow), iridium (turquoise), gold (magenta) and platinum (brown) coated MCP optics for modelled polyimide (top) and silicon nitride (bottom) detector windows. Bare glass MCPs are also displayed for comparison (pink).



Lobster-ISS modelled in conjunction with a silicon nitride detector window has been shown to result in greater sensitivity, largely independent of observation time, modelled source or MCP coating. The only configurations where this is not the case occur when observing the modelled AGN / GRB power law spectrum with minimal cold absorption. In this case, ruthenium and nickel are particularly responsive with the polyimide window below the C-K edge as previously detailed.

*Table 6.5* shows Lobster-ISS sensitivity as a function of modelled source, with an order of merit (or rank) assigned to each coating for each of the five input spectra (where 1 is the most sensitive, 6 the least sensitive). With the Lobster-ISS baseline polyimide detector windows, the order of coating preference is the same for every source, (in order: Ir, Pt, Au, Ru, Ni and bare glass) except for AGN / GRB with minimal cold absorption, where the Ni and Ru are more appropriate. The performance of nickel is largely independent of detector window, yet appears not to be the ideal choice given that flux from both AGN and GRB are very likely to show a large degree of cold absorption, either galactic, or from within the host galaxy itself. With a polyimide detector window, ruthenium is subject to the same difficulties, however, in conjunction with silicon nitride it becomes the coating of choice when observing the modelled Crab Nebula and stellar coronae (with a conservative degree of cold absorption).

Coating	W	$G_{LIM}$ ORDER OF MERIT				
		AGN/GRB (min)	AGN/GRB (max)	Coronal (min)	Coronal (max)	Crab Nebula
Bare Glass	S	6	6	6	6	6
	P	6	6	6	6	6
Nickel	S	1	5	5	5	5
	P	1	5	5	5	5
Iridium	S	2	1	1	1	2
	P	3	1	1	1	1
Ruthenium	S	5	4	4	2	1
	P	2	4	4	4	4
Platinum	S	3	2	2	3	3
	P	5	2	2	2	2
Gold	S	4	3	3	4	4
	P	4	3	3	3	3

*Table 6.5. Order of merit indices assigned to each MCP coating, showing the performance (in terms of  $G_{LIM}$ ) of each for combinations of source spectra and detector window, from the most effective (1) through to the least effective coating (6).*



## 6.6 Conclusions

A number of issues significant to the baseline design of Lobster-ISS have arisen as a result of this investigation, and are summarised as follows:

- *Events occurring on a timescale of up to 3 or 4 ISS orbits (nickel, ruthenium-coated MCPs) or 6 orbits (iridium, platinum or gold-coated MCPs) are photon-limited and will be best observed in both line and true foci to increase Lobster-ISS sensitivity, using the baseline 1  $\mu\text{m}$  polyimide detector window. For the modelled 200 nm silicon nitride detector window,  $N_{\text{ORB}}$  ranges between 5 (nickel) and 6-7 (ruthenium, iridium, platinum, gold).*
- *In the case of the ruthenium coating, the science projected to be achieved is heavily dependent on the selection of detector window. For the currently baselined polyimide detector window, background photons are more readily focused, reducing signal to noise ratios at the detector. With a silicon nitride detector window, the capacity of a ruthenium-coated optic to focus the diffuse background is suppressed by the N-K edge and ruthenium becomes the coating of choice for the detection of the Crab Nebula.*
- *The heavier metals (iridium, platinum and gold) appear the most appropriate MCP optic coatings due to the projected breadth of science achievable in the modelled 0.1 – 5 keV Lobster-ISS waveband, their effectiveness largely independent of source spectra and detector window. Of these heavier metals, after a year in orbit, modelling suggests that iridium-coated MCPs always provide the best sensitivity, independent of source spectra or detector window, with platinum and gold following respectively in every modelled case.*
- *The previously advertised baseline Lobster-ISS 1 day limiting flux detection limit of 1 mCrab (PPN) is five times more sensitive than that uncovered in this ‘worst case scenario’ investigation.*

In the light of this investigation, iridium appears the most appropriate coating for the Lobster-ISS MCP optics. However, as shown in *Chapters 4 and 5*, the application of a reproducible, uniform metal coating representative of the channel geometry poses a significant technological challenge. Ultimately, the choice of coating may be limited by technological advancement.



## Chapter 7      Conclusions and Future Work

This chapter will highlight the major findings of this thesis and recommend ideas for further work to ensure the continual development of MCP optics for future terrestrial and space-based applications.

### 7.1      The Imaging X-ray Fluorescence Spectrometer

The development of the Imaging X-ray Fluorescence Spectrometer from two initial proof of principle experiments to its current status sees the first successful, practical application of MCP optics. Applications in mineralogy and scientific calibration have been realised in this work, with elemental maps generated and correlated against optical images of the sample in each case. A large amount of image processing, including the mosaicing of multiple elemental maps into larger arrays was performed successfully. Future standardisation of the image processing software into one IXRFS specific package would greatly facilitate image and spectral analysis for prospective users. IXRFS is currently being applied to the field of marine biology (*Section 2.6.2*) in the specific case of the common mussel (*Mytilus Edulis*), in this case, retrieved from a coastal environment shared by a nuclear power station (Su, 2005). In addition, contact has been made with the synchrotron community (specifically Daresbury SRS) with regard to the further application of the technology in this environment. Following the work of Price et al (2004b), further investigation into the ultimate sensitivity of IXRFS should be performed using the fundamental parameters method outlined in *Section 2.7*. Appropriate background fitting techniques should be identified and applied, making for more complete, quantitative analyses using the instrument in the future. Recently, the development of the annular anode has reached a conclusion; the copper-coated ceramic has been procured and soldered onto the annular anode itself. Preliminary testing of the ring anode source is expected to take place over the next few months with a view to imaging the distribution of low Z element contaminants on silicon wafers. The successful development of IXRFS also bodes well for the MIXS-T instrument baselined for the future Bepi-Colombo mission to Mercury, which is based on the same principle of operation.

### 7.2      X-ray Focusing with MCP Optics

The spatial resolution of the IXRFS system is limited by the angular resolution of the MCP optic; the work detailed in *Chapter 3* contributes toward the continual development of MCPs as



focusing optics, with particular emphasis on their application on Lobster-ISS. A 4 arcmin angular resolution is baselined for Lobster-ISS; the current optics are around a factor of two from this goal. At best focus, FWHM angular resolutions of both slumped and planar MCPs tested were evaluated at  $9.1 \times 9.1$  and  $9.4 \times 7.5$  square arcminutes respectively. It is vital that an ongoing laboratory program at Leicester testing the focal properties of the ‘new generation’ of MCP optics continues, with regular feedback provided to Photonis SAS. Multifibre misalignment has been shown to be the major source of error, resulting in the observation of fissures in the planar MCP tested in *Chapter 3*. As discussed in *Section 3.3.2*, the future development of a simple scanning aperture used to isolate individual multifibres during focusing would enable us to identify which multifibres were responsible for specific defects in the focused image. With regard to the slumped MCP optics, slump radii should be measured and verified using a surface profilometer. For Lobster-ISS, the co-alignment and fixing of slumped MCPs onto an optic support present significant technological challenges in the future, especially given their mechanical flexibility and fragility. Finally, the focusing properties of metallised MCP optics must be investigated in preparation for their application on Bepi-Colombo’s MIXS-T and Lobster-ISS.

### **7.3 Characterisation of Bare Glass and Metallised MCP Optic Reflecting Surfaces**

In *Chapters 4* and *5*, the techniques of Auger Electron Spectroscopy and X-Ray Reflectivity were used to characterise the microchannel plate reflecting surfaces (both bare glass and metallised). Both techniques suggested that in the case of the bare glass MCPs (manufactured from Philips type 297 glass by Photonis SAS) the channel surfaces may be described using a single silica-like layer; with regard to the AES studies, lead, bismuth, and potassium were not detected down to a depth of 2400 Å.

The metal coatings investigated over the course of this thesis were ruthenium, iridium (deposited by ALD at the University of Helsinki) and nickel (deposited by EN at Photonis SAS). The variation in coating thickness as a function of distance down the channel observed in the ruthenium-coated sample RU-1 changed by a factor of  $\sim 2$ , believed to be a result of the unidirectional flow of the vapour reactants through the MCP channels; this hypothesis could be tested by recording the orientation of the MCP during the ALD coating process. Further nickel, ruthenium and iridium MCP optic coatings should be characterised in the near future to better understand the nature of the deposition in each case, with a more long term aim being to analyse



a multitude of samples of each coating; the coatings must be reproducible, as it is currently envisaged that a total of 288 MCPs are to be employed on the Lobster-ISS ASM for example. Encouragingly, with each coating, the interpretation of MCP reflectivity data suggests that channels do not appear to be blocked on a large scale.

Shortfalls in the measured reflectivity of ruthenium and nickel-coated MCPs at low grazing angles are hypothesised to be a result of rough surface specular reflection and photoelectric absorption due to island formations in the coatings. The same shortfall is not observed in the iridium-coated MCP IRID-1; the reflectivity profile is modelled at bulk density, but with an RMS surface roughness of 26 Å (around three times that desired for Lobster-ISS). In order to verify the above hypothesis and complement the surface roughness modelling, the true morphology of the coated channel surfaces should be determined experimentally using Atomic Force Microscopy (AFM). In addition, assessing the validity of the proposed model in *Figure 5.9* is made complicated by the presence of the other channel walls. The procurement of Philips type 297 lead glass flats from Photonis SAS, subsequently coated with nickel (Photonis SAS), ruthenium and iridium (University of Helsinki) would remove this complication and should be investigated at future Daresbury SRS runs. However, fluid flow through microchannels is complex and currently poorly understood; the coating on the flats may therefore not be representative of that along an MCP microchannel. Regardless, the procurement of coated flats will give us insight into the qualities of coatings that may currently be achieved on the Philips glass.

The effectiveness of the EN process (in terms of the soft X-ray reflectivity from the MCP channel surfaces) appears to be enhanced by maximising chemical bath temperature and minimising immersion time; to this end, and as a result of this study, Photonis SAS began to optimise the EN process at higher bath temperatures, and recently nickel-coated an MCP at a characteristic temperature of 95 °C (as opposed to 84 °C, the hottest in this study) for an immersion time of 30 seconds. To enhance nickel coverage toward the midpoint of the channel, the reactants are also now ‘pumped’ through the channels. Those at the Laboratory of Inorganic Chemistry at the University of Helsinki have also further optimised the ALD process in response to the high surface roughness reported from the MCP IRID-1 in this study. Rather than simply using air as one of the vapour reactants, nitrous oxide (N<sub>2</sub>O) and ozone (O<sub>3</sub>) are currently being investigated, with the belief that they will produce a more amorphous (and smoother) coating (Nenonen, 2005). MCPs coated from both organisations have recently been procured, in preparation for more reflectivity measurements at Daresbury SRS in July 2005.



## 7.4 The Lobster-ISS All-Sky Monitor

As a result of the modelling of Lobster-ISS in *Chapter 6*, there have been two changes to the baseline configuration of the instrument:

- *Iridium MCP coating*

Iridium is found to be the most effective MCP coating, largely independent of the modelled input spectra and detector window; the previously baselined nickel coatings perform unfavourably in almost every case. Ultimately however, the choice of coating will be based on what can be achieved in practise and reproduced. A coating of some description is vital to the Lobster-ISS mission however; for example, ignoring the contributions of the line foci, the limiting sensitivity improves by a factor of two with iridium-coated MCPs (over bare glass) when imaging the Crab Nebula in conjunction with silicon nitride detector windows.

- *Silicon nitride detector windows*

The theoretical modelling in this work, coupled with an experimental feasibility study into the development of large area silicon nitride windows (Fraser and Pearson, 2004) funded by a PPARC (Particle Physics and Astronomy Research Council) PIPSS (PPARC Industrial Programme Support Scheme) research grant (reference: PPA/I/S/2000/00707) is responsible for the change in the baseline detector windows on Lobster-ISS.

In its new [*Ir / silicon nitride*] configuration, Lobster-ISS is modelled to have a 1 day limiting flux detection limit of  $7.59 \times 10^{-12} \text{ ergs cm}^{-2} \text{ s}^{-1}$  (0.32 mCrab) as opposed to the previous [Ni / polyimide] baseline limit of  $12.4 \times 10^{-12} \text{ ergs cm}^{-2} \text{ s}^{-1}$  (0.53 mCrab).



## *List of Addresses*

**BESSY (Berliner Elektronenspeicherring-Gesellschaft für Synchrotronstrahlung mbH.),**  
15 Albert-Einstein-Straße, 12489 Berlin, Germany.

**Brush Wellman Engineered Materials,** 17876 St. Clair Avenue, Cleveland, OH 44110, USA.

**CCLRC Daresbury Laboratory,** Daresbury, Warrington, Cheshire, WA4 4AD, UK.

**CCLRC Rutherford Appleton Laboratory,** Chilton, Didcot, Oxon, OX11 0QX, UK.

**CTI Cryogenics, Helix Technology Corporation,** Mansfield, Massachusetts 02048-9171, USA.

**E2V Technologies,** 106 Waterhouse Lane, Chelmsford, Essex, CM1 2QU, UK.

**Engineering and Physical Sciences Research Council,** Polaris House, North Star Avenue,  
Swindon, Wiltshire, SN2 1UH, UK.

**Image Photonics,** Tadworth, 7 Whitebeam Way, Tadworth, Surrey, KT20 5DL, UK.

**JEOL (U.K.) Ltd.,** JEOL House, Silver Court, Watchmead, Welwyn Garden City, Hertfordshire,  
AL7 1LT, UK.

**JMAR Technologies Inc.,** 5800 Armada Drive, Carlsbad, CA 92008, USA.

**JVC (U.K.) Ltd.,** JVC House, JVC Business Park, Priestley Way, London, NW2 7BA, UK.

**KeveX X-ray Inc.,** 320 El Pueblo Road, Scotts Valley, CA 95066, USA.

**LEO Electron Microscopy Ltd.,** 511 Coldhams Lane, Cambridge, Cambridgeshire, CB1 3JS,  
UK.

**MacDermid Inc.,** 1401 Blake Street, Denver, Colorado 80202, USA.



**Melcor Corp., 1040 Spruce Street, Trenton, NJ 08648, USA.**

**Micro-Analysis Consultants Ltd., Unit 3, Edison Road, St. Ives, PE17 4LF, UK.**

**NASA / Goddard Space Flight Center, Code 661, Greenbelt, MD 20771, USA.**

**Nikon UK Ltd., 380 Richmond Road, Kingston upon Thames, Surrey, KT2 5PR, UK.**

**Nova Scientific Inc., 7 Third Street, P.O. Box 1328, Bondsville, MA 01009, USA.**

**Open University, Walton Hall, Milton Keynes, MK7 6AA, UK.**

**Oxford Instruments Analytical Oy, Nihtisillankuja, P.O. Box 85, FIN-02631, ESPOO, Finland.**

**Photonis SAS, Avenue Roger Roncier, B.P. 520, F-19106, Brive, France.**

**Particle Physics and Astronomy Research Council, Polaris House, North Star Avenue, Swindon, Wiltshire, SN2 1UH, UK.**

**PSP Vacuum Technology, Unit 8, Heather Close, Lyme Green Business Park, Macclesfield, SK11 0LR, UK.**

**Shimadzu Research Laboratory Ltd., Wharfside, Trafford Wharf Road, Manchester, M17 1GP, UK.**

**University of Helsinki, P.O. Box 55, FIN-00014, Finland.**

**University of Loughborough, Ashby Road, Loughborough, Leicestershire, LE11 3TU, UK.**



## ***Bibliography***

- T. Aaltonen, P. Alén, M. Ritala and M. Leskelä, “*Ruthenium thin films grown by atomic layer deposition*”, Chem. Vap. Deposition, 9, 45 (2003a)**
- T. Aaltonen, M. Ritala, T. Sajavaara, J. Keinonen and M. Leskelä, “*Atomic layer deposition of platinum thin films*”, Chem. Mater., 15, 1924 (2003b)**
- T. Aaltonen, M. Ritala, V. Sammelselg and M. Leskelä, “*Atomic layer deposition of iridium thin films*”, J. Electrochem. Soc., 151, 8, G489 (2004)**
- A.T. AbdAllah and M.A. Moustafa, “*Accumulation of Lead and Cadmium in the Marine Prosobranch Nerita Saxtilis, Chemical Analysis, Light and Electron Microscopy*”, Environmental Pollution, 116, 185-191 (2002).**
- J. Adams and B.W. Manley, “*The channel electron multiplier*”, Electron. Eng. 37, 180 (1965).**
- J. Adema, “*UV auroral imager for the Freja project*”, Delft Electronic Products (1993).**
- J.R.P. Angel, “*Lobster Eyes as X-ray Telescopes*”, Astrophys.J., 233, 364 (1979).**
- K. Arnaud and B. Dorman, “*XSPEC – an X-ray spectral fitting package – version 11.3.x*”, Technical document, HEASARC, Laboratory for High Energy Astrophysics, NASA/GSFC, Greenbelt, MD 20771, USA (2003).**
- A.N. Artmeiev, A. Snigirev, V. Kohn, I. Snigireva, N. Artimiev, M. Grigoriev, S. Peredkov, L. Glinkin, M. Levtonov, V. Kvardakov, A. Zabelin and A. Maevskiy, “*Planar parabolic X-ray refractive lens made of carbon*”, Nucl. Instr. Meth. A, in press (2005).**
- N.P. Bannister, *Private communication*, University of Leicester (2004a).**
- N.P. Bannister, G.W. Fraser, T.J. Stevenson, J.F. Pearson, “*Lobster-ISS Instrument Definition Document, Issue 9.1*”, Technical Report, University of Leicester (2004b).**



**M. Bavdaz, A.J. Peacock, A.N. Parmar and M.W. Beijersbergen, “*The XEUS mission and instruments*”, Proc. SPIE., 4497, 31-40 (2002).**

**M. Bavdaz, A.J. Peacock, E. Tomaselli, M.W. Beijersbergen, M. Collon, E. Flyckt, R. Fairbend, J.P. Boutot, “*Progress at ESA on high energy optics technologies*”, Proc. SPIE., 5168, 136 (2004a).**

**M. Bavdaz, “*Microchannel plate (MCP) based X-ray optics*”, Presentation at ESA, Science Payloads and Advanced Concepts Office Science Directorate, 6<sup>th</sup> April (2004b).**

**J.A. Bearden and A.F. Burr, “*Reevaluation of X-ray atomic energy levels*”, Rev. Mod. Phys. 39, 125 (1967).**

**P. Beckmann and A. Spizzichino, “*The scattering of electromagnetic waves from rough surfaces*”, Pergamon Press (1963).**

**C. Binns, *Private communication*, University of Leicester (2005).**

**J.K. Black, A.N. Brunton, N.P. Bannister, P. Deines-Jones and K. Jahoda, “*The Imaging X-ray Detector for Lobster-ISS*”, Nucl. Instr. Meth. A, 513, 123-126 (2003).**

**S. Bowyer, J.J. Drake and S. Vennes, “*Extreme ultraviolet astronomy*”, Annu. Rev. Astron. Astrophys, 38, 231-288 (2000).**

**H.V. Bradt, J.H. Swank and R.E. Rothschild, “*The X-ray Timing Explorer*”, Adv. Space. Res, 11, 243, (1991).**

**A. Brenner, “*Electroless Plating*”, Modern Electroplating, 2<sup>nd</sup> Edition, Ed. Lowenheim, F. A., WILEY, 33, p.698-713 (1963).**

**J.E. Bringas, M.L. Wayman, “*The metals red book: nonferrous metals*”, Second Edition, Casti Publishing Inc. (1995).**



**A.C. Brinkman, C.J.T. Gunsing, J.S. Kaastra, R.L.J. van der Meer, R. Mewe, F. Paerels, A.J.J. Raassen, J.J. van Rooijen, H. Bräuninger, W. Burkert, V. Burwitz, G. Hartner, P. Predehl, J.-U. Ness, J.H.M.M. Schmitt, J.J. Drake, O. Johnson, M. Juda, V. Kashyap, S.S. Murray, D. Pease, P. Ratzlaff and B.J. Wargelin**, “*First light measurements of Capella with the low-energy transmission grating spectrometer aboard the CHANDRA X-ray observatory*”, *Astrophys. J.* 530, L111-L114 (2000).

**I. Brock**, *Private communication*, Image Photonics, Tadworth, 7 Whitebeam Way, Tadworth, Surrey, KT20 5DL, UK.

**A.N. Brunton**, “*MCP Optics*”, PhD Thesis, University of Leicester (1994).

**A.N. Brunton, G.W. Fraser, J.E. Lees, W.B. Feller and P.L. White**, “*X-ray focusing with 11  $\mu\text{m}$  square pore microchannel plates*”, *Proc. SPIE.* 2519, 40 (1995).

**A.N. Brunton, G.W. Fraser, J.E. Lees and I.C.E. Turcu**, “*Metrology and modelling of microchannel plate optics*”, *Appl. Opt.* 36, 5461 (1997).

**A.N. Brunton, A.P. Martin, G.W. Fraser and W.B. Feller**, “*A study of 8.5  $\mu\text{m}$  microchannel plate X-ray optics*”, *Nucl. Instr. Meth. A.*, 431, 356-365 (1999).

**A.N. Brunton, G.W. Fraser and J.F. Pearson**, “*High intensity X-ray sources, incorporating microchannel plate (MCP) optics*”, EPSRC Instrument Call for Proposals (2000).

**G. Cappuccio and S.B. Dabagov**, “*Capillary optics as an X-ray condensing lens: an alignment procedure*”, *Proc. SPIE.* 4138, 88 (2000).

**M. Cardona and L. Ley, Eds.**, “*Photoemission in solids I: general principles*”, Springer-Verlag, Berlin (1978).

**J.D. Carpenter**, “*Microchannel plates in astronomy and planetary science*”, PhD Thesis, University of Leicester (2005).



**R.C. Catura, L.W. Acton and H.M. Johnson**, *“Evidence for X-ray emission from Capella”*, *Astrophys. J.* 196, L47-L49 (1975).

**H.N. Chapman, K.A. Nugent and S.W. Wilkins**, *“X-ray focusing using square channel-capillary arrays”*, *Rev. Sci. Instrum.* 62, 1542-1561 (1991).

**E.L. Church, H.A. Jenkinson and J.M. Zavada**, *“Relationship between surface scattering and topographic features”*, *Opt. Eng.*, 18, 125 (1978).

**A. Comastri, G. Hasinger, G. Setti and G. Zamorani**, *“AGNs make the X-ray background”*, *ASP Conf.Ser.*, 54, *The First Stromlo Symposium: The Physics of Active Galaxies*, *Astron. Soc. Pac.*, San Francisco, 143 (1994).

**E. Costa, F. Frontera, J. Heise, M. Feroci, J. In’t Zand, F. Fiore, M.N. Cinti, D. Dal Fiume, L. Nicastro, M. Orlandini, E. Palazzi, M. Rapisarda, G. Zavattini, R. Jager, A. Parmar, A. Owens, S. Molendi, G. Cusumano, M.C. Maccarone, S. Giarrusso, A. Coletta, L.A. Antonelli, P. Giommi, J.M. Muller, L. Piro and R.C. Butler**, *“Discovery of an X-ray afterglow associated with the gamma-ray burst of 28 February 1997”*, *Nature*, 387, 783 (1997).

**R.A. Cowley and T.W. Ryan**, *“X-ray scattering studies of thin films and surfaces: thermal oxides on silicon”*, *J. Phys. D: Appl. Phys.*, 20, 61-68 (1987).

**T.A. Crabb, P.N. Gibson and K.J. Roberts**, *“REX – a program for the analysis of X-ray reflectivity data: user guide and programmer manual”*, Technical document, Daresbury Laboratory, (1992).

**A. Cravo, P. Foster and M.J. Bebianno**, *“Minor and Trace Elements in the Shell of Patella Aspera (Röding 1798)”*, *Environment International*, 28, 295-302 (2002).

**D.T. Cromer and D. Liberman**, *“Relativistic calculation of anomalous scattering factors for X-rays”*, LASL report LA-4403, Los Alamos Laboratory (1970).

**B. Czerny and M. Elvis**, *“Constraints on quasar accretion disks from the optical / ultraviolet / soft X-ray big bump”*, *Astrophys. J.* 321, 305-320 (1987).



**P. Deines-Jones, J.K. Black, S.D. Hunter, K. Jahoda and S.M. Owens, “*Large-area imaging micro-well detectors for high-energy astrophysics*”, Nucl. Instr. Meth. A., 478, 130-134 (2002).**

**W. Ehrenberg, short news item, Nature, 150, 330 (1947).**

**A.C. Fabian, K. Iwasawa, C.S. Reynolds and A.J. Young, “*Broad iron lines in active galactic nuclei*”, Publications of the Astronomical Society of the Pacific, 112, 1145-1161 (2000).**

**R. Fairbend, *private communication*, Photonis SAS, Brive, France (2003, 2004, 2005).**

**D.A. Frail, S.R. Kulkarni, L. Nicastro, M. Feroci and G.B. Taylor, “*The radio afterglow from the gamma-ray burst of 8 May 1997*”, Nature, 389, 261 (1997).**

**L.A. Frank, J.B. Sigwarth, J.D. Craven, J.P. Cravens, J.S. Dolan, M.R. Dvorsky, P.K. Hardebeck, J.D. Harvey and D.W. Muller, “*The visible imaging system (VIS) for the POLAR spacecraft*”, Space. Sci. Rev. 71, 297 (1995).**

**G.W. Fraser and E. Mathieson, “*Signal location by uniform resistive anodes. A: Square anodes in the D.C. limit*”, Nucl. Instr. Meth. A, 179, 591 (1981).**

**G.W. Fraser, “*X-ray detectors in astronomy*”, Cambridge University Press (1989).**

**G.W. Fraser, J.E. Lees, J.F. Pearson, M.R. Sims and K. Roxburgh, “*X-ray Focusing Using Microchannel Plates*”, Proc. SPIE., 1546, 41 (1991).**

**G.W. Fraser, A.N. Brunton, J.E. Lees, J.F. Pearson and W.B. Feller, “*X-ray focusing using square-pore microchannel plates: First observation of cruxiform image structure*”, Nucl. Instr. Meth. A, 334, 579 (1993).**

**G.W. Fraser, A. Holland, J.F. Pearson and A.N. Brunton, “*Development of an imaging X-ray fluorescence spectrometer (LXRFS)*”, EPSRC Instrument Call for Proposals (1999).**

**G.W. Fraser, M.J. Ward, R. Warwick, A.N. Brunton, R.E. Cole, M.G. Watson, P. O’Brien, W.C. Friedhorsky, S. Brumby, K. Borozin, T. Vestrand, N.E. White, K. Jahoda, K. Black,**



**R. Petre, S. Hunter, W. Zhang, A.C. Fabien, K. Nugent and A. Peele, “An Imaging All-Sky Monitor based on Lobster Eye X-ray Optics. An International Space Station (ISS) Attached Payload submitted in response to the ESA Call for Mission Proposals for the Flexi-Missions F2 and F3” (2000).**

**G.W. Fraser, A.N. Brunton, D. Ramsden, J.Zarnecki, M.G. Pia, J. Huovelin and S.O. Flyckt, “High Energy Remote-Sensing of Mercury’s Surface (HERMES)” Technical report, Intention to propose an instrument for Bepi-Colombo (2001).**

**G.W. Fraser, “IGR Report: Development of an Imaging X-ray Fluorescence Spectrometer”, Individual Grant Report to EPSRC (2002).**

**G.W. Fraser and J.F. Pearson, “Development of large area silicon nitride X-ray windows and filters”, PPARC PIPSS grant report, reference: PPA/IS/2000/00707 (2004).**

**J.C. Fuggle and N. Mårtensson, “Core-level binding energies in metals”, J. Electron. Spectrosc. Relat. Phenom. 21, 275 (1980).**

**T. Galama, P.J. Groot, J. van Paradijs, C. Kouveliotou, C.R. Robinson, G.J. Fishman, C.A. Meegan, K.C. Sahu, M. Livio, L. Petro, F.D. Macchetto, J. Heise, J. In’t Zand, R.G. Strom, J. Telting, R.G.M. Rutten, M. Pettini, N. Tanvir and J. Bloom, “The decay of optical emission from the gamma-ray burst GRB970228”, Nature, 387, 479 (1997).**

**N. Gehrels, G. Chincarini, P. Giommi, K.O. Mason, J.A. Nousek, A.A. Wells, N.E. White, S.D. Barthelmy, D.N. Burrows, L.R. Cominsky, K.C. Hurley, F.E. Marshall, P. Mészáros, P.W.A. Roming, L. Angelini, L.M. Barbier, T. Belloni, S. Campana, P.A. Caraveo, M.M. Chester, O. Citterio, T.L. Cline, M.S. Cropper, J.R. Cummings, A.J. Dean, E.D. Feigelson, E.E. Fenimore, D.A. Frail, A.S. Fruchter, G.P. Garmire, K. Gendreau, G. Ghisellini, J. Greiner, J.E. Hill, S.D. Hunsberger, H.A. Krimm, S.R. Kulkarni, P. Kumar, F. Lebrun, N.M. Lloyd-Ronning, C.B. Markwardt, B.J. Mattson, R.F. Mushotzky, J.P. Norris, J. Osborne, B. Paczynski, D.M. Palmer, H.-S. Park, A.M. Parsons, J. Paul, M.J. Rees, C.S. Reynolds, J.E. Rhoads, T.P. Sasseen, B.E. Schaefer, A.T. Short, A.P. Smale, I.A. Smith, L. Stella, G. Tagliaferri, T. Takahashi, M. Tashiro, L.K. Townsley, J. Tueller, M.J.L. Turner,**



**M. Vietri, W. Voges, M.J. Ward, R. Willingale, F.M. Zerbi, and W.W. Zhang, “The Swift gamma-ray burst mission”, Ap. J. 611, 1005 (2004).**

**G.W. Goodrich and W.C. Wiley, “Continuous channel electron multiplier”, Rev. Sci. Instrum, 33 (1962).**

**R. Grard, M. Novara and G. Scoon, “BepiColombo – a multidisciplinary mission to a hot planet”, ESA bulletin, 103, 11-19 (2000).**

**R.A. Greenwald, K.B. Baker, J.R. Dudeney, M. Pinnock, T.B. Jones, E.C. Thomas, J-P. Villan, J-C. Cerisier, C. Senior, C. Hanuise, R.D. Hunsucker, G. Sofko, J. Koehler, E. Nielsen, R. Pellinen, A.D.M. Walker, N. Sato and H. Yamagishi, “DARN / SuperDARN: A global view of the dynamics of high latitude convection”, Space. Sci. Rev. 71, 761 (1995).**

**M. Güdel, “X-ray astronomy of stellar coronae”, A&A. Rv. 12, 71-237 (2004).**

**F. Haardt and L. Maraschi, “X-ray spectra from two-phase accretion disks”, Astrophys. J. 413, 507-517 (1993).**

**B.L. Henke, “Low energy X-ray interactions: photoionization, scattering, specular and Bragg reflection”, Topical conference on low-energy X-ray diagnostics, 75, 146-155 (1981).**

**B.L. Henke, P. Lee, T.J. Tanaka, R.L. Shimabukuro and B.K. Fujikawa, “Low-energy X-ray interaction coefficients: photoabsorption, scattering and reflection”, Atomic data and nuclear data tables, 27, 1 (1982).**

**J.S. Heslop-Harrison and B.J. Reger, “X-ray Microprobe Mapping of Certain Elements in the Ovary of *Zea mays* L. ”, Annals of Botany, 57, 819-822 (1986).**

**J.S. Heslop-Harrison, “Energy Dispersive X-ray Analysis” Modern Methods of Plant Analysis, Physical Methods in Plant Sciences, Ed. H.F. Linskens and J.F. Jackson, Springer-Verlag Berlin Heidelberg, 11, 244 (1990).**

**D. Hibbard, “Electroless Nickel for Optical Applications”, Proc. SPIE., CR67, 179-205 (1997).**



- G.E. Hill**, *"Secondary electron emission and compositional studies on channel plate glass surfaces"*, Adv. Electron. Phys., 40A, 153-165 (1976).
- D. Hirst**, *"From the candle to the grave"*, Boxed Edition, Booth-Clibborn (2005a).
- D. Hirst**, *"I want to spend the rest of my life everywhere, with everyone, one to one, always, forever, now"*, Compact Edition, Booth-Clibborn (2005b).
- S.S. Holt and W. Friedhorsky**, *"All-Sky Monitors for X-ray Astronomy"*, Space. Sci. Rev, 45, 269-289 (1987).
- J.J.M. In't Zand, W.C. Friedhorsky, C.E. Moss and E.E Fenimore**, *"The MOXE X-ray All-Sky Monitor for Spectrum-X-Gamma"*, Proc. SPIE, 2279, 458 (1994).
- K. Jahoda, K. Black and P. Deines-Jones**, *"Lobster-ISS detector description document"*, Technical document (2000).
- F. Jansen, D. Lumb, B. Altieri, J. Clavel, M. Ehle, C. Erd, C. Gabriel, M. Guainazzi, P. Gondoin, R. Much, R. Munoz, M. Santos, N. Schartel, D. Texier and G. Vacanti**, *"XMM-Newton observatory: I. the spacecraft and operations"*, A & A, 365, L1-L6 (2001).
- Ming-Shiou Jeng, Woei-Lih Jeng, Tsu-Chang Hung, Ching-Ying Yeh, Rong-Jeng Tseng, Pei-Jie Meng, Bor-Cheng Han**, *"Mussel Watch: A Review of Cu and Other Metals in Various Marine Organisms in Taiwan, 1991-98"*, Environmental Pollution, 110, 207-215 (2000).
- M. Joy and M.C. Weisskopf**, *"Development of hard X-ray optics"*, Proc. SPIE. 1546, 303-311 (1992).
- J.S. Kaastra and R. Mewe**, *"Coronal plasmas modelling and the MEKAL code"*, Atomic Data Needs for X-ray Astronomy (2000).
- J. Kataoka, Y. Serino, N. Kawai, T. Arakuni, A. Yoshida, M. Uzawa, M. Kohama, I. Sakurai, T. Mihara, H. Negoro, N. Isobe, H. Katayama, K. Kawasaki, N. Kuramata, M. Matsuoka, H. Tomida, S. Ueno, T. Yokota, E. Miyata, M. Nomachi and H. Tsunemi**,



*"Ground-support electronics for testing the preflight performance of the MAXI-GSC"*, Proc. SPIE., 5165, 375 (2004).

N. Kawai, M. Matsuoka, A. Yoshida, T. Mihara, T. Kotani, H. Negoro, Y. Shirasaki, I. Sakurai, M. Namiki, K. Torii, H. Tsunemi, E. Miyata, K. Hayashida, S. Kitamoto, K. Yoshita, Y. Hashimoto and M. Yamauchi, *"Monitor of All-sky X-ray Image (MAXI) for JEM on the International Space Station"*, Astron. Nachr, 320, 372 (1999).

A. Keay, A.D. Holland, D.J. Burt and P. Pool, *"Development of MOS CCDs for the Next Generation of X-ray Observatories"*, Nucl.Instr.Meth. A., 436, 16-23 (1999).

H. Kiessig, *"Interferenz von Röntgenstrahlen an dunnen schichten"*, Ann. Phys. 10, 769-778 (1931).

P. Kirkpatrick and A.M. Baez, *"Formation of optical images by X-rays"*, J. Opt. Soc. Am. 38, 766 (1948).

M.O. Krause, *"Atomic radiative and radiationless yields for K and L shells"*, J. Phys. Chem. Ref. Data. 8, 307 (1979).

M.A. Kumakhov and F.F. Komorov, *"Multiple reflection from surface X-ray optics"*, Phys. Rep. 191, 289-350 (1990).

M.F. Land, *"Animal Eyes with Mirror Optics"*, Scientific American, 239, 126 (1978).

J.E. Lees and J.F. Pearson, *"A large area detector for X-ray imaging"*, Nucl. Instr. Meth. A, 384, 410 (1997).

J.E. Lees, G.W. Fraser, M.R. Sims, A.N. Brunton, R.E. Cole and J.F. Pearson, *"A wide field FUV auroral imager for low earth orbit missions"*, Internal report (1999).

B. Lengeler, C.G. Schroer, B. Benner, T.F. Günzler, M. Kuhlmann, J. Tümmeler, A.S. Simionovici, M. Drakopoulos, A. Snigirev and I. Snigireva, *"Parabolic refractive X-ray lenses: a breakthrough in X-ray optics"*, Nucl. Instr. Meth. A, 467-468, 944-950 (2001).



**J.E. Lees and J. Hales**, *“Imaging and quantitative analysis of tritium-labelled cells in lymphocyte proliferation assays using microchannel plate detectors originally developed for X-ray astronomy”*, J. Immunol. Methods, 247, 95 (2001).

**D.R. Lide**, *“CRC handbook of chemistry and physics, 73<sup>rd</sup> Edition”*, CRC Press (1993).

**B.S. Lim, A. Rahtu and R.G. Gordon**, *“Atomic layer deposition of transition metals”*, Nature Materials, 2, 749-754 (2003).

**D. McCammon and W.T. Sanders**, *“The soft X-ray background and its origins”*, ARA&A, 28, 657 (1990).

**K.A. McWilliams, T.K. Yeoman, J.B. Sigwarth, L.A. Frank and M. Brittnacher**, *“The dayside ultraviolet aurora and convection responses to a southward turning of the interplanetary magnetic field”*, Annales Geophysicae, 19, 707-721 (2001).

**B. Maddison, J.F. Pearson and S. Dunkin**, *“BepiColumbo Mercury Imaging X-ray Spectrometer (MLXS) scientific and technological plan”* (2004).

**A.P. Martin, A.N. Brunton, G.W. Fraser, A.D. Holland, A. Keay, J. Hill, N. Nelms, I.C.E. Turcu, R. Allott, N. Lisi and N. Spencer**, *“Imaging X-Ray Fluorescence Spectroscopy Using Microchannel Plate Relay Optics”*, X-Ray Spectrom. 28, 64-70 (1999).

**A.P. Martin**, *“Exploitation of MCP Optics”*, PhD Thesis, University of Leicester (2000).

**A.P. Martin, A.N. Brunton, G.W. Fraser, A.F. Abbey**, *“Imaging X-ray Fluorescence Spectroscopy: Laboratory Measurements”*, Nucl. Instr. Meth. A., 460, 316-325 (2001).

**I.M. Mason and J.L. Culhane**, *“The environmental background in gas-filled detectors for X-ray astronomy”*, IEEE Trans. Nucl. Sci. NS-30 (1), 485-490 (1983).

**S. Mathur, B.J. Walker and H. Ghosh**, *“Chandra detection of highest redshift ( $z \sim 6$ ) quasars in X-rays”*, Astrophys. J., 570, L5-L8 (2002).



**M. Matsuoka, M. Sugizaki, H. Tomida, K. Torii and S. Ueno, “MAXI Mission for Space Station and Future ASM”, Astron. Nachr, 320, 275-276 (1999).**

**A.G. Michette and C.J. Buckley, “X-ray science and technology”, Institute of Physics Publishing Ltd. (1993).**

**R. Morrison and D. McCammon, “Interstellar photoelectric absorption cross-sections, 0.03-10 keV”, Astrophys. J. 270, 119-122 (1983).**

**R.W. Morton and K.C. Witherspoon, “Elemental X-ray Imaging of Fossils”, Adv. X-ray Anal., 36, 97-104 (1992).**

**K. Nandra and K.A. Pounds, “Ginga observations of the X-ray spectra of Seyfert galaxies”, Mon. Not. R. Astron. Soc. 268, 405-429 (1994).**

**S. Nenonen, *Private communication*, Oxford Instruments Analytical Oy, Nihtisillankuja, P.O. Box 85, FIN-02631, ESPOO, Finland (2004, 2005).**

**J.-U. Ness, R. Mewe, J.H.M.M. Schmitt, A.J.J. Raassen, D. Porquet, J.S. Kaastra, R.L.J. van der Meer, V. Burwitz and P. Predehl, “Helium-like triplet diagnostics: applications to CHANDRA-LETGS X-ray observations of Capella and Procyon”, A & A, 367, 282-296 (2001).**

**J.-U. Ness, M. Güdel, J.H.M.M. Schmitt, M. Audard and A. Telleschi, “On the sizes of stellar coronae”, A & A, 427, 667-683 (2004).**

**P.T. O’Brien, *Private communication*, University of Leicester (2004).**

**P.K. Oschepakov, B.N. Skvortsov, B.A. Osanov and I.V. Siprikov, “Application of a continuous secondary electron multiplier for amplifying small currents”, Priory. Tekh. Eksper, 4, 89 (1960).**

**K.L. Page, N. Schartel, M.J.L. Turner, P.T. O’Brien, “XMM-Newton observations of seven soft X-ray excess quasi-stellar objects”, Mon. Not. R. Astron. Soc. 352, 523-534 (2004).**



**P.W. Palmberg, G.E. Riach, R.E. Weber and N.C. MacDonald**, *"Handbook of Auger Electron Spectroscopy"*, Physical Electronics Industries Inc., Minneapolis, Minnesota, USA (1972).

**L.G. Parratt**, *"Surface studies of solids by total reflection of X-rays"*, Phys. Rev. **95**, 359-369 (1954).

**J.F. Pearson**, *"Advances in soft X-ray performance of microchannel plate detectors"*, PhD Thesis, University of Leicester (1984).

**J.F. Pearson, J.E. Lees, A.N. Brunton**, *"The Q data analysis system"*, technical document, University of Leicester (2000).

**J.F. Pearson, N.P. Bannister and G.W. Fraser**, *"Lobster-ISS: All-Sky X-ray Imaging from the International Space Station"*, Astron. Nachr., **324**, 168 (2003).

**J.F. Pearson**, *Private communication*, University of Leicester (2005).

**A.G. Peele, G.W. Fraser, A.N. Brunton, A.P. Martin, R.M. Rideout, W. Zhang, N. White, R. Petre and B. Feller**, *"Recent Studies of Lobster-eye Optics"*, Proc SPIE, **3444**, 404-415 (1998).

**A.G. Peele**, *"Deconvolution of an extended object viewed by a lobster-eye telescope"*, Nucl. Instr. Meth. A. **459**, 354-364 (2000).

**A.G. Peele**, *Private communication*, Department of Physics, La Trobe University, Victoria 3086, Australia (2004).

**K.J.H. Phillips, R. Mewe, L.K. Harra-Murnion, J.S. Kaastra, P. Beiersdorfer, G.V. Brown and D.A. Liedahl**, *"Benchmarking the MEKAL spectral code with solar X-ray spectra"*, Astron. Astrophys. Suppl. Ser. **138**, 381-393 (1999).

**B. Praček and M. Kern**, *"AES studies of active intrachannel surface in microchannel plates"*, Appl. Surf. Sci., **70/71**, 169-171 (1992).



**G.J. Price, “Microchannel plates in astronomy”, PhD Thesis, University of Leicester (2001).**

**G.J. Price, A.N. Brunton, M.W. Beijersbergen, G.W. Fraser, M. Bavdaz, J-P. Boutot, R. Fairbend, S.O. Flyckt, A. Peacock and E. Tomaselli, “X-ray focusing with Wolter microchannel plate optics”, Nucl. Instr. Meth. A. 490, 276-289 (2002).**

**G.J. Price, G.W. Fraser, J.F. Pearson, I.B. Hutchinson, A.D. Holland, J.P. Nussey, D. Vernon, D. Pullan and K. Turner, “Imaging X-ray Fluorescence Spectroscopy using Microchannel Plate X-ray Optics”, Spectroscopy Europe, 15, 8-13 (2003a).**

**G.J. Price, J. P. Nussey, A.N. Brunton, N.P. Bannister, J.F. Pearson and G.W. Fraser, “Final report on Lobster / XRF microchannel plate optics block”, Lobster-ISS report LOB-LUX-RE-009/1 (2003b).**

**G.J. Price, “The Imaging X-ray Fluorescence Spectrometer”, Technical document, University of Leicester (2004a).**

**G.J. Price, G.W. Fraser, J.F. Pearson, J.P. Nussey, I.B. Hutchinson, A.D. Holland, K. Turner and D. Pullan, “Prototype imaging X-ray fluorescence spectrometer based on microchannel plate optics”, Rev. Sci. Instr., 75, 2314-2319 (2004b).**

**W.C. Friedhorsky, A.G. Peele, K.A. Nugent, “An X-ray All-Sky Monitor with Extraordinary Sensitivity”, Mon. Not. R. Astron. Soc, 279, 733-750 (1996).**

**W.C. Friedhorsky, J. Bloch, A.N. Brunton, S.A. Drake, D. Roussel-Dupre, R.I. Epstein, E.E. Fenimore, G.W. Fraser, J.T. McGraw, K. Mukai, K.A. Nugent, P.T. O’Brien, A. Peele, R. Petre, W.T. Sanders, M. Ward, R.S. Warwick, R.L. Webster, N. White and B. Wong-Swanson, “The LOBSTER All-Sky X-ray Monitor: Executing the First Comprehensive Study of the Variable X-ray Sky”, Proposal to NASA SMEX opportunity (1997).**

**W.C. Friedhorsky, Private communication, Threat Reduction Directorate, Los Alamos National Laboratory, Los Alamos, New Mexico 87545, USA (2004).**



**D. Pullan**, *“Beagle 2: the exobiological lander of Mars Express”*, ESA Special Publication SP-1240 (2004).

**D. Pullan**, *“PALI: A coordinated geological specimen library and experimental data resource for the planetary research community”*, Geophysical. Research. Abstracts. 7, 8158 (2005a).

**D. Pullan**, *“Optimising planetary instrumentation for in-situ astrobiology: preliminary results from laboratory based “field” experiments on specimens exhibiting morphological biosignatures”*, Geophysical. Research. Abstracts. 7, 1741 (2005b).

**D. Pullan**, *Private communication*, University of Leicester (2005c).

**P.G. Richards and J.E. Lees**, *“Functional proteomics using microchannel plate detectors”*, Proteomics, 2, 256 (2002).

**E. Rol, R.A.M.J. Wijers, C. Kouveliotou, L. Kaper and Y. Kaneko**, *“How special are gamma-ray bursts: a diagnostic tool”*, Astrophys. J. (in press) (2005).

**N. Rosenthal**, *“Sensation: young British artists from the Saatchi Collection”*, Thames & Hudson Ltd (1998).

**D.J. Ruggieri**, *“Microchannel plate imaging detectors”*, IEEE Trans. Nucl. Sci. NS-19, 74 (1972).

**P.W. Sanford**, *“The Ariel 5 and UK 6 satellites”*, ESA X-ray Astronomy and Related Topics, N76, 25 (1975).

**W.K.H. Schmidt**, *“A proposed X-ray focusing device with a wide field of view for use in X-ray astronomy”*, Nucl. Instr. Meth. A. 127, 285 (1975).

**E.J. Schreier**, *“X-ray imaging from Einstein to AXAF”*, J. Opt. Soc. Am. 70, 1588 (1980).



**S.L.M. Schroeder, G.D. Moggridge, T. Rayment, R.M. Lambert, “In Situ Probing of the Near-Surface Properties of Heterogeneous Catalysts under Reaction Conditions: An Introduction to Total Electron-Yield XAS”, Journal of Molecular Catalysts A: Chemical, 119, 357-365 (1997).**

**A.D. Short, A. Keay and M.J.L. Turner, “Performance of the XMM EPIC MOS CCD detectors”, Proc. SPIE, 3445, 13 (1998).**

**A.D. Short, R.M. Ambrosi and M.J.L. Turner, “Spectral Re-distribution and Surface Loss Effects in Swift XRT (XMM-Newton EPIC) MOS CCDs”, Nucl. Instr. Meth. A, 484, 211 (2002).**

**S.H. Siddiqui, “An investigation of active surfaces of microchannel plates using Auger electron and ESCA spectroscopic techniques”, J. Appl. Phys., 48, 3053-3059 (1977).**

**M.R. Sims, C.T. Pillinger, I.P. Wright, J. Dowson, S. Whitehead, A. Wells, J.E. Spragg, G.W. Fraser, L. Richter, H. Harmacher, A. Johnstone, N.P. Meredith, C. de la Nougerede, B. Hancock, R. Turner, S. Peskett, A. Brack, J. Hobbs, M. Newns, A. Senior, M. Humphries, H.U Keller, N. Thomas, J.S. Lingard, J.C. Underwood, N.M. Sale, M.F. Neal and G. Klingelhofer, “Beagle 2: a proposed exobiology lander for ESA’s 2003 Mars express mission’, Adv. Space. Res. 23, 1925-1928 (1999).**

**S. Smith, R. Willis, G.W. Fraser and N.P. Bannister, “Lobster-ISS Field Obscuration Study, Issue 1.0”, Technical report, University of Leicester (2001).**

**C. Solis, A. Oliver and L. Rodríguez-Fernández, “Elemental Analyses of Marine Skeletons”, Nucl. Instr. Meth. B, 109/110, 617-620 (1996).**

**T.J. Stevenson, Private communication, University of Leicester (2004).**

**H. Su, “Applications of IXRFs in marine biology”, Internal report (in preparation), University of Leicester (2005).**

**D.L. Talboys, “Analysis of the Beagle 2 calibration target plate”, Internal report, University of Leicester (2003).**



- R. Tertian and F. Claisse**, *"Principles of Quantitative X-ray Fluorescence Analysis"* Heyden, London, (1982).
- A.M. Then and C.G. Pantano**, *"Formation and behaviour of surface layers on electron emission glasses"*, J. Non\_Cryst. Solids., 120, 178-187 (1990).
- H. Tomida, M. Matsuoka, K. Torii, S. Ueno, M. Sugizaki, W.M. Yuan, Y. Shirasaki, M. Sakano, S. Komatsu, H. Tsunemi, E. Miyata, N. Kawai, A. Yoshida, T. Mihara and I. Tanaka**, *"Solid state Slit Camera (SSC) of the MAXI Mission for the JEM (Japanese Experiment Module) on the International Space Station (ISS)"*, Proc. SPIE., 4140, 304-311 (2000).
- M.J.L. Turner, A. Smith and H.U. Zimmermann** *"The medium energy instrument on EXOSAT"*, Space. Sci. Rev, 30, 513 (1981).
- M.J.L. Turner, A.F. Abbey, M. Arnaud, M. Balasini, M. Barbera, E. Belsole, P. J. Benniel, J. P. Bernard, G. F. Bignami, M. Boer, U. Briel, I. Butler, C. Cara, C. Chabaud, R. Cole, A. Collura, M. Conte, A. Cros, M. Denby, P. Dhez, G. Di Cocol, J. Dowson, P. Ferrando, S. Ghizzardi, F. Gianotttil, C. V. Goodall, L. Gretton, R. G. Griffiths, O. Hainaut, J. F. Hochedez, A. D. Holland, E. Jourdain, E. Kendziorra, A. Lagostina, R. Laine, N. La Palombara, M. Lortholary, D. Lumb, P. Marty, S. Molendi, C. Pigot, E. Poindron, K. A. Pounds, J. N. Reeves, C. Reppin, R. Rothenflug, P. Salvetat, J. L. Sauvageot, D. Schmitt, S. Sembayl, A. D. T. Short, J. Spragg, J. Stephen, L. Strüder, A. Tiengo, M. Trifoglio, J. Trümper, S. Vercellone, L. Vigroux, G. Villa, M. J. Ward, S. Whitehead and E. Zonca** *"The European Photon Imaging Camera on XMM-Newton: The MOS Cameras"*, Astronomy and Astrophysics, 365, L27-L35 (2001).
- J.H. Underwood**, *"X-ray Optics"*, American Scientist, 66, 476 (1978).
- J. van Paradijs, C. Kouveliotou and R.A.M.J. Wijers**, *"Gamma-ray burst afterglows"*, Annu. Rev. Astron. Astrophys., 38, 279 (2000).
- K. Vogt**, *"Zur Optik des Flußkrebsauges"*, Zs. Naturforschung, 300, 691 (1975).
- P.R. Wakeling**, *"Mariner 10"*, Appl. Opt. 14, 200 (1975).



- M.C. Weisskopf, H.D. Tananbaum, L.P. van Speybroek and S.L. O'Dell, "*Chandra X-ray observatory (CXO): Overview*", Proc. SPIE., 4012, 2-16 (2000).
- N.E. White and H. Tananbaum, "*The Constellation X-ray mission*", Nucl. Instr. Meth. A., 436, 201-204 (1999).
- S.W. Wilkins, A.W. Stevenson, K.A. Nugent, H. Chapman and S. Steenstrup, "*On the concentration, focusing and collimation of X-rays and neutrons using microchannel plates and configuration of holes*", Rev. Sci. Instrum. 60, 1026 (1989).
- R. Willingale, "*The Grazing Incidence Telescope*", Nucl. Instr. Meth. A, 221, 1 (1984).
- R. Willingale, G.W. Fraser, A.N. Brunton and A.P. Martin, "*Hard X-ray imaging with microchannel plate optics*", Exp. Astron. 8, 281-296 (1998).
- R. Willingale, "*The Q Reference Manual*", Technical document, University of Leicester (2000).
- D.L. Windt, "*IMD – software for modelling the optical properties of multilayer films*", Computers in Phys., 12, 360 (1998).
- C.E. Winkler, N.P. Cummings, J.L. Randolph and D.H. Talley, "*Science instruments for the advanced X-ray astrophysics facility (AXAF)*", Proc. SPIE. 1948, 63 (1993).
- J.L. Wiza, "*Microchannel plate detectors*", Nucl. Instr. Meth. A. 162, 587 (1979).
- D.A. Wollman, K.D. Irwin, G.C. Hilton, L.L. Dulcie, D.E. Newbury and J.M. Martinis, "*High-resolution, energy-dispersive microcalorimeter spectrometer for X-ray microanalysis*", J. Microscopy, 188, 196 (1997).
- H. Wolter, "*Spiegelsysteme streifenden einfalls als abbildende optiken für Röntgenstrahlen*", Ann. Physik, 10, 94 (1952).
- S.E. Woosley and A.I. MacFadyen, "*Central engines for gamma-ray bursts*", Astron. Astrophys. Suppl. Ser. 138, 499-502 (1999).



**T.K. Yeoman**, *Private communication*, University of Leicester (2005).

**M.V. Zombeck, J.H. Chappell, A. Kenter, R.W. Moore, S.S. Murray, G.W. Fraser and S. Serio**, “*The High Resolution Camera (HRC) on the Advanced X-ray Astrophysics Facility (AXAF)*”, Proc. SPIE. **2518**, 96 (1995).